Analysis of Sparse-Lagrangian Two-Phase Coupling Using Direct Numerical Simulation

Von der Fakultät Energie-, Verfahrens- und Biotechnik der Universität Stuttgart zur Erlangung der Würde eines Doktors der Ingenieurwissenschaften (Dr.-Ing.) genehmigte Abhandlung

Vorgelegt von
Marvin Sontheimer
aus Bietigheim-Bissingen

Hauptberichter:	Prof. Dr. Andreas Kronenburg
Mitberichter:	Prof. Dr. Matthew Cleary
Tag der mündlichen Prüfung:	11. Dezember 2023

Institut für Technische Verbrennung
der Universität Stuttgart
2024

Acknowledgments

The present work was conducted during my time as a research assistant at the Institute for Combustion Technology (Institut für Technische Verbrennung, ITV) at the University of Stuttgart.

First and foremost I would like to thank my supervisor Prof. Dr. Andreas Kronenburg for giving me the opportunity to work on this exciting research topic. His supervision gave me a lot of freedom for my research and allowed me to develop further. At the same time, his continuous interest and constant encouragement have kept the work moving in the right direction. Without him, a successful completion of the thesis would not have been possible.

Furthermore I would like to thank Prof. Dr. Oliver T. Stein for his dedicated support of my research. His valuable advice combined with constructive criticism, as well as his always friendly and open manner, have contributed significantly to the success of the present work.

I would like to thank Prof. Dr. Matthew Cleary from The University of Sydney for the constructive discussions we had during his stay in Stuttgart and beyond. I appreciate him being the co-examiner of my thesis.

I am sincerely grateful to Dr. Thorsten Zirwes, formerly at KIT and now at ITV, for the smooth and productive collaboration and for the fruitful discussions on the numerical accuracy of OpenFOAM.

I want to thank my colleagues at ITV for the great time we had and for the helpful discussions and suggestions on my work.

Another thanks goes to Ricarda Schubert for taking care of the administrative matters, which allowed me to focus on my research project.

Finally, financial support by the Deutsche Forschungsgemeinschaft (DFG, project number 390544712) and support by the state of Baden-Württemberg through bwHPC is gratefully acknowledged.

Abstract

Liquid fuels are used extensively in industry and transportation, with spray combustion being the predominant feature. At a short distance from the injection nozzle, the liquid jet is atomized, and the fuel is present as a fine mist of dispersed droplets that evaporate and burn. This regime can be well described by an Euler-Lagrange approach for two-phase flows, where the carrier gas is solved in an Eulerian framework while the liquid droplets are treated as point particles and traced in a Lagrangian manner. However, since evaporation and combustion take place at the smallest scales, these effects as well as their interactions with turbulence cannot be fully resolved in practical simulations, and additional modeling is required. Within the present work, the sparse-Lagrangian multiple mapping conditioning (MMC) model is used to model the interactions between chemistry, droplet evaporation and turbulence, in combination with a large eddy simulation (LES) of the turbulent flow field. The stochastic variant of MMC is used, which employs a Monte Carlo solution of the reactive scalars by means of stochastic particles that represent instantaneous and local realizations of the composition field. The major advantage of this approach is that the chemical source term appears in closed form, while the interactions between the stochastic particles need to be represented by a mixing model. The MMC model utilizes the concept of localness of the mixing operator by conditioning the particle selection on a reference space, where in non-premixed flames mixture fraction is used. This allows MMC to be implemented with significantly fewer particles, which is referred to as a sparse particle method. The main challenge lies in modeling the heat and mass transfer between the two phases by coupling the fuel droplets with the gas phase. Since the gas phase is represented by a sparse set of particles, the conventional techniques cannot be readily applied. In the present work, a one-to-one coupling strategy with particle selection conditional on a set of reference variables is introduced to ensure localness of the two-phase coupling in composition space. The objective of the present work is to provide an in-depth analysis and validation of the two-phase coupling in the context of the sparse-Lagrangian MMC-LES modeling framework. To this end, the MMC-LES model is coupled with a carrier-phase direct numerical simulation (CP-DNS), where LES-like input data are obtained by post-filtering the DNS fields.

For the CP-DNS to provide an accurate reference solution, it is necessary to know the error that is introduced by the two-way coupling between the droplets and the gas phase based on the particle-source-in cell (PSI-cell) model in conventional Euler-Lagrange simulations. Therefore, an in-depth analysis of the cell-size dependence of the PSI-cell model is performed. In a first step, closed-form expressions are derived to describe the error of the evaporation rate and time of an isolated droplet. It is found that the error depends mainly on three parameters: the ratio of cell size to droplet diameter, a modified liquid-to-gas mass ratio, and the cell Péclet number, which includes the effect of relative droplet motion. Furthermore, it is shown that in practical cases the relation for the error of the evaporation time often reduces to the simple relation $\epsilon_\tau = (\Delta x/d_0)^{-1}$, the

universal validity of which is further confirmed by CFD simulations involving the effects of turbulence and multiple droplets. The second part of the analysis examines the effect of the cell size on the resolved mixture fraction variance. It turns out that the variance is accurately reproduced regardless of the computational cell size, provided that the inter-droplet space is resolved by the numerical grid. The findings of the analysis eventually lead to the formulation of criteria for performing grid-independent Euler-Lagrange simulations.

The second part of the thesis presents a systematic analysis of various two-phase coupling models in the context of intensive and sparse particle distributions of the gas phase using statistically homogeneous turbulence with different droplet loadings. Good agreement of unconditional mean and rms of the reactive scalars is found for both, sparse particle methods utilizing the MMC mixing model and a one-to-one coupling technique between the droplets and the stochastic particles, and conventional intensive particle methods, where the droplet mass is distributed equally to all particles within the computational cell. While the conditional fluctuations are underestimated in both models, the preferential distribution of the evaporated mass to particles closest to saturation conditions leads to improved predictions of the conditional mean temperature and its conditional variance, but significantly overpredicts the unconditional variance. Attempts are presented to incorporate the latter approach into the sparse-Lagrangian one-to-one coupling strategy, which allow for some control of gas-phase variance generation due to droplet evaporation. Furthermore, a time delay model is proposed, in which the source terms are partially rather than entirely transferred to the gas-phase particles in order to overcome the artificial mixing induced by the large particle volume in a sparse method. However, improvements are obtained only for short periods but not for the entire duration of the spray combustion process, which raises the need for further research.

In the third part of the thesis, the sparse-Lagrangian two-phase MMC-LES model is validated by means of *a priori* and *a posteriori* analyses using a temporally evolving droplet-laden double shear layer. The simulations show that the unconditional mean and rms of mixture fraction are accurately reproduced and are largely independent of the specific form of two-phase coupling. In contrast, the conditionally and unconditionally averaged temperatures show strong sensitivity and are significantly underestimated if the reference mixture fraction is used for particle selection. This is due to a lack of correlation between temperature and mixture fraction caused by local flame extinction. The introduction of temperature as an additional conditioning variable for two-phase coupling leads to improved predictions of evaporation rates and droplet size distributions with partial improvements also for the gas phase temperature, but overall the temperatures remain too low. The remaining discrepancies are attributed to modeling errors associated with the application of the MMC mixing model to spray flames. Further, it is shown that the anisotropic mixing time model recently proposed for gaseous flames also provides a reasonable mixing time for spray flames, but may require an adjustment of the model constant.

Kurzfassung

Flüssige Kraftstoffe werden in der Industrie und im Verkehrswesen in großem Umfang verwendet, wobei die Sprayverbrennung das vorherrschende Merkmal ist. In geringer Entfernung von der Einspritzdüse ist der Flüssigkeitsstrahl zerstäubt und der Kraftstoff liegt als feiner Nebel aus kleinen Tröpfchen vor, die verdampfen und verbrennen. Dieser Bereich kann gut durch einen Euler-Lagrange-Ansatz für Zweiphasenströmungen beschrieben werden, bei dem das Trägergas mit einem Eulerschen Ansatz gelöst wird, während die Flüssigkeitströpfchen als Punktteilchen behandelt und in einer Lagrangeschen Darstellung beschrieben werden. Da Verdampfung und Verbrennung jedoch auf den kleinsten Skalen stattfinden, können diese Effekte und ihre Wechselwirkungen mit der Turbulenz in praktischen Simulationen nicht vollständig aufgelöst werden, sodass eine zusätzliche Modellierung erforderlich ist. In der vorliegenden Arbeit wird das Multiple Mapping Conditioning (MMC) Modell verwendet, um die Wechselwirkungen zwischen Chemie, Tropfenverdampfung und Turbulenz zu modellieren, in Kombination mit einer Large Eddy Simulation (LES) des turbulenten Strömungsfeldes. Es wird die stochastische Variante des MMC-Modells verwendet, bei welchem eine Monte-Carlo-Lösung für die reaktiven Skalare mittels stochastischer Partikel angewendet wird, die momentane und lokale Realisierungen der Stoffzusammensetzung darstellen. Der große Vorteil dieses Ansatzes besteht darin, dass der chemische Quellterm in geschlossener Form vorliegt, während die Wechselwirkungen zwischen den stochastischen Teilchen durch ein Mischungsmodell abgebildet werden müssen. Das MMC-Modell nutzt das Konzept der Lokalisierung des Mischungsoperators, indem es die Partikelauswahl auf einen Referenzraum konditioniert, wobei in nicht-vorgemischten Flammen der Mischungsbruch verwendet wird. Dadurch kann das MMC-Modell mit deutlich weniger Partikeln implementiert werden, was als dünnbesetzte Partikelmethode bezeichnet wird. Die größte Herausforderung liegt in der Modellierung des Wärme- und Stoffübergangs zwischen den beiden Phasen durch Kopplung der Brennstofftröpfchen mit der Gasphase. Da die Gasphase durch eine geringe Anzahl von Partikeln repräsentiert wird, können die herkömmlichen Techniken nicht ohne weiteres angewandt werden. In der vorliegenden Arbeit wird hierzu eine Eins-zu-Eins-Kopplungsstrategie eingeführt, bei der die Partikel durch Minimierung des Abstandes in einem Referenzraum ausgewählt werden, um die Lokalität der Zweiphasenkopplung im Stoffzusammensetzungsraum zu gewährleisten. Ziel der vorliegenden Arbeit ist es, eine umfassende Analyse und Validierung der Zweiphasenkopplung im Rahmen von dünnbesetzten Partikelmethoden unter Verwendung des MMC-LES Modells durchzuführen. Zu diesem Zweck wird das MMC-LES-Modell mit einer direkten numerischen Simulation der Trägerphase (carrier-phase direct numerical simulation, CP-DNS) gekoppelt, bei der LES-ähnliche Eingangsgrößen durch Filterung der DNS-Felder gewonnen werden.

Damit die CP-DNS eine genaue Referenzlösung liefern kann, muss der Fehler bekannt sein, der durch die wechselseitige Kopplung zwischen den Tröpfchen und der Gasphase auf der Grundlage des PSI-cell-Models in konventionellen Euler-Lagrange-Simulationen

entsteht. Aus diesem Grund wird eine detaillierte Analyse der Abhängigkeit des PSI-cell-Models von der Zellgröße durchgeführt. In einem ersten Schritt werden geschlossene Ausdrücke hergeleitet, um den Fehler der Verdampfungsrate und -zeit eines isolierten Tropfens zu beschreiben. Der Fehler hängt hauptsächlich von drei Parametern ab: dem Verhältnis zwischen Zellgröße und Tropfendurchmesser, einem modifizierten Massenverhältnis, und der Péclet-Zahl, gebildet mit der Zellgröße, die den Effekt der relativen Tropfenbewegung berücksichtigt. Darüber hinaus wird gezeigt, dass sich die Beziehung für den Fehler der Verdunstungszeit in praktischen Fällen oft auf die einfache Beziehung $\epsilon_\tau = (\Delta x/d_0)^{-1}$ reduziert, deren universelle Gültigkeit durch CFD-Simulationen unter Einbeziehung der Effekte von Turbulenz und mehreren Tropfen bestätigt wird. Im zweiten Teil der Analyse wird die Auswirkung der Zellgröße auf die aufgelöste Varianz des Mischungsbruches untersucht. Es stellt sich heraus, dass die Varianz unabhängig von der Größe der Berechnungszelle genau wiedergegeben wird, sofern der Raum zwischen den Tropfen durch das numerische Gitter aufgelöst wird. Die Ergebnisse der Analyse führen schließlich zur Formulierung von Kriterien für die Durchführung gitterunabhängiger Euler-Lagrange-Simulationen.

Im zweiten Teil der Arbeit wird eine systematische Analyse verschiedener Zweiphasen-Kopplungsmodelle im Kontext von dichten und dünnbesetzten Partikelverteilungen der Gasphase anhand von statistisch homogener Turbulenz mit unterschiedlichen Tröpfchenbeladungen vorgestellt. Eine gute Übereinstimmung des unbedingten Mittelwerts und des quadratischen Mittels der reaktiven Skalare wird sowohl für dünnbesetzter Partikelmethoden gefunden, die das MMC-Mischungsmodell und eine Eins-zu-Eins-Kopplung zwischen den Tropfen und den stochastischen Partikeln verwenden, als auch für konventionelle dichte Partikelmethoden, bei denen die Tropfenmasse gleichmäßig auf alle Partikel innerhalb der Berechnungszelle verteilt wird. Während die bedingten Fluktuationen in beiden Modellen unterschätzt werden, führt die bevorzugte Verteilung der verdampften Masse auf Partikel, die den Sättigungsbedingungen am nächsten sind, zu einer verbesserten Vorhersage der bedingten mittleren Temperatur und ihrer bedingten Varianz, überschätzt aber die unbedingte Varianz erheblich. Daraufhin werden Ansätze vorgestellt, welche die Verteilung auf Partikel nahe Sättigungsbedingungen in die Eins-zu-Eins-Kopplungsstrategie einbeziehen, was eine gewisse Kontrolle der durch die Tröpfchenverdampfung verursachte Varianz in der Gasphase ermöglicht. Darüber hinaus wird ein Zeitverzögerungsmodell vorgeschlagen, bei dem die Quellterme nicht vollständig, sondern nur teilweise auf die Gasphasenpartikel übertragen werden, um die künstliche Vermischung zu überwinden, die durch das große Partikelvolumen in einer dünnbesetzten Partikelmethode verursacht wird. Allerdings werden Verbesserungen nur für kurze Phasen erzielt, nicht aber für die gesamte Dauer des Sprayverbrennungsprozesses, was weiteren Forschungsbedarf aufwirft.

Im dritten Teil der Arbeit wird die dünnbesetzte Zweiphasen-MMC-LES-Methode mittels *a priori*- und *a posteriori*-Analysen unter Verwendung einer sich zeitlich entwickelnden, tropfenbeladenen Doppelscherschicht validiert. Die Simulationen zeigen, dass der unbedingte Mittelwert und das quadratische Mittel des Mischungsbruchs genau wie-

dergegeben werden und weitgehend unabhängig von der spezifischen Form der Zweiphasenkopplung sind. Im Gegensatz dazu zeigen die unbedingt und bedingt gemittelten Temperaturen eine starke Empfindlichkeit und werden deutlich unterschätzt, wenn der Referenzmischungsbruch für die Partikelauswahl verwendet wird. Dies ist auf eine mangelnde Korrelation zwischen Temperatur und Mischungsbruch zurückzuführen, die durch lokale Flammenlöschung verursacht wird. Die Einführung der Temperatur als zusätzliche Konditionierungsvariable für die Zweiphasenkopplung führt zu verbesserten Vorhersagen von Verdampfungsraten und Tröpfchenengrößenverteilungen, mit teilweisen Verbesserungen auch für die Gasphasentemperatur, aber insgesamt bleiben die Temperaturen zu niedrig. Die verbleibenden Diskrepanzen sind auf Modellierungsfehler im Zusammenhang mit der Anwendung des MMC-Mischungsmodells auf Sprühflammen zurückzuführen. Des Weiteren wird gezeigt, dass das kürzlich für gasförmige Flammen vorgeschlagene anisotrope Mischungszeitmodell auch für Sprühflammen eine angemessene Mischungszeit liefert, aber gegebenenfalls eine Anpassung der Modellkonstante erfordert.

List of Publications

Parts of this thesis have been presented at conferences and published in the archival literature. The contents included in the present work have been modified with respect to the originally published texts and have been considerably extended to ensure the completeness, coherence and consistency of the present manuscript.

Journal Publications

(1) M. Sontheimer, A. Kronenburg, and O. T. Stein. Two-phase coupling for MMC-LES of spray combustion. *Proceedings of the Combustion Institute*, 38(2):3361-3369, 2021, doi: 10.1016/j.proci.2020.06.107.

- The simulations corresponding to this publication have been repeated using the latest code version and are presented in Ch. 7.
- Author's contribution: Programming (100 %), data generation (100 %), scientific originality (60 %).

(2) M. Sontheimer, A. Kronenburg, and O. T. Stein. Grid dependence of evaporation rates in Euler-Lagrange simulations of dilute sprays. *Combustion and Flame*, 232:111515, 2021, doi: 10.1016/j.combustflame.2021.111515.

- This paper forms the content of Sec. 5.2.
- Author's contribution: Programming (100 %), data generation (100 %), scientific originality (80 %).

(3) M. Sontheimer, A. Kronenburg, and O. T. Stein. A comparative study of two-phase coupling models for a sparse-Lagrangian particle method. *Proceedings of the Combustion Institute*, 39(2):2643-2652, 2023, doi: 10.1016/j.proci.2022.07.188.

- Data and results discussed in this paper are presented in Ch. 6.
- Author's contribution: Programming (100 %), data generation (100 %), scientific originality (70 %).

(4) T. Zirwes, M. Sontheimer, F. Zhang, A. Abdelsamie, F. E. Hernández Pérez, O. T. Stein, H. G. Im, A. Kronenburg, and H. Bockhorn. Assessment of numerical accuracy and parallel performance of OpenFOAM and its reacting flow extension EBIdnsFoam. *Flow, Turbulence and Combustion*, 111(2):567-602, 2023, doi: 10.1007/s10494-023-00449-8.

- Parts of the results as well as complementary studies are presented in Appendix D.
- Author's contribution: Programming (10 %), data generation (10 %), scientific originality (15 %).

Conference Publications

(1) M. Sontheimer, A. Kronenburg, and O. T. Stein. Analysis of Multiphase MMC Coupling Using DNS of a Reacting Double Shear Layer. *Proceedings of the 9th European Combustion Meeting*, Lisbon, Portugal, 2019.

- This paper has been published in the conference proceedings and parts of the analysis are incorporated into Ch. 7.
- Author's contribution: Programming (100 %), data generation (100 %), scientific originality (50 %).

(2) M. Sontheimer, O. T. Stein, A. Kronenburg. Analysis of multiphase MMC coupling using DNS of an evolving droplet-laden double shear layer. *17th Int. Conference on Numerical Combustion*, Aachen, Germany, 2019.

- The results presented at the conference were reproduced using the latest code version and are included in Ch. 7.
- Author's contribution: Programming (100 %), data generation (100 %), scientific originality (60 %).

(3) M. Sontheimer, A. Kronenburg, and O. T. Stein. Analysis of the particle-source-in-cell model for LES of spray combustion. *29. Deutscher Flammentag*, Bochum, Germany, 2019.

- This paper has been published in the conference proceedings and is part of Sec. 5.2.
- Author's contribution: Programming (100 %), data generation (100 %), scientific originality (60 %).

(4) M. Sontheimer, A. Kronenburg, and O. T. Stein. Effects of PSI-cell modeling on subgrid-scale mixture fraction variance for LES of spray combustion. *30. Deutscher Flammentag*, Hannover-Garbsen, Germany, 2021.

- This paper has been published in the conference proceedings and parts of it are incorporated into Sec. 5.3 and Sec. 6.2.
- Author's contribution: Programming (100 %), data generation (100 %), scientific originality (70 %).

Contents

List of Figures

List of Tables

Nomenclature

Latin Letters

a_{ik}	Number of atoms in element i (-)
A	Pre-exponential factor (various units)
A	Cross-sectional area (m^2)
B_M	Spalding mass transfer number (-)
B_T	Spalding heat transfer number (-)
c	Specific heat capacity (J/(kg K))
c_p	Specific heat capacity at constant pressure (J/(kg K))
C	A constant (various units)
C_D	Drag coefficient (-)
C_f	Constant in the model for mixture fraction variance (-)
C_L	Constant in the mixing time scale model (-)
C_{lam}, C_{turb}	Constants in the time delay model (-)
C_m	Constant in the isoscalar sliver relation (-)
C_{mix}	Constant in the mixing model (-)
C_s	Smagorinsky constant (-)
C_σ	Constant in the σ-model (-)
CFL	Courant number (-)
d	Droplet diameter (m)
d_f	Distance in mixture fraction space (-)
d_s	Distance in saturation space (-)
d_T	Distance in temperature space (K)
d_x	Distance in physical space (m)
d_ξ	Distance in conditioning space (various units)
$\hat{d}^2$	Effective square distance (-)
$\mathrm{d}\omega_i$	Increment of a Wiener process ($s^{1/2}$)
D_f	Fractal dimension (-)
$\mathcal{D}$	Effective binary diffusion coefficient (m^2/s)
$\mathcal{D}_t$	Turbulent diffusivity (m^2/s)
E_A	Activation energy (J/kmol)

E_k	Kinetic energy per unit mass (J/kg)
f	Mixture fraction (-)
f_m	Parameter controlling the distance in mixture fraction space (-)
f_V	Mixture fraction variance (-)
f_1, f_2	Correction factors (-)
$\mathbf{F}$	Force vector (N)
$\mathbf{F}_D$	Drag force vector (N)
F_L	Filtered mass density function (kg/m^3)
F_M, F_T	Correction factors for the film thicknesses (-)
$\mathcal{F}$	A function (various units)
$\mathcal{F}$	Face flux (kg/(m^2 s))
G	Kernel function (m^{-3})
h	Absolute enthalpy per unit mass (J/kg)
h_f°	Enthalpy of formation at standard-state pressure (J/kg)
h_s	Sensible enthalpy per unit mass (J/kg)
H	Absolute enthalpy (J)
H	Height of the central jet or fuel layer (m)
I	Turbulence intensity (-)
$\mathbf{I}$	Momentum (kg/(m s))
j_j^{sgs}	Subgrid scalar flux in j direction (kg/(m^2 s))
j_{kj}	Diffusional mass flux of species k in j direction (kg/(m^2 s))
k	Turbulent kinetic energy (J/kg)
k_f	Rate constant of the forward reaction (s^{-1})
k_r	Rate constant of the reverse reaction (s^{-1})
K	Evaporation constant (m^2/s)
l_{int}	Integral length scale (m)
l_{x_i}, l_f	Scaled spans in physical and mixture fraction space (-)
L	Length (m)
L_v	Latent heat of vaporization (J/kg)
Le	Lewis number (-)
m	Mass (kg)
$\dot{m}$	Evaporation rate (kg/s)
M	Mach number (-)
M_α	Mixing term (various units)
$\mathcal{M}$	Molar mass (kg/kmol)
n	Number of particles per unit volume (m^{-3})
N_d	Number of droplets (-)
N_r	Number of reactions (-)

N_s	Number of species (-)
N^{sp}	Number of stochastic particles (-)
$N^{sp,d}$	Number of stochastic particles per droplet (-)
N_t	Number of time steps (-)
N_{total}	Total number of grid cells (-)
N_x, N_y, N_z	Number of grid cells in the three spatial directions (-)
N_ξ	Number of conditioning variables (-)
Nu	Nusselt number (-)
p	Pressure (Pa)
p_{mix}	Mixing probability (-)
p_{sat}	Saturated vapor pressure (Pa)
P	Characteristic polynomial (-)
Pe	Péclet number (-)
$\text{Pe}_{\Delta x}$	Péclet number based on the cell size (-)
Pr	Prandtl number (-)
q	A variable (-)
q_d	Droplet heating term per unit evaporative mass (J/kg)
q_j	Heat flux in j direction (W/m^2)
$\dot{Q}_d$	Droplet heating term (W)
r	Radius (m)
r_c	Cutoff length (m)
r_m	Parameter controlling the distance in physical space (m)
R	Radius (m)
$\mathcal{R}$	Specific gas constant (J/(kg K))
$\mathscr{R}$	Universal gas constant (J/(kmol K))
Re	Reynolds number (-)
Re_λ	Taylor Reynolds number (-)
s_m^*	Parameter controlling the distance in saturation space (-)
S	Surface area (m^2)
S_{ij}	Components of the rate-of-strain tensor (s^{-1})
$\dot{S}_M$	Mass source term due to evaporation ($\text{kg/(m}^3\,\text{s)}$)
$\dot{S}_{u,i}$	Momentum source term due to evaporation ($\text{kg/(m}^2\,\text{s}^2\text{)}$)
$\dot{S}_h$, $\dot{S}_{h_s}$, $\dot{S}_T$	Energy source term due to evaporation ($\text{J/(m}^3\,\text{s)}$)
Sc	Schmidt number (-)
Sc_t	Turbulent Schmidt number (-)
Sh	Sherwood number (-)
St	Stokes number (-)
t	Time (s)

t_c	Characteristic time (s)
t_j	Characteristic jet time scale (s)
T	Temperature (K)
T_{boil}	Boiling temperature (K)
T_m^*	Parameter controlling the distance in temperature space (K)
$\mathbf{u} = (u, v, w)^\mathsf{T}$	Cartesian velocity vector (m/s)
$\mathbf{u} = (u_1, u_2, u_3)^\mathsf{T}$	Cartesian velocity vector using index notation (m/s)
u_r	Velocity in radial direction (m/s)
U	Characteristic velocity (m/s)
V	Volume (m^3)
V_{cell}	Cell volume (m^3)
W_α	Generalized chemical source term (various units)
$\mathbf{x} = (x, y, z)^\mathsf{T}$	Cartesian coordinate vector (m)
$\mathbf{x} = (x_1, x_2, x_3)^\mathsf{T}$	Cartesian coordinate vector using index notation (m)
X_k	Mole fraction of species k (-)
Y_k	Mass fraction of species k (-)
z	Mixture fraction solved on the stochastic particles (-)
$\mathcal{Z}_i$	Mass fraction of element i (-)

Greek Letters

α	Thermal diffusivity (m^2/s)
α, β	Parameters (-)
β	Temperature exponent (-)
β	Constant in the C&K model (-)
γ	Averaging parameter (-)
γ	Mixing extent (-)
Γ	Gamma function (-)
δ	Parameter controlling the source term distribution (-)
δ_{ij}	Kronecker delta (-)
δ_M, δ_T	Film thicknesses (m)
Δ	Length for source term distribution (m)
Δ_L	Nominal particle distance (m)
Δ_{LES}	LES filter width (m)
Δr	Grid spacing in radial direction (m)
Δt	Time step width (s)
Δx	Cell size (m)
ε	Dissipation rate of kinetic energy (m^2/s^3)
$\epsilon_{\dot{m}}$	Relative error of the evaporation rate (-)

ϵ_τ	Relative error of the evaporation time (-)
ζ	Fine-grained density (-)
η	Kolmogorov length scale (m)
κ	Wavenumber (m^{-1})
λ	Taylor length scale (m)
λ	Thermal conductivity ($\mathrm{W/(m\,K)}$)
λ_x, λ_f, λ_T, λ_{ξ_i}	Boolean variables (-)
μ	Dynamic viscosity ($\mathrm{kg/(m\,s)}$)
μ_t	Turbulent dynamic viscosity ($\mathrm{kg/(m\,s)}$)
ν	Dimension (-)
ν	Kinematic viscosity (m^2/s)
ν_t	Turbulent kinematic viscosity (m^2/s)
ν'_{ik}	Stoichiometric coefficients on the reactants side (-)
ν''_{ik}	Stoichiometric coefficients on the products side (-)
ξ	Random variable (-)
ξ_i	Conditioning variable (various units)
$\xi^*_{i,m}$	Parameter controlling the distance in conditioning space (various units)
π	Pi (-)
Π	Non-dimensional group (-)
Π_α	Generalized evaporation source term (various units)
ρ	Density ($\mathrm{kg/m}^3$)
σ_1, σ_2, σ_3	Singular values of the velocity gradient tensor (s^{-1})
ς	Enstrophy (s^{-2})
τ_d	Droplet response time (s)
$\tau_\mathcal{D}$	Diffusive time scale (s)
τ_E	Eulerian time scale (s)
τ_{evap}	Evaporation time (s)
τ_{ij}	Viscous stress tensor ($\mathrm{kg/(m\,s^2)}$)
τ_{ij}^{sgs}	Subgrid-scale stress tensor ($\mathrm{kg/(m\,s^2)}$)
τ_L	Lagrangian mixing time (s)
τ_{mix}	A (general) mixing time (s)
τ_{relax}	Relaxation time (s)
τ_0	Eddy turnover time (s)
ϕ	Parameter in the droplet evaporation model (-)
ϕ_α	Composition vector (various units)
ϕ_α^E	Equivalent composition (various units)
$\phi_\alpha^{\mathrm{mean}}$	A mean composition (various units)

ϕ_d	Dispersed phase volume fraction (-)
φ	Mass ratio parameter (-)
Φ	Equivalence ratio (-)
χ	Scalar dissipation rate (s^{-1})
$\check{\chi}$	Scalar dissipation rate based on filtered variables (s^{-1})
ψ_α	Sample space for ϕ_α (various units)
ω	Vorticity (s^{-1})
$\dot{\omega}_k$	Chemical reaction rate of species k ($kg/(m^3\,s)$)

Operators

$\overline{\cdot}$	Filtered quantity
$\widetilde{\cdot}$	Density-weighted filtered quantity
$\lvert\cdot\rvert$	Absolute value
$\lVert\cdot\rVert$	Norm of a vector
$\langle\cdot\rangle$	Averaged quantity
$\langle\cdot\lvert\cdot\rangle$	Conditionally filtered or averaged quantity
∇	Nabla operator
$\exp(\cdot)$	Exponential function
$\ln(\cdot)$	Natural logarithm
$\log(\cdot)$	Common logarithm (base 10)
$\sin(\cdot)$	Sine function
$\cos(\cdot)$	Cosine function
$\tanh(\cdot)$	Hyperbolic tangent
$\max(\cdot,\cdot)$	Maximum function
$\min(\cdot,\cdot)$	Minimum function

Subscripts

a	Air
d	Droplet
eff	Effective value
F	Fuel species
Fu	Fuel stream
g	Gas
i, j	Indices
k	Species index
l	Liquid
max	Maximum value

min	Minimum value
Ox	Oxidizer stream
ref	Reference value
s	Surface
st	Stoichiometric value
α, β	Indices for the composition vector
0	Initial value
∞	Far-field value

Superscripts

k	Iteration index
n	Time step index
o	Value at standard-state pressure
sp, p, q	Stochastic particle property
T	Transpose of a vector
$'$	Subfilter fluctuation
$'$	Integration variable
$''$	Subfilter fluctuation related to density-weighted filtering
$*$	Modified quantity
$*$, $**$	Intermediate value
$\widehat{\ }$	Normalized quantity

Acronyms

CFD	Computational fluid dynamics
CMC	Conditional moment closure
CP-DNS	Carrier-phase direct numerical simulation
CPU	Central processing unit
DNS	Direct numerical simulation
EBU	Eddy breakup
EDC	Eddy dissipation concept
EDM	Eddy dissipation model
FDF	Filtered density function
FMDF	Filtered mass density function
IEA	International Energy Agency
IEM	Interaction by exchange with the mean
LES	Large eddy simulation
LMSE	Linear mean-square estimation

MMC	Multiple mapping conditioning
ODE	Ordinary differential equation
PDF	Probability density function
PISO	Pressure implicit with splitting of operators
PSI-cell	Particle-source-in-cell
RANS	Reynolds-averaged Navier-Stokes
SGS	Subgrid scale
SIMPLE	Semi-implicit method for pressure linked equations
TVD	Total variation diminishing

Conventions

Scalars are represented by *italic* characters.

Vectors are represented by **bold** characters.

Chapter 1

Introduction

1.1 Motivation

Liquid fuels have been the largest source of energy for decades, as illustrated in Fig. 1.1, and still account for about 30 % of the world's primary energy consumption nowadays [175]. Compared to other fuels, liquid fuels offer a number of decisive advantages, such as their high calorific value, their good transportability and storability without energy losses, and their high combustion efficiency without the formation of residues such as ash. These features make them particularly attractive for the transportation sector, where liquid fuels account for more than 90 % of the energy consumption in 2021 [91]. Typical applications of liquid-fueled combustion devices are internal combustion engines in passenger cars, trucks and ships, gas-turbine engines used in aviation and marine applications, liquid-rocket engines and oil-fired furnaces.

The vast majority of liquid fuels, including gasoline, diesel and kerosene, are derived from fossil fuels by refining naturally occurring crude oil. The burning of fossil fuels releases large amounts of carbon dioxide (CO_2) as well as other pollutants such as NO_x into the air, making them largely responsible for air pollution and global warming, with petroleum accounting for about 32 % of the global CO_2 emissions [174]. The negative consequences on humanity and the environment are becoming increasingly clear, so that a rethinking of the energy market is currently taking place with the aim of replacing fossil fuels by alternative energy sources with low-carbon fuels.

The International Energy Agency (IEA) has developed projections for future energy markets based on three scenarios, which are shown in Fig. 1.2 for the transportation sector, which has traditionally been the core of oil consumption. In the stated policies scenario (Fig. 1.2(a)), which reflects current policy settings, liquid fuels remain the predominant energy source for the next decades. However, the sce-

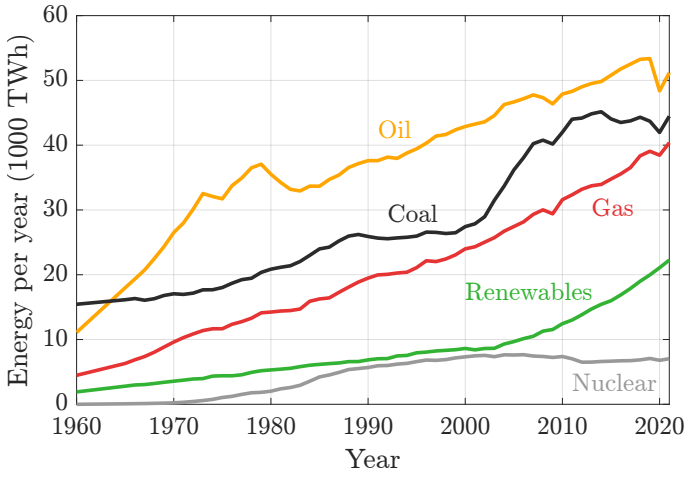

Figure 1.1: World primary energy consumption by source. Traditional biomass (including mainly wood fuels) is not shown. The data is provided by Ritchie *et al.* [175] and based on [153, 191].

nario would lead to an increase in global average temperatures of about 2.5 °C by 2100, posing a serious threat to the well-being of humans and global ecosystems. In the announced pledges scenario (Fig. 1.2(b)), which assumes that all climate commitments announced by governments around the world are met in full and on time, conventional petroleum-based fuels are increasingly displaced by alternative forms of energy such as electricity and liquid biofuels, but still remain the largest source of energy in the transportation sector through 2050. The third scenario shows a pathway to achieve net zero CO_2 emissions by 2050 and limit global warming to 1.5 °C while ensuring universal access to modern energy by 2030 (Fig. 1.2(c)). Here, global oil consumption in the transportation sector will drop drastically by 2050, as passenger cars will increasingly be replaced by electric vehicles, but also liquid biofuels and hydrogen-based fuels will gain in importance, especially in road freight, aviation and shipping. Regardless of which scenario will come to pass, the transition to clean energy alternatives will take several more decades, leaving conventional petroleum-based fuels as the dominant energy source in the transportation sector until at least 2040. Furthermore, liquid-fueled combustion systems will continue to play an important role in the future through renewable low-carbon fuels. It is therefore more important than ever to develop modern and more efficient combustion systems that make optimal use of fossil and alternative fuels in order to significantly reduce pollutant emissions.

In most liquid-fueled combustion devices, including diesel engines and gas-turbine engines, turbulent spray combustion is the predominant feature, where the liquid fuel jet is injected into the combustion chamber and atomizes into a dispersed spray of small droplets that undergo evaporation and subsequent combustion. Turbulent spray combustion is a typical multiscale problem due to the presence of a

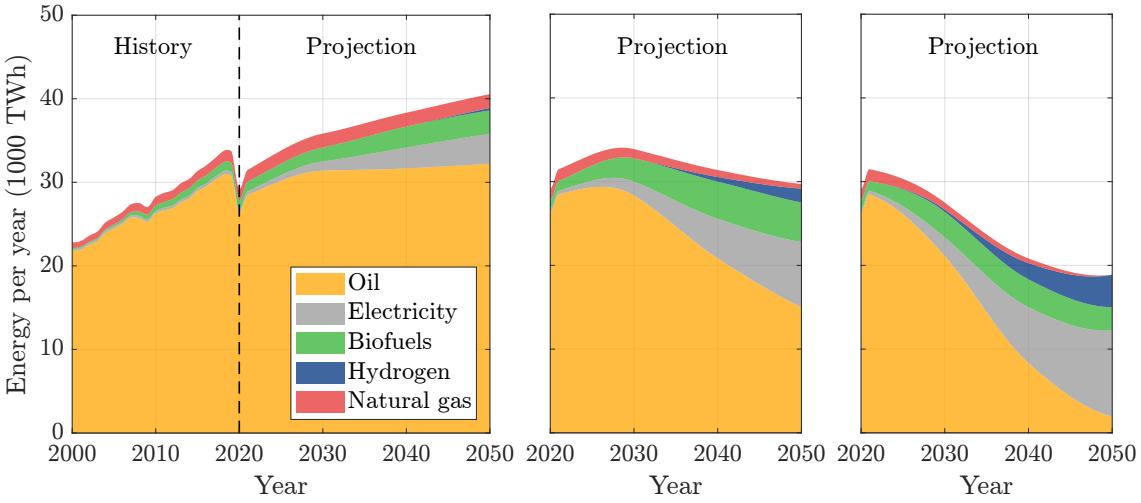

(a) Stated policies scenario. **(b)** Announced pledges scenario. **(c)** Net zero emissions scenario.

Figure 1.2: World energy consumption in the transportation sector for years 2000 to 2050 assuming different scenarios developed by the IEA [91]. The stated policies scenario shows the evolution resulting from today's policy settings. The announced pledges scenario assumes that all climate commitments announced by governments around the world are met in full and on time. The net zero emissions scenario shows a way to achieve net zero CO_2 emissions by 2050 and to limit global warming to 1.5 °C while ensuring universal access to modern energy by 2030.

wide range of length and time scales, and the complex interactions between the turbulent flow field, the combustion processes and the evaporating droplets are still not fully explored. With the increasing availability of computational resources in the last decades, computational fluid dynamics (CFD) has become a valuable tool for gaining insight into the complex spray phenomena as well as for the design and optimization of modern combustion systems. An efficient simulation tool, as required by the industry, cannot resolve all the details of spray combustion phenomena, since the resolution down to the smallest scales would drastically increase the computational costs. Accordingly, sophisticated models are required to describe the strongly nonlinear interactions between turbulence, chemistry, and droplet evaporation at the subgrid level, where higher efficiency is usually accompanied by sacrifices in accuracy. The present work aims to develop and validate a modeling framework for the simulation of turbulent spray combustion that achieves both an accurate representation of the underlying physics and a relatively low computational cost.

1.2 State of the Art

Large eddy simulation (LES) holds the greatest potential for predicting the turbulent flow field, as it computes the large energy-containing turbulent motions directly and only models the small scales that behave more universally. Combustion, however, is

a molecular process that occurs almost exclusively at the smallest scales that are not resolved by the computational grid in LES, and thus requires a model for the correlations between combustion and turbulence at subgrid level. Since chemical kinetics are highly nonlinear and depend on a large number of reacting species, modeling of the turbulence-chemistry interactions is a challenging task and cannot be achieved solely based on information from the resolved fields. A promising approach is given by the transported probability density function (PDF) method [45, 79, 145, 158], which employs a probabilistic description of the reactive scalars (i.e., species mass fractions and enthalpy) by means of their joint scalar PDF, whose evolution is usually determined by a Monte Carlo particle method [156, 161]. The major advantage of the transported PDF method is that the highly nonlinear chemical source terms appear in closed form. Furthermore, the method is not confined to a specific combustion regime and thus has the ability to successfully predict complex phenomena such as extinction and re-ignition [134, 218, 230]. While the turbulence-chemistry interactions are accurately captured by the transported PDF method, modeling is required for the effect of molecular diffusion, which is represented by a particle interaction model that emulates mixing. Conventional mixing models [38, 44, 46, 94, 203, 216] require a relatively high number of stochastic particles in each computational cell and thus increasing the computational cost, while often failing to satisfy important properties of the mixing operator such as localness in composition space, which is crucial for combustion to prevent unphysical mixing [56, 163, 203]. The sparse-Lagrangian multiple mapping conditioning (MMC) model [28, 30, 31, 108] has been proposed as a highly efficient alternative to the classical mixing models, which satisfies all of the desired properties of a good mixing model. In particular it enforces localness in composition space by conditioning the selection of mixing partners on an independent reference space. This allows the model to be implemented with a significantly lower number of particles, typically less than the number of LES cells, which reduces the computational cost and thus enables the use of detailed finite-rate chemical kinetics. The MMC-LES model has been successfully applied to a number of non-premixed [69, 89, 142, 177, 205, 218], partially premixed [60, 70, 186] and premixed [90, 200, 201] flames, demonstrating its superior performance over the classical combustion models. Recently, the MMC-LES model was extended to turbulent spray flames by Khan *et al.* [101, 102] and to solid fuel combustion by Zhao *et al.* [240].

The extension of transported PDF methods to spray flames requires additional modeling for the coupling of mass and energy between the gas phase, whose composition is represented by stochastic particles, and the liquid phase, which is modeled as spherical droplets following a Lagrangian formulation [54, 96]. The two-phase

coupling requires the distribution of the evaporated mass and associated energy (in general the evaporation source terms) to the gas phase. Several models are available for the conventional particle methods utilizing a large number of stochastic particles per cell, including an even distribution of the source terms among the particles within each cell [66, 67], preferential distribution to individual particles [83, 140], as well as the generation of new gas-phase particles [47, 93, 113]. An evaluation of various two-phase coupling models is presented in Tang *et al.* [208], revealing qualitative differences between the models in particular for conditionally averaged quantities. If a sparse particle distribution is used, as is the case with the MMC-LES mixing model, the coupling between the gas phase and the dispersed droplets is more challenging, as there is not always a stochastic particle close to each droplet. Therefore, more sophisticated models are required, which may use concepts from the MMC mixing pair selection by conditioning the two-phase coupling on a set of reference variables [102, 197]. Although there are already several applications of the two-phase MMC-LES model to spray flames [102, 103, 184, 185], little research has been done on the sparse-Lagrangian two-phase coupling so far. For this reason, the scope of the present work is to provide a detailed systematic analysis and validation of the two-phase MMC-LES model in the context of dilute spray flames.

1.3 Objectives

The primary objective of the present work is to provide an in-depth analysis and validation of the two-phase MMC-LES model by means of a carrier-phase direct numerical solution (CP-DNS), which fully resolves the turbulent reacting gas phase while treating droplets as point particles. In contrast to experiments, the CP-DNS provides high-quality time- and space-resolved data, and allows for an unbiased comparison of the results, since finite rate chemistry, droplet evaporation modeling and thermophysical properties are exactly known and identical in the CP-DNS and the MMC-LES. The model validation can be done using *a priori* and *a posteriori* analyses [210]. In an *a priori* analysis, the MMC-LES model is coupled with the CP-DNS (so no actual LES is performed), making use of explicitly filtered quantities from the CP-DNS. This eliminates uncertainties from LES subgrid modeling and allows errors to be directly associated with the MMC model. In an *a posteriori* analysis, a real, independent MMC-LES is performed, and the results are subsequently compared with the (filtered) CP-DNS data. This provides a more realistic approach to testing the two-phase MMC-LES model but does not allow separation between individual modeling errors. Therefore, an in-depth validation usually requires both, *a priori* and *a posteriori* analyses.

The main building blocks of the present analysis along with the specific key questions are as follows:

(1) *Quantification of the cell-size dependence of the particle-source-in-cell (PSI-cell) model in the context of Euler-Lagrange simulations of dilute sprays.*
For the CP-DNS to provide an accurate reference solution, it is necessary to have knowledge of the error introduced by the PSI-cell model, which is used to couple the droplets with the gas phase. This requires answering the following questions:

- How can the error of the evaporation rate and time be estimated prior to the simulation?
- How does a lack of resolution of the near-droplet fields affect the mixture fraction variance?

(2) *Evaluation of various two-phase coupling models by means of CP-DNS.*
Based on a simplified configuration assuming homogeneous isotropic turbulence, several two-phase coupling models are to be evaluated in the context of intensive and sparse particle methods, where all input data for the stochastic particle methods are extracted from the CP-DNS. The following questions are to be addressed:

- What is a suitable mixing time scale for dilute spray flames?
- How can the evaporated mass be distributed among stochastic particles in order to mimic real evaporation?
- How does the relative performance of the sparse-Lagrangian MMC-LES model compare to conventional intensive particle methods?

(3) *Performing an in-depth analysis and validation of the sparse-Lagrangian two-phase MMC-LES model.*
The MMC-LES model is applied to a temporally evolving droplet-laden double shear layer and tested using *a priori* and *a posteriori* analyses. The following questions are in the focus:

- How can the evaporation rate be determined if the gas phase is represented by a sparse distribution of stochastic particles?
- How robust is the two-phase MMC-LES model with respect to the modeling parameters?

1.4 Thesis Outline

Chapter 2 covers the fundamental aspects of modeling turbulent spray combustion, allowing a better classification of the methods and models used in the present work. The mathematical description of dilute spray flames is given in Ch. 3, and involves the specification of the instantaneous balance equations for the gas phase as well as a detailed derivation of the Lagrangian equations governing the fuel droplets. Chapter 4 presents the two-phase MMC-LES model for dilute spray combustion along with details on the numerical implementation. Special emphasis is given to the presentation of models for two-phase coupling, including a discussion of their basic properties. An in-depth analysis of the grid dependence of the PSI-cell model is provided in Ch. 5, where closed-form expressions describing the cell-size dependence of the evaporation rate and time are derived. Further, the effect of the cell size on the mixture fraction variance is discussed. Chapter 6 provides a systematic analysis of various two-phase coupling models in the context of both dense and sparse particle distributions based on homogeneous isotropic turbulence, and outlines possible options to improve the model predictions. This is followed by a detailed analysis and validation of the sparse-Lagrangian two-phase MMC-LES model using *a priori* (Ch. 7) and *a posteriori* (Ch. 8) analyses based on a temporally evolving double shear layer. In addition to discussing the need for conditioning of the two-phase coupling, the influence of the MMC modeling parameters is examined. Finally, Ch. 9 summarizes the work and the main findings and provides suggestions for future work. The extensive appendix contains additional derivations and analyses accompanying the main text.

Chapter 2

Fundamentals of Turbulent Spray Combustion

This chapter provides fundamental knowledge of turbulent spray combustion and its modeling as required for the subsequent chapters. The chapter is divided into the topics of turbulent flows, turbulent combustion and spray characteristics, where for each topic the basic theory is summarized and the numerical modeling is addressed.

2.1 Turbulent Flows

Flows are classified to be either laminar or turbulent. Laminar flows are characterized by a well-ordered motion, with layers "sliding" past one another at different velocities without fluid elements being exchanged perpendicular to the flow direction. In contrast, turbulent flows are inherently three-dimensional and unsteady, and exhibit a chaotic and seemingly random behavior, resulting in strongly increased mixing among the fluid elements. Turbulent flows are frequently observed in everyday phenomena (e.g., smoke from a chimney, atmospheric streams, water in a waterfall) and play an important role in most industrial applications. A characteristic feature of turbulent flows is the occurrence of eddies in a wide range of length scales. The largest eddies, whose size is comparable to the dimensions of the flow, extract kinetic energy from the mean flow. These energy-containing eddies, which are highly inertial and anisotropic, tend to be unstable and break up, transferring kinetic energy to smaller eddies. The smallest eddies, whose size is described by the Kolmogorov length scale η, have a universal character independent of the flow geometry and conditions, and dissipate their energy into heat through the molecular viscosity of the fluid. This process is known as the energy cascade, as depicted in Fig. 2.1.

Whether a fluid flow is laminar, transitional or turbulent is characterized by

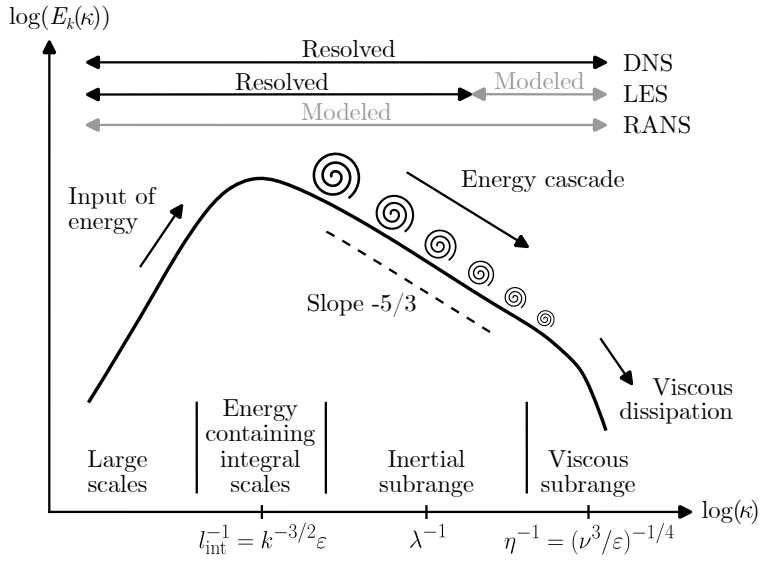

Figure 2.1: Schematic sketch of the turbulent kinetic energy spectrum $E_k(\kappa)$ as a function of the wavenumber κ. The characteristic length scales are the integral length scale l_{int}, the Taylor length scale λ, and the Kolmogorov length scale η.

the Reynolds number, which relates inertial forces (i.e., forces that resist a change in the velocity) to viscous forces (i.e., forces due to friction between the fluid layers). It is defined as

$$\text{Re} = \frac{UL}{\nu}, \tag{2.1}$$

where U and L are the characteristic velocity and length scale, respectively, and ν is the kinematic viscosity of the fluid. For $\text{Re} \ll 1$, viscous forces dominate and the flow is laminar and steady, which is referred to as Stokes flow or creeping flow. As the Reynolds number increases, transient effects and separation of boundary layers may occur, while the flow still remains laminar. The transition to turbulence occurs when the Reynolds number exceeds a certain threshold called the critical Reynolds number, whose value depends on the particular problem. For Reynolds numbers above the critical value, any disturbance leads to the development of a turbulent flow with the aforementioned characteristics.

The dynamics of a fluid flow are described mathematically by the Navier-Stokes equations, which are generally valid for both laminar and turbulent flows. A direct solution, which is referred to as direct numerical simulation (DNS), requires the resolution of all length and time scales occurring in the flow up to the Kolmogorov length scale. Assuming homogeneous isotropic turbulence, it can be shown that the total number of grid cells in a three-dimensional simulation scales with $N_{\text{total}} \sim \text{Re}^{9/4}$, where Re is the turbulent Reynolds number based on the root-mean-square velocity and the integral length scale [55, 163]. The computational cost is proportional to the number of grid cells and the number of time steps, and thus grows with Re^3.

These high requirements on computational resources limit the application of DNS to simple configurations for fundamental research, and make it virtually impossible to be used as a tool for industrial applications with high Reynolds numbers.

The computational complexity can be significantly reduced if the Reynolds-averaged Navier-Stokes (RANS) equations are solved. This involves a decomposition of the instantaneous flow quantities into their time-averaged and fluctuating components, which is referred to as Reynolds decomposition. The time-averaged quantities are solved directly, while the effects of the fluctuations, which are represented by the nonlinear Reynolds stress term, must be modeled. Many different turbulence models are available, which can be classified into the two groups of eddy viscosity models and Reynolds stress models. In eddy viscosity models, the Reynolds stress term is linked to the mean rate-of-strain tensor via the turbulent eddy viscosity, which is obtained either from an algebraic model (mixing length models) or from the solution of additional transport equations (Spalart-Allmaras model, k-ε model, k-ω model). A more complete modeling approach is given by the Reynolds stress model, where additional transport equations are solved for the individual components of the Reynolds stress tensor. While this approach allows to solve the mean flow equations directly (i.e., without a model), the transport equations for the components of the Reynolds stress tensor introduce new unknown correlations that must be modeled (second-order closures). All turbulence models in the RANS context have in common that all turbulent fluctuations and thus the entire kinetic energy spectrum is modeled, as shown in Fig. 2.1. For this reason, RANS is preferred for large-scale industrial devices with focus on average or integral quantities such as body forces or mass flow rates, where the high degree of modeling leads to a quick availability of results.

Large eddy simulation (LES) is motivated by the limitations of RANS and DNS, and represents a compromise between accuracy and efficiency. In LES, the large-scale anisotropic and three-dimensional unsteady turbulent motions are directly represented, whereas the effects of the small-scale dissipative motions are modeled due to their universal character (cf. Fig. 2.1). The scale separation is achieved by applying a spatial filter operator to the Navier-Stokes equations, decomposing the flow quantities into a filtered (or resolved) component and a residual (or subgrid) component. The filtered equations contain an additional subgrid-scale stress tensor representing the effects of the unresolved scales, which is usually modeled using an eddy viscosity model similar to RANS. Several models are available for the turbulent viscosity, most of which are simple algebraic models, such as the Smagorinsky model [190], the Vreman model [221], or the σ-model [143]. Compared to RANS, LES provides a more accurate and reliable representation of the turbu-

lent flow field, and has now become a popular tool for the simulation of practical engineering systems with complex geometry or flow configurations in a variety of applications, including combustion, multiphase flows, aeroacoustics, and atmospheric and oceanic flows [242].

2.2 Turbulent Combustion

The main challenge in modeling turbulent reacting flows arises from the closure of the chemical reaction rates, which account for the chemical conversion of the reacting species. Since combustion is a process that is mainly determined by molecular mixing on the smallest turbulent scales, and since the reaction rate is a highly nonlinear function of the species mass fractions and temperature, a first-order closure that evaluates the filtered (or averaged) reaction rate with filtered (or averaged) quantities is generally not valid and leads to poor results,

$$\overline{\dot{\omega}_k(\mathbf{Y}, T)} \neq \dot{\omega}_k(\overline{\mathbf{Y}}, \overline{T}). \tag{2.2}$$

Therefore, more sophisticated combustion models have been developed in the last decades, which are summarized in a number of review articles [11, 152, 159, 165, 215] and text books [48, 56, 72, 150, 154]. These models generally take similar forms in the LES and RANS modeling context, but LES offers significant advantages over RANS in that it predicts scalar mixing processes, which are of crucial importance in turbulent combustion, with considerably improved accuracy [152]. Turbulent combustion models are often based on a conserved scalar that is independent of the chemistry, where a distinction is made between premixed and nonpremixed combustion. For premixed flames, the combustion process is characterized by the reaction progress variable, while for nonpremixed flames the rate of mixing of fuel and oxidizer is described by the mixture fraction. These quantities then form the basis for most of the turbulent combustion models. In the following, the essential combustion models are briefly presented. Since spray combustion is predominantly nonpremixed, the focus here is on the modeling of nonpremixed turbulent combustion.

One of the first models for closure of the chemical source term are the eddy breakup (EBU) model [199], which was derived for premixed combustion, and the eddy dissipation model (EDM) [124], which can be applied to both premixed and nonpremixed flames. The models are based on the assumption that the chemistry is infinitely fast and therefore the reaction rates are determined by the characteristic turbulent mixing time provided by the turbulence model. The resulting models are simple and robust, but they rely on the use of single-step chemistry and do not account for finite-rate chemistry and non-equilibrium effects (such as local extinction).

An extension of the EBU model that incorporates detailed and finite-rate chemistry effects is the eddy dissipation concept (EDC) [52, 123], which assumes that the chemical reactions take place in small turbulent eddies (so-called fine structures) that occupy a small fraction of the actual gas volume and are treated as well-stirred reactors.

An alternative approach for modeling turbulent nonpremixed flames is the laminar flamelet model [149, 150], which is based on the assumption that the chemical time scales are much shorter than the turbulence time scales (high Damköhler number), so that reactions occur in a thin layer around the stoichiometric mixture on scales smaller than the smallest scales of turbulence. As a consequence, the turbulent flame can be described as an ensemble of laminar flamelets that are governed by the one-dimensional flamelet equations with mixture fraction as an independent coordinate. The steady-state flamelets are computed prior to the simulation and are tabulated as a function of the mixture fraction and the scalar dissipation rate, where the latter incorporates the effects of turbulence on the flame, resulting in a deviation from chemical equilibrium. During the CFD computation, only the transport equations for the turbulent flow field and other characteristic variables (such as mixture fraction) are solved, while the thermochemical state (species mass fractions and temperature) is retrieved from the precalculated flamelet tables. The evaluation of mean quantities in the LES or RANS context requires knowledge of the statistical distribution of mixture fraction and scalar dissipation, usually assuming a beta and log-normal distribution, respectively. The laminar flamelet model represents a simple and efficient way to include complex chemical kinetic models in turbulent flame calculations, and enjoys great popularity in both research and industry. However, a major limitation of pretabulated chemistry is the description of the flame structure by a greatly reduced number of characteristic variables, which particularly complicates the application to spray flames [7, 85, 86].

The conditional moment closure (CMC) method [9, 105, 106, 141] incorporates concepts of the laminar flamelet model, but does not generally rely on the assumption of thin reaction zones. The basic idea of CMC is that in non-premixed combustion the reactive scalars are strongly correlated with mixture fraction, and that the fluctuations with respect to the averages conditioned on mixture fraction are often small (in contrast to the unconditional fluctuations in physical space or time). In CMC, transport equations are derived for the conditional averages of the reactive scalars, which mainly require closure of the conditional scalar dissipation rate and the conditionally averaged reaction rates. Since conditional fluctuations are often small, the conditionally averaged reaction rates are well approximated using a first-order closure based on the conditional averages of the reactive scalars. In flames

with significant local extinction and re-ignition or in spray combustion applications, the lack of correlation between the reactive scalars and mixture fraction requires a second-order closure of the reaction rates or alternatively the introduction of an additional conditioning variable [212, 213]. However, both approaches increase the number of unclosed terms and thus the complexity of the CMC model.

A more general modeling framework that is, in principle, independent of the combustion regime is given by the transported probability density function (PDF) method [45, 79, 145, 158], which employs a direct solution for the one-point one-time joint PDF of the reactive scalars rather than using a pre-assumed shape, as is the case with flamelet and CMC methods. The method was originally developed in the RANS context but later extended to LES using the filtered density function (FDF) [33, 62, 92, 159], which represents the PDF of the subgrid scalar quantities. A transport equation for the joint scalar PDF/FDF of the reactive scalars is derived, where the chemical reaction rates appear in closed form while molecular mixing, which depends on multipoint information, has to be modeled. Due to the high dimensionality of the joint scalar PDF/FDF, its transport equation is usually solved using a Monte Carlo particle method, where stochastic particles (also referred to as notional or gas-phase particles) emulate the evolution of the reactive scalars [156, 161]. The Monte Carlo solution generally requires a sufficiently high number of particles per computational cell (up to 100), which is referred to as an intensive or dense particle method. The effect of mixing is implemented as a particle interaction model, where a large number of mixing models is available, most dominantly the IEM model [46, 216] and Curl's coalescence/dispersion model [38, 44, 94]. More recently, the sparse-Lagrangian multiple mapping conditioning (MMC) model [28, 30, 31, 108] has been proposed as an alternative to the classical mixing models, which allows to use substantially fewer particles. This is achieved by conditioning the mixing operator on the mixture fraction space, which avoids unphysical mixing and thus ensures localness during combustion. Due to these advantages, the sparse-Lagrangian MMC model combined with an LES of the turbulent flow field is the method of choice for the present work, and further details will be presented in Ch. 4.

2.3 Spray Characteristics

In practical spray combustion devices, the liquid fuel jet is injected into the combustion chamber, breaks up, atomizes and produces a dispersed spray of small droplets, as illustrated in Fig. 2.2. The breakup process is generally classified into primary breakup, which refers to the breakup of the liquid core into distinct liquid ligaments and larger drops due to instabilities at the gas-liquid interface, and sec-

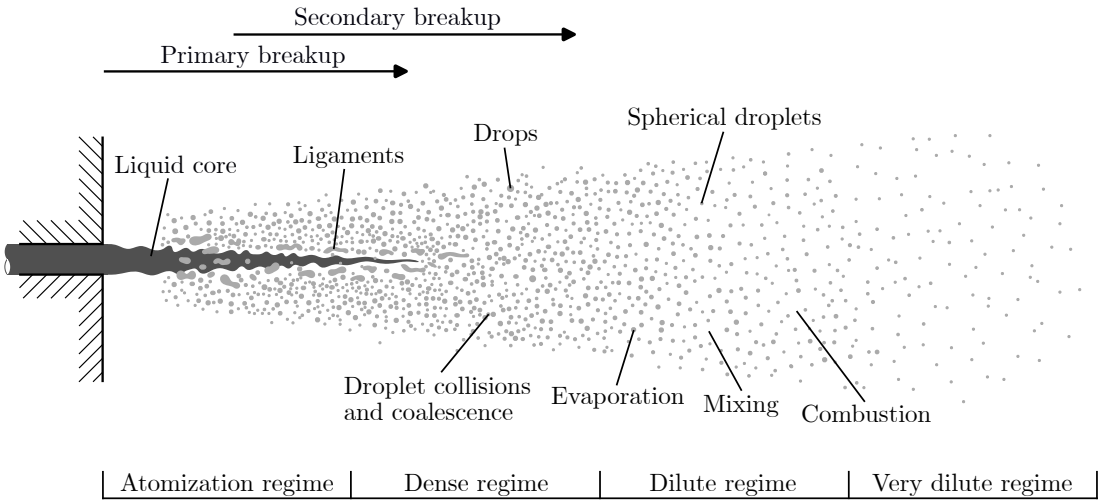

Figure 2.2: Schematic representation of the spray breakup, indicating the different flow regimes and atomization processes.

ondary breakup, which describes the further breakup of the primary fuel particles into smaller spherical droplets due to aerodynamic forces. The corresponding models are described in the literature [6, 117]. The various phenomena that occur inside the dispersed spray can be characterized based on the dispersed phase volume fraction ϕ_d, and are grouped into three regimes [49, 96]. The dense regime, corresponding to $\phi_d > 10^{-3}$, is dominated by atomization processes, where droplet collisions and coalescence (i.e., the process by which two or more droplets collide and merge) occur frequently. In the dilute regime, where the liquid volume fraction is in the range between 10^{-6} and 10^{-3}, the effect of the dispersed phase on the gas-phase turbulence is significant, while droplet collisions can usually be neglected. Here, the liquid phase is represented predominantly by spherical droplets, which evaporate and release fuel into the gas phase, where mixing of the fuel with the ambient air eventually leads to combustion in the gas phase. Depending on the spacing between the droplets, single droplet combustion or group combustion occurs [25, 26, 189]. Finally, the very dilute regime with $\phi_d < 10^{-6}$ characterizes the region where the influence of the dispersed phase on the continuous phase is insignificant. The different regimes of interaction between the dispersed particles and the continuous gas phase are summarized in Tab. 2.1, which also translates volume fraction into a nominal distance between spherical particles.

For the numerical modeling of two-phase sprays, the gas phase is generally considered as a continuum using an Eulerian framework, while the dispersed liquid phase can be treated with either an Eulerian or a Lagrangian approach, which is referred to as Euler-Euler or Euler-Lagrange modeling, respectively. If an Eulerian representation of the dispersed phase is used, the two phases interpenetrate and

Table 2.1: Regimes of interaction between dispersed particles and the continuous flow field [49, 96]. For each regime, the table lists the dispersed phase volume fraction ϕ_d and the equivalent nominal particle distance Δ_L normalized by the particle diameter d assuming spherical particles.

Regime	Dispersed phase volume fraction	Nominal particle distance	Modeling
Dense	$\phi_d > 10^{-3}$	$\Delta_L/d < 8$	4-way coupling
Dilute	$10^{-6} < \phi_d < 10^{-3}$	$8 < \Delta_L/d < 80$	2-way coupling
Very dilute	$\phi_d < 10^{-6}$	$\Delta_L/d > 80$	1-way coupling

are identified by the volume fraction of the dispersed phase. A distinction must be made whether the two phases are treated as different fluids with two separate sets of transport equations (two-fluid approach), or as a mixed fluid that is governed by a single set of transport equations (mixed-fluid or homogeneous approach) [97]. A more accurate description of the dispersed phase is obtained if an interphase tracking algorithm is used. In this approach, the different phases are treated as a single fluid with phase-specific material properties, and a phase indicator function is introduced from which the liquid-gas interface can be reconstructed (e.g., by using the volume of fluid method). The Eulerian representation of the liquid phase is useful if the dispersed phase volume fraction is high, or if the size of the dispersed particles is significantly larger than the smallest scales of the flow so that they are resolved by the numerical grid. These criteria are met in the atomization regime of the jet, but not in the dilute regime, where the liquid phase is represented by a fine mist of spherical droplets (cf. Fig. 2.2). Here, a Lagrangian representation of the dispersed phase is more appropriate, where the individual droplets are treated as point particles using a Lagrangian particle tracking algorithm. Since the droplets are not resolved, models are required to describe the heating and evaporation of the individual droplets, which are usually based on semi-analytical solutions of an isolated droplet in an infinite environment. Depending on the nominal droplet distance, a one-way coupling (gas $\rightarrow$ droplets), two-way coupling (gas $\leftrightarrow$ droplets) or four-way coupling (gas $\leftrightarrow$ droplets, droplets $\leftrightarrow$ droplets) is applied (cf. Tab. 2.1), where the backward coupling from the droplets to the carrier gas is done via source terms. The Lagrangian representation of the dispersed phase allows the use of a large number of particles, which then provides an accurate representation of the droplet distribution in the spray at a relatively low computational cost.

Chapter 3

Mathematical Description of Reacting Two-Phase Flows

This chapter presents the instantaneous governing equations for chemically reacting two-phase flows in the context of Euler-Lagrange simulations of dilute sprays, and thus provides the basis for the derivation of the two-phase MMC-LES model. The first part introduces the transport equations of the carrier gas phase along with the thermodynamic relations and expressions for the diffusive fluxes and chemical kinetics. No models for turbulence and combustion are applied at this point. In the second part, the equations for the Lagrangian fuel droplets are formulated and models for the evaporation rate and the droplet heating term are derived based on the isolated droplet theory.

3.1 Gas-Phase Description

3.1.1 The Conservation Equations

The governing equations of chemically reacting flows are given by the Navier-Stokes equations, which are extended by the conservation of species mass and energy [72, 114, 154, 209, 226]. Source terms account for the production and consumption of mass due to chemical reactions as well as for the mass, momentum and heat exchange between the evaporating droplet field and the carrier gas in the Euler-Lagrange approach. The instantaneous balance equations for overall mass, species mass, momentum and absolute enthalpy in the absence of volume forces (such as

gravity) and radiation are given in Cartesian coordinates by

$$\frac{\partial \rho}{\partial t} + \frac{\partial (\rho u_j)}{\partial x_j} = \dot{S}_M, \tag{3.1}$$

$$\frac{\partial (\rho Y_k)}{\partial t} + \frac{\partial (\rho u_j Y_k)}{\partial x_j} = -\frac{\partial j_{kj}}{\partial x_j} + \dot{\omega}_k + \dot{S}_{M,k}, \tag{3.2}$$

$$\frac{\partial (\rho u_i)}{\partial t} + \frac{\partial (\rho u_i u_j)}{\partial x_j} = -\frac{\partial p}{\partial x_i} + \frac{\partial \tau_{ij}}{\partial x_j} + \dot{S}_{u,i}, \tag{3.3}$$

$$\frac{\partial (\rho h)}{\partial t} + \frac{\partial (\rho u_j h)}{\partial x_j} - \frac{\partial p}{\partial t} - u_j \frac{\partial p}{\partial x_j} = -\frac{\partial q_j}{\partial x_j} + \tau_{ij} \frac{\partial u_i}{\partial x_j} + \dot{S}_h, \tag{3.4}$$

where ρ is the density, Y_k the mass fraction of species k, u_i the velocity components, and h the absolute enthalpy. The expression τ_{ij} denotes the components of the viscous stress tensor, j_{kj} is the diffusional mass flux of species k in j direction, and q_j is the heat flux in j direction. The term $\dot{\omega}_k$ denotes the chemical reaction rate of species k and represents the production and consumption of species mass. The source terms $\dot{S}_M$, $\dot{S}_{M,k}$, $\dot{S}_{u,i}$ and $\dot{S}_h$ account for the mass, momentum and heat transfer between the droplets and the carrier gas, with the total mass source term in the continuity equation given by $\dot{S}_M = \sum_{k=1}^{N_s} \dot{S}_{M,k}$. The expressions for these terms will be presented in Sec. 3.2.4.

Note that the equations for the species mass fractions, which are given by Eq. (3.2), are additionally subject to the condition $\sum_{k=1}^{N_s} Y_k = 1$, resulting in $N_s + 1$ equations for the N_s unknowns Y_k. To eliminate possible inconsistencies in global mass conservation arising from the modeling of the diffusion coefficients, it is common to solve Eq. (3.2) for only $N_s - 1$ species and to calculate the remaining species mass fraction, usually that of the inert species such as N_2, from the condition $\sum_{k=1}^{N_s} Y_k = 1$ [154].

3.1.2 Thermodynamic Relations

An additional equation is required to relate density to pressure and temperature in order to close the system of balance equations. For a mixture of ideal gases, this relation is given by the ideal gas law,

$$p = \rho \mathscr{R} T \sum_{k=1}^{N_s} \frac{Y_k}{\mathcal{M}_k}, \tag{3.5}$$

where $\mathscr{R}$ is the universal gas constant, and $\mathcal{M}_k$ is the molar mass of species k.

The temperature that is required to calculate the pressure using the ideal gas law is not a direct result of the solution of the transport equations, and has to be calculated from the energy variable. The enthalpy of the gas mixture is defined as

the mass-weighted average of the pure species enthalpies,

$$h = \sum_{k=1}^{N_s} Y_k h_k. \tag{3.6}$$

The pure species enthalpy h_k is the sum of the enthalpy of formation at a reference state and the sensible enthalpy that represents the integral over the specific heat capacity at constant pressure,

$$h_k = h_{f,k}^{\circ} + h_{s,k}, \qquad h_{s,k} = \int_{T_{\text{ref}}}^{T} c_{p,k}(T')\mathrm{d}T'. \tag{3.7}$$

The reference temperature is given by $T_{\text{ref}} = 298.15\,\text{K}$, and the superscript $\circ$ indicates that the enthalpy is evaluated at standard-state pressure $p^{\circ} = 10^5\,\text{Pa}$ [130].

3.1.3 Diffusive Transport

Viscous Stress Tensor

Assuming a Newtonian fluid and Stokes' hypothesis, the components of the viscous stress tensor are given by

$$\tau_{ij} = 2\mu\left(S_{ij} - \frac{1}{3}\delta_{ij}S_{kk}\right), \tag{3.8}$$

where μ is the dynamic viscosity, δ_{ij} denotes the Kronecker delta, and S_{ij} are the components of the rate-of-strain tensor, which are given by

$$S_{ij} = \frac{1}{2}\left(\frac{\partial u_i}{\partial x_j} + \frac{\partial u_j}{\partial x_i}\right). \tag{3.9}$$

Heat Flux

The heat flux vector per unit area for a multicomponent gas mixture is given by [154]

$$q_j = -\lambda\frac{\partial T}{\partial x_j} + \sum_{k=1}^{N_s} h_k j_{kj}. \tag{3.10}$$

The first term on the right-hand side of the equation describes heat conduction by Fourier's Law with λ being the thermal conductivity of the mixture, and the second term is associated with the diffusion of species with different enthalpies.

Diffusional Mass Flux

There are several approaches of different complexity and accuracy to model the phenomena of multicomponent diffusion. A commonly used approach is the approximate method of Hirschfelder and Curtiss [84] that calculates equivalent binary

diffusion coefficients of the species into the rest of the mixture analogous to Fick's law,

$$j_{kj} = -\rho \mathcal{D}_k \frac{\partial Y_k}{\partial x_j}. \tag{3.11}$$

The effective binary diffusion coefficients $\mathcal{D}_k$ can be calculated from the individual binary diffusion coefficients [211]. Note that the Hirschfelder and Curtiss approximation generally requires a correction term to satisfy overall mass conservation, in particular if diffusion coefficients vary strongly [72, 154, 211]. An advantage of this method is that the diffusion coefficients $\mathcal{D}_k$ can be linked to the heat diffusivity $\alpha = \lambda/(\rho c_p)$ via the Lewis number, $\mathrm{Le}_k = \mathcal{D}_k/\alpha$, which often has a constant value even across the flame [154].

Note that there are other modes of diffusion besides ordinary diffusion due to concentration gradients, such as thermal diffusion resulting from temperature gradients (also known as Soret effect), pressure diffusion resulting from pressure gradients, and forced diffusion due to unequal body forces among the species. However, these additional modes of diffusion modes can often be neglected and are therefore not considered here.

3.1.4 Simplified Forms of the Conservation Equations

In many combustion systems, flame and flow speeds are small compared to the speed of sound, leading to low Mach numbers. In these cases, the material derivative of pressure, $\partial p/\partial t + u_j \, \partial p/\partial x_j$, can be set to zero, provided there are no significant pressure changes over time. Furthermore, the viscous heating term $\tau_{ij} \, \partial u_i/\partial x_j$, which describes the conversion of kinetic energy into internal energy, can be neglected [72, 154]. Accordingly, the balance equation for absolute enthalpy, Eq. (3.4), simplifies to

$$\frac{\partial(\rho h)}{\partial t} + \frac{\partial(\rho u_j h)}{\partial x_j} = -\frac{\partial q_j}{\partial x_j} + \dot{S}_h. \tag{3.12}$$

Another assumption that is often made is to neglect differential diffusion (i.e., assuming equal diffusion coefficients $\mathcal{D}_k = \mathcal{D}$ in Eq. (3.11)). The components of the heat flux vector that are given by Eq. (3.10) can then be expressed in terms of gradients of enthalpy as

$$q_j = -\frac{\mu}{\mathrm{Pr}} \frac{\partial h}{\partial x_j} + \left(\frac{\mu}{\mathrm{Pr}} - \frac{\mu}{\mathrm{Sc}} \right) \sum_{k=1}^{N_s} h_k \frac{\partial Y_k}{\partial x_j}, \tag{3.13}$$

where $\mathrm{Pr} = \mu c_p/\lambda$ is the Prandtl number and $\mathrm{Sc} = \mu/(\rho\mathcal{D})$ the Schmidt number. Assuming a Lewis number equal to one such that $\mathrm{Sc} = \mathrm{Pr}$, the heat flux further simplifies to

$$q_j = -\frac{\mu}{\mathrm{Pr}} \frac{\partial h}{\partial x_j} = -\rho\alpha \frac{\partial h}{\partial x_j}, \tag{3.14}$$

where α denotes the thermal diffusivity, which is equal to the diffusion coefficient $\mathcal{D}$ for $\mathrm{Le} = 1$.

Applying both the assumption of low-Mach numbers and Lewis numbers equal to one, the balance equation for absolute enthalpy can be written as

$$\frac{\partial(\rho h)}{\partial t} + \frac{\partial(\rho u_j h)}{\partial x_j} = \frac{\partial}{\partial x_j}\left(\rho\alpha\frac{\partial h}{\partial x_j}\right) + \dot{S}_h, \tag{3.15}$$

which represents a convection-diffusion equation with evaporation source term. The equation for absolute enthalpy, Eq. (3.15), can be transformed into an equivalent equation based on sensible enthalpy,

$$\frac{\partial(\rho h_s)}{\partial t} + \frac{\partial(\rho u_j h_s)}{\partial x_j} = \frac{\partial}{\partial x_j}\left(\rho\alpha\frac{\partial h_s}{\partial x_j}\right) - \sum_{k=1}^{N_s} h_{f,k}^{\circ}\dot{\omega}_k + \dot{S}_{h_s}. \tag{3.16}$$

As the sensible enthalpy does not take into account the energy associated with chemical bonds, an additional source term arises from chemical reactions, which represents the heat released by combustion. Note that the expression for the evaporation source term has also changed and is now denoted as $\dot{S}_{h_s}$. Details will be given in Sec. 3.2.4. From the simplified balance equation of sensible enthalpy, Eq. (3.16), one can further derive an energy equation based on temperature,

$$c_p\left(\frac{\partial(\rho T)}{\partial t} + \frac{\partial(\rho u_j T)}{\partial x_j}\right) = \frac{\partial}{\partial x_j}\left(\lambda\frac{\partial T}{\partial x_j}\right) - \frac{\partial T}{\partial x_j}\sum_{k=1}^{N_s} c_{p,k} j_{kj} - \sum_{k=1}^{N_s} h_k\dot{\omega}_k + \dot{S}_T. \tag{3.17}$$

Note that the heat release term now includes the absolute enthalpy instead of the enthalpy of formation, which gives rise to different definitions of the heat release rate [154]. Compared to the balance equation for sensible enthalpy, Eq. (3.16), an additional term occurs, which results from the diffusion of species with different enthalpies.

The fact that the transport equations for species mass fractions and for absolute enthalpy are formally equivalent under the assumptions of low Mach numbers and unity Lewis numbers gives reason to express Eqs. (3.2) and (3.15) in a general form according to

$$\frac{\partial(\rho\phi_\alpha)}{\partial t} + \frac{\partial(\rho u_j\phi_\alpha)}{\partial x_j} = \frac{\partial}{\partial x_j}\left(\rho\mathcal{D}\frac{\partial\phi_\alpha}{\partial x_j}\right) + \rho W_\alpha + \rho\Pi_\alpha, \tag{3.18}$$

where $\boldsymbol{\phi} = (\mathbf{Y}, h)^\mathsf{T}$ is referred to as the composition vector, which contains $N_s + 1$ scalar fields comprising the species' mass fractions and mixture enthalpy. In combination with the pressure, the composition vector uniquely determines the thermochemical gas state. The generalized chemical source term in Eq. (3.18) is defined as $W_\alpha = \dot{\omega}_\alpha/\rho$ for $\phi_\alpha \in \mathbf{Y}$ and $W_\alpha = 0$ for $\phi_\alpha = h$. The generalized evaporation source term is given by $\Pi_\alpha = \dot{S}_{M,\alpha}/\rho$ for $\phi_\alpha \in \mathbf{Y}$ and $\Pi_\alpha = \dot{S}_h/\rho$ for $\phi_\alpha = h$.

3.1.5 Chemical Kinetics

The chemical mechanism, which consists of N_r elementary reversible (or irreversible) reactions involving N_s chemical species denoted as $\mathcal{S}_k$, can be represented in the general form

$$\sum_{k=1}^{N_s} \nu'_{ik} \mathcal{S}_k \underset{k_{r,i}}{\overset{k_{f,i}}{\rightleftharpoons}} \sum_{k=1}^{N_s} \nu''_{ik} \mathcal{S}_k, \qquad i = 1, ..., N_r, \tag{3.19}$$

with ν'_{ik} and ν''_{ik} being the stoichiometric coefficients on the reactants and products side of the equation, respectively, for the i-th reaction and species k. The reaction rate of species k is then given by

$$\dot{\omega}_k = \mathcal{M}_k \sum_{i=1}^{N_r} (\nu''_{ik} - \nu'_{ik}) \left[k_{f,i} \prod_{j=1}^{N_s} \left(\frac{\rho Y_j}{\mathcal{M}_j} \right)^{\nu'_{ij}} - k_{r,i} \prod_{j=1}^{N_s} \left(\frac{\rho Y_j}{\mathcal{M}_j} \right)^{\nu''_{ij}} \right]. \tag{3.20}$$

The forward rate constant $k_{f,i}$ of reaction i is usually obtained from the modified Arrhenius law,

$$k_{f,i} = A_i T^{\beta_i} \exp\left(-\frac{E_{A,i}}{\mathscr{R} T} \right), \tag{3.21}$$

with pre-exponential factor A_i, temperature exponent β_i and activation energy $E_{A,i}$. The reverse rate constants $k_{r,i}$ are calculated from the equilibrium constant. More details can be found in the literature [72, 99, 154, 211, 226].

3.1.6 Thermophysical Properties

The species enthalpies and heat capacities are typically expressed as a function of temperature, where NASA polynomials with coefficients taken from Burcat and Ruscic [20] are used in the present work. The corresponding mixture properties are given by their mass-weighted average. The viscosity of the species is calculated using Sutherland's law [206], and the viscosity of the mixture is obtained using the method of Herning and Zipperer [80, 155]. The thermal conductivity of the species is obtained from the modified Eucken equation [155], and the mixture-averaged value is determined using a linear mixing rule [127]. The effective binary diffusion coefficients $\mathcal{D}_k$ are calculated based on the Chapman-Enskog theory [155]. In the case of equal diffusion coefficients and constant Schmidt and Prandtl numbers, the diffusion coefficient is instead obtained from $\mathcal{D} = \nu/\mathrm{Sc}$ with $\nu = \mu/\rho$ being the kinematic viscosity, and the thermal conductivity is given by $\lambda = \mu c_p/\mathrm{Pr}$.

3.2 Liquid-Phase Description

3.2.1 Lagrangian Equations

The Lagrangian treatment of the liquid fuel droplets assumes inertial point particles that are transported by the turbulent flow field and carry distinct properties of the droplets such as mass and (mean) temperature. The position $\mathbf{x}_d$, velocity $\mathbf{u}_d$, mass m_d and temperature T_d of each droplet are obtained from the solution of the following equations:

$$\frac{\mathrm{d}\mathbf{x}_d}{\mathrm{d}t} = \mathbf{u}_d, \tag{3.22}$$

$$\frac{\mathrm{d}\mathbf{u}_d}{\mathrm{d}t} = \frac{1}{m_d}\mathbf{F}, \tag{3.23}$$

$$\frac{\mathrm{d}m_d}{\mathrm{d}t} = -\dot{m}, \tag{3.24}$$

$$\frac{\mathrm{d}T_d}{\mathrm{d}t} = \frac{\dot{Q}_d}{m_d c_l}. \tag{3.25}$$

Here, $\mathbf{F}$ represents the sum of all forces acting on the droplet, $\dot{m}$ is the evaporation rate, $\dot{Q}_d$ denotes the droplet heating term, and c_l is the specific heat capacity of the liquid. Although Eq. (3.23) reflects the momentum equation for particles of constant mass, it also applies to evaporating droplets if the mass flux is uniform over the droplet surface and thus the net thrust generated by the mass release is zero [37]. The droplet diameter d can be calculated from the droplet mass via $d = (\frac{6}{\pi}\frac{m_d}{\rho_l})^{1/3}$, where ρ_l is the liquid density. Expressions for the mass and heat transfer rates describing the evaporation and heating of the liquid fuel droplets, as well as for the forces that drive the droplet motion are derived in the next two sections.

3.2.2 Mass and Heat Transfer Rates

Modeling Assumptions

Closed-form expressions for the heat and mass transfer rates of the droplets are derived based on a semi-analytical solution describing the heating and evaporation of an isolated droplet in an infinite environment. The corresponding theory is summarized in a number of review articles, including the classic ones [53, 54, 115, 187] and the more recent and comprehensive ones mainly by Sazhin [179, 180], as well as in several text books [8, 178, 181, 188]. Within the present work, the following assumptions are applied:

(1) The droplet has a spherical shape that is retained throughout the evaporation process.
(2) The droplet is composed of a single-component liquid with zero solubility for gases.
(3) Only subcritical heating and evaporation with a well-defined boiling temperature are considered.
(4) Liquid-vapor equilibrium at the droplet surface is assumed, neglecting the effect of surface tension.
(5) The droplet temperature is uniform but time-varying (infinite liquid conductivity model).
(6) The processes in the gas phase are assumed to be quasi-steady.
(7) The ambient gas is treated as an ideal gas. Chemical reactions are not considered at this point and are only accounted for in the equations of the carrier gas (see Sec. 3.1). Radiation is neglected.
(8) Low Mach numbers and a uniform pressure are assumed.
(9) Thermophysical properties do not vary in space and are evaluated at a suitable reference gas state between the droplet surface and the far field.

The neglect of chemical reactions in the evaporation model (assumption 7) requires that the mixing of the fuel vapor with the environment is fast and that no local flame structure influences the evaporation process [96]. While this is true for a CP-DNS, where the Eulerian cell size and thus the region of interactions with the gas phase is of the order of the droplet size (cf. Sec. 5.3.2), the two-phase MMC-LES model cannot per se account for local flame structures around the droplets and thus generally requires modeling of an envelope flame. However, as the use of different model formulations in the CP-DNS and the MMC-LES does not allow for a consistent and unbiased comparison of the results, the present work refrains from using an envelope flame model in the MMC-LES. This constraint does not affect the results, as the evaporation rate is taken from the CP-DNS (Ch. 6), or the droplets are located in a fuel-rich and non-burning environment (Chs. 7 and 8).

Stagnant Droplets

In the absence of relative motion between the droplet and the gas, a spherically symmetric gas field exists around the droplet, reducing the governing equations to their one-dimensional form. The fuel mass fraction and temperature profiles of the spherically symmetric system as well as the corresponding heat and mass flows are sketched in Fig. 3.1. Fuel vapor is transported by convection (Stefan flow) and diffusion from the droplet surface to the ambient gas, while heat is conducted

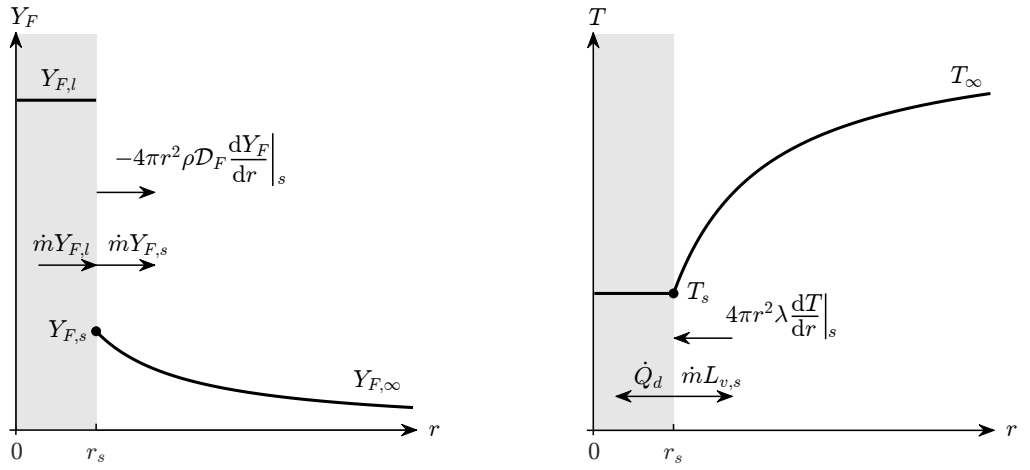

(a) Fuel mass fraction. **(b)** Temperature.

Figure 3.1: Sketch of fuel mass fraction and temperature profiles in the liquid phase (gray region) and gas phase along with heat and mass flows. The arrows indicate the mass and energy balance at the droplet surface.

radially against the convection towards the droplet surface. At the droplet surface, the heat from the gas is partially used for the phase change, while the remainder is transferred into the interior of the liquid droplet and is responsible for heating of the droplet, which is indicated by the droplet heating term $\dot{Q}_d$.

The expression for the evaporation rate is derived based on a mass perspective. Conservation of total mass is represented by the continuity equation, which takes the form

$$\frac{1}{r^2}\frac{\mathrm{d}}{\mathrm{d}r}\left(r^2 \rho u_r\right) = 0. \tag{3.26}$$

Integrating the equation in radial direction shows that the total mass flow, which is equivalent to the evaporation rate, is constant in radial direction,

$$\dot{m} = 4\pi r^2 \rho u_r = \text{const.} \tag{3.27}$$

The governing equation of the fuel mass fraction under the given assumptions can be written as

$$\frac{1}{r^2}\frac{\mathrm{d}}{\mathrm{d}r}\left(\dot{m}Y_F\right) = \frac{1}{r^2}\frac{\mathrm{d}}{\mathrm{d}r}\left(4\pi r^2 \rho \mathcal{D}_F \frac{\mathrm{d}Y_F}{\mathrm{d}r}\right), \tag{3.28}$$

where the radial velocity was replaced by the evaporation rate using Eq. (3.27). Multiplication of the equation by r^2, integration in radial direction and re-arranging the terms results in

$$\frac{\mathrm{d}Y_F}{\dot{m}Y_F + C_1} = \frac{\mathrm{d}r}{4\pi r^2 \rho \mathcal{D}_F}, \tag{3.29}$$

where C_1 is an integration constant. A second integration leads to

$$\frac{1}{\dot{m}}\ln(\dot{m}Y_F + C_1) = -\frac{1}{4\pi r \rho \mathcal{D}_F} + C_2. \tag{3.30}$$

Applying the boundary conditions at the droplet surface, $Y_F(r = r_s) = Y_{F,s}$, and far from the droplet, $Y_F(r \to \infty) = Y_{F,\infty}$, finally leads to

$$Y_F(r) = Y_{F,\infty} + (Y_{F,s} - Y_{F,\infty}) \frac{1 - \exp\left(-\frac{\dot{m}}{4\pi r \rho \mathcal{D}_F}\right)}{1 - \exp\left(-\frac{\dot{m}}{4\pi r_s \rho \mathcal{D}_F}\right)}. \tag{3.31}$$

This equation describes the fuel mass fraction profile from the droplet surface to infinity for given values of $Y_{F,s}$ and $Y_{F,\infty}$ and evaporation rate $\dot{m}$. An additional relation is required to find an expression for the yet unknown evaporation rate. Formulating a mass balance at the droplet surface (see Fig. 3.1(a)) gives

$$\dot{m} Y_{F,l} = \dot{m} Y_{F,s} - 4\pi r_s^2 \rho \mathcal{D}_F \left.\frac{\mathrm{d}Y_F}{\mathrm{d}r}\right|_s, \tag{3.32}$$

with $Y_{F,l} = 1$ for single-component liquids. Substituting the expression for the derivative, which is obtained from Eq. (3.31), into the surface mass balance and solving for the evaporation rate finally yields

$$\dot{m} = 4\pi r_s \rho \mathcal{D}_F \ln(1 + B_M), \tag{3.33}$$

with Spalding mass transfer number B_M defined as

$$B_M = \frac{Y_{F,s} - Y_{F,\infty}}{1 - Y_{F,s}}. \tag{3.34}$$

Inserting the expression for the evaporation rate, Eq. (3.33) into Eq. (3.31) the solution for the fuel mass fraction profile can also be written as

$$Y_F(r) = 1 - (1 - Y_{F,\infty}) \exp\left(-\frac{\dot{m}}{4\pi r \rho \mathcal{D}_F}\right). \tag{3.35}$$

Note that these relations are also valid for the case of condensation with $Y_{F,s} < Y_{F,\infty}$. In that case, the evaporation rate is negative, corresponding to a mass flux from the ambient gas to the droplet surface.

Equation (3.31) can also be used to describe the profiles of the non-evaporating species, as it is solely based on the general conservation equation and the fixed-value boundary conditions. Assuming equal diffusion coefficients, the surface mass balance for non-evaporating species $k \neq F$ takes the form

$$0 = \dot{m} Y_{k,s} - 4\pi r_s^2 \rho \mathcal{D}_F \left.\frac{\mathrm{d}Y_k}{\mathrm{d}r}\right|_s. \tag{3.36}$$

By inserting the expression for the derivative that is derived from the respective mass fraction profile one finally finds

$$\frac{Y_{k,s}}{Y_{k,\infty}} = \frac{1 - Y_{F,s}}{1 - Y_{F,\infty}} = \text{const}, \qquad k \neq F. \tag{3.37}$$

This relation shows that the ratio of surface values to far-field values is constant for non-evaporating species, and therefore their surface values are equal to the corresponding far-field values but scaled by a normalization constant to ensure that the sum of mass fractions is equal to one. As Eq. (3.37) is based on ratios, it also holds if mass fractions are replaced by mole fractions, which then allows the calculation of the surface mole fractions from their respective far-field values and the given surface mole fraction of the fuel species,

$$Y_{F,s} = \frac{X_{F,s}\mathcal{M}_F}{X_{F,s}\mathcal{M}_F + (1 - X_{F,s})\mathcal{M}_a}, \qquad \mathcal{M}_a = \frac{1}{1 - X_{F,\infty}} \sum_{k \neq F} X_{k,\infty}\mathcal{M}_k. \tag{3.38}$$

This relation is also reported in Darabiha *et al.* [39] and Yang *et al.* [234]. The mole fraction of the fuel species at the droplet surface is obtained from liquid-vapor equilibrium via $X_{F,s} = p_{\mathrm{sat},s}/p_\infty$, where $p_{\mathrm{sat},s}$ is the saturated vapor pressure at the droplet surface, which is evaluated using an appropriate theoretical (Clausius-Clapeyron) or experimental relation (see Sec. 3.2.5 for details).

The expression for the droplet heating term is derived based on an energy perspective. Using the given assumptions, and neglecting the term associated with the diffusion of species with different enthalpies (see Eq. (3.17)), the energy equation of the spherically symmetric system can be written as

$$\frac{1}{r^2}\frac{\mathrm{d}}{\mathrm{d}r}\left(\dot{m}c_pT\right) = \frac{1}{r^2}\frac{\mathrm{d}}{\mathrm{d}r}\left(4\pi r^2\lambda\frac{\mathrm{d}T}{\mathrm{d}r}\right), \tag{3.39}$$

where the radial velocity was again replaced by the evaporation rate using Eq. (3.27). Note that there are contradictory opinions in the literature regarding the specific heat capacity in the energy equation. Several publications use the (suitably averaged) value of the gas mixture here [54, 114, 211], while Sazhin [179] argues that the value of pure vapor should be used, which is also consistent with the model formulation of Abramzon and Sirignano [2]. Due to the widespread use of the latter two works, the present study adopts the use of the specific heat capacity of the pure vapor species in the energy equation. Accordingly, c_p is replaced by $c_{p,F}$ in Eq. (3.39). Introducing the Lewis number of the fuel species, $\mathrm{Le} = \lambda/(\rho\mathcal{D}_F c_p)$, the conservation of energy can be written as

$$\frac{1}{r^2}\frac{\mathrm{d}}{\mathrm{d}r}\left(\dot{m}T\right) = \frac{1}{r^2}\frac{\mathrm{d}}{\mathrm{d}r}\left(4\pi r^2\frac{\rho\mathcal{D}_F}{\phi}\frac{\mathrm{d}T}{\mathrm{d}r}\right), \tag{3.40}$$

with

$$\phi = \left(\frac{c_{p,F}}{c_p}\right)\frac{1}{\mathrm{Le}}. \tag{3.41}$$

This equation is equivalent to the equation for the fuel mass fraction, Eq. (3.31), but with additional parameter ϕ. The temperature profile is then given by

$$T(r) = T_\infty + (T_s - T_\infty)\frac{1 - \exp\left(-\frac{\dot{m}\phi}{4\pi r \rho \mathcal{D}_F}\right)}{1 - \exp\left(-\frac{\dot{m}\phi}{4\pi r_s \rho \mathcal{D}_F}\right)}, \tag{3.42}$$

with $T_s = T_d$ due to the assumption of a uniform temperature profile inside the droplet. To find an expression for the heat flux into the liquid droplet, which is responsible for the heating of the droplet and is represented by the droplet heating term $\dot{Q}_d$, the energy balance at the droplet surface is considered (see Fig. 3.1(b)),

$$4\pi r_s^2 \lambda \left.\frac{\mathrm{d}T}{\mathrm{d}r}\right|_s = \dot{m} L_{v,s} + \dot{Q}_d, \tag{3.43}$$

where $L_{v,s}$ is the latent heat of vaporization at droplet surface conditions. Note that this energy balance is also valid for the case of condensation, where the negative evaporation rate leads to a reversed sign of the latent heat term, which is then associated with heat release at the droplet surface. By inserting the expression for the temperature gradient at the droplet surface, which is obtained from Eq. (3.42), into the surface energy balance, one finally finds the expression for the droplet heating term,

$$\dot{Q}_d = \dot{m}\left(\frac{c_{p,F}(T_\infty - T_s)}{B_T} - L_{v,s}\right), \tag{3.44}$$

with Spalding heat transfer number defined as

$$B_T = (1 + B_M)^\phi - 1. \tag{3.45}$$

For Le = 1 and $c_p = c_{p,F}$ the Spalding heat and mass transfer numbers are the same.

The case $\dot{m} = 0$ (if $Y_{F,s} = Y_{F,\infty}$) requires special treatment, as the previous derivations are not valid in that situation. Setting the radial velocity to zero, the energy balance, Eq. (3.39), takes the form of the pure heat equation,

$$\frac{1}{r^2}\frac{\mathrm{d}}{\mathrm{d}r}\left(4\pi r^2 \lambda \frac{\mathrm{d}T}{\mathrm{d}r}\right) = 0 \tag{3.46}$$

Its solution is given by

$$T(r) = T_\infty + (T_s - T_\infty)\left(\frac{r}{r_s}\right)^{-1}. \tag{3.47}$$

The droplet heating term is derived from the surface energy balance in an analogous way, where now the entire heat from the gas conducts into the liquid droplet, resulting in

$$\dot{Q}_d = 4\pi r_s \lambda (T_\infty - T_s). \tag{3.48}$$

Convective Environments

The presence of a relative velocity between the droplet and the gas will affect mass and heat transfer rates, and hence corrections to the previous relations are necessary. Although the existence of a flow field leads to a loss of spherical symmetry, the common approach is to introduce semi-empirical correction factors for the transfer rates of a symmetrical gas field based on the film theory [15]. According to that, the boundary conditions at infinity are moved inward to the film radii, which steepens mass fraction and temperature gradients and therefore increases mass and heat transfer rates. For non-evaporating droplets, the thicknesses of the diffusional and thermal films are given by

$$\frac{\delta_M}{r_s} = \frac{2}{\mathrm{Sh} - 2}, \qquad \frac{\delta_T}{r_s} = \frac{2}{\mathrm{Nu} - 2}, \tag{3.49}$$

with Sh and Nu being the Sherwood and Nusselt number, respectively. These non-dimensional parameters are evaluated using the following correlations [32]:

$$\mathrm{Sh} = 1 + (1 + \mathrm{Re}\,\mathrm{Sc})^{1/3} \max\left(1, \mathrm{Re}^{0.077}\right), \tag{3.50a}$$

$$\mathrm{Nu} = 1 + (1 + \mathrm{Re}\,\mathrm{Pr})^{1/3} \max\left(1, \mathrm{Re}^{0.077}\right), \tag{3.50b}$$

with $\mathrm{Sc} = \mu/(\rho \mathcal{D}_F)$ being the Schmidt number, $\mathrm{Pr} = c_p \mu/\lambda$ the Prandtl number, and Re the Reynolds number (based on the slip velocity). These relations are valid for $\mathrm{Re} < 400$ and $0.25 \leq \{\mathrm{Sc}, \mathrm{Pr}\} \leq 100$.

The presence of the Stefan flow will influence the values of δ_M and δ_T, since a surface blowing results in the thickening of the laminar boundary layer [183]. To take into consideration this effect, Abramzon and Sirignano [2] introduced modified film thicknesses according to

$$\delta_M^* = F_M \delta_M, \qquad \delta_T^* = F_T \delta_T, \tag{3.51}$$

where the correction factors F_M and F_T are given as functions of their corresponding Spalding transfer numbers B_M and B_T by the universal functions F_M and F_T, respectively,

$$F_M = (1 + B_M)^{0.7} \frac{\ln(1 + B_M)}{B_M}, \qquad F_T = (1 + B_T)^{0.7} \frac{\ln(1 + B_T)}{B_T}. \tag{3.52}$$

Note that this function reproduces the classical film theory in the limiting case of a vanishing evaporation rate, as $\{F_M, F_T\} \to 1$ if $\{B_M, B_T\} \to 0$. A similar relation to Eq. (3.49) is now defined for modified film thicknesses using a modified Sherwood and Nusselt number, respectively,

$$\frac{\delta_M^*}{r_s} = \frac{2}{\mathrm{Sh}^* - 2}, \qquad \frac{\delta_T^*}{r_s} = \frac{2}{\mathrm{Nu}^* - 2}, \tag{3.53}$$

which results in the following relation between the modified and unmodified non-dimensional parameters,

$$\mathrm{Sh}^* = 2 + \frac{\mathrm{Sh} - 2}{F_M}, \qquad \mathrm{Nu}^* = 2 + \frac{\mathrm{Nu} - 2}{F_T}. \tag{3.54}$$

Integrating the balance equation for the fuel mass fraction and applying the boundary condition at the modified film radii $r_s + \delta_M^*$ finally leads to a new expression for the evaporation rate,

$$\dot{m} = 2\pi r_s \rho \mathcal{D}_F \mathrm{Sh}^* \ln(1 + B_M). \tag{3.55}$$

In an analogous way, the energy perspective gives a new expression for the parameter ϕ that is required to calculate the Spalding heat transfer number,

$$\phi = \left(\frac{c_{p,F}}{c_p}\right)\left(\frac{\mathrm{Sh}^*}{\mathrm{Nu}^*}\right)\frac{1}{\mathrm{Le}}. \tag{3.56}$$

For a stagnant medium ($\mathrm{Re} = 0$), the presented correlations result in $\mathrm{Sh}^* = \mathrm{Nu}^* = 2$ and therefore reproduce the previously derived solution for stagnant droplets. For the case of pure heat transfer without evaporation, the classical film theory can be used, which gives

$$\dot{Q}_d = 2\pi r_s \lambda \mathrm{Nu}(T_\infty - T_s). \tag{3.57}$$

Evaluation of Thermophysical Properties

The assumption of constant thermophysical properties within the gas phase is compensated by the use of average values, which are evaluated at a reference gas state defined as

$$Y_{k,\mathrm{ref}} = \gamma Y_{k,\infty} + (1 - \gamma) Y_{k,s}, \tag{3.58a}$$

$$T_{\mathrm{ref}} = \gamma T_\infty + (1 - \gamma) T_s, \tag{3.58b}$$

where γ is an averaging parameter. By comparison with variable properties calculations, Hubbard *et al.* [88] found best agreement for $\gamma = 1/3$. This value, which is known as the 1/3 rule, is the most common choice and will also be used in the present work, although other studies suggest different values [245]. All thermodynamic and transport properties such as the gas density ρ, fuel vapor diffusivity $\mathcal{D}_F$, thermal conductivity λ, viscosity μ and specific heat capacities c_p and $c_{p,F}$ are then evaluated at the reference gas state that is defined by Eqs. (3.58a) and (3.58b).

3.2.3 Particle Forces

A particle that is moving through a turbulent flow field is subject to several fluid dynamic forces, such as forces due to pressure gradients and shear stresses of the

undisturbed flow, the steady-state drag, the virtual mass effect (due to acceleration of the displaced fluid), the Basset force (due to the temporal delay in the boundary layer development), and the Saffman and Magnus lift (due to velocity gradient and rotation of the particle, respectively) [37, 128]. For particles with a high density ratio (as is the case with liquid droplets in a gaseous flow), the forces other than the steady-state drag do not contribute to the particle motion [4, 50, 96]. Therefore, only the drag force is considered within the present work, which is given by [37]

$$\mathbf{F}_D = \frac{1}{2}\rho_\infty C_D A_d \|\mathbf{u}_\infty - \mathbf{u}_d\| \left(\mathbf{u}_\infty - \mathbf{u}_d\right), \tag{3.59}$$

where ρ_∞ and $\mathbf{u}_\infty$ are the free-stream density and velocity, respectively, C_D is the drag coefficient, and $A_d = \pi r_s^2$ is the cross-sectional area of the droplet. Note that the net thrust generated by evaporation is zero, as mass is expelled from the surface uniformly in all directions [37]. The drag coefficient is usually expressed as a function of the Reynolds number. Yuen and Chen [237] showed that the drag coefficient of an evaporating droplet can be approximated by the standard drag curve for solid spheres, provided that the Reynolds number is based on the free-stream density and the viscosity is evaluated using the 1/3 rule,

$$\mathrm{Re} = \frac{\rho_\infty \|\mathbf{u}_\infty - \mathbf{u}_d\| d}{\mu}. \tag{3.60}$$

A widely used relation for the drag coefficient of a sphere is given by Putnam [169],

$$C_D = \max\left[\frac{24}{\mathrm{Re}}\left(1 + \frac{1}{6}\mathrm{Re}^{2/3}\right), 0.424\right], \tag{3.61}$$

which is valid for $\mathrm{Re} < 3 \cdot 10^5$. The drag coefficient is often expressed as a correction to Stokes drag, $C_D = f_1 C_{D,\mathrm{Stokes}}$, with $C_{D,\mathrm{Stokes}} = 24/\mathrm{Re}$ [37]. Using the relation of Putnam, the correction factor f_1 takes the form

$$f_1 = \max\left[1 + \frac{1}{6}\mathrm{Re}^{2/3}, 0.0177\mathrm{Re}\right]. \tag{3.62}$$

By inserting the expression for the drag force, Eq. (3.59), into the equation of motion for the fuel droplet, Eq. (3.23), and replacing the drag coefficient by the correction factor f_1, the equation of motion can be written as

$$\frac{\mathrm{d}\mathbf{u}_d}{\mathrm{d}t} = \frac{f_1}{\tau_d}\left(\mathbf{u}_\infty - \mathbf{u}_d\right), \tag{3.63}$$

with $\tau_d = (\rho_l d^2)/(18\mu)$ being the response time of the droplet.

3.2.4 Two-Way Coupling

A two-way coupling between the carrier gas and the fuel droplets is employed, where the local cell values provide the ambient conditions for the dispersed droplets (i.e., $\mathbf{u}_\infty = \mathbf{u}(\mathbf{x}_d)$, $p_\infty = p(\mathbf{x}_d)$, $Y_{k,\infty} = Y_k(\mathbf{x}_d)$ and $T_\infty = T(\mathbf{x}_d)$), while the effect of the fuel droplets onto the carrier gas is accounted for via source terms in the balance equations of the gas phase [37, 54, 96, 168]. This approach is known as the particle-source-in-cell (PSI-cell) model [36].

The expressions for the source terms that appear in the transport equations of the carrier gas (see Sec. 3.1) are derived based on the conservation of mass, momentum and energy between a finite gas volume and the liquid droplets, and are given by

$$\dot{S}_M = -\frac{1}{V}\sum_d \frac{\mathrm{d}m_d}{\mathrm{d}t}, \tag{3.64}$$

$$\dot{S}_{u,i} = -\frac{1}{V}\sum_d \frac{\mathrm{d}(m_d u_{d,i})}{\mathrm{d}t}, \tag{3.65}$$

$$\dot{S}_h = -\frac{1}{V}\sum_d \frac{\mathrm{d}(m_d h_d)}{\mathrm{d}t}. \tag{3.66}$$

Here, V denotes the gas volume that receives the source terms (typically the computational cell, but other options are also possible) and h_d is the enthalpy of the liquid droplet. The summation is performed over all droplets within the volume under consideration. Due to the assumption of single-component liquids, the source term in the transport equation for the fuel mass fraction is given by $\dot{S}_{M,F} = \dot{S}_M$, whereas it is zero for non-evaporating species, $\dot{S}_{M,k} = 0$ for $k \neq F$. If the energy equation is expressed in terms of sensible enthalpy or temperature, the evaporation source terms take the form

$$\dot{S}_{h_s} = -\frac{1}{V}\sum_d \left(\frac{\mathrm{d}(m_d h_d)}{\mathrm{d}t} - h^\circ_{f,F}\frac{\mathrm{d}m_d}{\mathrm{d}t}\right), \tag{3.67}$$

$$\dot{S}_T = -\frac{1}{V}\sum_d \left(\frac{\mathrm{d}(m_d h_d)}{\mathrm{d}t} - (h_F - c_p T)\frac{\mathrm{d}m_d}{\mathrm{d}t}\right), \tag{3.68}$$

where h_F and $h^\circ_{f,F}$ denote the absolute enthalpy and enthalpy of formation of the gaseous fuel, respectively, and c_p and T are the specific heat capacity and temperature of the carrier gas. Note that it is still the absolute enthalpy that is conserved between the droplet and the gas, even though an energy equation for sensible enthalpy or temperature is solved. For details on the derivation the reader is referred to Appendix A.1.

It should be noted that the use of local cell values as the ambient conditions for the droplets requires a large enough cell size to represent the state far from the

droplet. This condition imposes a limit on the use of the PSI-cell model, which will be discussed in detail in Ch. 5.

3.2.5 Liquid Properties

Liquid properties, such as density, specific heat capacity, absolute enthalpy, and latent heat of vaporization, are expressed as functions of the temperature and are calculated using correlations from the Design Institute for Physical Properties (DIPPR) [41, 148]. For the saturated vapor pressure, which is required to determine the liquid-vapor equilibrium at the droplet surface (i.e., the fuel mole fraction), an empirical relation from the same database is used instead of the theoretical Clausius-Clapeyron equation.

3.2.6 Solution Procedure

The calculation of the evaporation rate, the droplet heating term and the drag force, which are required to calculate the right-hand side of the Lagrangian droplet equations, Eqs. (3.22) to (3.25), is summarized in the following step-by-step procedure:

1. Determine the fuel mole fraction at the droplet surface from the saturated vapor pressure via $X_{F,s} = p_{\mathrm{sat}}(T_d)/p_\infty$, The surface mole fractions of the non-evaporating species are calculated using the mole-based equivalent of Eq. (3.37), $X_{k,s} = X_{k,\infty}(1-X_{F,s})/(1-X_{F,\infty})$. Then convert mole fractions to mass fractions using $Y_{k,s} = X_{k,s}\mathcal{M}_k/\sum_i X_{i,s}\mathcal{M}_i$.
2. Evaluate the average gas properties ρ, c_p, $c_{p,F}$, μ, λ and $\mathcal{D}_F$ using the 1/3 rule that is given by Eqs. (3.58a) and (3.58b).
3. Calculate the non-dimensional parameters $\mathrm{Sc} = \mu/(\rho\mathcal{D}_F)$, $\mathrm{Pr} = c_p\mu/\lambda$, $\mathrm{Le} = \mathrm{Sc}/\mathrm{Pr} = \lambda/(\rho\mathcal{D}_F c_p)$ and $\mathrm{Re} = \rho_\infty\|\mathbf{u}_\infty - \mathbf{u}_d\|d/\mu$. Then calculate the Sherwood and Nusselt number using the relations given by Eqs. (3.50a) and (3.50b).
4. Calculate the droplet response time $\tau_d = (\rho_l d^2)/(18\mu)$ and the correction factor to Stokes drag using Eq. (3.62).
5. Calculate the Spalding mass transfer number B_M from Eq. (3.34), and the modified Sherwood number using Eqs. (3.52) and (3.54).
6. Iterate the Spalding heat transfer number B_T using Eqs. (3.45), (3.52), (3.54) and (3.56).
7. Calculate the evaporation rate $\dot{m}$ from Eq. (3.55), and the droplet heating term $\dot{Q}_d$ from Eq. (3.44).

Note that in the case of $\dot{m} = 0$, steps 6 and 7 are not required, and the droplet heating term is calculated from Eq. (3.57).

The time evolution of the droplet properties (x_d, $\mathbf{u}_d$, m_d, T_d) is obtained by numerically solving the set of ordinary differential equations governing the droplet motion, evaporation and heating, Eqs. (3.22) to (3.25). To avoid stability problems that occur when the droplet diameter approaches zero (resulting in stiffness of the equations, in particular the temperature equation), an implicit method must be used. Here, the equations are discretized using the second-order implicit trapezoidal rule (in the context of partial differential equations the method is also known as the Crank-Nicolson method), which is a combination of the forward Euler method and the backward Euler method [138]. It can be written in general form as

$$\mathbf{q}^{n+1} - \mathbf{q}^n - \frac{\Delta t}{2}\left[\boldsymbol{\mathcal{F}}(\mathbf{q}^n) + \boldsymbol{\mathcal{F}}(\mathbf{q}^{n+1})\right] = 0, \tag{3.69}$$

where $\mathbf{q} = (\mathbf{x}_d, \mathbf{u}_d, m_d, T_d)^\mathsf{T}$ is a vector containing the droplet properties, $\boldsymbol{\mathcal{F}}(\mathbf{q})$ indicates the right-hand side of the Lagrangian droplet equations, the superscript n denotes the time step index, and Δt is the time step width. Equation (3.69) represents a system of eight nonlinear scalar equations (position $\mathbf{x}_d = (x_d, y_d, z_d)^\mathsf{T}$, velocity $\mathbf{u}_d = (u_d, v_d, w_d)^\mathsf{T}$, mass m_d, temperature T_d) that must be solved in each time step. The standard approach is to use Newton's method, which provides fast convergence but also involves a high computational cost as it requires the evaluation and inversion of the Jacobian matrix. This makes a solution impractical for systems containing thousands or millions of droplets. Alternative iteration methods that do not rely on the evaluation of the Jacobian matrix, such as fixed-point iteration, generally show poorer convergence behavior and often fail when they are used to solve the entire set of equations in a coupled way. However, it is possible to combine both methods to significantly reduce the size of the Jacobian matrix and thus the computational cost without compromising convergence. Accordingly, Newton's method will only be used to solve for droplet mass and temperature. The resulting size of the Jacobian matrix is two, which allows for an analytical calculation of the inverse matrix. The entries of the Jacobian matrix are approximated by finite differences [211], where forward differences are used for derivatives with respect to droplet mass and backward differences for derivatives with respect to droplet temperature. This ensures that the physically reasonable ranges ($m_d > 0$, $T_d < T_{\text{boil}}$) are not exceeded during the calculation. Further, since the droplet mass is several orders of magnitude smaller than the droplet temperature, a normalization based on the values at the beginning of each time step is employed. The vector quantities position and velocity of the droplet are found based on fixed-point iteration, where the rather simple form of the equations allows for a direct solution of the new quantities based on the values from the previous iteration. Assuming that the ambient conditions are constant over Δt, the discretized versions of Eqs. (3.22) and (3.63)

are rewritten as

$$\mathbf{x}_d^{k+1} = \mathbf{x}_d^n + \frac{\Delta t}{2}\left(\mathbf{u}_d^n + \mathbf{u}_d^k\right), \tag{3.70}$$

$$\mathbf{u}_d^{k+1} = \frac{\mathbf{u}_d^n\left(1 - \frac{\Delta t}{2}\frac{f_1^n}{\tau_d^n}\right) + \mathbf{u}_\infty \frac{\Delta t}{2}\left(\frac{f_1^n}{\tau_d^n} + \frac{f_1^k}{\tau_d^k}\right)}{1 + \frac{\Delta t}{2}\frac{f_1^k}{\tau_d^k}}, \tag{3.71}$$

where k is the iteration number. The initial values that are used to start the iteration are given by the values at time level n, and the converged state represents the values at the new time level $n+1$. Typically around three to four iterations are necessary to reach residuals at machine precision.

The limit $d \to 0$ requires special treatment to prevent the droplet mass from becoming negative. The common approach is to remove the droplet when its mass falls below a user-defined threshold value [122, 140]. However, if an accurate estimation of the evaporation time is required (see Ch. 5), this approach cannot be used, and the entire time history of the droplet properties up to $d = 0$ needs to be predicted accurately. Therefore, the present work adopts an alternative approach that is based on the d^2-law and thus provides an analytical solution. The d^2-law is obtained by assuming a constant droplet temperature, such that the droplet surface conditions and the average thermophysical properties of the gas phase remain constant. Under these assumptions, and neglecting the temporal variation of the Sherwood number and the ambient conditions, the instantaneous evaporation rate is only a function of the droplet diameter, resulting in a linear variation of the squared droplet diameter with time,

$$d^2(t) = d_0^2 - Kt, \tag{3.72}$$

where the subscript 0 denotes the initial value and K is the evaporation constant (see Turns [211] for details). The evaporation time is then given by

$$\tau_{\text{evap}} = \frac{d_0^2}{K}. \tag{3.73}$$

Replacing the evaporation constant by the evaporation rate allows to write the evaporation time in terms of the initial droplet mass and evaporation rate,

$$\tau_{\text{evap}} = \frac{3}{2}\frac{m_{d,0}}{\dot{m}_0}. \tag{3.74}$$

The proposed procedure for calculating the droplet evaporation time in a CFD code is as follows. At the beginning of each time step, the remaining evaporation time is calculated based on Eq. (3.74) by inserting the current droplet properties (i.e., by replacing $m_{d,0}$ and $\dot{m}_0$ by m_d^n and $\dot{m}^n$, respectively). If the remaining evaporation time is close to the time step width ($\tau_{\text{evap}} < 2\Delta t$ is recommended),

it is likely that the droplet will disappear in the current or next time step. In that case, the analytical solution based on the d^2-law is used in place of solving the droplet equations numerically. In detail this means that the droplet mass is explicitly set to zero, while the droplet temperature is kept constant. As the droplet has no appreciable inertia in the limiting case of vanishing droplet mass, the droplet velocity is set equal to the gas velocity, and the final position of the droplet can be calculated using the known droplet velocity and the remaining evaporation time. The total evaporation time is then obtained by adding the remaining evaporation time to the time at the beginning of the time step.

The numerical solution procedure described above is implemented in a MATLAB code, which is used for validation purposes (see next section) and for the analysis presented in Ch. 5, as well as in the OpenFOAM-based two-phase MMC-LES solver (see Sec. 4.7 for details). It should be noted that the present evaporation model differs from the standard models available in OpenFOAM in both the theoretical formulation and the numerical solution procedure.

3.2.7 Model Validation

Validation of the Numerical Method

To demonstrate the robustness and accuracy of the numerical method, three sets of different fuel species and initial conditions are considered, as reported in Tab. 3.1. The first set describes a millimeter-sized water droplet in a quiescent environment and is referred to as WAT-500K, while the other two sets, denoted as ETH-1500K and HEP-2500K, represent typical spray combustion conditions. In all three cases, the numerical solver accurately predicts droplet properties up to $d = 0$ without any numerical instabilities, and the proposed treatment of $d \to 0$ preserves the slope according to the d^2-law, leading to an accurate prediction of the evaporation time (not shown). In Figs. 3.2(a) to 3.2(c) the relative errors of droplet diameter, droplet temperature and velocity at time $t/\tau_{\text{evap}} \approx 0.1$ are plotted versus the number of time steps per evaporation time. The reference solution was generated using the classical 4th-order Runge-Kutta method with a very small time step width. The plots show that the order of convergence is two for droplet diameter, temperature and velocity, which confirms the iterative solution consisting of Newton's method and fixed-point iteration. Finally, Fig. 3.2(d) shows the effect of the time step width on the calculated evaporation times. For large to moderate time step sizes, the error decays quadratically as a refinement of the time step causes an improvement in the overall solution. Note that already a coarse resolution of the time history yields errors on a relatively low level (about 1 % for $\tau_{\text{evap}}/\Delta t = 10$, and 0.01 %

Table 3.1: Definition of different scenarios of droplet evaporation in an infinite environment to validate the numerical method. The ambient gas is pure nitrogen at atmospheric pressure. The droplet is initially at rest with an initial temperature of $T_{d,0} = 300\,\mathrm{K}$.

Name	Fuel	d_0	T_∞	u_∞
WAT-500K	Water	1 mm	500 K	0 m/s
ETH-1500K	Ethanol	50 µm	1500 K	1 m/s
HEP-2500K	*n*-Heptane	20 µm	2500 K	10 m/s

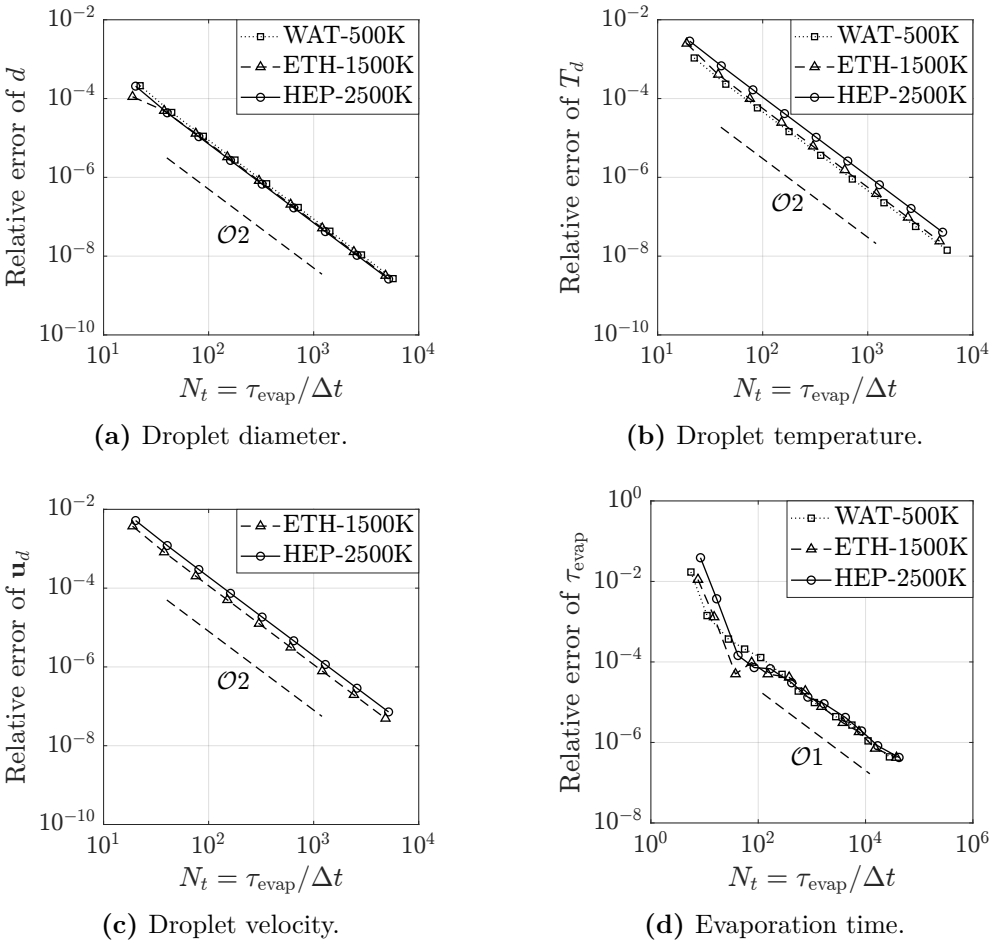

(a) Droplet diameter.

(b) Droplet temperature.

(c) Droplet velocity.

(d) Evaporation time.

Figure 3.2: Relative errors (L_2 norm) of droplet diameter, droplet temperature and droplet velocity at time $t/\tau_{\mathrm{evap}} \approx 0.1$ as well as of the evaporation time. The reference solution was generated using the classical 4th-order Runge-Kutta method with a very small time step width.

for $\tau_{\mathrm{evap}}/\Delta t = 100$). With further refinement of the time step, the error of the evaporation time is determined by the treatment of $d = 0$. Using the closure based on the d^2-law results in a linear decay of the error, as it represents a first-order approximation. It should be noted that the existence of a relative velocity between the gas and the droplet (cases ETH-1500K and HEP-2500K) leads to a deviation from the d^2-law, but this does not affect the error behavior as demonstrated by Fig. 3.2(d).

Comparison With Experimental Data and Comprehensive Model Results

The models describing the heating and evaporation of droplets are often validated by comparison with experimental data [102, 104, 121, 132, 182]. Most experiments have been conducted in a hot furnace with the droplet supported on a fiber system to allow for an accurate measurement of the time variation of the droplet size. The droplet size is usually of the order of millimeters, and therefore much larger than droplet sizes in typical spray combustion applications. As a result, additional effects play a role that are usually not considered in the evaporation model, which can lead to discrepancies between theoretical and experimental results. In detail, these are:

- *Effect of support fiber:* Several studies, experimentally and numerically, have shown that the additional heat input through fiber conduction is often not negligible, and can affect the droplet heat and mass transfer processes [24, 232, 233]. Further, the fiber affects the symmetrical shape of the droplet and the flame if combustion takes place.
- *Effect of radiation:* At high temperatures and large droplet sizes (as used in the experiments), thermal radiation becomes important, and the emission from the furnace wall must be taken into account [232]. The additional heat input will decrease the evaporation time.
- *Buoyancy effects:* According to Sirignano [188], buoyancy effects are relevant if the droplet size is of the order of millimeters, but can be neglected for droplet sizes of the order of micrometers. As a result, natural convection must be taken into account for experiments with millimeter-sized droplets conducted under normal gravity.

Yang and Wong [232] have incorporated the effects of heat conduction into the droplet through the fiber and the liquid-phase absorption of the radiation from the furnace wall into their comprehensive numerical model. They showed that these effects enhance the evaporation rate significantly, and a match with the experimental results of Nomura *et al.* [144] could only be achieved if radiative absorption and fiber conduction were included in the model.

Since both the effect of the support fiber and thermal radiation are not considered in the present evaporation model, the validation is not done on the basis of experimental data, but rather by using the results of the comprehensive model of Yang and Wong [232] that are obtained by ignoring both fiber conduction and radiative absorption. Note that their model includes unsteady mass and heat transport in the liquid and gas phase and thus provides a suitable reference solution for validation. The initial and ambient conditions are given by the experimental

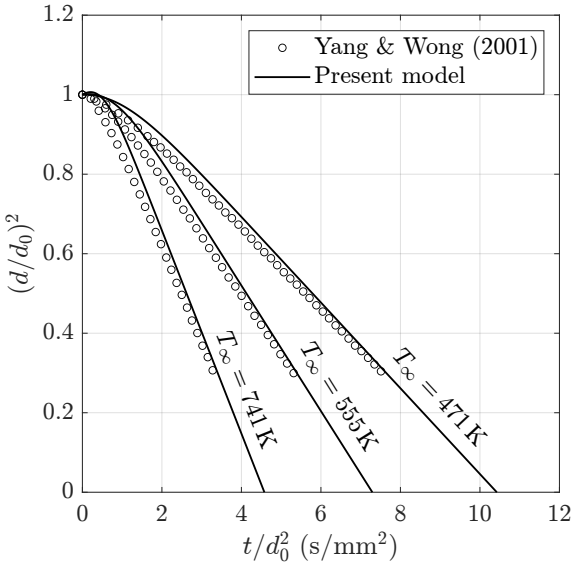

Figure 3.3: Comparison of the present evaporation model with results from the comprehensive model of Yang and Wong [232] ignoring both fiber conduction and radiative absorption. The setup is based on the experiments of Nomura *et al.* [144], where the case at atmospheric pressure is chosen.

setup of Nomura *et al.* [144], where the case at atmospheric pressure is selected here. Droplets are composed of liquid *n*-heptane and evaporate in a quiescent environment consisting of nitrogen at microgravity conditions. In the experiments, the initial droplet diameter ranges from 0.6 mm to 0.8 mm and is set to $d_0 = 0.7\,\mathrm{mm}$ in the numerical calculations. The initial droplet temperature is not reported by Nomura *et al.* nor by Yang and Wong. As the droplet is reported to be initially at room temperature its initial temperature is set to $T_{d,0} = 300\,\mathrm{K}$. Figure 3.3 shows the time evolution of the squared droplet diameter for different ambient temperatures. There is very good agreement between the present model and the comprehensive model by Yang and Wong, although the present model contains a number of simplifications, such as using a simplified energy equation and assuming quasi-steady processes and constant thermophysical properties in the gas phase. This proves that the present model formulation is capable of correctly predicting the time evolution of the droplet properties, and it is expected that it would also reproduce the experimental data of Nomura *et al.* if the effects of fiber conduction and radiative absorption were taken into account.

Chapter 4

MMC-LES Modeling of Dilute Spray Combustion

In the following chapter, the two-phase MMC-LES model for dilute spray combustion is presented. The starting point are the instantaneous transport equations as derived in the previous chapter. By applying a spatial filter operator, the filtered transport equations describing the turbulent flow and reference mixture fraction field are derived and models for the closure of the subgrid terms are presented. Subsequently, the filtered density function describing the evolution of the reactive scalars is introduced and its transport equation is derived. The corresponding solution is represented by a set of stochastic differential equations employing the sparse-Lagrangian MMC mixing model. Afterwards, models for the coupling between the Eulerian and Lagrangian fields are presented, with special focus on the two-phase coupling between the fuel droplets and the stochastic particles. Finally, the numerical implementation in OpenFOAM is briefly discussed.

4.1 Preliminary Remarks

4.1.1 General Modeling Approach and Assumptions

The two-phase MMC-LES model employs a hybrid Eulerian/Lagrangian/Lagrangian method, as shown in Fig. 4.1. An Eulerian LES of the turbulent flow and reference mixture fraction field is performed, the latter of which is required for the MMC model, where standard models are used for the closure of the subgrid terms (see Sec. 4.2). The turbulent composition field is modeled using the filtered density function (FDF) approach, whose solution is obtained from a set of equivalent stochastic differential equations describing the transport of notional particles in physical and composition space (Sec. 4.3). A mixing model is required to account for the inter-

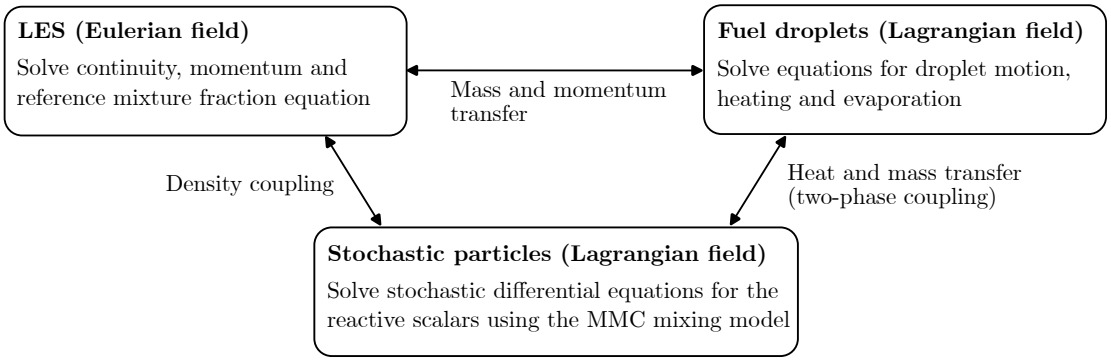

Figure 4.1: Overview of the two-phase MMC-LES model with schematic of the coupling relations.

actions between the stochastic particles, with the sparse-Lagrangian MMC model used in the present work (Sec. 4.4). The liquid fuel droplets are treated as Lagrangian point particles and follow the deterministic formulation that was presented in Sec. 3.2. In order to account for subgrid turbulent fluctuations, stochastic dispersion terms are often added to the droplet equations [12–14, 166]. However, as LES resolves the dynamics of the large-scale motions and a large portion of the turbulent kinetic energy (typically up to 80 % [163, 164]), the role of the stochastic dispersion terms is often minor [5]. Therefore, these terms are not considered in the present work.

The mass and momentum coupling between the Eulerian LES and the dispersed fuel droplets follows conventional modeling as described in Sec. 3.2.4. The heat and mass transfer between the droplets and the gas phase is accounted for by coupling the fuel droplets with the stochastic particles, which is referred to as two-phase coupling. The corresponding models will be presented in Sec. 4.5. The stochastic particles feed back their density to the Eulerian LES in order to accommodate the effect of chemical reactions in the Eulerian field. Details will be given in Sec. 4.6.

As already mentioned in Sec. 3.1, radiation and gravity are not considered in this work. Furthermore, low Mach numbers and Lewis numbers equal to one as well as constant Schmidt and Prandtl numbers are assumed, where $\mathrm{Sc} = \mathrm{Pr} = 0.7$ is used throughout the present work.

4.1.2 Definition of Mixture Fraction

Mixture fraction describes the mixing between the fuel stream and the oxidizer stream and hence plays a key role in the modeling of nonpremixed combustion. In single-phase flows, mixture fraction is a strictly conserved and bounded scalar that obeys a scalar transport equation without source terms, where the boundary conditions are one in the fuel stream and zero in the oxidizer stream. In two-phase

flows, the definition of mixture fraction is not trivial, as the balance equation for mixture fraction contains a source term to account for the fuel originating from the evaporating droplet field. As a result, evaporation will lead to an increase of the maximum mixture fraction value over time, so that mixture fraction is no longer a conserved and bounded scalar. In order to keep mixture fraction between two well-defined limits also for two-phase flows, the upper bound is defined here as pure fuel as given by the liquid droplets (which cannot be exceeded), while the lower bound is still given by the conditions of the oxidizer stream.

From a mathematical point of view, mixture fraction is defined on the basis of the conservation of chemical elements. The mass fraction of element i is given by

$$\mathcal{Z}_i = \sum_{k=1}^{N_s} \frac{a_{ik}\mathcal{M}_i}{\mathcal{M}_k} Y_k, \tag{4.1}$$

where a_{ik} is the number of atoms of element i in a molecule of species k, and $\mathcal{M}_i$ and $\mathcal{M}_k$ denote the molar mass of element i and molecule k, respectively [150]. By adding the transport equations for mass fractions Y_k, which are given by Eq. (3.2), in the same way as indicated by Eq. (4.1), and assuming equal diffusion coefficients, the balance equation for the mass fraction of element i can be written as

$$\frac{\partial(\rho\mathcal{Z}_i)}{\partial t} + \frac{\partial(\rho u_j \mathcal{Z}_i)}{\partial x_j} = \frac{\partial}{\partial x_j}\left(\rho\mathcal{D}\frac{\partial \mathcal{Z}_i}{\partial x_j}\right) + \frac{a_{iF}\mathcal{M}_i}{\mathcal{M}_F}\dot{S}_M, \tag{4.2}$$

where the subscript F denotes the fuel species. Note that no chemical source term appears in the transport equation, as elements are conserved during combustion. Details on the derivation (for single-phase flows) can be found in Peters [150]. Mixture fraction is defined as a normalized element mass fraction according to

$$f = \frac{\mathcal{Z}_i - \mathcal{Z}_{i,\mathrm{Ox}}}{\mathcal{Z}_{i,\mathrm{Fu}} - \mathcal{Z}_{i,\mathrm{Ox}}}, \tag{4.3}$$

where the subscripts Ox and Fu indicate the oxidizer and fuel stream, respectively (not to be confused with the fuel species denoted as F). By inserting the definition of mixture fraction, Eq. (4.3), into the balance equation for the element mass fraction, Eq. (4.2), and making use of the continuity equation, the balance equation for mixture fraction is derived,

$$\frac{\partial(\rho f)}{\partial t} + \frac{\partial(\rho u_j f)}{\partial x_j} = \frac{\partial}{\partial x_j}\left(\rho\mathcal{D}\frac{\partial f}{\partial x_j}\right) + \dot{S}_M, \tag{4.4}$$

which is equivalent to the general scalar transport equation that is given by Eq. (3.18) but without the chemical source term. Note that the derivation is based on the assumption that the fuel stream consists of pure fuel (otherwise, a prefactor would

remain in front of the source term). The balance equation for mixture fraction is valid regardless of which element is chosen to define mixture fraction. However, the absolute values of the mixture fraction depend on the choice of the element i in Eq. (4.3). This is in contrast to single-phase flows, where mixture fraction is identical for all elements. To ensure monotonicity, it is generally required that the element mass fraction has its minimum in the oxidizer stream and its maximum in the fuel stream. Therefore, mixture fraction is defined here based on the conservation of carbon. This definition is common in single-phase combustion processes involving hydrocarbons or alcohols, and also provides a reasonable definition for spray flames with pre-evaporation while fulfilling the requirements of monotonicity and boundedness between zero and one.

4.2 Large Eddy Simulation of the Flow and Mixture Fraction Field

4.2.1 Definition of the Filter Operator

In LES, a spatial filter operator is applied in order to separate the flow variables into a large-scale (filtered) part and a small-scale (residual or subfilter) contribution,

$$q(\mathbf{x},t) = \bar{q}(\mathbf{x},t) + q'(\mathbf{x},t), \tag{4.5}$$

where $\bar{q}(\mathbf{x},t)$ denotes the filtered part of a space-time variable $q(\mathbf{x},t)$, and $q'(\mathbf{x},t)$ represents the subfilter fluctuation. The spatial filter operator is defined formally as

$$\bar{q}(\mathbf{x},t) = \int_{-\infty}^{+\infty} G(\mathbf{x}'-\mathbf{x}) q(\mathbf{x}',t) \mathrm{d}\mathbf{x}', \tag{4.6}$$

where G is a kernel function of characteristic width Δ_{LES}. The specific form of the kernel function is not required for the derivation of the filtered transport equations, but it is assumed that the filter satisfies the fundamental properties of conservation of constants (consistency), linearity and commutation with differentiation [64]. Furthermore, only positive ($G(\mathbf{x}) \geq 0$) and symmetric ($G(\mathbf{x}) = G(-\mathbf{x})$) kernel functions are considered.

In flows with density variations, it is common to use a density-weighted filter analogous to Favre averaging,

$$\widetilde{q} = \frac{\overline{\rho q}}{\bar{\rho}}, \tag{4.7}$$

which is often referred to as a Favre filter. This results in filtered equations that are structurally similar to their corresponding non-filtered equations, and reduces the

number of unclosed terms. The decomposition of any variable can then be written as

$$q(\mathbf{x},t) = \widetilde{q}(\mathbf{x},t) + q''(\mathbf{x},t), \tag{4.8}$$

where fluctuations $q''(\mathbf{x},t)$ are now defined with respect to the density-weighted filtered variable $\widetilde{q}(\mathbf{x},t)$.

It should be noted that practical LES calculations usually do not use an explicit filter operator. Instead, the model filtered equations (which result from the formal application of a filter operator) are solved numerically on a mesh that is significantly larger than the smallest scales of turbulence using standard discretization techniques. In that case, the numerical grid acts as an effective filter while the model for residual stress tensor provides the required stability of the numerical solution, which is referred to as implicit filtering [119]. In that sense, the terms 'resolved' and 'subgrid' are commonly used equivalently with 'filtered' and 'subfilter'.

4.2.2 Filtered Transport Equations

By applying the filter operator that is given by Eq. (4.6) to the instantaneous transport equations from Sec. 3.1 and using the definition of density-weighted variables, the transport equations for the filtered variables are derived. Note that the MMC-LES model employs LES only for the turbulent flow field (velocity and pressure) and the reference mixture fraction field (the latter is required for the MMC model), while the reactive scalars are obtained from the filtered mass density function method (Sec. 4.3).

The calculation of the turbulent flow field requires the continuity equation and the momentum equation, whose instantaneous equations are given by Eq. (3.1) and Eq. (3.3), respectively. The filtered continuity equation takes the form

$$\frac{\partial \bar{\rho}}{\partial t} + \frac{\partial(\bar{\rho}\widetilde{u}_j)}{\partial x_j} = \bar{\dot{S}}_M, \tag{4.9}$$

where no unclosed term appears due to the use of density-weighted variables. Applying the filter operator to the momentum equation results in

$$\frac{\partial(\bar{\rho}\widetilde{u}_i)}{\partial t} + \frac{\partial(\bar{\rho}\widetilde{u}_i\widetilde{u}_j)}{\partial x_j} = -\frac{\partial \bar{p}}{\partial x_i} + \frac{\partial \bar{\tau}_{ij}}{\partial x_j} - \frac{\partial \tau_{ij}^{\mathrm{sgs}}}{\partial x_j} + \bar{\dot{S}}_{u,i}, \tag{4.10}$$

where τ_{ij}^{sgs} is the subgrid-scale (SGS) stress tensor, which represents the effect of the subgrid fluctuations on the resolved scales. It is defined as

$$\tau_{ij}^{\mathrm{sgs}} = \bar{\rho}\left(\widetilde{u_i u_j} - \widetilde{u}_i\widetilde{u}_j\right), \tag{4.11}$$

and its modeling will be described in the next section. The filtered viscous stress tensor appears in unclosed form due to the nonlinearity that is introduced by the

temperature dependence of the viscosity. However, the effect of temperature fluctuations on the thermophysical properties is usually small, such that the term can be approximated by its computable part [64, 220],

$$\bar{\tau}_{ij} = 2\mu \left(\widetilde{S}_{ij} - \frac{1}{3}\delta_{ij}\widetilde{S}_{kk} \right), \tag{4.12}$$

where the viscosity μ is evaluated using the filtered temperature, and $\widetilde{S}_{ij}$ denotes the rate-of-strain tensor based on the resolved velocity field.

Applying the filter operator to the instantaneous transport equation of mixture fraction that is given by Eq. (4.4) yields

$$\frac{\partial(\bar{\rho}\widetilde{f})}{\partial t} + \frac{\partial(\bar{\rho}\widetilde{u}_j\widetilde{f})}{\partial x_j} = \frac{\partial}{\partial x_j}\left(\bar{\rho}\mathcal{D}\frac{\partial \widetilde{f}}{\partial x_j} \right) - \frac{\partial j_j^{\mathrm{sgs}}}{\partial x_j} + \bar{\dot{S}}_M, \tag{4.13}$$

where the nonlinearity that results from the temperature dependence of the thermophysical properties (here the diffusion coefficient) has been neglected. The subgrid scalar flux is defined as

$$j_j^{\mathrm{sgs}} = \bar{\rho}\left(\widetilde{u_j f} - \widetilde{u}_j\widetilde{f} \right), \tag{4.14}$$

and requires closure by a subgrid model.

4.2.3 Subgrid Modeling

The modeling of the SGS stress tensor in the filtered momentum equation is based on the Boussinesq hypothesis [18], which states that the subgrid-scale stresses can be modeled in analogy to the viscous stress tensor, with the molecular viscosity being replaced by a turbulent viscosity. In these kind of eddy viscosity models, the deviatoric (traceless) part of the SGS stress tensor, which is obtained by subtracting the isotropic part $\frac{1}{3}\delta_{ij}\tau_{kk}^{\mathrm{sgs}}$, is expressed as

$$\tau_{ij}^{\mathrm{sgs}} - \frac{1}{3}\delta_{ij}\tau_{kk}^{\mathrm{sgs}} = -2\bar{\rho}\nu_t \left(\widetilde{S}_{ij} - \frac{1}{3}\delta_{ij}\widetilde{S}_{kk} \right), \tag{4.15}$$

with ν_t being the turbulent viscosity [64]. The isotropic part of the SGS stress tensor must generally be modeled separately (see for example Yoshizawa [236]). However, for incompressible flows it is usually added to the filtered pressure to avoid modeling, while for compressible flows it can be argued that its contribution is small compared to the thermodynamic pressure and can therefore be neglected [51]. Accordingly, the modeled form of the filtered momentum equation can be written as

$$\frac{\partial(\bar{\rho}\widetilde{u}_i)}{\partial t} + \frac{\partial(\bar{\rho}\widetilde{u}_i\widetilde{u}_j)}{\partial x_j} = -\frac{\partial \bar{p}}{\partial x_i} + \frac{\partial}{\partial x_j}\left[\mu_{\mathrm{eff}} \left(2\widetilde{S}_{ij} - \frac{2}{3}\delta_{ij}\widetilde{S}_{kk} \right) \right] + \bar{\dot{S}}_{u,i}, \tag{4.16}$$

where $\mu_{\text{eff}} = \mu + \mu_t$ is the effective viscosity, with the turbulent component given by $\mu_t = \bar{\rho}\nu_t$.

The most popular model for estimating the turbulent viscosity is the Smagorinsky model [190], which reads as

$$\nu_t = (C_s \Delta_{\text{LES}})^2 \sqrt{2\widetilde{S}_{ij}\widetilde{S}_{ij}}, \tag{4.17}$$

where C_s is the Smagorinsky constant and Δ_{LES} is the filter width. The Smagorinsky constant can be calculated theoretically as $C_s \approx 0.17$ [163], but practically it takes values ranging from 0.1 to 0.2 depending on the flow [64]. The filter width is generally associated with the computational grid and is evaluated as the cubic root of the cell volume, $\Delta_{\text{LES}} = V_{\text{cell}}^{1/3}$. Note that the Smagorinsky model is implemented here using a more general and compressible formulation [58], which reduces to Eq. (4.17) in the limit of incompressible flows.

An alternative and more recent subgrid model is the σ-model that was proposed by Nicoud *et al.* [143]. It calculates the turbulent viscosity based on the singular values of the resolved velocity gradient tensor according to

$$\nu_t = (C_\sigma \Delta_{\text{LES}})^2 \, \frac{\sigma_3 \, (\sigma_1 - \sigma_2) \, (\sigma_2 - \sigma_3)}{\sigma_1^2}, \tag{4.18}$$

with singular values $\sigma_1 \geq \sigma_2 \geq \sigma_3 \geq 0$ given by the square roots of the eigenvalues of the matrix $G_{ij} = \partial\widetilde{u}_k/\partial x_i \; \partial\widetilde{u}_k/\partial x_j$. For the model constant, a value of $C_\sigma = 1.5$ has shown to provide good agreement with results from direct numerical simulation and experimental data [143, 173].

The subgrid scalar flux in the filtered transport equation for mixture fraction is modeled by a gradient diffusion model [176],

$$j_j^{\text{sgs}} = -\bar{\rho}\mathcal{D}_t \frac{\partial \widetilde{f}}{\partial x_j}, \tag{4.19}$$

where $\mathcal{D}_t$ is the turbulent diffusivity, which is linked to the turbulent viscosity via the turbulent Schmidt number,

$$\mathcal{D}_t = \frac{\nu_t}{\text{Sc}_t}. \tag{4.20}$$

By inserting the model into Eq. (4.13), the filtered mixture fraction transport equation can be written as

$$\frac{\partial(\bar{\rho}\widetilde{f})}{\partial t} + \frac{\partial(\bar{\rho}\widetilde{u}_j\widetilde{f})}{\partial x_j} = \frac{\partial}{\partial x_j}\left(\bar{\rho}\mathcal{D}_{\text{eff}} \frac{\partial \widetilde{f}}{\partial x_j}\right) + \bar{\dot{S}}_M, \tag{4.21}$$

with $\mathcal{D}_{\text{eff}} = \mathcal{D} + \mathcal{D}_t$ being the effective diffusivity in analogy to the effective viscosity.

4.3 The Filtered Density Function (FDF) Approach

4.3.1 Definition and Properties of the FDF

To overcome the closure problem associated with the filtered reaction rates in LES, the turbulent composition field $\boldsymbol{\phi} = (\mathbf{Y}, h)^{\mathsf{T}}$ is represented probabilistically by the filtered mass density function (FMDF) [92], defined as

$$F_L(\boldsymbol{\psi}; \mathbf{x}, t) = \int_{-\infty}^{+\infty} \rho(\mathbf{x}', t)\zeta[\boldsymbol{\psi}, \boldsymbol{\phi}(\mathbf{x}', t)]G(\mathbf{x}' - \mathbf{x})\mathrm{d}\mathbf{x}', \tag{4.22}$$

where $\boldsymbol{\psi}$ denotes the sample space for the composition vector $\boldsymbol{\phi}$, ρ is the gaseous density, and G is the kernel function of the filter. The term $\zeta[\boldsymbol{\psi}, \boldsymbol{\phi}(\mathbf{x}', t)]$ is called the fine-grained density [145, 158], and is given by the $(N_s + 1)$-dimensional Dirac delta function,

$$\zeta[\boldsymbol{\psi}, \boldsymbol{\phi}(\mathbf{x}, t)] = \delta[\boldsymbol{\psi} - \boldsymbol{\phi}(\mathbf{x}, t)] = \prod_{\alpha=1}^{N_s+1} \delta[\psi_\alpha - \phi_\alpha(\mathbf{x}, t)]. \tag{4.23}$$

Note that for constant-density flows, the FMDF reduces to the filtered density function (FDF). In the present work, the term FDF is used to describe both the FDF and the FMDF.

Filtered quantities are derived from the FMDF by integration in the scalar composition space. By design, the zeroth moment corresponds to the filtered density,

$$\int_{-\infty}^{+\infty} F_L(\boldsymbol{\psi}; \mathbf{x}, t)\mathrm{d}\boldsymbol{\psi} = \bar{\rho}(\mathbf{x}, t), \tag{4.24}$$

and the first moment of the FMDF yields the density-weighted filtered composition variables,

$$\int_{-\infty}^{+\infty} \psi_\alpha F_L(\boldsymbol{\psi}; \mathbf{x}, t)\mathrm{d}\boldsymbol{\psi} = \bar{\rho}(\mathbf{x}, t)\widetilde{\phi}_\alpha(\mathbf{x}, t). \tag{4.25}$$

More general, the Favre-filtered value of any arbitrary random function $q(\mathbf{x}, t)$ is obtained from

$$\int_{-\infty}^{+\infty} \langle q(\mathbf{x}, t)|\boldsymbol{\psi}\rangle \, F_L(\boldsymbol{\psi}; \mathbf{x}, t)\mathrm{d}\boldsymbol{\psi} = \bar{\rho}(\mathbf{x}, t)\widetilde{q}(\mathbf{x}, t), \tag{4.26}$$

where the density-weighted conditionally filtered value of the variable $q(\mathbf{x}, t)$ is defined as

$$\langle q(\mathbf{x}, t)|\boldsymbol{\psi}\rangle = \frac{\int_{-\infty}^{+\infty} \rho(\mathbf{x}', t)q(\mathbf{x}', t)\zeta[\boldsymbol{\psi}, \boldsymbol{\phi}(\mathbf{x}', t)]G(\mathbf{x}' - \mathbf{x})\mathrm{d}\mathbf{x}'}{F_L(\boldsymbol{\psi}; \mathbf{x}, t)}. \tag{4.27}$$

Note that angle brackets are used in place of the tilde symbol for better readability. In the case where the variable $q(\mathbf{x}, t)$ can be completely described by the composition space $\boldsymbol{\phi}(\mathbf{x}, t)$ (such as the composition variables themselves or the chemical source term), the conditional filtered value takes the form $\langle q(\mathbf{x}, t)|\boldsymbol{\psi}\rangle = q(\boldsymbol{\psi})$.

4.3.2 The FDF Transport Equation

The transport equation for the temporal and spatial evolution of the FDF with application to two-phase flows is reported in a number of previous works [43, 67, 68, 82, 102, 136, 208], but will be repeated here for the sake of completeness and uniformity of notation. Note that in some of the works, including the recent two-phase MMC-LES formulation of Khan *et al.* [102], a phase indicator is introduced to distinguish between the gas phase and the liquid phase. Since only dilute sprays are considered in the present work, where all the liquid fuel is stored in the dispersed droplets, the phase indicator is omitted here. Accordingly, the two-phase FDF transport equation differs from its single-phase formulation only in the existence of the evaporation source terms.

Exact Form of the FDF Transport Equation

The derivation of the FDF transport equation is usually based on the fine-grained density utilizing the method developed by Lundgren [120]. Using the chain rule and the properties of the Dirac delta function, the derivative of the fine-grained density can be expressed as [106, 163]

$$\frac{\partial \zeta}{\partial \eta} = -\frac{\partial \zeta}{\partial \psi_\alpha}\frac{\partial \phi_\alpha}{\partial \eta} = -\frac{\partial}{\partial \psi_\alpha}\left(\zeta \frac{\partial \phi_\alpha}{\partial \eta}\right), \tag{4.28}$$

where the variable η indicates space (x_j) or time (t). The second step is valid because ϕ_α is independent of the sample space variable ψ_α. Multiplication of Eq. (4.28) with $\eta = t$ by the gaseous density ρ and using the chain rule results in

$$\frac{\partial(\rho\zeta)}{\partial t} - \zeta\frac{\partial \rho}{\partial t} = -\frac{\partial}{\partial \psi_\alpha}\left[\zeta\left(\frac{\partial(\rho\phi_\alpha)}{\partial t} - \phi_\alpha\frac{\partial \rho}{\partial t}\right)\right], \tag{4.29}$$

where it was used that density ρ is independent of the independent sample space variable ψ_α [72, 106]. Inserting the scalar transport equation, Eq. (3.18), and the continuity equation, Eq. (3.1) with $\dot{S}_M = \rho\Pi_F$, yields

$$\begin{aligned}
&\frac{\partial(\rho\zeta)}{\partial t} - \zeta\left(-\frac{\partial(\rho u_j)}{\partial x_j} + \rho\Pi_F\right) \\
&\quad = -\frac{\partial}{\partial \psi_\alpha}\Bigg[\zeta\Bigg(-\frac{\partial(\rho u_j \phi_\alpha)}{\partial x_j} + \frac{\partial}{\partial x_j}\left(\rho\mathcal{D}\frac{\partial \phi_\alpha}{\partial x_j}\right) + \rho W_\alpha + \rho\Pi_\alpha \\
&\qquad\qquad - \phi_\alpha\left(-\frac{\partial(\rho u_j)}{\partial x_j} + \rho\Pi_F\right)\Bigg)\Bigg].
\end{aligned} \tag{4.30}$$

With some further manipulations involving the chain rule and using Eq. (4.28) with $\eta = x_j$, the equation for the fine-grained density takes the form

$$\frac{\partial(\rho\zeta)}{\partial t} + \frac{\partial(\rho u_j \zeta)}{\partial x_j} = -\frac{\partial}{\partial \psi_\alpha}\left[\frac{\partial}{\partial x_j}\left(\rho\mathcal{D}\frac{\partial \phi_\alpha}{\partial x_j}\right)\zeta + \rho W_\alpha \zeta + \rho\Pi_\alpha\zeta - \phi_\alpha\rho\Pi_F\zeta\right] + \rho\Pi_F\zeta. \tag{4.31}$$

Weighting the equation by the filter kernel and integrating over the physical space according to Eqs. (4.22) and (4.26) finally yields the FDF transport equation,

$$\begin{aligned}\frac{\partial F_L}{\partial t} + \frac{\partial(\langle u_j|\boldsymbol{\psi}\rangle\, F_L)}{\partial x_j} = &-\frac{\partial}{\partial \psi_\alpha}\left[\left\langle \frac{1}{\rho}\frac{\partial}{\partial x_j}\left(\rho\mathcal{D}\frac{\partial\phi_\alpha}{\partial x_j}\right)\middle|\boldsymbol{\psi}\right\rangle F_L\right] - \frac{\partial(\langle W_\alpha|\boldsymbol{\psi}\rangle\, F_L)}{\partial \psi_\alpha} \\ &- \frac{\partial}{\partial\psi_\alpha}\left[\langle \Pi_\alpha - \phi_\alpha\Pi_F|\boldsymbol{\psi}\rangle\, F_L\right] + \langle\Pi_F|\boldsymbol{\psi}\rangle\, F_L. \end{aligned} \tag{4.32}$$

This is an exact transport equation that describes the evolution of the FMDF due to transport in physical and composition space. The left-hand side of the equation contains the time derivative of the FMDF and a conditional convective term. The first term on the right-hand side accounts for molecular diffusion, and the second term is the chemical source term, which appears in closed form via $\langle W_\alpha|\boldsymbol{\psi}\rangle = W_\alpha(\boldsymbol{\psi})$. The final two terms on the right-hand side describe the effects of heat and mass transfer due to evaporation. Note that there are different versions of the FDF transport equation for spray flames in the literature, mainly due to different definitions of the evaporation source terms. The form presented here is consistent with the works of Tang *et al.* [207, 208] and Zhao and Haworth [241], but has minor differences compared to the work of Khan *et al.* [102]. Details can be found in Appendix A.2.

Modeled Form of the FDF Transport Equation

Modeling is required for the conditional convection, molecular diffusion and evaporation terms. The conditional velocity term is decomposed into its resolved and subgrid-scale components, where the latter is modeled using a gradient diffusion model [92],

$$\langle u_j|\boldsymbol{\psi}\rangle\, F_L = \widetilde{u}_j F_L + (\langle u_j|\boldsymbol{\psi}\rangle - \widetilde{u}_j)\, F_L = \widetilde{u}_j F_L - \bar{\rho}\mathcal{D}_t\frac{\partial(F_L/\bar{\rho})}{\partial x_j}, \tag{4.33}$$

with turbulent diffusivity $\mathcal{D}_t$. The conditional diffusion term is reformulated according to [30, 33, 72, 106]

$$\begin{aligned}&-\frac{\partial}{\partial\psi_\alpha}\left[\left\langle\frac{1}{\rho}\frac{\partial}{\partial x_j}\left(\rho\mathcal{D}\frac{\partial\phi_\alpha}{\partial x_j}\right)\middle|\boldsymbol{\psi}\right\rangle F_L\right] \\ &\qquad = \frac{\partial}{\partial x_j}\left[\bar{\rho}\mathcal{D}\frac{\partial(F_L/\bar{\rho})}{\partial x_j}\right] - \frac{\partial^2}{\partial\psi_\alpha\partial\psi_\beta}\left[\left\langle\mathcal{D}\frac{\partial\phi_\alpha}{\partial x_j}\frac{\partial\phi_\beta}{\partial x_j}\middle|\boldsymbol{\psi}\right\rangle F_L\right]. \end{aligned} \tag{4.34}$$

The first term on the right-hand side represents the resolved-scale molecular diffusion in physical space, while the second term is linked with mixing processes on subgrid scale (also referred to as micro-mixing term) and is closed by a mixing model. The mixing model is usually formulated as a particle interaction model in the context of a Monte Carlo solution of the FDF transport equation (see the following sections), where the equivalent modeling expression in the Eulerian form of the FDF transport equation is given by

$$\frac{\partial^2}{\partial\psi_\alpha\partial\psi_\beta}\left[\left\langle \mathcal{D}\frac{\partial\phi_\alpha}{\partial x_j}\frac{\partial\phi_\beta}{\partial x_j}\middle|\boldsymbol{\psi}\right\rangle F_L\right] = -\frac{\partial}{\partial\psi_\alpha}\left[\frac{C_{\mathrm{mix}}}{\tau_L}\left(\psi_\alpha-\phi_\alpha^{\mathrm{mean}}\right)F_L\right]. \tag{4.35}$$

Here, C_{mix} is a modeling constant, τ_L is the (Lagrangian) mixing time scale, and $\phi_\alpha^{\mathrm{mean}}$ denotes a mean composition, the determination of which depends on the choice of the mixing model. The classical mixing models for dense particle methods are summarized in Sec. 4.3.4, and the sparse-Lagrangian MMC mixing model is presented in Sec. 4.4. The modeling of the conditional evaporation term is discussed in detail in Sec. 4.5, and therefore the conditionally filtered expressions are retained here. By incorporating the aforementioned closures into the exact transport equation of the FMDF, one finally obtains

$$\begin{aligned}\frac{\partial F_L}{\partial t}+\frac{\partial(\widetilde{u}_j F_L)}{\partial x_j} = {}& \frac{\partial}{\partial x_j}\left[\bar{\rho}(\mathcal{D}+\mathcal{D}_t)\frac{\partial(F_L/\bar{\rho})}{\partial x_j}\right]-\frac{\partial(W_\alpha(\boldsymbol{\psi})F_L)}{\partial\psi_\alpha}\\ &+\frac{\partial}{\partial\psi_\alpha}\left[\frac{C_{\mathrm{mix}}}{\tau_L}\left(\psi_\alpha-\phi_\alpha^{\mathrm{mean}}\right)F_L\right]\\ &-\frac{\partial}{\partial\psi_\alpha}\left[\langle\Pi_\alpha-\phi_\alpha\Pi_F|\boldsymbol{\psi}\rangle\,F_L\right]+\langle\Pi_F|\boldsymbol{\psi}\rangle\,F_L.\end{aligned} \tag{4.36}$$

The terms in the first row of the equation are conventional for FDF methods and appear in closed form, while the terms in the second and third row represent mixing and evaporation and require further modeling details (see Secs. 4.4 and 4.5).

4.3.3 Monte Carlo Solution

The FDF transport equation is (N_s+3)-dimensional with $N_s \gg 1$ for a realistic treatment of the chemical kinetics, thus making an Eulerian solution (e.g., by using a finite-difference method) impractical. Therefore, the FDF transport equation is replaced by a set of equivalent stochastic differential equations that govern the evolution of notional particles in physical and composition space, each of them representing an instantaneous and local realization of the composition field [156, 158, 161]. By comparison of the FDF transport equation with the Fokker-Plank equation [63], the set of stochastic particle equations that emulate the solution of

Eq. (4.36) is found,

$$\mathrm{d}x_i^{sp} = \left[\widetilde{u}_i + \frac{1}{\bar{\rho}}\frac{\partial(\bar{\rho}\mathcal{D}_{\mathrm{eff}})}{\partial x_i}\right]^{sp}\mathrm{d}t + \left[\sqrt{2\mathcal{D}_{\mathrm{eff}}}\right]^{sp}\mathrm{d}\omega_i, \tag{4.37}$$

$$\mathrm{d}\phi_\alpha^{sp} = \left[W_\alpha - \frac{C_{\mathrm{mix}}}{\tau_L}\left(\phi_\alpha - \phi_\alpha^{\mathrm{mean}}\right) + \langle \Pi_\alpha - \phi_\alpha \Pi_F | \boldsymbol{\psi}\rangle\right]^{sp}\mathrm{d}t, \tag{4.38}$$

$$\mathrm{d}m^{sp} = m^{sp}\,\langle \Pi_F | \boldsymbol{\psi}\rangle^{sp}\,\mathrm{d}t, \tag{4.39}$$

where the superscript *sp* indicates properties that are evaluated on or assigned to the stochastic particles. Equation (4.37) describes the transport of the notional particles with the turbulent flow field and superimposed by a random walk, with $\mathrm{d}\omega_i$ being the increment of an independent Wiener process. The additional drift term containing the gradient of the effective diffusivity results from a decomposition of the diffusion term that is required for the comparison with the Fokker-Plank equation. The filtered velocity and density as well as the effective diffusivity and its gradient that appear in Eq. (4.37) are interpolated from the Eulerian LES fields to the respective particle positions. Equation (4.38) represents the transport in composition space and describes the change of the gas composition of the notional particles due to chemical reactions, mixing and evaporation. Equivalent to the FDF transport equation, the chemical source term W_α appears in closed form and can be evaluated directly from the composition vector of the notional particles. Finally, Eq. (4.39) accounts for the change of the stochastic particle mass due to evaporation. The set of stochastic differential equations is supplemented with the equation of state, Eq. (3.5) that is used here to calculate the density, where the pressure is obtained from the Eulerian LES field and interpolated to the respective particle positions.

It should be noted that, unlike single-phase flows, the two-phase FDF transport equation is strictly speaking not a Fokker-Planck equation due to the existence of the last evaporation term in Eq. (4.36). However, as this term is accounted for in the particle mass equation, it can be ignored for the comparison with the Fokker-Plank equation, thus allowing to find the stochastic differential equations for transport in physical and composition space.

The Monte Carlo solution generally requires a sufficiently high number of particles per computational cell (typically 10 to 100) to accurately reproduce the lower moments (such as mean values and subfilter fluctuations) locally and instantaneously, which is referred to as an intensive particle method. In contrast, sparse particle simulations do not aim to reproduce the statistics of the reactive scalars locally and instantaneously, but rather predict unconditionally and conditionally averaged quantities while still accounting for subfilter fluctuations [205], which allows significantly fewer particles to be used.

4.3.4 The Classical Mixing Models

The Mixing Substep

Using the stochastic form given by Eq. (4.38), the effect of mixing on the composition of a notional particle can be written as

$$\frac{\mathrm{d}\phi_\alpha^{sp}}{\mathrm{d}t} = -\frac{C_{\mathrm{mix}}}{\tau_L}\left(\phi_\alpha^{sp} - \phi_\alpha^{\mathrm{mean}}\right). \tag{4.40}$$

By integrating Eq. (4.40) over the time interval Δt, the following relation for the particle composition after mixing is obtained,

$$\phi_\alpha^{sp}(t+\Delta t) = \phi_\alpha^{sp}(t) + \gamma\left(\phi_\alpha^{\mathrm{mean}} - \phi_\alpha^{sp}(t)\right), \tag{4.41}$$

with the mixing extent γ given by

$$\gamma = 1 - \exp(-C_{\mathrm{mix}}\Delta t/\tau_L). \tag{4.42}$$

It describes the degree of mixing and is bounded between zero and one, where $\gamma = 0$ indicates no mixing at all and $\gamma = 1$ is equivalent to complete mixing. While Eq. (4.41) forms the basis for the mixing substep, the specific form of the interactions between the notional particles and with the mean is the subject of the mixing model. In the following, the conventional mixing models for intensive Lagrangian simulations are briefly presented, where mixing is usually limited to the computational cell. The sparse-Lagrangian MMC mixing model, which is the focus of the present work, will be discussed in more detail in the subsequent section.

The IEM Model

The simplest mixing model is the interaction by exchange with the mean (IEM) model [216], which is also known as the linear mean-square estimation (LMSE) model [46]. It employs a deterministic relaxation of the scalar values of the notional particles towards their unconditional mean, $\phi_\alpha^{\mathrm{mean}} = \langle\phi_\alpha\rangle$. The mean composition is calculated locally from the instantaneous particle compositions weighted by their mass,

$$\langle\phi_\alpha\rangle = \frac{\sum_{sp} m^{sp}\phi_\alpha^{sp}}{\sum_{sp} m^{sp}}, \tag{4.43}$$

where summation is performed over all particles that are located within the LES cell. The modeling constant in Eq. (4.42) takes the value $C_{\mathrm{mix}} = 0.5$. Due to its simplicity, the IEM model is widely used in combustion simulations, although it has some well-known limitations, such as that it preserves the shape of the scalar PDF [22, 45, 131, 134, 167].

Coalescence/Dispersion Models

Another class of mixing models is based on Curl's coalescence/dispersion model [38], which employs pairwise particle mixing. For a pair of particles denoted as p and q, the mixing step given by Eq. (4.41) is expressed as

$$\phi_\alpha^p(t+\Delta t) = \phi_\alpha^p(t) + \gamma\left(\langle\phi_\alpha\rangle^{p,q} - \phi_\alpha^p(t)\right), \tag{4.44a}$$

$$\phi_\alpha^q(t+\Delta t) = \phi_\alpha^q(t) + \gamma\left(\langle\phi_\alpha\rangle^{p,q} - \phi_\alpha^q(t)\right), \tag{4.44b}$$

where the mean value $\phi_\alpha^{\text{mean}} = \langle\phi_\alpha\rangle^{p,q}$ is calculated from the scalars of the particle pair using the mass-weighted average,

$$\langle\phi_\alpha\rangle^{p,q} = \frac{m^p\phi_\alpha^p + m^q\phi_\alpha^q}{m^p + m^q}. \tag{4.45}$$

The mixing pairs are selected randomly in each time step from the ensemble of particles within each LES cell. The following three variants of Curl's mixing model are common:

- **Original Curl model**: In the original model formulation of Curl [38], a subset of the particle pairs formed mixes completely ($\gamma = 1$), whereas the remaining particle pairs do not change their values. The number of mixing pairs is determined from the mixing probability, which is given by $p_{\text{mix}} = C_{\text{mix}}\Delta t/\tau_L$ with $C_{\text{mix}} = 2$ [157].
- **Modified Curl model**: In the modified Curl model [44, 94], the subset of particle pairs that are selected for mixing mix partially towards their particle pair mean, where the mixing extent is given by a uniform random variable $\xi \in [0,1]$. Due to partial mixing, the mixing probability needs to be increased by setting $C_{\text{mix}} = 3$ [157].
- **Continuous Curl model**: The variant where *all* particle pairs mix partially towards their weighted particle pair mean is referred to as the continuous Curl model [87], as it attempts to overcome the problem of time discontinuity of the particle compositions. In the original model formulation of Hsu and Chen [87], the mixing extent is given by $\gamma = 2\xi\Delta t/\tau_L$, where $\xi \in [0,1]$ is a uniform random variable. A slight modification of this model is obtained by using a deterministic mixing extent given by Eq. (4.42) with $C_{\text{mix}} = 1$.

A comparison of properties fulfilled by the three variants of Curl's mixing model is provided in Tab. 4.1. Both the original and the modified Curl model converge to a Gaussian-like (but not exactly Gaussian) PDF, which is desirable in homogeneous isotropic turbulence [22, 45, 134, 158]. In contrast, the continuous Curl model features similarities with the IEM model, since all particles are mixed partially with

Table 4.1: Summary of properties fulfilled by the conventional mixing models [22, 45, 134] and the sparse-Lagrangian MMC mixing model [29, 108, 231]. For details on the respective properties the reader is referred to the literature [56, 163, 203].

	IEM	Orig. Curl	Mod. Curl	Cont. Curl	MMC
Conservation of the means	✓	✓	✓	✓	✓
Boundedness of scalar values	✓	✓	✓	✓	✓
Linearity and independence	✓	✓	✓	✓	✓
Decay of scalar variances	✓	✓	✓	✓	✓
Relaxation to Gaussian PDF	-	(✓)	(✓)	-	✓
Localness in composition space	-	-	-	-	✓

a rather small mixing extent, and is therefore not able to reproduce a Gaussian PDF [231]. Note that more advanced mixing models exist that employ pairwise mixing based on Curl's coalescence/dispersion model, such as the Euclidean minimum spanning tree (EMST) model [203], which selects particle pairs in such a way that their separation in composition space is minimized, and the sparse-Lagrangian MMC mixing model, which is discussed in detail in Sec. 4.4.

Mixing Time Scale

For the intensive Lagrangian particle methods, the mixing model controls the dissipation of the subgrid fluctuations of the reactive scalars. The corresponding Lagrangian time scale is found by analogy with the time scale of the Eulerian subgrid fluctuations, which is justified since mixing is restricted to the LES cell and thus the filter scale associated with the Lagrangian particle method is the same as in the Eulerian LES [218]. Since the turbulent fluctuations of reactive scalars are strongly correlated with mixture fraction, the time scale of the Eulerian subgrid scalar fluctuations is modeled according to [150, 163],

$$\tau_E = f_V / \widetilde{\chi}, \tag{4.46}$$

where $f_V = \widetilde{f^2} - \widetilde{f}^2$ denotes the subgrid-scale mixture fraction variance (see Appendix B for details on the variance definition), and $\widetilde{\chi} = 2\overline{\rho \mathcal{D} \nabla f \nabla f}/\bar{\rho}$ is the filtered scalar dissipation rate. In order to obtain a closed-form expression for the mixing time in LES, these quantities need to be replaced by algebraic models. The subgrid-scalar mixture fraction variance is modeled according to [151]

$$f_V = C_f \Delta_{\mathrm{LES}}^2 \nabla \widetilde{f} \cdot \nabla \widetilde{f}, \tag{4.47}$$

with model constant $C_f = 0.1$. The closed-form expression for the filtered scalar dissipation rate is derived by assuming local equilibrium between dissipation and production (see Appendix B for details), and is given by [151]

$$\widetilde{\chi} = 2(\mathcal{D} + \mathcal{D}_t) \nabla \widetilde{f} \cdot \nabla \widetilde{f}. \tag{4.48}$$

By inserting these models into Eq. (4.46) and using the relation $\tau_L = \tau_E$, the expression for the Lagrangian mixing time scale becomes

$$\tau_L = \frac{C_f \Delta_{\mathrm{LES}}^2}{2(\mathcal{D} + \mathcal{D}_t)}. \tag{4.49}$$

The modeling constant is usually determined such that the mixing model predicts the correct decay rate of the variance of a passive scalar, though the default value $C_f = 0.1$ was found to work well for most single-phase flames.

4.4 The MMC Mixing Model

4.4.1 Background

The multiple mapping conditioning (MMC) model was originally introduced by Klimenko and Pope [108] as a modeling framework for turbulent reacting flows that combines concepts of the conditional moment closure (CMC) [9, 105, 106, 141] and generalized mapping closure [160], with both deterministic and stochastic implementations in RANS and LES [29]. The stochastic implementation, which is used nowadays, converts the MMC modeling framework into a transported PDF approach employing a Monte Carlo solution, where MMC plays the role of a mixing model that incorporates ideas from the flamelet-like approaches by conditioning the mixing operator on a mathematically independent reference space. The conditioning achieves localness of the mixing model [203] and allows MMC to be implemented with a significantly reduced number of particles, thus giving it a computational advantage over intensive Lagrangian methods, in particular if realistic chemical kinetics are involved. Accordingly, the MMC model fulfills all requirements for an ideal mixing model (cf. Tab. 4.1).

Cleary and Klimenko [28, 30, 31] have developed a generalized sparse-Lagrangian MMC model in the context of LES of turbulent nonpremixed flames, which forms the basis for all MMC-LES applications to date. The reference space is selected to be the mixture fraction $\widetilde{f}$, which is obtained from the Eulerian LES by solving Eq. (4.21). Unlike the particle mixture fraction z^{sp}, which is calculated from the mass fractions via Eqs. (4.1) and (4.3), the Eulerian mixture fraction is mathematically independent of the instantaneous composition ϕ_α^{sp}, thus making mixing independent and linear for all scalars [30]. Mixing is realized using a modified Curl's model, in which particle pairs are selected conditionally on the reference mixture fraction space rather than randomly to enforce localness of the mixing operator (note that this requires a high correlation between $\widetilde{f}$ and z^{sp}). Accordingly, the mean value of the particle pair is to be interpreted as a conditional mean, $\phi_\alpha^{\mathrm{mean}} = \langle \phi_\alpha | \widetilde{f} \rangle^{p,q}$, so

that the MMC variant of Curl's mixing formula, Eq. (4.44), is written as

$$\phi_\alpha^p(t+\Delta t) = \phi_\alpha^p(t) + \gamma\left(\langle\phi_\alpha|\widetilde{f}\rangle^{p,q} - \phi_\alpha^p(t)\right), \tag{4.50a}$$

$$\phi_\alpha^q(t+\Delta t) = \phi_\alpha^q(t) + \gamma\left(\langle\phi_\alpha|\widetilde{f}\rangle^{p,q} - \phi_\alpha^q(t)\right). \tag{4.50b}$$

Note that mixing is no longer restricted to the LES cell but typically occurs across several LES cells due to the sparse particle distribution, with particle pairs usually selected from the entire computational domain. The mixing extent γ is given by Eq. (4.42) with $C_{\mathrm{mix}} = 1$ and is evaluated locally and instantaneously for each mixing pair. Once the particle pairs are chosen, the evaluation of the conditional mean is equivalent to the unconditional particle pair mean that is given by Eq. (4.45). In the following, details on the MMC variant of Curl's mixing model are presented, which includes the conditional selection of the particle pairs and the modeling of the mixing time scale that determines the mixing extent.

4.4.2 Particle Pair Selection

Localness of the MMC mixing model in reference space is achieved by selecting particle pairs in such a way that mixing partners are close to each other in both physical space and reference mixture fraction space, as illustrated in Fig. 4.2. This is achieved by the minimization of the effective square distance defined as [28, 30, 31],

$$\hat{d}_{p,q}^2 = \sum_{i=1}^{3}\left(\frac{d_{x_i}^{p,q}}{r_m/\sqrt{3}}\right)^2 + \left(\frac{d_f^{p,q}}{f_m}\right)^2, \tag{4.51}$$

where $d_{x_i}^{p,q} = |x_i^p - x_i^q|$ is the distance between two particles p and q in physical space and $d_f^{p,q} = |\widetilde{f}(\mathbf{x}^p) - \widetilde{f}(\mathbf{x}^q)|$ is the distance in reference mixture fraction space, which is interpolated from the Eulerian LES to the respective particle positions. The parameters r_m and f_m represent the characteristic mixing distances in physical and reference mixture fraction space, respectively, and the factor $\sqrt{3}$ results from the assumption that the mixing distance is isotropic in each spatial direction, $r_i = r_m/\sqrt{3}$. Although the actual mixing distances vary locally, the parameters r_m and f_m are treated as global input parameters and can, in principle, be adjusted individually to control the level of localness in reference mixture fraction space. Cleary and Klimenko [30] derived an algebraic relation between r_m and f_m through the concept of an isoscalar sliver with fractal-like turbulent stretching, thus reducing the choice of mixing parameters to a single-parameter problem. The relation is given by

$$r_m = C_m\left(\frac{\mathrm{d}\widetilde{f}}{\mathrm{d}n}\frac{\Delta_L^3}{r_c^{2-D_f}}\frac{1}{f_m}\right)^{1/D_f}, \tag{4.52}$$

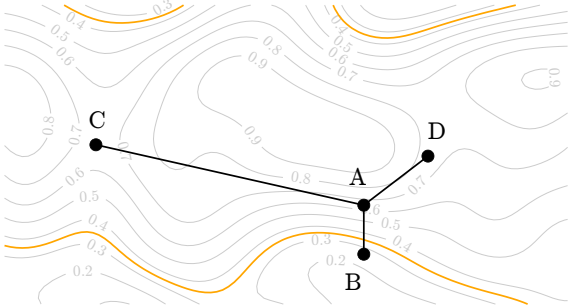

Figure 4.2: Schematic sketch of the MMC particle pair selection. The contour plot shows a 2D region of the instantaneous reference mixture fraction field, where the orange line indicates the stoichiometric value and thus the flame position. Points A to D denote the locations of four stochastic particles, with emphasis on selecting a mixing partner for particle A. Particle B is closest in physical space but has a large separation in composition space (indicated by mixture fraction), which may result in unphysical mixing across the flame front. In contrast, selecting particle C, which is closest in reference mixture fraction space, imposes a flamelet-like closure on the mixing model. The MMC model selects particle D, which is close in both physical and composition space, and thus reflects real mixing.

where $C_m = 0.5$ is a scaling constant, $\mathrm{d}\widetilde{f}/\mathrm{d}n$ is the gradient of the filtered mixture fraction normal to the isoscalar sliver, $\Delta_L = (V/N^{sp})^{1/3}$ is the nominal distance between the stochastic particles, r_c is the inner cutoff scale of the fractal surface given by the LES cell size, and $D_f = 2.36$ is the fractal dimension. For a given f_m, Eq. (4.52) allows the calculation of r_m, where Δ_L, r_c and $\mathrm{d}\widetilde{f}/\mathrm{d}n$, all of which are spatially variable, are evaluated at a characteristic location in the flow. Based on several studies [60, 60, 70, 89, 205, 218] it was found that the value $f_m = 0.03$ works well in most single-phase flames, but may need to be adjusted for two-phase flows. A detailed discussion on this will be given later in Secs. 7.1.2 and 7.3.2.

4.4.3 Models for the Mixing Time Scale

In the MMC mixing model, particles mix towards mean values conditionally averaged on the reference mixture fraction space. As a result, the mixing time scale primarily controls the dissipation of composition fluctuations with respect to averages conditioned on the reference variable, and only indirectly determines the unconditional fluctuations. Models for the mixing time scale in sparse-Lagragian methods are derived by analogy to the characteristic Eulerian time scale (cf. Eq. (4.46)) but using equivalent Lagrangian expressions for the subfilter variance and dissipation rate. Cleary and Klimenko [30] derived a model on the basis of simple geometrical reasoning, which reads

$$\tau_L = C_L^{-1} \frac{\beta C_f (d_f^{p,q})^2}{2\mathcal{D}_{\mathrm{eff}} \nabla\widetilde{f} \cdot \nabla\widetilde{f}}, \tag{4.53}$$

with model parameters $C_L = 1$, $\beta = 3$ and $C_f = 0.1$. This model is referred to as the Cleary & Klimenko (C&K) model and has been used in many MMC-LES simulations of practical flames. Vo *et al.* [218] developed a new model for the mixing time scale that takes a more rigorous anisotropic view of the turbulent structures at the subfilter scale. It is referred to as the anisotropic (a-ISO) model and is given by [61, 218]

$$\tau_L = C_L^{-1} \frac{C_f (d_x^{p,q})^2}{2(\mathcal{D} + \mathcal{D}_{t,L})}, \tag{4.54}$$

where the model constants C_L and C_f are the same as in Eq. (4.53), and $\mathcal{D}_{t,L} = \frac{d_x^{p,q}}{\Delta_{\mathrm{LES}}} \mathcal{D}_t$ is a turbulent subgrid-scale diffusivity that acts at the relevant Lagrangian length scales. This model shares similarities with the Eulerian model for the mixing time scale, Eq. (4.49), but with the Eulerian filter width being replaced by a Lagrangian filter width associated with the distance between mixing particles. Recently, Sharma *et al.* [186] proposed a dynamic version of the a-ISO model, where the modeling constants are evaluated locally using a test filter. However, such a procedure will not be used in the present work.

The mixing time is evaluated per mixing pair, where the Eulerian quantities (such as $\nabla \widetilde{f}$ and $\mathcal{D}_{\mathrm{eff}}$) are interpolated to the respective particle positions. As mixing typically occurs with particles located in different LES cells, the interpolated quantities of the selected particles p and q may vary significantly. Therefore, the mixing time scale of the mixing pair is taken as the harmonic mean of the individual time scales of the mixing partners, $\tau_L = 2/(1/\tau_L^p + 1/\tau_L^q)$. Note that this is equivalent to taking the arithmetic mean of the interpolated quantities, since the Eulerian quantities appear in the denominator of the mixing time and the numerator is the same for both particles of a pair.

4.5 Two-Phase Coupling

4.5.1 General Modeling Strategy

The two-phase coupling between the liquid droplets and the gas phase that is represented by the stochastic particles follows the concept of the particle-source-in cell model introduced in Sec. 3.2.4, and consists essentially of two steps:

1. The ambient conditions required for the Lagrangian droplet evaporation model to calculate the heat and mass transfer rates must be determined from the ensemble of the notional particles representing the gas phase.

2. Once the droplet properties have been updated, heat and mass are transferred to the stochastic particles via source terms in the transport equations (or, alternatively, by creating new stochastic particles).

For intensive particle methods, where each computational cell includes several notional particles, the determination of the ambient conditions (step 1) is not difficult and is usually done by interpolating the gas-phase properties of the Eulerian field, sampled from the stochastic particles, to the respective droplet positions. The closure of the conditional evaporation term that appears in the stochastic differential equations, Eqs. (4.38) and (4.39), requires a model to distribute the source terms among the stochastic particles (step 2). In the context of intensive particle methods, several models are available, which will be summarized in Sec. 4.5.2.

In sparse particle methods, the difficulty arises that there are no gas-phase particles in the immediate vicinity of the droplets, so it is not clear how the ambient conditions for the evaporation process can be determined from the sparse set of gas-phase particles (step 1) and how the source terms should be distributed among the particles (step 2). A new model is formulated in Sec. 4.5.3 that adopts the concept of the MMC particle pair selection by applying a one-to-one coupling technique between the liquid fuel droplets and the notional gas-phase particles with the particle pair selection conditional on a set of suitable conditioning variables.

4.5.2 Conventional Two-Phase Coupling Models

The EQUAL Model

The EQUAL model [66, 67] distributes the evaporation source terms evenly to all stochastic particles within the computational cell in proportion to their particle mass, as illustrated in Fig. 4.3(a). This is equivalent to an approximation of the conditional evaporation term by its unconditional filtered average,

$$\langle \Pi_F | \boldsymbol{\psi} \rangle^{sp} \approx \widetilde{\Pi}_F^{sp}, \qquad \langle \Pi_\alpha - \phi_\alpha \Pi_F | \boldsymbol{\psi} \rangle^{sp} \approx \widetilde{\Pi}_\alpha^{sp} - \phi_\alpha^{sp} \widetilde{\Pi}_F^{sp}. \tag{4.55}$$

For the fuel mass fraction, $\phi_\alpha = Y_F$, the filtered average is given by

$$\widetilde{\Pi}_F^{sp} = -\frac{\sum_d \frac{\mathrm{d}m_d}{\mathrm{d}t}}{\sum_{sp} m^{sp}}, \tag{4.56}$$

while it is zero for the non-evaporating species. For the enthalpy, $\phi_\alpha = h$, the filtered evaporation term is given by

$$\widetilde{\Pi}_h^{sp} = -\frac{\sum_d \frac{\mathrm{d}(m_d h_d)}{\mathrm{d}t}}{\sum_{sp} m^{sp}}. \tag{4.57}$$

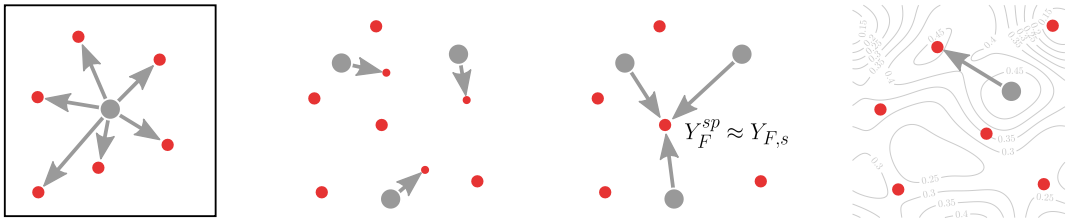

(a) EQUAL model. **(b)** NEW model. **(c)** SAT model. **(d)** One-to-one coupling conditional on $\widetilde{f}$.

Figure 4.3: Schematic sketch of the two-phase coupling models. Gray dots mark droplets, and red dots indicate the stochastic particles.

The summation is performed over all notional particles and fuel droplets within the computational cell. Since all particles within the cell receive the same source term, the model features similarity with the particle-source-in-cell model that would be used in an Eulerian simulation of the composition field, and is not able to generate any subfilter fluctuations that would arise from composition-evaporation rate correlations. Nevertheless, due to its simplicity and robustness, the EQUAL model has been used in numerous transported PDF studies of turbulent spray combustion [67, 82, 113, 146].

The NEW Model

Another approach to maintain mass and energy conservation between the gas phase and the fuel droplets is to generate new gas-phase particles at the positions of the liquid droplets (see Fig. 4.3(b)) [47, 93, 113]. These new gas-phase particles are characterized by unity fuel mass fraction and contain the evaporated mass and enthalpy. This allows the model to capture the high levels of local gas-phase fuel concentration and temperature fluctuations in the regions interacting with evaporation. However, the use of the NEW model is also associated with some difficulties. To keep the number of gas-phase particles per cell within reasonable bounds, a particle number control algorithm [172] is required. Furthermore, the assignment of the enthalpy source term to the new gas-phase particles can lead to unrealistically low temperatures [113, 208, 229]. Due to these difficulties, the NEW model will not be used in the present work, but according to previous studies [208], the results are likely to be similar to those of the SAT model presented below.

The SAT Model

In order to overcome the limitations of the EQUAL model, Naud [140] proposed a model based on the idea that gas-phase conditions in the immediate vicinity of

a droplet are close to saturation conditions. Accordingly, the evaporation source terms are distributed preferentially to notional particles that are close to the saturation state (see Fig. 4.3(c)). The SAT model thus exhibits similarities with the NEW model by allowing locally high fuel concentrations, but without exceeding the saturation limit. The algorithm is as follows. For each droplet, a gas-phase particle within the same computational cell is selected that is closest to but still below the saturation state, i.e., that has the smallest value of $(Y_{F,s} - Y_F^{sp})$ with $Y_F^{sp} < Y_{F,s}$. The selected particle then receives the evaporation source terms from the droplet. If the particle becomes supersaturated during the heat and mass transfer, it receives sources until it reaches saturation, and the remaining sources are added to the next particle following the same procedure. The corresponding closed-form expressions are the same as for the one-to-one coupling technique and are presented there (cf. Sec. 4.5.3). Since most gas-phase particles in spray combustion applications have a fuel mass fraction far from the saturation limit, the SAT model often leads to a distribution of the source terms among only a few selected stochastic particles. Similar to the NEW model, the SAT model can lead to unrealistically low temperatures, which is due to the fact that the source terms are transferred to a different gas state than was used to calculate the heat and mass transfer rates of the liquid droplets. Therefore, the additional condition that the temperature of the gas-phase particle must be above a user-defined value (here the boiling temperature) is imposed when selecting the particles.

4.5.3 Sparse-Lagrangian Two-Phase Coupling

The use of a sparse set of stochastic particles requires a different strategy for the coupling between the liquid fuel droplets and the notional particles, since there is not always a gas-phase particle in the vicinity of the droplet. In a real spray, the evaporating droplets interact with the surrounding gas, thus making the two-phase coupling inherently local in composition space. Accordingly, the two-phase coupling model should emulate that localness in the same way that mixing models emulate the localness of molecular diffusion. In analogy to the MMC reference variables, a set of suitable conditioning variables that are obtained from the Eulerian LES and denoted as $\widetilde{\boldsymbol{\xi}}$ are introduced to serve as a proxy for localness of the two-phase coupling in composition space. Note that the conditioning variables generally do not encompass the entire composition space but rather individual characteristic variables representing the gas composition, and details on the selection of appropriate conditioning variables are given later. The evaluation of the conditional evaporation

terms is then approximated by an evaluation conditional on $\widetilde{\boldsymbol{\xi}}$,

$$\langle \Pi_F | \boldsymbol{\psi} \rangle^{sp} \approx \langle \Pi_F | \widetilde{\boldsymbol{\xi}} \rangle^{sp}, \qquad \langle \Pi_\alpha - \phi_\alpha \Pi_F | \boldsymbol{\psi} \rangle^{sp} \approx \langle \Pi_\alpha - \phi_\alpha \Pi_F | \widetilde{\boldsymbol{\xi}} \rangle^{sp}. \tag{4.58}$$

This modeling features similarities with spray closures from CMC methods [16, 212] as well as with the doubly-conditioned distribution model proposed by Tang [207]. The conditional evaluation of the evaporation terms is implemented at the particle level by adopting the concept of minimizing the effective square distance,

$$\hat{d}^2_{d,sp} = \lambda_x \sum_{i=1}^{3} \left(\frac{d^{d,sp}_{x_i}}{r^*_m/\sqrt{3}} \right)^2 + \sum_{i=1}^{N_\xi} \lambda_{\xi_i} \left(\frac{d^{d,sp}_{\xi_i}}{\xi^*_{i,m}} \right)^2, \tag{4.59}$$

where $d^{d,sp}_{x_i} = |x_{i,d} - x^{sp}_i|$ and $d^{d,sp}_{\xi_i} = |\widetilde{\xi}_i(\mathbf{x}_d) - \widetilde{\xi}_i(\mathbf{x}^{sp})|$ are the distances between the droplets and the stochastic particles in physical space and conditional space, respectively, with the conditioning variables being interpolated from the filtered Eulerian field to the respective particle and droplet positions. The terms λ_x and λ_{ξ_i} are Boolean variables that are used to enable or disable individual terms in the effective square distance, e.g., setting $\lambda_{\xi_i} = 0$ for all i leads to a particle selection in pure physical space. The coupling parameters r^*_m and $\xi^*_{i,m}$ are marked by an asterisk to distinguish them from the mixing parameters in Eq. (4.51). Their estimation will be discussed later in Sec. 7.1.2.

The conditioning variables should be chosen so that the minimization of the effective square distance selects a gas-phase particle that represents a gas state similar to that found at the droplet position even if they are several cells apart, as illustrated in Fig. 4.3(d). Using the entire composition vector, i.e., $\boldsymbol{\xi} = \boldsymbol{\phi}$, would give the most accurate results but is not practically feasible as it would require the solution of a number of additional transport equations and thus significantly increase the computational cost. In MMC-LES of non-premixed flames, the reference mixture fraction obtained from the LES is usually used as a proxy for localness in composition space, and thus may also provide a suitable conditioning variable for two-phase coupling, as proposed by Khan *et al.* [102]. Setting $\boldsymbol{\xi} = f$ in Eq. (4.59), the effective square distance between the droplets and the stochastic particles can be written as

$$\hat{d}^2_{d,sp} = \lambda_x \sum_{i=1}^{3} \left(\frac{d^{d,sp}_{x_i}}{r^*_m/\sqrt{3}} \right)^2 + \lambda_f \left(\frac{d^{d,sp}_{f}}{f^*_m} \right)^2, \tag{4.60}$$

which bears resemblance to the MMC mixing pair selection that is given by Eq. (4.51). In contrast to the work of Khan *et al.* [102], the physical space is included here, since a particle that is close in both physical space and reference mixture fraction space provides a suitable gas phase reflecting the composition in the vicinity of the droplet. Furthermore, this is consistent with the particle pair selection of the MMC mixing model and is numerically advantageous, as will be explained in Sec. 4.7.2.

Once a droplet is assigned to a stochastic particle, the heat and mass transfer rates of the liquid droplet are calculated using the properties of the stochastic particle as ambient conditions. It is natural to return the evaporation source terms entirely to the selected gas-phase particle, which provides a consistent one-to-one (or pairwise) coupling technique. The evaporation source terms are then given by their instantaneous evaluation,

$$\Pi_F^{sp} = -\frac{1}{m^{sp}} \frac{\mathrm{d}m_d}{\mathrm{d}t}, \qquad \Pi_h^{sp} = -\frac{1}{m^{sp}} \frac{\mathrm{d}(m_d h_d)}{\mathrm{d}t}. \tag{4.61}$$

Note that each droplet is assigned to only one stochastic particle, but it is possible for a stochastic particle to receive the source terms of more than one droplet, depending on the ratio of droplet number to stochastic particle number.

The one-to-one coupling approach is not confined to sparse-Lagrangian particle methods, but can equally be applied to intensive particle methods. In this case, however, the conditioning on the reference mixture fraction field is not useful, since the coupling partners are typically selected within the LES cell. Instead, particles may be selected by minimizing their distance in pure physical space or by random selection in analogy to Curl's mixing model. The latter approach was used by Heye *et al.* [83] in order to prevent artificial mixing that would result from the use of the EQUAL model, where the pairing between the droplet and the gas-phase particle was retained as long as both were in the same computational cell. Note that a similar effect is achieved automatically by selecting the closest particle in physical space, although the pairing time is likely to be shorter.

Finally it should be noted that the SAT model also implements a one-to-one coupling strategy between the droplets and the stochastic particles. However, within the present work it is treated as a separate model, with the one-to-one coupling referring only to models that are based on the minimization of the effective square distance, Eq. (4.59).

4.5.4 Properties of Two-Phase Coupling Models

Similar to the properties of a mixing model (cf. Tab. 4.1), one can formulate requirements that should be fulfilled by an ideal two-phase coupling model. In the following, such requirements are presented and their fulfillment by the two-phase coupling models is discussed. A summary is provided in Tab. 4.2.

Conservation of Mass and Energy

The two-phase coupling model must ensure that mass and energy are conserved between the liquid and the gas phase. This requirement is obvious, but is not

strictly fulfilled by all coupling models, for example if an artificial limitation of the gas-phase temperature is necessary [208].

Consistency

A consistent coupling technique is required in order to avoid unrealistic values of the gas composition. This is achieved by the EQUAL model, where interactions between the droplets and the gas phase take place in terms of the cell averages, and by the one-to-one coupling strategy, where the same gas-phase particle is used to determine the ambient conditions and to receive the source terms. This limits the transfer rates of the liquid droplets to the mass and energy available in the gas phase. In contrast, both the NEW and SAT models can lead to unrealistically low gas-phase temperatures due to lack of correlation between the gas state that provides the ambient conditions (usually the local cell averages) and thus determines the size of the source terms, and the gas state that eventually receives the evaporation source terms (new gas-phase particles or particles close to the saturation state).

Independence From Numerical Parameters

The coupling model should be independent of the numerical time step and the number of stochastic particles. These requirements are fulfilled by the EQUAL model, where the coupling between the fuel droplets and the gas phase is a function of the Eulerian cell size, thus emphasizing the numerical robustness of the model. For the NEW and SAT models, a dependence on the numerical parameters emerges through the interaction with the mixing model. Both models generate gas-phase particles with high fuel concentrations. Since saturation is reached earlier on particles having a smaller mass of gas, a higher number of particles results in more fuel-rich particles, which then requires more mixing by the mixing model as discussed in Naud [140]. For the one-to-one coupling strategy, a distinction must be made as to how the particles are selected. With random selection, the generated scalar variance depends on the number of gas-phase particles and the numerical time step, since both a higher number of particles and a smaller time step result in the source terms being distributed among a larger set of potential coupling partners. In contrast, a particle selection based on the minimization of the effective square distance provides pairing of the particles with the same droplets for a given time interval and thus largely independence from the numerical parameters. Note that a dependence on the stochastic particle number may remain, since the change in the gas-phase properties due to the evaporation source terms depends on the local gas volume, analogous to the particle-source-in-cell model (see Sec. 3.2.4). This effect is particularly evident

if a dense particle distribution is used, whereas it is likely to be small for a sparse particle method due to the relatively large gas-phase volume represented by each particle.

Generation of Subfilter Variance

Evaporation leads to high levels of local gas-phase fuel concentration and temperature fluctuations, thus increasing the subfilter variance (see Appendix B for details on the mechanisms of variance generation). Accordingly, this effect should be reproduced by the two-phase coupling model. With the exception of the EQUAL model, which employs a homogeneous distribution of the source terms, all models presented here are capable of generating subfilter variance by distributing the source terms to individual gas-phase particles only. However, the amount of variance generated varies, where it is expected that the NEW and SAT models lead to the highest variance due to the generation of particles with high fuel concentration.

Localness

Evaporation and thus the coupling between the droplets and the gas-phase particles should be local in composition space, as discussed previously. Localness is particularly important in the case of a sparse particle distribution, where the nearest particle in physical space may represent a different gas composition. Both the NEW and SAT models can be considered as models that are fully local in composition space, while the EQUAL model is local in pure physical space [208]. The one-to-one coupling strategy with particle selection conditional on the reference mixture fraction provides localness in both physical and composition space, and thus may combine concepts from the EQUAL and the NEW or SAT models.

Table 4.2: Summary of the properties fulfilled by the two-phase coupling models.

	EQUAL	NEW	SAT	One-to-one coupling	
				random	Eq. (4.60)
Conservation of mass and energy	✓	(✓)	✓	✓	✓
Consistency (no unrealistic values)	✓	-	-	✓	✓
Independent of Δt	✓	-	-	-	✓
Independent of N^{sp}	✓	-	-	-	(✓)
Generation of subfilter variance	-	✓	✓	✓	✓
Localness	-	✓	✓	-	✓

4.6 Density Coupling

The stochastic particles provide the gas density (as a function of the composition vector) to the Eulerian field, where density is required for the solution of the filtered transport equations. However, the density is also part of the Eulerian solution and results from the continuity equation. To ensure mass consistency between the Lagrangian stochastic particle field and the Eulerian LES field, an accurate and consistent coupling technique is required, which is referred to as thermophysical coupling or density coupling. The density feedback from the stochastic particle field to the Eulerian LES field uses an adaptation of the equivalent enthalpy concept [139, 170], where additional Eulerian transport equations for an equivalent composition field, denoted as ϕ_α^E, are solved. Note that it is not necessary for the equivalent composition to include all species but only the major ones, so that solving the additional transport equations does not add a significant computational cost. For a known pressure, the density in the Eulerian field can then be calculated algebraically from the equivalent composition field using the equation of state.

The equivalent composition field obeys a conventional scalar transport equation similar to Eq. (3.18). Using the same subgrid closures as presented in Sec. 4.2.3, the filtered form is given by

$$\frac{\partial(\bar{\rho}\widetilde{\phi}_\alpha^E)}{\partial t} + \frac{\partial(\bar{\rho}\widetilde{u}_j\widetilde{\phi}_\alpha^E)}{\partial x_j} = \frac{\partial}{\partial x_j}\left(\bar{\rho}\mathcal{D}_{\text{eff}}\frac{\partial\widetilde{\phi}_\alpha^E}{\partial x_j}\right) + \bar{\rho}\widetilde{W}_\alpha^E. \tag{4.62}$$

In contrast to the real composition, the transport equation for the equivalent composition does not contain source terms for chemical reactions and evaporation. Instead, these effects are implicitly taken into account by implementing the source term in Eq. (4.62) as a relaxation towards the real composition, in the following denoted as target composition $\phi_\alpha^{\text{target}}$, according to [30]

$$\widetilde{W}_\alpha^E = \frac{\phi_\alpha^{\text{target}} - \widetilde{\phi}_\alpha^E}{\tau_{\text{relax}}}. \tag{4.63}$$

The relaxation time scale τ_{relax} is a numerical parameter and must be chosen to produce smooth equivalent composition fields. Small values of τ_{relax} can cause instabilities, while large values lead to a deviation of $\widetilde{\phi}_\alpha^E$ from $\phi_\alpha^{\text{target}}$. Typically, τ_{relax} is set to ten times the numerical time step [30, 61].

The calculation of the relaxation source term requires an evaluation of the target composition $\phi_\alpha^{\text{target}}$ from the notional particles in each LES cell. Unlike dense particle methods, where each cell contains a number of particles, a direct evaluation is not possible with sparse particle methods, as not every LES cell contains a notional particle and scalar variations in physical space may be large. Therefore, the target

composition is evaluated as a conditional mean that is calculated from an ensemble of notional particles in the nearby surroundings of the computational cell. This is realized either by using precomputed flamelet tables [30], or based on the concept of smoothed particle hydrodynamics [135], which is referred to as kernel estimation. The kernel estimation provides a more general solution approach and is therefore used here. In that approach, the interpolation of a variable ϕ_α is based on the integral interpolation [61, 135],

$$\phi_\alpha^{\text{interp}}(\mathbf{r}) = \int_{-\infty}^{+\infty} \phi_\alpha(\mathbf{r}')G(\mathbf{r}' - \mathbf{r})\mathrm{d}\mathbf{r}', \tag{4.64}$$

where G is a kernel function of characteristic width $\mathbf{\Delta}_r$, and $\mathbf{r}$ denotes the space over which the integration is performed (conventionally the physical space). Due to the finite number of notional particles, the integral interpolation is replaced by a summation over the entire ensemble of notional particles, which results in the following expression for the estimation of the target value [61, 135],

$$\phi_\alpha^{\text{target}}(\mathbf{r}) = \sum_{sp} m^{sp} \frac{\phi_\alpha^{sp}}{\rho^{sp}} G(\mathbf{r}^{sp} - \mathbf{r}), \tag{4.65}$$

with $\mathbf{r}$ evaluated at the cell centers of the LES cell. Due to the sparse distribution of the notional particles, the interpolation cannot be based solely on the physical space, and therefore the integration is additionally performed over the mixture fraction space, i.e., $\mathbf{r} = (\mathbf{x}, \widetilde{f})$ and $\mathbf{r}^{sp} = (\mathbf{x}^{sp}, z^{sp})$. As a result, the target value can be interpreted as a conditionally interpolated quantity. The kernel function is given by the product of one-dimensional kernel functions, each given by a cubic spline kernel [135] with appropriate normalization factor, which gives more weight to particles that have a smaller distance $\mathbf{r}^{sp} - \mathbf{r}$. The characteristic length scale in mixture fraction space, Δ_f, is fixed, while the characteristic length scale in physical space, Δ_x, is computed dynamically to ensure that the kernel function reduces to a Delta function in the limit of an infinite number of particles [61].

4.7 Numerical Implementation

4.7.1 Implementation of Stochastic MMC in OpenFOAM

OpenFOAM (short for open field operation and manipulation) is an open-source library for the numerical solution of problems in the field of continuum mechanics, most prominently including computational fluid dynamics. Its initial version has been developed at Imperial College London in the late 1990s [95, 227] with the intention of making the top-level syntax of the code as close as possible to the

conventional mathematical notation for tensors and partial differential equations, which is realized by the extensive use of object-orientated programming techniques provided by the C++ programming language. The OpenFOAM toolbox implements a second-order finite volume method that allows for the use of unstructured meshes and complex boundary conditions in combination with an efficient parallelization technique, and provides a variety of well-established solvers for a wide range of applications, including turbulent flows, chemically reacting flows, multiphase flows and particle-laden flows. For a detailed documentation of the numerical methods and algorithms used in OpenFOAM the reader is referred to the books of Greenshields and Weller [75] and Moukalled *et al.* [137]. Due to its free availability along with the possibility to access, modify and extend the source code, OpenFOAM enjoys a broad user community and has developed into a powerful software package that is widely used in both research and industry.

The aforementioned advantages of OpenFOAM have led to the implementation of the stochastic MMC model for single-phase flows in an OpenFOAM-compatible code called `mmcFoam`, which then provides a comprehensive LES and RANS modeling framework for turbulent reacting flows allowing for both sparse and intensive particle methods. The computational implementation is described in detail in Galindo-Lopez *et al.* [61] and is only briefly summarized here. In general, the MMC solver consists of an Eulerian LES or RANS solver and a Lagrangian solver for the evolution of the stochastic particles. The Eulerian solver is derived from the OpenFOAM solver `reactingFoam`, thus forming a compressible pressure-based solver, and is extended by the MMC-specific features such as the solution of the transport equations for the MMC reference fields and the density coupling. The implementation of the stochastic particles is based on OpenFOAM's native particle tracking algorithm and is extended by the physical features of the stochastic MMC model such as mixing and reaction using several nested template class layers [61]. The OpenFOAM implementation of the MMC model has been validated against numerous experimental investigations and several DNS studies, showing good to excellent agreement as described in Galindo-Lopez *et al.* [61].

For the present work, the single-phase MMC-LES solver is extended to include the effect of droplet evaporation, forming a new solver called `mmcDropletFoam` that implements the two-phase MMC-LES model presented earlier. For model examination, an additional solver called `mmcDropletDNSFoam` is created that couples the two-phase MMC-LES model with a CP-DNS. Details on the two solvers are given in the following sections.

4.7.2 Two-Phase MMC-LES Solver

The extension of the single-phase MMC-LES solver by the effect of droplet evaporation involves the implementation of a second Lagrangian solver for the liquid fuel droplets, following the formulation given in Sec. 3.2, as well as the two-phase coupling between the fuel droplets and the stochastic particles, as described in Sec. 4.5. The newly implemented two-phase MMC-LES solver is called `mmcDropletFoam`, and the sequence of the individual computational steps of the solver is illustrated in Fig. 4.4. First, the Eulerian and the Lagrangian fields are initialized. Then the time loop is initiated, in which the stochastic particles are evolved first, followed by the fuel droplets. Based on the solutions of the Lagrangian fields, the evaporation source terms are calculated and the density coupling is applied. Afterwards, the filtered transport equations of the Eulerian fields are solved in an iterative way using a combination of the PISO and SIMPLE algorithms for the pressure-velocity coupling [55, 137, 214], which is referred to as the PIMPLE algorithm [75]. This sequence of solution steps is repeated until the final simulation time is reached.

The transport of the notional particles in physical and composition space, as described by Eqs. (4.37) to (4.39), is carried out sequentially utilizing a first-order operator splitting technique for the composition equation, Eq. (4.38), which divides the change in particle compositions into the three subproblems of chemical reactions, mixing, and evaporation. This allows to treat the physical processes independently from each other and enables the use of different numerical solution methods for each subproblem. Although the particle mixture fraction, z^{sp}, can be calculated from the transported mass fractions Y_k^{sp}, it is incorporated here into the composition vector and solved on the notional particles. The corresponding stochastic differential equation is the same as for the fuel mass fraction but without the chemical source term. The numerical solution of the stochastic differential equations governing the transport of the notional particles in physical and composition space deserves further attention and will be discussed in the following.

Particle Initialization and Management

In addition to the standard finite volume mesh for solving the filtered transport equations of the Eulerian field, a mesh referred to as super mesh is defined, which is used for the initialization of the stochastic particles and to control the particle resolution. In sparse-Lagrangian particle methods, the super cells are typically much larger than the LES cells, as illustrated in Fig. 4.5, whereas in dense particle methods, where mixing is restricted to the LES cell, the two meshes are usually the same. At the beginning of the simulation, the gas-phase particles are randomly

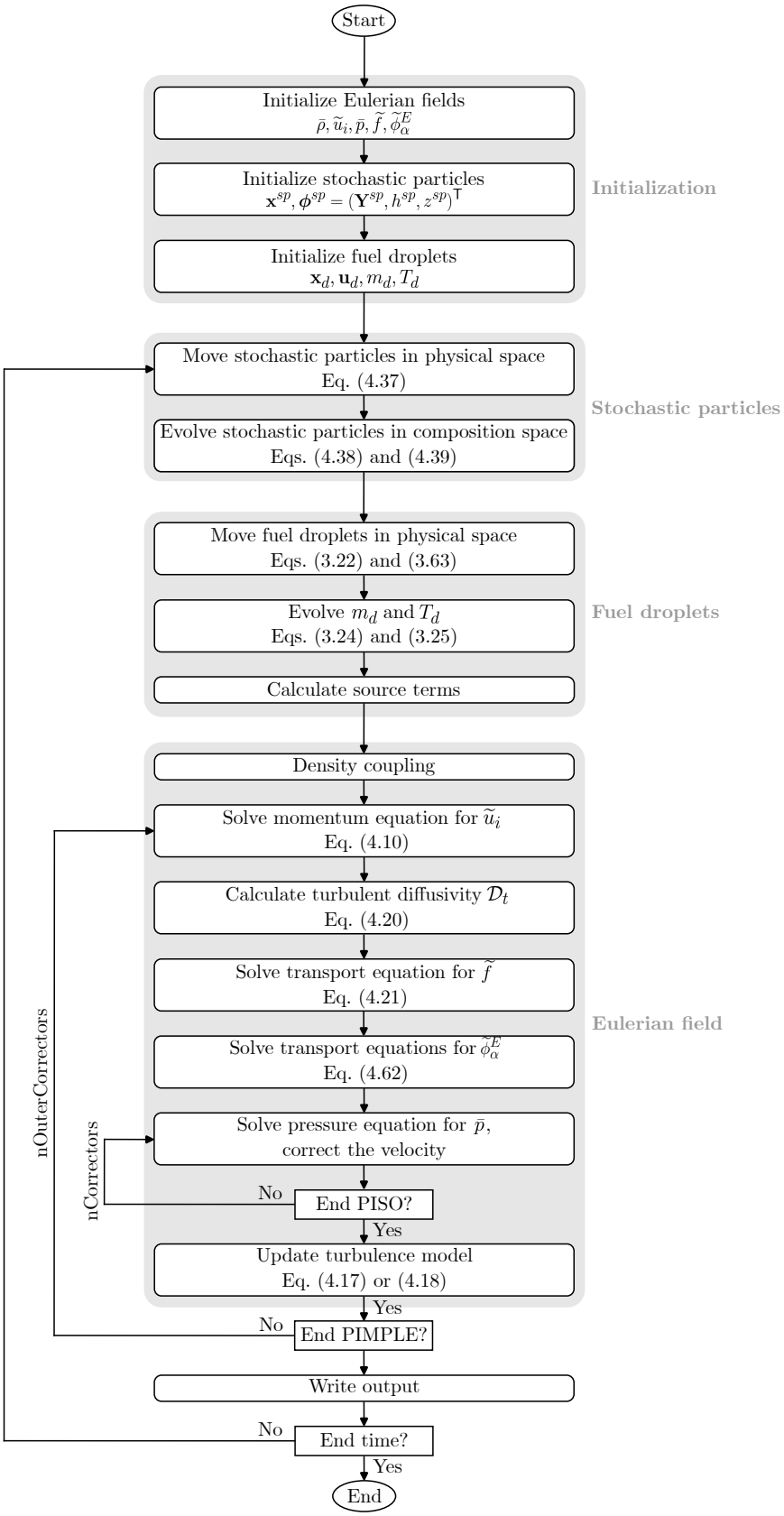

Figure 4.4: Flow chart of the two-phase MMC-LES solver `mmcDropletFoam`.

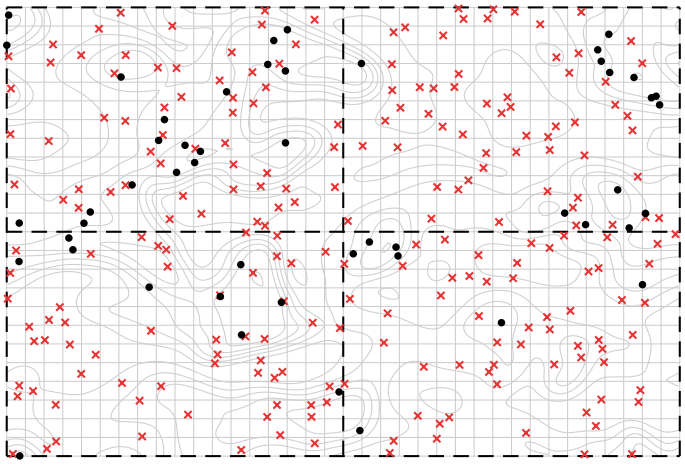

Figure 4.5: Sketch of the meshes used by the hybrid Eulerian/Lagrangian/Lagrangian method. Gray lines indicate the LES mesh that is used to solve the Eulerian transport equations, while black dashed lines mark the super cells that are used to control the particle resolution. The background shows contour lines of the reference mixture fraction field obtained from the LES, black dots mark the fuel droplets, and red crosses indicate the stochastic particles.

distributed within each super cell, with the number of notional particles per super cell being specified by the user. The initial values of the composition vector of the notional particles are then set to the corresponding mean values of the local LES cell. The initial mass of the stochastic particles is obtained from the mass of the super cell and weighted by the density of the local LES cell. This allows for the resolution of initial gradients in the LES field, while ensuring mass consistency between the Lagrangian and Eulerian fields even if there are fewer notional particles than LES cells.

During the simulation, the number of particles within the super cell is subject to fluctuations, as particles may leave and enter the cell at different rates. For instance, the effect of the random walk, which is proportional to the effective diffusivity, is stronger in hot regions than in cold regions, causing particles to jump out of the flame. To keep the particle resolution within reasonable bounds, a particle number control algorithm can be applied, in which stochastic particles are cloned or deleted in a mass-conserving way if the number of particles within the super cell falls below or above the lower and upper limits specified by the user.

Transport in Physical Space

Equation (4.37), which describes the transport of the notional particles in physical space, is solved numerically using the Euler-Maruyama method [109], which is the extension of the first-order explicit Euler method to stochastic differential equations.

Accordingly, the discretized form of Eq. (4.37) is expressed as

$$x_i^{sp}(t+\Delta t) = x_i^{sp}(t) + \left[\widetilde{u}_i + \frac{1}{\bar{\rho}}\frac{\partial(\bar{\rho}\mathcal{D}_{\text{eff}})}{\partial x_i}\right]^{sp}\Delta t + \left[\sqrt{2\mathcal{D}_{\text{eff}}}\right]^{sp}\Delta\omega_i, \tag{4.66}$$

where the terms in square brackets are interpolated from the Eulerian field to the respective particle positions. The increment of the Wiener process is given by $\Delta\omega_i = \xi\sqrt{\Delta t}$ with ξ being a normally distributed random variable with zero mean and standard deviation of one.

Chemistry Substep

For the chemistry substep a direct integration can be used, since the chemical source term appears in closed form. The stiffness and high nonlinearity of the chemical reaction rates lead to chemical time scales that are orders of magnitude smaller than the characteristic flow time scales, and thus require the use of dedicated stiff ODE solvers in combination with adaptive time stepping to provide an efficient solution and to avoid numerical problems. The OpenFOAM toolbox offers a variety of stiff ODE solvers, including several Rosenbrock solvers of variable order and a semi-implicit extrapolation method known as SEULEX [76], the latter of which is used in the present work.

Mixing Substep

The OpenFOAM framework `mmcFoam` implements two mixing models, the sparse-Lagrangian MMC mixing model and the continuous Curl model with deterministic mixing extent that is used in intensive particle methods. The selection of the mixing pairs for the MMC mixing model is realized using a computationally efficient algorithm based on the k-d tree [57], which recursively divides the list of particles based on their separation in the multidimensional $(\mathbf{x}, \widetilde{f})$ space. Details on the algorithm can be found in Appendix C. The particle selection is usually performed globally within the entire domain, but can also be limited to the super cell. The continuous Curl model selects mixing pairs randomly within the super cell, which is equal to the LES cell in intensive particle methods.

Evaporation Substep

The evaporation substep of the notional particles is incorporated into the solution procedure of the liquid droplets, i.e., the properties of the gas-phase particles are updated immediately after solving the equations of a single droplet. In contrast to a segregated treatment, where the properties of the stochastic particles are updated

after all droplets have evolved, the coupled approach ensures that the properties of the gas phase are instantly adapted to the local evaporation process, thus ensuring that the saturation conditions are not exceeded, which is particularly important if the SAT model is used. For coupling models that result in fuel mass fractions that are far from saturation conditions (such as the EQUAL model or the one-to-one coupling), tests have shown that the differences between the two approaches are negligible.

Both the SAT model and the one-to-one coupling strategy require the minimization of distances between the fuel droplets and the stochastic particles, either in saturation space or in physical and reference mixture fraction space. This is achieved by employing a direct search, since the k-d tree algorithm, which is used by the MMC mixing model for selecting the mixing pairs, cannot be readily applied to the case with two particle clouds. To reduce the high computational costs associated with a direct search method, the minimization of the distances between the droplets and the gas-phase particles is performed locally within each super cell. Note that this may affect the particle selection if particles are selected in pure composition space (saturation space or reference mixture fraction space), since the super mesh artificially limits the maximum possible distances in physical space. If particles are selected by (partially) minimizing their distance in physical space (i.e., $\lambda_x \neq 0$ in Eq. (4.59)), the effect of the super mesh is usually negligible, since distances in physical space are kept small so that droplets are often coupled with particles that are located within the same super cell.

4.7.3 Two-Phase MMC-LES Model Coupled With CP-DNS

The primary objective of Chs. 6 and 7 is to provide an in-depth analysis of the two-phase coupling between the gas-phase particles and the liquid fuel droplets. In order to eliminate possible modeling errors associated with the turbulence model, a new solver called `mmcDropletDNSFoam` is created based on the MMC-LES solver `mmcDropletFoam`, in which the Eulerian LES is replaced by an Eulerian DNS of the carrier gas (CP-DNS). This allows discrepancies between the Lagrangian FDF method and the CP-DNS to be directly attributed to the modeling of particle mixing and two-phase coupling. Previous studies [112, 208, 218] have demonstrated the success of this *a priori* analysis for combustion modeling, and it has been shown that this approach may produce results similar to those obtained with a real LES utilizing the MMC model [219].

The schematic diagram of the `mmcDropletDNSFoam` solver is shown in Fig. 4.6.

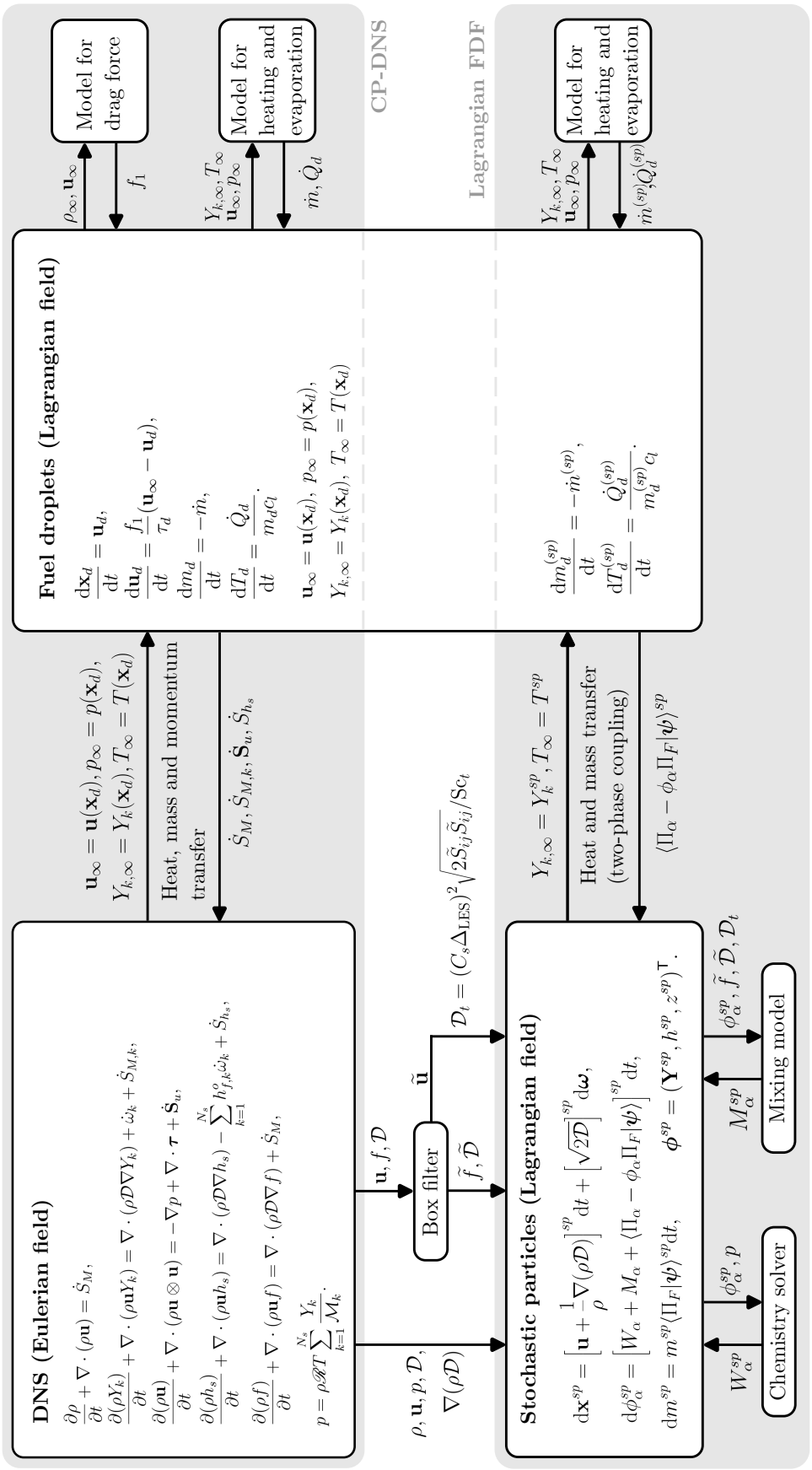

Figure 4.6: Schematic diagram of the `mmcDropletDNSFoam` solver, which couples the two-phase MMC-LES model with a CP-DNS.

The CP-DNS solves the Eulerian transport equations for density, species mass fractions, velocity, sensible enthalpy and reference mixture fraction without any models for turbulence and combustion, as specified in Sec. 3.1 and shown in Fig. 4.6, along with the set of Lagrangian equations governing the motion, heating and evaporation of the liquid fuel droplets, following the formulation presented in Sec. 3.2. A two-way coupling between the Eulerian DNS and the Lagrangian fuel droplets is applied, with exchange of heat, mass, and momentum, as described in Sec. 3.2.4. To ensure consistency with the MMC-LES model, the assumptions of low Mach numbers and unity Lewis numbers with constant Schmidt and Prandtl numbers are applied in the CP-DNS. The solution of the Lagrangian FDF is represented by the set of stochastic particles that are transported in physical and composition space, employing the models for mixing and evaporation introduced earlier. Since the two-phase coupling with the notional particles generally leads to a different evaporation rate than predicted by the CP-DNS, the Lagrangian droplet fields are extended to include two additional fields for droplet mass and temperature that evolve based on the evaporation process determined by the stochastic particles, which then provides a consistent Lagrangian FDF solution. Note that a second solution of the reactive scalar fields and droplet mass and temperature is redundant, but allows for a direct comparison between the (modeled) stochastic particle solution and the (exact) CP-DNS solution. Quantities normally provided by the Eulerian LES, such as the instantaneous velocity and diffusivity, are interpolated here from the DNS fields to the respective particle positions. Since the flow field is fully resolved by the DNS, the turbulent diffusivity is set to zero in the transport equation in physical space, while it is retained for the mixing model and the two-phase coupling model [218]. Here, LES-like input data are required for the particle selection based on the reference mixture fraction space as well as for the mixing time scale model. These quantities are obtained by explicitly filtering the instantaneous DNS fields, and the turbulent diffusivity is calculated from Eq. (4.20), with the turbulent viscosity given by the Smagorinsky model using the filtered velocity field. The filtering of the DNS fields is realized using a box filter and requires the definition of an additional LES mesh, resulting in a total of three meshes in the simulation (DNS mesh, LES mesh, super mesh). Since the CP-DNS is an independent solution that contains all the information about the composition field, no backward coupling in the form of a density feedback from the stochastic particles to the Eulerian DNS is applied.

Although OpenFOAM is only second-order accurate, several studies [125, 217, 218, 222, 224, 238, 243, 244] have demonstrated its good capabilities for DNS of turbulent reacting flows, and a detailed analysis of the numerical accuracy of OpenFOAM's discretization schemes is provided in Appendix D. Accordingly, the

DNS of the carrier gas provides an accurate reference solution for validation of the Lagrangian FDF method. As for the Lagrangian treatment of the fuel droplets, the point-particle assumption imposes further requirements on the grid resolution for an accurate simulation, which will be quantified in the next chapter.

Chapter 5

Resolution Requirements for Grid-Independent Euler-Lagrange Simulations

The following chapter addresses the grid dependence of the particle-source-in-cell (PSI-cell) model, which is used in Euler-Lagrange simulations of dilute sprays, but also forms the basis for many two-phase coupling models in Lagrangian FDF methods, as presented in the previous chapter. The analysis is split into two parts. First, the error of the evaporation rate and time of the liquid droplets that results from the cell-size dependence of the PSI-cell model is analyzed in detail and closed-form expressions for the error are derived, reproducing the study published by Sontheimer et al. [196]. Afterwards, the effect of the cell size on the resolution of the gaseous fields in the vicinity of the droplets is examined, with focus on the mixture fraction variance. The chapter concludes with a brief summary of the main outcomes and the formulation of guidelines for performing grid-independent CFD simulations of dilute sprays.

5.1 Objectives of the Study

The particle-source-in-cell (PSI-cell) model [36], as introduced in Sec. 3.2.4, is the standard model for the two-way coupling between the dispersed droplets and the Eulerian gas phase in Euler-Lagrange simulations of dilute sprays, where local cell values provide the ambient conditions for the evaporation model and droplets return mass, momentum and energy to the gas phase via source terms. The model also forms the basis for the development of two-phase coupling models in Lagrangian FDF methods, as discussed in Sec. 4.5. Although the PSI-cell is widely used in CFD of dilute sprays, it has some known limitations. On the one hand, the use of local

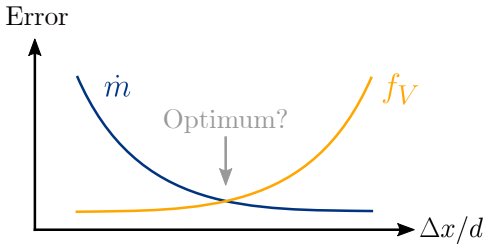

Figure 5.1: Schematic sketch of the effect of the computational cell size on evaporation rate (blue line) and mixture fraction variance (orange line) for calculations employing a two-way coupling based on the PSI-cell model.

cell values as ambient conditions in combination with the backward coupling via source terms introduces a dependence of the droplets' heat and mass transfer rates on the computational cell size [77, 121, 171, 188, 196, 229]. This effect is particularly evident for cell sizes of the order of the droplet size, as local gas properties are more strongly affected by the source terms with decreasing cell size. In that case, the point-source approximation of the droplets is no longer valid, and local cell values do no longer represent the conditions far from the droplet surface, which provides the basis for the derivation of the evaporation model (see Sec. 3.2.2). As a result, the calculated heat and mass transfer rates are subject to errors. On the other hand, the distribution of the source terms to the computational cell, which is usually larger than the droplet size, implies artificial mixing of the fuel vapor with the surrounding gas, and thus eliminates the variance generation due to the evaporating droplets on subgrid level. This lack of resolution increases with increasing cell size and therefore conflicts with the requirement of large cell sizes for an accurate determination of the evaporation rate, as illustrated in Fig. 5.1, such that the optimal cell size that keeps both errors low can be expected to be at moderate $\Delta x/d$.

Although the numerical error induced by the cell-size dependence of the PSI-cell model has received more attention in recent years, since the increase in available computing power allows CP-DNS and LES with much smaller cell sizes to be used, there are only a few studies to date that have attempted to quantify this error. A first error assessment of the PSI-cell model was conducted in the late 1980s by Rangel and Sirignano [171] and is reviewed in Sirignano [188]. For the case of steady-state evaporation of isolated droplets in quiescent and convective environments they showed that errors in the evaporation rate can be of the order of 10 % to 50 % if the cell size is comparable to the droplet size. However, as their study focuses on steady-state processes only and as their analytical solution involves additional assumptions for the case of stagnant droplets, some uncertainty persists how their results can be transferred to practical and time-dependent spray calculations. More recently, Luo *et al.* [121] discussed the cell-size dependence of single droplet evaporation in

an infinite environment for a setup based on the experiments of Nomura *et al.* [144], and established that the cell size must be at least ten times the droplet diameter to achieve cell-size independence. Although this criterion has become widely established, it suffers from the fact that it was only derived for one specific set of process conditions, and therefore the application to further configurations is uncertain. Further studies exist that have discussed the validity of the PSI-cell approach by comparison with droplet-resolved simulations [77, 223, 245]. These *a posteriori* analyses show that the PSI-cell model is a reasonable approximation under some circumstances, but do not provide any reliable method for estimating the error for arbitrary process conditions in advance. Finally, there are techniques that attempt to eliminate the effect of the cell size by distributing the source terms to the surrounding grid nodes in a grid-independent way [17, 129, 204, 229, 239]. However, the efficiency of such methods depends on a set of modeling parameters, and they are also more complex to implement and require more computational effort. Therefore, these techniques are not in the focus of the present work.

The present chapter provides a detailed analysis of the numerical error induced by the use of the PSI-cell model in Euler-Lagrange simulations of dilute sprays, with the following objectives:

(1) Quantify the effect of the cell size on the evaporation rate and time, and derive relations that allow for an *a priori* estimate of the error induced by the PSI-cell model in CFD simulations of dilute sprays.
(2) Quantify the effect of the cell size on the resolution of the gaseous fields near the droplet, and discuss the impact on the subgrid-scale mixture fraction variance.

Objective (1) is the topic of Sec. 5.2, while objective (2) is addressed in Sec. 5.3. It should be noted that the present analysis does not intend to improve the existing models for droplet evaporation or the prediction of subgrid variance, and only focuses on the numerical error that is introduced by the PSI-cell model and how it can be quantified. The analysis is performed in the context of an Eulerian representation of the gas phase, but the results are equally applicable to Lagrangian FDF methods if the volume of the computational cell size is replaced by the volume of the individual gas-phase particles.

5.2 Grid Dependence of Evaporation Rates

5.2.1 Computational Setup

Since dilute sprays are considered here, where the interactions between the droplets can be neglected, the analysis of the grid dependence of the evaporation rate is based on an isolated droplet in an infinite environment, as illustrated in Fig. 5.2. Later, it will be discussed how the analysis can be applied to moderately dense systems, where the surroundings of the droplet can no longer be assumed to be infinitely large (cf. Appendix E.5). The gas consists of two species, fuel vapor and air denoted as F and a, and is governed by the equations presented in Sec. 3.1 using the assumption of low Mach numbers. Chemical reactions are not considered in the analysis. Instead, the effect of heat release from combustion is accounted for by prescribing a high temperature for the ambient gas. The equations governing the liquid droplet follow the formulation given in Sec. 3.2, where the position of the droplet is fixed in the present analysis ($\mathbf{u}_d = 0$). More advanced models incorporating non-equilibrium effects and a non-uniform droplet temperature [132] have also been tested, but did not show any significant deviations from the reported trends. A discussion of the main results obtained from other evaporation models can be found in Appendix E.2. The ambient conditions that are required for the evaporation model are usually obtained from the gas-phase properties in an appropriate neighborhood of the droplet. To keep the analysis simple, the local cell values are used without interpolation, and source terms are transferred entirely to the cell that contains the droplet. For other approaches, in which the coupling is done using the neighboring grid points, the reader is referred to Appendix E.3.

The governing equations of the gas phase are discretized using the finite-volume method utilizing standard second-order schemes in combination with an implicit second-order time integration method, and the droplets are evolved using the method described in Sec. 3.2.6. In the case of quiescent environments, the gas field around the droplet is spherically symmetric and therefore allows for a one-dimensional solution in a radial coordinate system. However, as conventional CFD typically has a Cartesian mesh, the spherical treatment of the cell containing the droplet does not seem to be appropriate. Therefore, a Cartesian treatment of the droplet cell is employed, while the surrounding cells are still assumed to be spherical. This allows to obtain results very similar to a three-dimensional Cartesian solution while maintaining the one-dimensional formulation of the governing equations and thus low computational costs at high accuracy. More details are provided in Appendix E.1. Simulations involving a convective environment are performed using a three-dimensional Cartesian mesh.

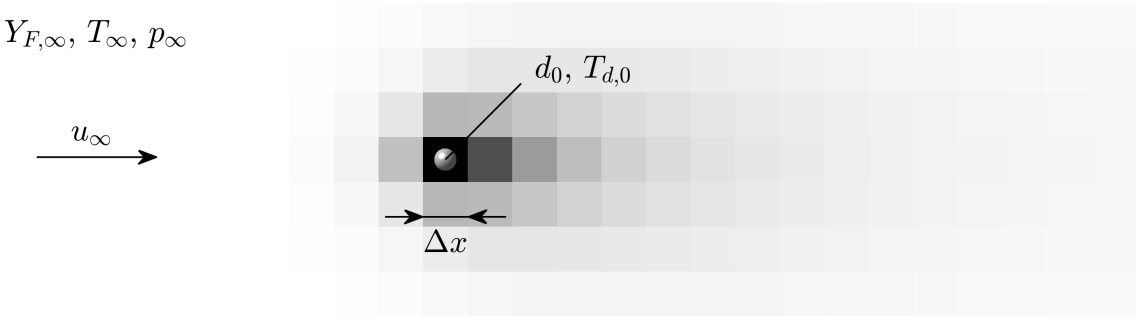

Figure 5.2: Sketch of the computational setup that is used for the analysis of the PSI-cell model, showing cell averages of the fuel mass fraction in the surroundings of the liquid droplet.

To assess the error of the evaporation process that is introduced by the PSI-cell model, a relative error based on the evaporation time is defined,

$$\epsilon_\tau = \frac{|\tau_{\text{evap}} - \tau_{\text{evap,ref}}|}{\tau_{\text{evap,ref}}}. \tag{5.1}$$

For steady-state calculations the error is based on the evaporation rate,

$$\epsilon_{\dot{m}} = \frac{|\dot{m} - \dot{m}_{\text{ref}}|}{\dot{m}_{\text{ref}}}. \tag{5.2}$$

The reference solution is given by the grid-independent solution of the evaporation process, i.e, the solution that is obtained if the cell size approaches infinity, thus ensuring that the error is eliminated. For the isolated droplet in an infinite environment considered here, this is achieved by inserting the true ambient conditions (i.e., the values far from the droplet instead of the local cell values) into the evaporation model. Note that the choice of the reference solution only affects the definition of the error but does not represent a limit of the validity of the relationships derived within this study (cf. Appendix E.5).

5.2.2 Dimensional Analysis

A dimensional analysis based on the Buckingham Π theorem [19] is performed to identify a set of physically independent non-dimensional quantities from the given variables. Here, the objective is to find the characteristic parameters that determine the droplet evaporation time and thus the error defined by Eq. (5.1) for the setup shown in Fig. 5.2. To keep the analysis simple and to focus on the essential parameters, only mass transfer with the assumption of a constant gas density is considered at this point. Note that these assumptions are relaxed later. The droplet has an initial diameter d_0 with liquid density ρ_l, and the fuel mass fraction at the droplet surface is given by $Y_{F,s}$. The ambient gas is characterized by fuel mass fraction $Y_{F,\infty}$, density ρ, dynamic viscosity μ, and fuel vapor diffusivity $\mathcal{D}_F$, and the free-stream

velocity is u_∞. The characteristic cell size is denoted by Δx. Note that the local cell values are not included in the dimensional analysis, since they are not known prior to the simulation and result from the given far-field conditions and cell size. Accordingly, the evaporation time of the droplet shown in Fig. 5.2 is expected to be a function of nine parameters,

$$\tau_{\text{evap}} = \mathcal{F}(d_0, \rho_l, Y_{F,s}, Y_{F,\infty}, u_\infty, \mu, \mathcal{D}_F, \rho, \Delta x). \tag{5.3}$$

The number of parameters can be reduced by defining non-dimensional groups,

$$\begin{aligned} \Pi_1 = \frac{\Delta x}{d_0}, \qquad \Pi_2 = \frac{\rho_l}{\rho}, \qquad \Pi_3 = Y_{F,\infty}, \qquad \Pi_4 = Y_{F,s}, \\ \Pi_5 = \frac{\rho u_\infty d_0}{\mu}, \qquad \Pi_6 = \frac{\mu}{\rho \mathcal{D}_F}, \qquad \Pi_7 = \frac{\tau_{\text{evap}} \mathcal{D}_F}{d_0^2}, \end{aligned} \tag{5.4}$$

which obey the functional relationship

$$\Pi_7 = \mathcal{F}(\Pi_1, \Pi_2, \Pi_3, \Pi_4, \Pi_5, \Pi_6). \tag{5.5}$$

Parameter Π_1 represents the ratio of cell size to initial droplet diameter, while parameter Π_2 denotes the ratio of liquid to gaseous density. They can be combined to form a new parameter,

$$\varphi = \frac{\pi}{6} \Pi_1^{-3} \Pi_2 = \frac{\frac{\pi}{6} \rho_l d_0^3}{\rho \Delta x^3} = \frac{m_{d,0}}{m_g}, \tag{5.6}$$

which indicates the initial ratio of droplet mass to gaseous mass in the computational cell. The definition of the mass transfer number, Eq. (3.34), allows to merge parameters Π_3 and Π_4. As the mass transfer number is based on the true ambient condition, it represents the reference value $B_{M,\text{ref}}$. Parameters Π_5 and Π_6 are equal to Reynolds and Schmidt number, respectively, and are usually combined to the Péclet number,

$$\text{Pe} = \text{Re}\,\text{Sc} = \Pi_5 \Pi_6 = \frac{u_\infty d_0}{\mathcal{D}_F}, \tag{5.7}$$

which represents the ratio of convective to diffusive transport rates. Since the focus is on numerical errors introduced by the computational grid, it is more convenient to define a Péclet number based on the cell size,

$$\text{Pe}_{\Delta x} = \Pi_1 \Pi_5 \Pi_6 = \frac{u_\infty \Delta x}{\mathcal{D}_F}, \tag{5.8}$$

which is called the cell Péclet number. Finally, parameter Π_7 indicates a normalized evaporation time with reference time being the diffusive time scale, defined as $\tau_\mathcal{D} = d_0^2/\mathcal{D}_F$. Since the diffusive time scale is a constant, it can be substituted by a

general reference time. To be consistent with the definition of the error, Eq. (5.1), the evaporation time in an infinite environment is chosen as reference time, such that $\Pi_7 = \tau_{\text{evap}}/\tau_{\text{evap,ref}}$. The relative error of the evaporation rate, which is directly related to the normalized evaporation time via $\epsilon_\tau = |\Pi_7 - 1|$, can then be expressed as a function of four non-dimensional parameters,

$$\epsilon_\tau = \mathcal{F}\left(\Delta x/d_0, \varphi, B_{M,\text{ref}}, \text{Pe}_{\Delta x}\right). \tag{5.9}$$

This shows that the relative error of the evaporation time is a function of the length ratio $\Delta x/d_0$, the mass ratio φ, the reference mass transfer number $B_{M,\text{ref}}$, and the cell Péclet number $\text{Pe}_{\Delta x}$. The effect of these parameters on the error will be briefly discussed in the following. A smaller cell size leads to more significant changes of properties within the droplet's cell with earlier saturation, and therefore increases the evaporation time and thus the error. The mass ratio φ is a direct function of the length ratio $\Delta x/d_0$ but additionally involves the density ratio, and is therefore expected to have a similar effect on the error. The reference mass transfer number quantifies the driving force for the evaporation process itself as it includes the difference between surface and ambient fuel mass fraction, yet it is unclear how this affects the error. The cell Péclet number characterizes the effect of a convective flow relative to the droplet. A higher cell Péclet number indicates stronger convection, and thus a smaller error, as the accumulated vapor is replaced by fresh gas at a faster rate. The exact relation between the parameters in Eq. (5.9) cannot be obtained from dimensional analysis alone and must be determined by the underlying equations. This will be the topic of the next two sections, starting with steady-state solutions (Sec. 5.2.3) and followed by the transient case (Sec. 5.2.4).

5.2.3 Steady-State Investigations

Pure Mass Transfer With Constant Density

As the evaporation model involves the quasi-steady assumption, it is natural to start with the steady-state solution for the governing equations. In a first step, quiescent environments and pure mass transfer are considered to retrieve the results of Rangel and Sirignano [171], and later the analysis is extended to the case of heat transfer and convective environments. Accordingly, the temperature and pressure fields are assumed to be uniform, and density is also initially kept constant, implying equal molar masses (cf. Eq. (3.5)). Further, all gaseous and liquid properties (including the droplet surface conditions) are assumed to be constant and known.

The assumptions made allow for an analytical solution of the vapor field around the droplet, which is given by Eq. (3.35). This analytical solution was used in

the study of Rangel and Sirignano [171] to discuss the error that is introduced if the mass transfer number is evaluated in an appropriate neighborhood of the droplet, i.e., using a local value $Y_F(r)$ instead of the far-field value $Y_{F,\infty}$ in the expression for the mass transfer number. They showed that the resulting error of the evaporation rate follows the relation $\epsilon_{\dot{m}} = (1+r/r_s)^{-1}$ and thus only depends on the normalized distance from the origin. As the study of Rangel and Sirignano relies on the analytical solution, effects of the numerical discretization are not included, and it is expected that in particular the vapor mass fraction value in the cell that contains the droplet and thus determines the evaporation rate will deviate from the analytical solution.

To be consistent with practical calculations, the present study does not rely on the analytical solution and instead employs a numerical solution utilizing the PSI-cell model. Considering only mass transfer, the set of gas-phase equations, which are solved in their spherically symmetric form, is given by

$$\frac{\partial \rho}{\partial t} + \frac{1}{r^2}\frac{\partial}{\partial r}\left(r^2 \rho u_r\right) = \dot{S}_M, \tag{5.10}$$

$$\frac{\partial (\rho Y_F)}{\partial t} + \frac{1}{r^2}\frac{\partial}{\partial r}\left(r^2 \rho u_r Y_F\right) = \frac{1}{r^2}\frac{\partial}{\partial r}\left(\rho \mathcal{D}_F \frac{\partial Y_F}{\partial r}\right) + \dot{S}_M, \tag{5.11}$$

where the transient terms are set to zero due to the assumption of steady-state processes. The source term $\dot{S}_M$ is given by Eq. (3.64) and is non-zero only in the cell that contains the droplet placed at $r = 0$. Note that the steady-state equation system requires an iterative solution, where the velocity field results solely from the Stefan flow and is obtained from the continuity equation. In order to examine the dependence on the characteristic parameters predicted by the dimensional analysis, a large number of calculations is performed with varying gas and droplet properties. Figure 5.3(a) shows the calculated errors of the evaporation rate and plotted versus the ratio of cell size to droplet diameter. Similar to the results of Rangel and Sirignano [171], where the error was a function of the ratio r/r_s, the error is now a function of the ratio $\Delta x/d$, and can be described by an equivalent relation,

$$\epsilon_{\dot{m}} = \frac{1}{1 + \alpha(\Delta x/d)}, \tag{5.12}$$

with parameter $\alpha \approx 2/3$ found by least-squares fitting. It is remarkable that the other parameters found by dimensional analysis such as the reference mass transfer number do not affect the error here. This is probably a result of the assumptions made and will be discussed later.

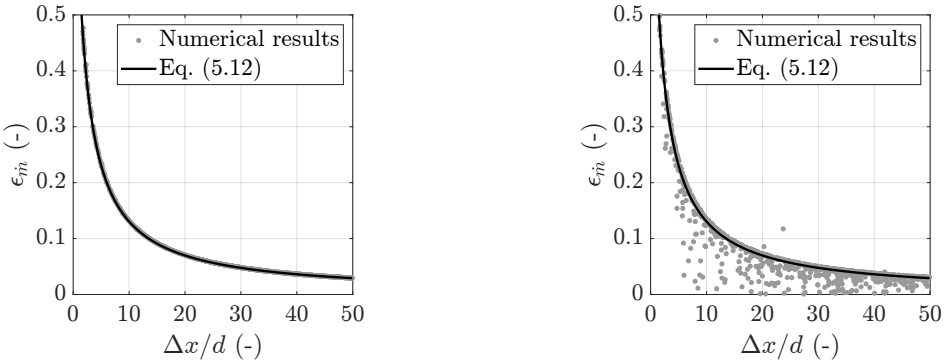

(a) Constant density. **(b)** Variable density.

Figure 5.3: Relative error of the steady-state evaporation rate in a quiescent environment obtained from numerical calculations (gray dots) based on pure mass transfer with (a) constant density and (b) variable density with molar masses $\mathcal{M}_F = 100\,\mathrm{kg/kmol}$ and $\mathcal{M}_a = 30\,\mathrm{kg/kmol}$ (approximately the values of n-heptane and air) and compared to Eq. (5.12) (solid line).

Variable Density Effects

In general, the molar masses of fuel and air are not equal, resulting in a spatially variable density field. Accordingly, the equation of state, Eq. (3.5), is now used to calculate the density, where velocity and vapor mass fraction are obtained from Eqs. (5.10) and (5.11), respectively. Note that the temperature as well as the thermodynamic properties are still assumed to be constant at this point. The variable density is also taken into account in the evaporation model using an average density value that is based on the mixture composition given by the 1/3 rule (cf. Eq. (3.58a)). The calculation of density requires the specification of molar masses, for which values similar to those of air and n-heptane are used here to account for the effect of having widely different molar masses.

Figure 5.3(b) shows the results that are obtained with variable density being taken into account. It can be seen that the relative error of the evaporation rate largely follows the relation from the constant-density solution given by Eq. (5.12), although there is now some scatter, which tends to reduce the errors and which increases if the ratio between the molar masses of fuel and air is further increased (not shown). The existence of the scatter can be explained by inserting the expression for the evaporation rate, Eq. (3.33), into the definition of the error, Eq. (5.2), leading to

$$\epsilon_{\dot{m}} = \left| \frac{\dot{m}}{\dot{m}_{\mathrm{ref}}} - 1 \right| = \Bigg| \underbrace{\frac{\ln(1+B_M)}{\ln(1+B_{M,\mathrm{ref}})}}_{f_1} \cdot \underbrace{\frac{\rho}{\rho_{\mathrm{ref}}}}_{f_2} - 1 \Bigg|. \tag{5.13}$$

The first factor, f_1, is a function of the mass transfer numbers B_M and $B_{M,\mathrm{ref}}$ and is independent of the density. Its effect can be described as a function of the ratio $\Delta x/d$ as shown previously. The second factor, f_2, accounts for the variable density and is

calculated based on the equation of state and the 1/3 rule, and thus depends additionally on the ratio of molar masses and the averaging parameter γ (cf. Eq. (3.58)). According to Eq. (5.13), for a fixed ratio of molar masses and averaging parameter, the error can tend to zero not only if the cell size is sufficiently large (and thus the local cell values match the true ambient conditions), but also for a certain value of $B_{M,\mathrm{ref}}$ corresponding to the singularity $f_1 f_2 = 1$. This singularity explains why the error is generally smaller than predicted by Eq. (5.12) and is associated with the scatter in Fig. 5.3(b). Furthermore, values above the singularity ($f_1 f_2 > 1$) can be associated with evaporation rates larger than the reference value, resulting in faster evaporation than in infinite environments. However, the calculations showed that the singularity arises at rather large mass transfer numbers that rarely occur for practically relevant conditions. As the following section will show, the effect of a variable density is generally small if the effect of heat transfer is taken into account, and therefore variable density effects are expected to be second-order effects only.

Extension to Heat Transfer

The analysis is now extended to include the effect of heat transfer, where the spatially variable temperature field is obtained from the solution of the energy equation. The energy equation is expressed here in terms of the absolute enthalpy using the assumption of low Mach numbers, and thus takes the form given by Eq. (3.12), where the heat flux vector reduces to Eq. (3.13) since only two species are considered. In contrast to the case of pure mass transfer, the vapor mass fraction at the droplet surface is no longer specified and results from liquid-vapor equilibrium, where the unknown steady-state droplet temperature (referred to as the wet-bulb temperature) is calculated from the condition that there is no heat flow into the liquid droplet, $\dot{Q}_d = 0$ (Eq. (3.44)). Since the temperatures at the droplet surface and far from the droplet can differ greatly for combustion-relevant conditions, temperature-dependent and mixture-averaged thermophysical properties are used for both the gas and the liquid phase, as described in Secs. 3.1.6 and 3.2.5.

A set of calculations is performed using various process conditions and cell sizes. The gas around the droplet is composed of nitrogen and fuel vapor, where *n*-heptane and ethanol are chosen to serve as representative fuels for the analysis due to their relevance for spray combustion and because of their different molar masses ($\mathcal{M}_{\mathrm{C_2H_5OH}} = 46.07\,\mathrm{kg/kmol}$, $\mathcal{M}_{\mathrm{C_7H_{16}}} = 100.20\,\mathrm{kg/kmol}$). Other fuels were also tested but did not show any significant deviations from the reported results. The far-field conditions are selected randomly within $T_\infty \in [500\,\mathrm{K}, 3000\,\mathrm{K}]$ and $p_\infty \in [0.1\,\mathrm{atm}, 10\,\mathrm{atm}]$. To include the effect of pre-evaporation the ambient fuel vapor mass fraction is also varied within $Y_{F,\infty} \in [0, 0.5]$. The droplet diameter

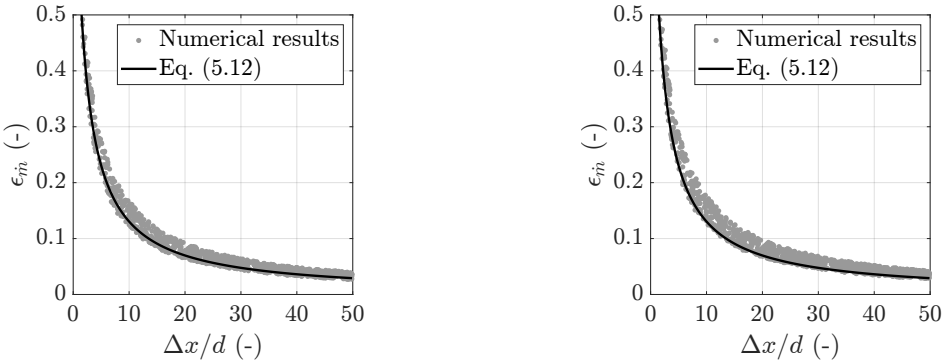

(a) Ethanol droplet. **(b)** n-Heptane droplet.

Figure 5.4: Relative error of the steady-state evaporation rate in a quiescent environment obtained from numerical calculations based on heat and mass transfer (gray dots) and compared to Eq. (5.12) (solid line). The ambient gas is a mixture of nitrogen and fuel, with fuel species (a) ethanol and (b) n-heptane.

ranges from $d = 1\,\mu\text{m}$ to $d = 1\,\text{cm}$, and the ratio of cell size to droplet diameter is selected within the range $\Delta x/d \in [1, 50]$.

Figure 5.4 shows the calculated errors of the evaporation rate and plotted versus $\Delta x/d$. Although the constant-density relation given by Eq. (5.12) does not include the additional effect of heat transfer, it can still approximate the error quite accurately. Compared to the case of pure mass transfer with variable density (cf. Fig. 5.3(b)), the scatter is smaller now for similar molar masses of gas and fuel (Fig. 5.4(b)). This is because the droplet surface conditions are no longer (arbitrarily) selectable but result from liquid-vapor equilibrium according to the given ambient conditions, which generally leads to a smaller range for the mass transfer numbers. As the scatter around the constant-density relation, Eq. (5.12), is related to the mass transfer number, as discussed previously, a smaller range of B_M directly leads to lower dispersion of the results.

Effect of Free-Stream Velocity

The previous investigations have assumed that there is no droplet motion relative to the gas. While this is true for droplets in a quiescent environment, it is not realistic for spray combustion where a liquid fuel is injected into the combustion chamber, leading to a relative velocity between droplets and the carrier gas phase. The relative velocity replaces accumulated vapor in the surroundings of the droplet with fresh gas, and it is expected that errors induced by the accumulation of fuel vapor within a cell of finite size are reduced.

To allow for an analytical treatment of the effects of an external flow field on the error, the case of pure mass transfer with constant density and constant properties is considered, which seems justified following the preceding investigations that

demonstrated small effects of heat transfer and variable thermophysical properties on the error estimate. Further, it is assumed that convective fluxes dominate over diffusive fluxes, so the latter can be ignored. Assuming a laminar flow aligned with the x-axis, the fuel mass balance for the cell containing the droplet can be written as

$$\underbrace{\rho u_\infty \Delta x^2 Y_{F,\infty}}_{\text{Inflow}} + \underbrace{\dot{m}}_{\text{Evaporation}} = \underbrace{\rho u_\infty \Delta x^2 Y_F}_{\text{Outflow}}. \tag{5.14}$$

The evaporation rate is given by Eq. (3.55) and evaluated using the cell value Y_F, which is equal to the fuel mass fraction at the outflow. By inserting the expression for the evaporation rate, it is possible to rewrite Eq. (5.14) in non-dimensional form,

$$\ln(1 + B_M) = \frac{1}{\pi} \frac{\mathrm{Pe}_{\Delta x}}{\mathrm{Sh}^*} \frac{\Delta x}{d} (Y_F - Y_{F,\infty}), \tag{5.15}$$

with the cell Péclet number defined by Eq. (5.8). This shows that the solution of the fuel mass balance equation is governed by the non-dimensional parameters $\mathrm{Pe}_{\Delta x}/\mathrm{Sh}^*$ and $\Delta x/d$ and by the difference between the fuel mass fractions associated with the ambient state, the droplet surface condition and the cell value. The assumption of a small mass transfer number, implying $Y_{F,s} \ll 1$ and thus leading to $\ln(1 + B_M) \approx B_M \approx Y_{F,s} - Y_F$, in combination with the assumption of a constant Sh^* allows to solve Eq. (5.15) analytically for the unknown cell value Y_F that determines the error of the evaporation rate. If the solution is inserted into the equation for the evaporation rate given by Eq. (3.55), the expression for the relative error is found,

$$\epsilon_{\dot{m}} = \left(1 + \frac{1}{\pi} \frac{\mathrm{Pe}_{\Delta x}}{\mathrm{Sh}^*} \frac{\Delta x}{d}\right)^{-1}. \tag{5.16}$$

Details on the derivation can be found in Appendix E.4.1. This relation has a similar form as the relation for quiescent environments, Eq. (5.12), but now the prefactor is no longer constant but a function of the cell Péclet number and modified Sherwood number and thus depends on the cell size and the free-stream velocity. Due to these facts, the error can be much smaller than in quiescent environments. As the prefactor is now a function of the cell size, the error effectively shows a quadratic dependence on the cell size. Numerical calculations confirm that the analytical solution is also valid if the assumptions of small vapor mass fractions and constant Sh^* are relaxed (not shown).

The error relation given by Eq. (5.16) is a good approximation if convective fluxes dominate over diffusive fluxes, that is, if the cell Péclet number is large. However, the equation is not valid for smaller values of $\mathrm{Pe}_{\Delta x}$ associated with smaller velocities or smaller cell sizes, where it predicts too large an error due to the omission of the diffusive fluxes. In that case, the error relation for quiescent environments,

Eq. (5.12), provides a better approximation. This fact gives reason to quantify the error in the whole range of Péclet numbers and cell sizes by taking the minimum of both relations,

$$\epsilon_{\dot{m}} = \min \left[\underbrace{\left(1 + \frac{2}{3}\frac{\Delta x}{d}\right)^{-1}}_{\text{Eq. (5.12)}}, \underbrace{\left(1 + \frac{1}{\pi}\frac{\mathrm{Pe}_{\Delta x}}{\mathrm{Sh}^*}\frac{\Delta x}{d}\right)^{-1}}_{\text{Eq. (5.16)}} \right]. \tag{5.17}$$

With this blending function, the relation based on pure convection, Eq. (5.16), is used for $\mathrm{Pe}_{\Delta x} > 2\pi\mathrm{Sh}^*/3 \approx 4$, while for smaller values the relation for quiescent environments, Eq. (5.12), is used. Note that the fuel vapor diffusivity that appears in the definition of the cell Péclet number refers to the gas state far from the droplet, and the modified Sherwood number is evaluated in the same way as in the evaporation model (see Sec. 3.2) using the true ambient conditions.

To assess the applicability of the simplifying assumptions and therefore the validity of Eq. (5.17), the equations governing the evaporation of the single droplet in an infinite environment are solved numerically in their three-dimensional form. To be consistent with the analytical investigations, the case of pure mass transfer with constant density is considered first, where the velocity field around the droplet is approximated by a potential flow solution that results from the superposition of a uniform flow, a doublet and a point source, as proposed by Rangel and Sirignano [171]. In a second step, the effects of heat transfer and variable thermophysical properties are added, and the velocity field is obtained from the solution of the momentum equation to include viscous effects. Similar to the preceding investigations, all gas and droplet properties are selected randomly within a large range of typical conditions, with free-stream velocities ranging from 0.001 m/s to 100 m/s. The ratio of cell size to droplet diameter is varied within $1 \leq \Delta x/d \leq 50$, resulting in cell Péclet numbers between 10^{-3} and 10^5. Figure 5.5(a) compares calculated errors with error predictions based on Eq. (5.17) for the case of pure mass transfer and shows overall good agreement. This confirms the applicability of the simplifying assumptions as well as the choice of the blending function. The color in Fig. 5.5(a) indicates which of the two relations in Eq. (5.17) is used to calculate the error. It can be seen that the relation for quiescent environments, Eq. (5.12), is generally associated with larger errors, whereas the relation for convective environments, Eq. (5.16), is associated with smaller errors. However, some overlap of the errors exists which is due to the fact that the same error value can be achieved by both relations by changing either $\Delta x/d$ alone, or $\Delta x/d$ and u_∞. Finally, Figs. 5.5(b) and 5.5(c) demonstrate that Eq. (5.17) also holds for the case of combined heat and mass transfer with variable thermophysical properties, where the trends are essentially the same as for the case of pure mass transfer.

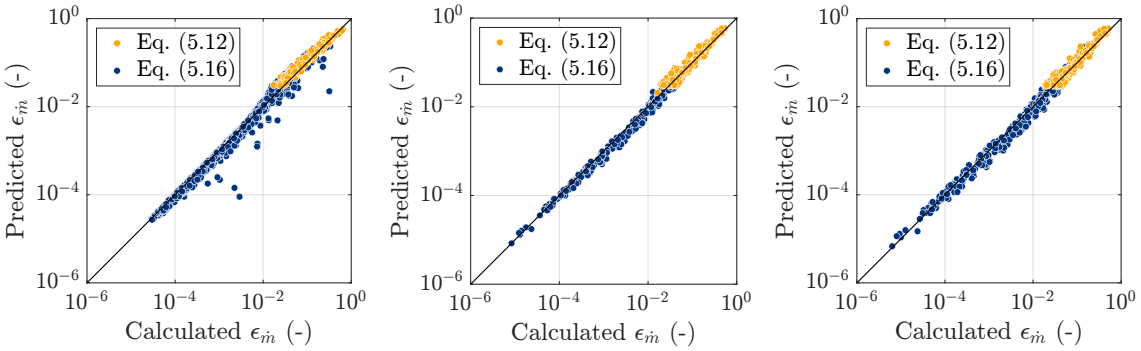

(a) Pure mass transfer with constant density.

(b) Heat and mass transfer, ethanol droplet.

(c) Heat and mass transfer, *n*-heptane droplet.

Figure 5.5: Comparison of predicted and calculated errors of the steady-state evaporation rate in convective environments. The calculated error is obtained from the numerical solution of the three-dimensional governing equations. In (a) only the effect of mass transfer with constant density is considered, while in (b) and (c) heat and mass transfer are taken into account, where the ambient gas is a mixture of nitrogen and fuel with fuel species (b) ethanol and (c) *n*-heptane. The predicted error is obtained from Eq. (5.17), where the color indicates which of the two relations, Eq. (5.12) or Eq. (5.16), determines the error.

Discussion

The focus of the previous investigations was on steady-state solutions. Starting with the very simple case of pure mass transfer and constant density, the analysis was successively extended by adding further effects such as variable density effects, heat transfer and convective environments. Two error relations were derived, which are given by Eqs. (5.12) and (5.16), corresponding to the limits of $\mathrm{Pe}_{\Delta x} = 0$ and $\mathrm{Pe}_{\Delta x} \gg 1$, respectively. These are combined by Eq. (5.17), which then provides an adequate error prediction for arbitrary cell Péclet numbers. For quiescent environments, the error is only a function of ratio $\Delta x/d$, which is consistent with the study of Rangel and Sirignano [171]. Based on Eq. (5.12) one finds that the ratio $\Delta x/d = 10$, as established by Luo *et al.* [121], leads to an error in the evaporation rate of about 13 %, where doubling the cell size approximately halves the error. The existence of a relative velocity between the droplet and the gas can greatly reduce the error and introduces the cell Péclet number as an additional parameter. To demonstrate that behavior, values typical for spray combustion applications with ethanol droplets, $d = 20\,\mu\mathrm{m}$ and $\mathcal{D}_F = 10^{-4}\,\mathrm{m}^2/\mathrm{s}$, are inserted into the error relation given by Eq. (5.17), and the ratio of cell size to droplet diameter is kept at $\Delta x/d = 10$. While for $u_\infty = 1\,\mathrm{m/s}$ the predicted error is still the same as in a quiescent environment (13 %), it decreases to only 3 % for $u_\infty = 10\,\mathrm{m/s}$. To achieve this error in a quiescent environment, a ratio of $\Delta x/d \approx 50$ would be necessary.

In addition to parameters $\Delta x/d$ and $\mathrm{Pe}_{\Delta x}$, the dimensional analysis has provided other parameters such as the reference mass transfer number $B_{M,\mathrm{ref}}$ and the

mass ratio φ (cf. Eq. (5.9)). For the mass transfer number it was shown that it has only a secondary effect in steady-state calculations, which can be neglected if only realistic values that result from phase equilibrium are chosen. The mass ratio φ differs from parameter $\Delta x/d$ only by incorporation of the density ratio ρ_l/ρ. As the liquid density solely appears in the conversion of droplet mass to volume, it is not part of the steady-state equation system (where the droplet mass is constant), and therefore the mass ratio φ is irrelevant here. However, it is expected that this parameter becomes important for the case of transient droplet evaporation, which will be the topic of the next section.

5.2.4 Transient Droplet Evaporation

Pure Mass Transfer

The error analysis is continued with the practically more relevant case of transient droplet evaporation, where the error is now expressed in terms of the evaporation time, as defined by Eq. (5.1). The sequence of investigation is the same as in the preceding steady-state analysis, starting with the case of pure mass transfer at constant density in quiescent environments and successively adding the effects of heat transfer and convective environments. The governing equations of the gas phase are given by Eqs. (5.10) and (5.11), now including the transient terms, and the droplet mass evolves according to Eq. (3.24) with the evaporation rate given by Eq. (3.33).

It is possible to transfer the known error relation for the steady-state evaporation rate into a relation for the relative error of the evaporation time. Assuming quasi-steady conditions for the modeling of the evaporation rate and using Eq. (5.12), the instantaneous evaporation rate can be estimated by

$$\frac{\mathrm{d}m_d}{\mathrm{d}t} = -\dot{m} = -f_1 \dot{m}_{\mathrm{ref}}, \qquad f_1 = \frac{\alpha(\Delta x/d)}{1+\alpha(\Delta x/d)}. \tag{5.18}$$

The factor f_1 represents a correction to the reference evaporation rate, which is obtained by using the true ambient conditions, and depends on the ratio of cell size to droplet diameter. Since $f_1 < 1$, the correction factor leads to an increase of the evaporation time. Substituting the time derivative of the droplet mass by the time derivative of the squared droplet diameter results in

$$\frac{\mathrm{d}d^2}{\mathrm{d}t} = -f_1 K_{\mathrm{ref}}, \tag{5.19}$$

with the evaporation constant $K_{\mathrm{ref}} = (8\rho\mathcal{D}_F/\rho_l)\ln(1+B_{M,\mathrm{ref}})$ based on the reference solution. Since the correction factor f_1 is a function of the instantaneous

droplet diameter, an analytical solution of Eq. (5.19) is complicated. Therefore, the correction factor is approximated by a suitable average value, which is determined from the mean droplet diameter based on the d^2-law given by $\langle d \rangle = \frac{2}{3} d_0$. With the right-hand side being a constant now (representing a modified evaporation constant), Eq. (5.19) can be solved analytically to obtain the evaporation time. The relative error of the evaporation time is then given by

$$\epsilon_\tau = \frac{\tau_{\text{evap}}}{\tau_{\text{evap,ref}}} - 1 = \frac{2}{3\alpha} \left(\frac{\Delta x}{d_0} \right)^{-1} = \left(\frac{\Delta x}{d_0} \right)^{-1}, \tag{5.20}$$

where the value $\alpha = 2/3$ found from the steady-state calculations was inserted. A detailed derivation including all substeps can be found in Appendix E.4.2. This simple relation states that the relative error of the evaporation time is given by the inverse of the ratio of cell size to initial droplet diameter.

Since Eq. (5.20) is based on the quasi-steady assumption, it cannot be valid for arbitrary process conditions. An analysis of the terms in the vapor mass fraction equation, evaluated in the cell that contains the droplet, shows that for cell sizes similar to the droplet diameter, the convective and diffusive fluxes are of the same order of magnitude as the source term but of opposite sign, such that the time derivative is relatively small, justifying the use of steady-state relationships. Note that the time derivative is still large in absolute terms and therefore leads to a large variation of the vapor mass fraction value. In contrast, for cell sizes being much larger than the droplet diameter, the convection and diffusion terms are negligible compared to the other terms, so that the dominant terms are the time derivative and the source term. This is equivalent to treating the cell containing the droplet as a closed system, which then allows for an analytical approach. Appendix E.4.3 provides a detailed analysis of the single droplet in a finite and closed environment, with the result that the evaporation time is governed by the parameter

$$\varphi^* = \frac{\varphi}{\ln(1 + B_{M,\text{ref}})} = \frac{\pi}{6} \frac{\rho_l}{\rho_\infty} \left(\frac{\Delta x}{d_0} \right)^{-3} \frac{1}{\ln(1 + B_{M,\text{ref}})}, \tag{5.21}$$

which represents a modified mass ratio that incorporates the effect of the mass transfer number. For sufficiently small φ^* (corresponding to large $\Delta x/d_0$), the error of the evaporation time follows the simple linear relation

$$\epsilon_\tau = 0.6 \varphi^*. \tag{5.22}$$

With Eqs. (5.20) and (5.22) there now exist two relations describing the error of the evaporation time, corresponding to the limits of small and large $\Delta x/d_0$, respectively. Since both error relations overestimate the error in the range where they are not

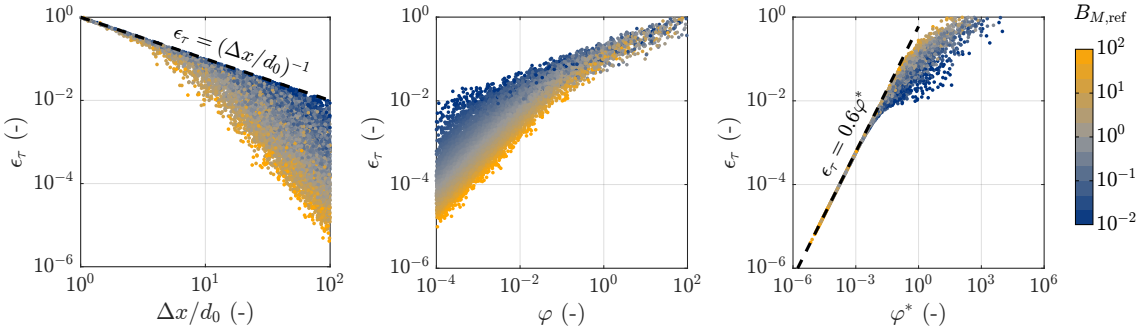

(a) Error ϵ_τ versus $\Delta x/d_0$. **(b)** Error ϵ_τ versus φ. **(c)** Error ϵ_τ versus φ^*.

Figure 5.6: Relative error of the evaporation time for single droplet evaporation in quiescent environment based on pure mass transfer with constant density, as a function of (a) $\Delta x/d_0$, (b) mass ratio φ, and (c) modified mass ratio φ^*. The color indicates the reference mass transfer number $B_{M,\mathrm{ref}} \in [0.01, 100]$ (logarithmic scale).

valid, the minimum of the two relations is taken to describe the error in the entire range of $\Delta x/d_0$,

$$\epsilon_\tau = \min\left[\underbrace{\left(\frac{\Delta x}{d_0}\right)^{-1}}_{\text{Eq. (5.20)}}, \underbrace{0.6\varphi^*}_{\text{Eq. (5.22)}}\right]. \tag{5.23}$$

To assess the validity of Eqs. (5.20) and (5.22) as well as their combination given by Eq. (5.23), the governing equations of the gas phase, Eqs. (5.10) and (5.11), and the equation for droplet mass, Eq. (3.24), are solved numerically as described in Sec. 5.2.1. Similar to the previous investigations, a set of calculations is performed with varying gas and droplet properties, covering a wide range of typical values, to examine the dependence on the characteristic parameters. The ratio of cell size to initial droplet diameter is varied within $1 \leq \Delta x/d_0 \leq 100$, resulting in modified mass ratios in the range $10^{-5} \lesssim \varphi^* \lesssim 10^4$. Figure 5.6(a) shows the calculated errors of the evaporation time plotted versus the length-scale ratio $\Delta x/d_0$. For cell sizes of the order of the initial droplet diameter ($\Delta x/d_0 \lesssim 5$), there is good agreement between calculated errors and Eq. (5.20) (dashed line), whereas a large deviation exists for cell sizes much larger than the initial droplet diameter, which is due to the reasons explained above. The deviation at larger $\Delta x/d_0$ shows that the error must depend on at least one further characteristic quantity that have previously been identified using dimensional analysis. In particular the reference mass transfer number $B_{M,\mathrm{ref}}$ introduces a systematic deviation from Eq. (5.20), as indicated by the color. However, since some scatter exists, further parameters need to be taken into account. If the error is plotted against the mass ratio φ, the scatter associated with the mass transfer number at larger $\Delta x/d_0$ (smaller φ) is eliminated, as shown in Fig. 5.6(b), but the strong dependence on the mass transfer number persists.

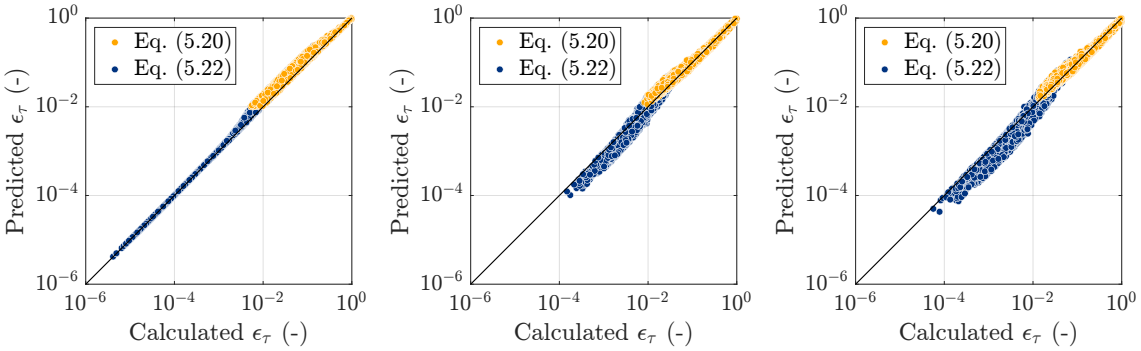

(a) Pure mass transfer with constant density.

(b) Heat and mass transfer, ethanol droplet.

(c) Heat and mass transfer, *n*-heptane droplet.

Figure 5.7: Comparison of predicted and calculated errors of the evaporation time in quiescent environments. In (a) only the effect of mass transfer with constant density is considered, while in (b) and (c) heat and mass transfer are taken into account, where the ambient gas is a mixture of nitrogen and fuel with fuel species (b) ethanol and (c) *n*-heptane. The predicted error is obtained from Eq. (5.23), where the color indicates which of the two relations, Eq. (5.20) or Eq. (5.22), determines the error.

Only the use of the modified mass ratio φ^* can largely eliminate the influence of the reference mass transfer number, as can be seen in Fig. 5.6(c), where good agreement with Eq. (5.22) (dashed line) is obtained for sufficiently large cells ($\varphi^* \lesssim 10^{-2}$). Finally, Fig. 5.7(a) compares calculated errors with the suggested combination of the two relations based on Eq. (5.23), showing very good agreement. Only in the transition region between the two respective relations there is a small deviation, where the error is slightly overpredicted. Again, color is used to distinguish between the relations determining the error, where it can be seen that the relation based on the quasi-steady assumption is associated with larger errors due to its validity for smaller $\Delta x/d_0$ only.

Heat and Mass Transfer

Since the previous section has only focused on pure mass transfer with constant density, the analysis is now extended by the effect of heat transfer, including the effects of variable density and variable thermophysical properties. The same initial droplet diameters and ambient gas conditions are used as in the corresponding steady-state analysis, and the ratio of cell size to droplet diameter is varied within the range $1 \leq \Delta x/d_0 \leq 100$, leading to modified mass ratios within $10^{-4} \lesssim \varphi^* \lesssim 10^{3}$. Figures 5.7(b) and 5.7(c) compare the calculated error with the predicted error based on Eq. (5.23) for fuel species ethanol and *n*-heptane, showing overall good agreement. This confirms that the relationships found based on pure mass transfer also hold for the case of combined heat and mass transfer, as was the case in the steady-state investigations. Compared to the results based on pure mass transfer

(Fig. 5.7(a)), some increased scatter is present, in particular in the relation for the closed system, Eq. (5.22), resulting in slightly underpredicted errors. Note that the reference mass transfer number is no longer constant, since the initial heating phase of the droplet leads to time-varying droplet surface conditions. For the calculation of the modified mass ratio φ^*, the value of $B_{M,\mathrm{ref}}$ that corresponds to the wet-bulb conditions is used. In contrast, the liquid density is evaluated using the initial droplet temperature, as φ represents the initial ratio of liquid to gaseous mass in the computational cell.

Convective Environments

Finally, the effect of a relative velocity between the droplet and the gas on the error in the transient case will be investigated. Again, the relation for the steady-state evaporation rate that incorporates the effect of convection, Eq. (5.16), can be transferred to an error relation for the evaporation time, finally leading to

$$\epsilon_\tau = \frac{2\pi}{3} \left(\frac{\mathrm{Pe}_{\Delta x}}{\mathrm{Sh}^*} \right)^{-1} \left(\frac{\Delta x}{d_0} \right)^{-1} . \tag{5.24}$$

Details on the derivation can be found in Appendix E.4.4. The extension of Eq. (5.23) to convective environments is then given by

$$\epsilon_\tau = \min \Bigg[\underbrace{\left(\frac{\Delta x}{d_0} \right)^{-1}}_{\text{Eq. (5.20)}}, \underbrace{0.6\varphi^*}_{\text{Eq. (5.22)}}, \underbrace{\frac{2\pi}{3} \left(\frac{\mathrm{Pe}_{\Delta x}}{\mathrm{Sh}^*} \right)^{-1} \left(\frac{\Delta x}{d_0} \right)^{-1}}_{\text{Eq. (5.24)}} \Bigg]. \tag{5.25}$$

The relation is validated by numerical calculations using the same setup as for the corresponding steady-state analysis. Gas and droplet properties are selected randomly within the same ranges as reported previously, and the ratio of cell size to initial droplet diameter is varied within $1 \leq \Delta x/d_0 \leq 100$. For the case of pure mass transfer with constant density, the mass transfer number of the reference solution lies within $B_{M,\mathrm{ref}} \in [10^{-2}, 10^2]$, and the resulting modified mass ratio and cell Péclet number are within $\varphi^* \in [10^{-5}, 10^2]$ and $\mathrm{Pe}_{\Delta x} \in [10^{-3}, 10^6]$, respectively. The calculations including the effect of heat transfer show a significantly lower range of mass transfer numbers, as discussed earlier, resulting in $\varphi^* \in [10^{-3}, 10^3]$. The cell Péclet numbers are similar to those obtained from calculations based on pure mass transfer. Figure 5.8(a) compares the calculated errors resulting from the pure mass transfer problem with the predicted errors based on Eq. (5.25) and shows good agreement. As before, color is used to highlight the usage of the individual error relations that comprise Eq. (5.25). It can be seen that Eq. (5.20), which is based on the quasi-steady assumption, is again prone to somewhat larger errors, whereas

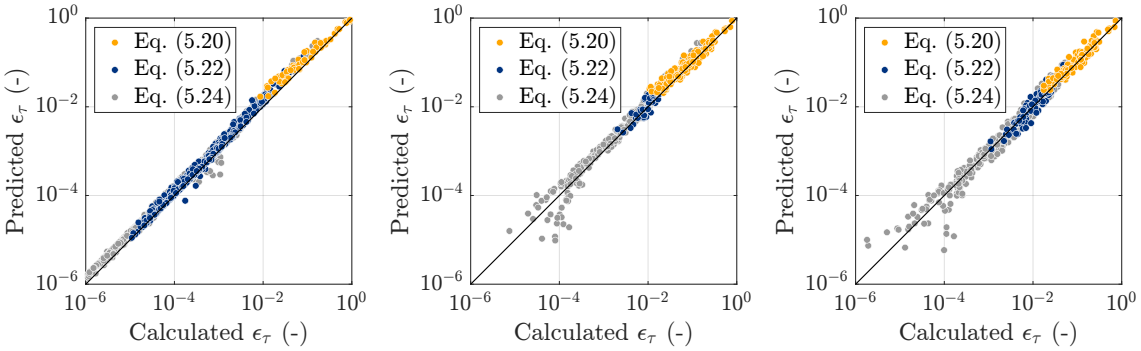

(a) Pure mass transfer with constant density.

(b) Heat and mass transfer, ethanol droplet.

(c) Heat and mass transfer, *n*-heptane droplet.

Figure 5.8: Comparison of predicted and calculated errors of the evaporation time in convective environments. The calculated error is obtained from the numerical solution of the three-dimensional governing equations. In (a) only the effect of mass transfer with constant density is considered, while in (b) and (c) heat and mass transfer are taken into account, where the ambient gas is a mixture of nitrogen and fuel with fuel species (b) ethanol and (c) *n*-heptane. The predicted error is obtained from Eq. (5.25), where the color indicates which of the three relations, Eq. (5.20), Eq. (5.22), or Eq. (5.24), determines the error.

Eq. (5.22), which corresponds to the assumption of a closed cell, is associated with medium to small errors. The relation for convective environments, Eq. (5.24), can dominate the error estimate throughout the entire error range, as was discussed earlier. Finally, Figs. 5.8(b) and 5.8(c) compare the error relation with errors that are obtained from calculations involving heat transfer and using fuel species ethanol and *n*-heptane. Again, the trends are essentially the same as for the case of pure mass transfer, confirming that Eq. (5.25) also holds for the case of combined heat and mass transfer with variable thermophysical properties.

Discussion

Following the same procedure as established for steady-state conditions, the error has been investigated for the case of transient droplet evaporation. Again, the analysis has been started with the simplest case of pure mass transfer and constant density, with other effects such as heat transfer and convective environments added step by step. While for steady-state calculations only the length ratio $\Delta x/d$ and the cell Péclet number $\mathrm{Pe}_{\Delta x}$ determine the error, now the mass ratio φ and the reference mass transfer number $B_{M,\mathrm{ref}}$ gain importance. Their influence can be combined by introducing the modified mass ratio φ^*. This is consistent with the dimensional analysis, which, however, could not predict the specific form of φ^*. The error of the evaporation time is therefore a function of the three parameters $\Delta x/d_0$, φ^* and $\mathrm{Pe}_{\Delta x}$, and obeys the functional relationship given by Eq. (5.25).

In practical applications, the cell size is often of the order of $\Delta x/d_0 \lesssim 20$.

Assuming a density ratio of $\rho_l/\rho_\infty \approx 1000$ and a mass transfer number of $B_{M,\mathrm{ref}} \approx 1$ in combination with $\mathrm{Pe}_{\Delta x} \lesssim 4$, the error relation given by Eq. (5.25) reduces to Eq. (5.20). This provides a very simple estimate for the error, in which the error is inversely proportional to the ratio of cell size to initial droplet diameter. According to that, a ratio of $\Delta x/d_0 = 10$ corresponds to an error of 10 %, and doubling the cell size halves the error. Since errors in the range of 5 % to 10 % are often within the accuracy of the evaporation model and hence acceptable, this study recommends cell sizes of the order of 10 to 20 droplet diameters for practical calculations. This is in agreement with the criterion proposed by Luo *et al.* [121], although the present study tends to require slightly larger cell sizes. Note that this requirement can often not be realized due to the resolution requirements of turbulence and chemistry, which require smaller cell sizes. Also note that the requirements on the cell size can be relaxed if there are other effects such as a relative velocity between the gas and the droplet, as discussed before, or if the source term is distributed to multiple grid nodes (see Appendix E.3). A universally valid estimate of the error for all cell sizes, droplet and gas conditions is given only by the complete relationships as derived within this study.

5.3 Grid Dependence of Mixture Fraction Variance

5.3.1 Outline of the Analysis

After having discussed the dependence of the evaporation process on the computational cell size, the focus is now on the effects in the gas phase resulting from the use of the PSI-cell model. Here, the distribution of the source terms to the computational cell, as imposed by the PSI-cell model, implies infinitely fast mixing in the surroundings of the droplets and eliminates any variance on subgrid level. This lack of resolution is then expected to reduce the variance of the resolved fields, as illustrated in Fig. 5.1.

In a first step, the analytical solution of a single droplet in an infinite and quiescent environment is used to quantify the characteristic mixing time scale in the vicinity of the droplet, which can then provide insight into the validity of the assumption of infinitely fast mixing within the computational cell. Afterwards, a numerical solution of the gas-phase equations is employed in order to discuss the dependence of the resolved mixture fraction variance on the cell size, where the analytical solution serves as a reference solution.

5.3.2 Assessment of Infinitely Fast Mixing Within the Cell

Immediately at the droplet surface, the gradients and thus the diffusive transport are large. This suggests that the characteristic mixing time near the droplet surface is small, and infinitely fast mixing can be assumed. This hypothesis will be examined in the following in more detail on the basis of the analytical solution of a single droplet in an infinite and quiescent environment, as was derived in Sec. 3.2.2.

In the absence of chemical reactions, mixture fraction as defined in Sec. 4.1.2 is identical to the fuel mass fraction. Assuming quasi-steady processes and constant properties (specifically the product $\rho\mathcal{D}_F$), the fuel mass fraction field around the droplet is given by Eq. (3.35), which is expressed here in terms of mixture fraction,

$$f(r) = 1 - (1 - f_\infty)\exp\left(-\frac{\dot{m}}{4\pi r\rho\mathcal{D}_F}\right). \tag{5.26}$$

In the spherically symmetric coordinate system, the scalar dissipation rate is expressed as $\chi = 2\mathcal{D}_F(\mathrm{d}f/\mathrm{d}r)^2$, and given based on Eq. (5.26) in analytical form by

$$\chi(r) = 2\mathcal{D}_F(1 - f_\infty)^2\left(\frac{\dot{m}}{4\pi\rho\mathcal{D}_F}\right)^2\frac{1}{r^4}\exp\left(-\frac{\dot{m}}{2\pi r\rho\mathcal{D}_F}\right). \tag{5.27}$$

Since the scalar dissipation rate decreases with r^{-4}, mixing effects are expected to be limited to the immediate vicinity of the droplet. The mixing time is defined as $\tau_{\mathrm{mix}} = f_V/\langle\chi\rangle$ (cf. Eq. (4.46)), where $f_V = \langle f^2\rangle - \langle f\rangle^2$ denotes the mixture fraction variance. Averages, denoted by the angle brackets, are calculated by integrating the corresponding expressions in the spherically symmetric coordinate system from the droplet surface, denoted as r_s, to a radius R in the surroundings of the droplet, which is associated here with the computational cell size, $R/r_s \sim \Delta x/d$. The integration must be performed numerically and therefore does not provide a closed-form expression for the mixing time. However, by considering the limiting case of small mass transfer numbers, thus neglecting the Stefan flow, an analytical solution of the (simplified) integral equations can be found, where the expression for the variance is given by

$$\frac{f_V}{(f_s - f_\infty)^2} = \frac{3}{4}\frac{(R/r_s - 1)^2}{((R/r_s)^2 + R/r_s + 1)^2}, \tag{5.28}$$

and the expression for the spatially averaged and normalized scalar dissipation rate takes the form

$$\frac{\langle\chi\rangle\tau_\mathcal{D}}{(f_s - f_\infty)^2} = \frac{6}{(R/r_s)^3 + (R/r_s)^2 + (R/r_s)}, \tag{5.29}$$

with the diffusive time scale defined as $\tau_\mathcal{D} = r_s^2/\mathcal{D}$. The numerical calculations along with the analytical solution (assuming small mass transfer numbers) are shown in

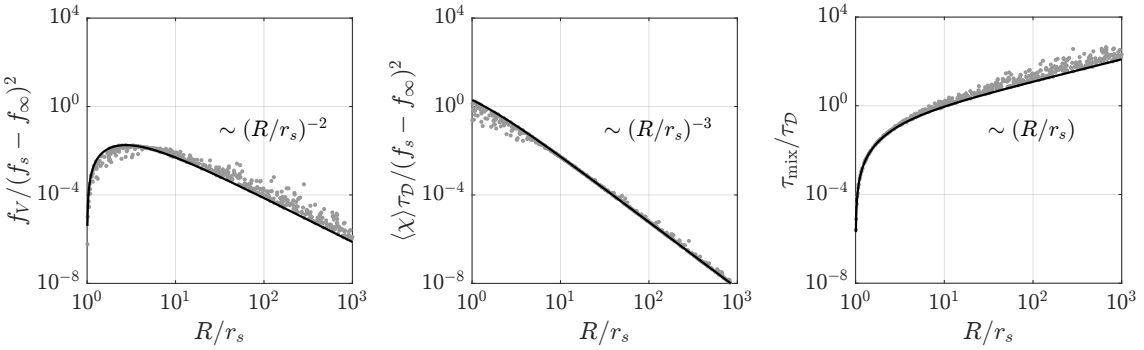

(a) Variance. **(b)** Scalar dissipation rate. **(c)** Mixing time.

Figure 5.9: Analytical solution for mixture fraction variance, mean scalar dissipation rate and mixing time defined as $\tau_{\mathrm{mix}} = f_V/\langle\chi\rangle$ in a spherical region around the droplet with $r \in [r_s, R]$. Gray dots denote the results obtained from a numerical solution of the integrals using various gas and droplet properties, while the black line corresponds to the approximation that assumes small mass transfer numbers and neglects the Stefan flow (Eqs. (5.28) and (5.29)). The diffusive time scale used for normalization is given by $\tau_\mathcal{D} = r_s^2/\mathcal{D}_F$.

Fig. 5.9, where the mixture fraction variance, mean scalar dissipation rate and mixing time are plotted versus the normalized radius R/r_s. It can be seen that the numerical solution of the integral equations agrees quite well with the simplified analytical solution. As the domain size is increased, the variance first increases due to the approximately linear decay of the mixture fraction profile near the droplet surface, and then decreases as the mixture fraction profile becomes flatter with increasing distance from the droplet surface, with the maximum value occurring at about $R/r_s \approx 2.7$. In contrast, the mean scalar dissipation rate decreases continuously due to the large gradient at the droplet surface, while the mixing time increases continuously. For sufficiently large R/r_s, the normalized quantities exhibit an asymptotic region, where the variance decays with $(R/r_s)^{-2}$ (cf. Eq. (5.28)) and the average dissipation rate with $(R/r_s)^{-3}$. The asymptotic behavior of the normalized mixing time is then given by $\tau_{\mathrm{mix}}/\tau_\mathcal{D} \sim R/r_s$. This relation is valid for $R/r_s \gtrsim 10$, and can be expressed in dimensional form as

$$\tau_{\mathrm{mix}} \sim \frac{r_s R}{\mathcal{D}_F}. \tag{5.30}$$

The result is remarkable, since it represents the geometric mean of the time scales of the smallest and the largest scales, which are given by $\tau_{\mathcal{D},r_s} = r_s^2/\mathcal{D}_F$ and $\tau_{\mathcal{D},R} = R^2/\mathcal{D}_F$, respectively. Accordingly, the mixing time is a function of both, the droplet size and the domain size, and increases linearly with both parameters. The dependence on the droplet size can be explained by the fact that smaller droplets produce larger gradients and thus enhance the diffusive transport in the vicinity of the droplet, while the domain size is an indicator for the time required to transport the vapor to the surroundings of the droplet. The proportionality constant corre-

sponding to Eq. (5.30) is determined analytically from Eqs. (5.28) and (5.29) to be 1/8 for the pure diffusion case, whereas it takes values between 0.1 and 1 if the Stefan flow is included.

In numerical simulations employing the PSI-cell model, the size of the spherical domain, R, can be associated with the computational cell size, Δx. To assess the assumption of infinitely fast mixing within the computational cell, the derived mixing time is related to the time scales found in CFD of dilute sprays. By comparing the time scale given by Eq. (5.30) with the time scale of the resolved scales, $\tau_{\mathcal{D},R} = R^2/\mathcal{D}_F$ (considering only diffusion), the ratio of time scales can be expressed as

$$\frac{\tau_{\mathrm{mix}}}{\tau_{\mathcal{D},R}} \sim \left(\frac{R}{r_s}\right)^{-1} \sim \left(\frac{\Delta x}{d}\right)^{-1}. \tag{5.31}$$

Since $\Delta x/d > 1$, the ratio is less than one, indicating that the mixing of the evaporated fuel vapor within the surroundings of the droplet is faster than the diffusion processes on the resolved scales. This behavior is induced by the large gradients at the droplet surface and shows that infinitely fast mixing within the computational cell can be a valid assumption. In particular in CP-DNS, where all scales are resolved except for the droplets, the PSI-cell model is therefore a good approximation. With increasing cell size, as found in LES, the ratio of time scales further decreases, so that the mixing near the droplets generally becomes less significant with respect to the resolved scales, thus enhancing the assumption of infinitely fast mixing. However, other effects may become important in that case, such as turbulence-chemistry interactions, which usually exhibit much smaller time scales as associated with the resolved scales. These effects are not captured by the analysis, and therefore the present findings should be viewed with caution if applied to the LES of turbulent reacting flows.

5.3.3 Effect of the Cell Size on the Resolved Variance

Computational Setup

In order to incorporate discretization effects into the analysis, a numerical solution of the gas-phase equations is employed, where the focus is now on the variance of the resolved mixture fraction field. Although the evaporation process and thus the generated variance is generally a function of time, stationary conditions are assumed to simplify the problem. This is justified, since the large gradients at the droplet surface lead to the establishment of quasi-steady conditions after a short time. Furthermore, pure mass transfer with the assumption of small mass transfer numbers is assumed, following the preceding investigations. The variance

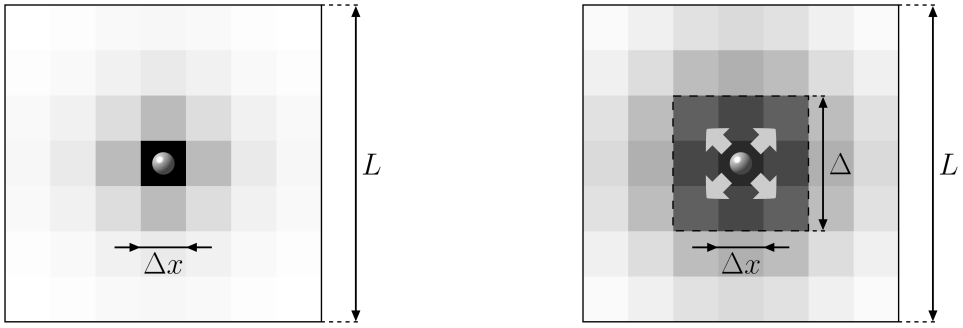

(a) Source terms are transferred entirely to the cell that contains the droplet.

(b) Source terms are distributed homogeneously to multiple cells within a cube of length Δ.

Figure 5.10: Computational setup for the numerical analysis of the grid dependence of the mixture fraction variance.

is calculated within a cubic domain of length L that is discretized by computational cells of size Δx with the droplet placed in the center of the domain, as shown in Fig. 5.10. The domain length L represents the region of influence of the droplet that is associated with the calculation of the variance. In systems involving multiple droplets, it is convenient to use the nominal distance between the droplets and set $L = \Delta_L$, which then allows to break down a system involving multiple droplets to the single-droplet problem. It can be shown that the single-droplet system reflects the variance of the multiple-droplet system, provided that the droplet distribution is homogeneous and the local mean values associated with the characteristic volume of each droplet do not differ significantly. Periodic boundary conditions are applied to eliminate the effect of numerical boundary conditions, which is particularly crucial for a coarse discretization, and to mimic the possible existence of further droplets. To allow for the establishment of a stationary state, the evaporated mass must be removed from the system, which is achieved here by subtracting the volume-averaged source term in each cell. Note that this does not affect the gradients and thus the calculation of the variance, but only the mean value, which now remains constant and is given by the initial conditions, which are equal to the prescribed far-field conditions. The evaporation rate is calculated using the mean fuel mass fraction in the domain, which eliminates the error that would result if the evaporation rate is evaluated based on the local cell values. Source terms are either transferred to the cell that contains the droplet (standard PSI-cell model, cf. Fig. 5.10(a)), or distributed to multiple cells within a cube of length Δ surrounding the droplet, as illustrated in Fig. 5.10(b).

Changing the Computational Cell Size

The most obvious approach to discuss the grid dependence of the mixture fraction variance is to change the computational cell size directly, while the evaporation source terms are transferred entirely to the cell that contains the droplet, as visualized in Fig. 5.10(a). An increase of the cell size thereby implies that the source terms are distributed among a larger volume and thus a reduction of the variance is to be expected, as sketched in Fig. 5.1. To verify this hypothesis, a set of calculations is performed with varying gas and droplet properties, and using different domain sizes and cell sizes. The results are shown in Fig. 5.11. In Fig. 5.11(a) the normalized variance is plotted as a function of the domain size normalized by the droplet diameter. The analytical solution given by Eq. (5.28), which is evaluated here using an equivalent radius corresponding to a sphere of equal volume, $R = (\frac{3}{4\pi})^{1/3}L$, is also shown for comparison. It can be seen that the normalized variance is mainly a function of the normalized domain size and decays proportional to $(L/d)^{-2}$. Contrary to expectations, it does not show a significant dependence on other parameters, in particular on the computational cell size. Good agreement between the numerical results and the analytical solution is obtained in the asymptotic region ($L/d \gtrsim 10$), demonstrating the capability of the PSI-cell model to predict the correct variance of an isolated droplet. For smaller domain sizes there are different trends, where the numerical results continue to show the asymptotic behavior, whereas the analytical solution predicts a decrease of the variance when approaching the limit $L/d \to 1$. Note that this trend is also obtained if the analytical solution is mapped to a Cartesian domain instead of using a sphere of equal volume.

In order to quantify the (weak) dependence on the computational cell size, the normalized variance is multiplied by $(L/d)^{-2}$ and plotted versus $\Delta x/L$ (using $\Delta x/d$ does not lead to a clear correlation). The corresponding plot is shown in Fig. 5.11(b), which indicates that the variance generally increases with an increasing cell size, but the changes remain in a relatively small range, thus making the variance almost independent of the cell size. This result contradicts the initially formulated hypothesis that the variance decreases with increasing cell size, and indicates that the variance is accurately reproduced regardless of the computational cell size, provided that the characteristic volume around the droplet is resolved by the numerical grid (i.e., $\Delta x < L$). An explanation is that as the cell size increases, the local cell values become smaller since the source term is transferred to a larger volume, but at the same time the number of cells decreases so that each cell is weighted more strongly when calculating the variance in the domain. The reason why these effects cancel each other out is due to the fact that the mass flow, which determines the gradients, is imposed by the given source term and is thus independent of the cell size.

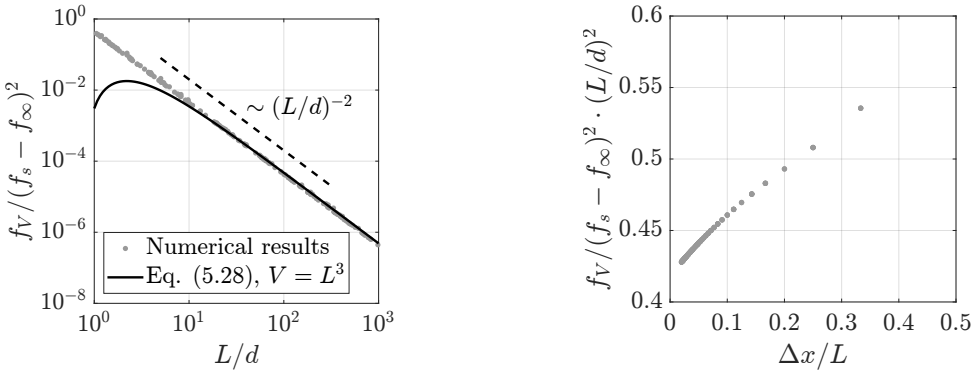

(a) Normalized variance versus normalized domain size L/d.

(b) Normalized variance, multiplied by $(L/d)^2$, versus normalized cell size $\Delta x/L = 1/N$.

Figure 5.11: Effect of cell size on mixture fraction variance. The variance is calculated in a cubic domain of length L, as illustrated in Fig. 5.10(a). Calculations are performed for a set of varying gas and droplet properties with $\rho \in [0.1\,\mathrm{kg/m^3}, 10\,\mathrm{kg/m^3}]$, $\mathcal{D}_F \in [10^{-6}\mathrm{m^2/s}, 10^{-1}\mathrm{m^2/s}]$, $Y_{F,\infty} \in [0, 0.5]$, $d \in [1\,\mu\mathrm{m}, 1\,\mathrm{cm}]$, $Y_{F,s} \in [Y_{F,\infty}, 1]$ as well as for different domain sizes and cell sizes. Pure mass transfer with the assumption of small mass transfer numbers (no Stefan flow) is considered.

Changing the Source Term Distribution

The previous section has demonstrated that there are two counteracting mechanisms that affect the variance when the cell size is increased. In order to examine the effect of distributing the source terms to a larger volume separately from other effects (such as discretization effects), the source terms are now distributed homogeneously to multiple cells within a cube of length Δ surrounding the droplet, as illustrated in Fig. 5.10(b). The length of the cube is determined by $\Delta = (1 + 2\delta)\Delta x$, where $\delta = 0, 1, 2, ...$ indicates the number of cell layers around the cell that contains the droplet. This approach is also expected to more accurately reflect the effects associated with the distribution of the source terms among the stochastic particles, where there is no such discretization effect. Again, a set of calculations is performed with varying gas and droplet properties, and using different domain sizes, cell sizes and source term distributions indicated by the parameter Δ. As can be seen from Fig. 5.12(a), the normalized variance not only decreases proportional to $(L/d)^{-2}$, but also with an increasing value for Δ/L, where again the cell size has no significant effect on the variance. To eliminate the effect of the domain length and to focus on the dependence on the parameter Δ/L, Fig. 5.12(b) shows the normalized variance multiplied by $(L/d)^2$ and plotted versus Δ/L, revealing two branches with different trends. For the case where the source term is distributed only to the cell that contains the droplet ($\Delta = \Delta x$, blue dots in Fig. 5.12(b)), the variance increases slightly with increasing Δ, reflecting the results shown in Fig. 5.11(b). In contrast, if the source term is distributed to multiple cells ($\Delta > \Delta x$, gray dots in Fig. 5.12(b)),

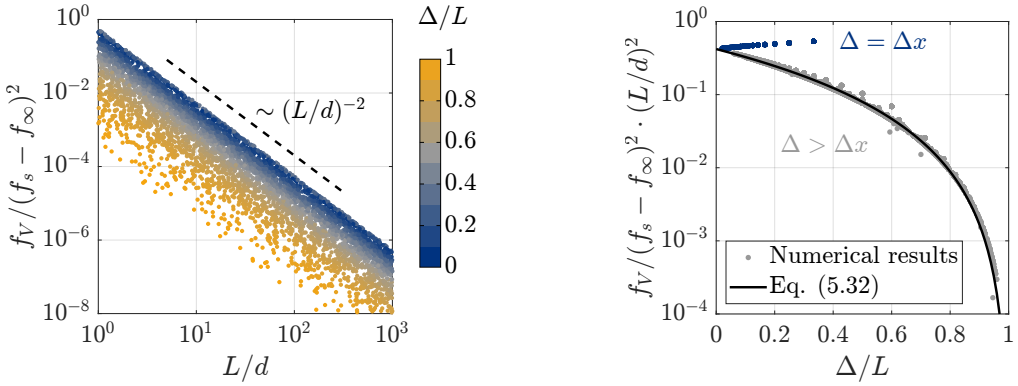

(a) Normalized variance versus normalized domain size L/d and colored by Δ/L.

(b) Normalized variance, multiplied by $(L/d)^2$, versus Δ/L.

Figure 5.12: Effect of source term distribution on mixture fraction variance. The variance is calculated in a cubic domain of length L, and source terms are distributed homogeneously to multiple cells within a cube of length Δ, as illustrated in Fig. 5.10(b). Calculations are performed for a set of varying gas and droplet properties (see caption of Fig. 5.11) as well as different domain sizes, cell sizes and source term distributions, considering pure mass transfer with the assumption of small mass transfer numbers (no Stefan flow).

an exponential decay of the variance with increasing Δ/L is observed, as originally assumed and illustrated in Fig. 5.1. A simple approximation can be found to describe the effect of Δ/L on the variance, which is given by

$$\frac{f_V}{(f_s - f_\infty)^2} = 0.42\left(1 - \frac{\Delta}{L}\right)^{2.4}\left(\frac{L}{d}\right)^{-2}, \tag{5.32}$$

and shown by the black line in Fig. 5.12(b). The limit $\Delta \to 0$ in Eq. (5.32) represents the reference solution that is obtained with sufficiently small $\Delta = \Delta x$, which also reproduces the analytical solution of an isolated droplet for $L/d \gtrsim 10$ (cf. Fig. 5.11(a)). Using this reference solution and keeping all parameters constant except for Δ/L, the normalized and scaled variance has decreased to 60 % of the reference value for $\Delta/L = 0.2$, and only 30 % of the variance is captured for $\Delta/L = 0.4$.

As mentioned earlier, the results can be readily applied to systems involving multiple droplets if the domain length is replaced by the nominal distance between the droplets, $L = \Delta_L$, as well as to Lagrangian FDF methods, where source terms are transferred to the gas-phase particles and thus Δ is associated with the volume represented by the particles, $\Delta_L = (V^{sp})^{1/3}$. Equation (5.32) then provides a simple estimate of the loss in the resolved variance for a given Δ/Δ_L and Δ_L/d.

5.4 Summary and Discussion

The purpose of the present chapter was to examine the grid dependence induced by the standard PSI-cell model when using an Euler-Lagrange approach in the context of dilute spray evaporation and combustion. Based on an isolated droplet in an infinite environment, several criteria were derived to quantify the numerical error resulting from the use of the PSI-cell model, thus providing guidelines for performing grid-independent CFD simulations of dilute sprays. The analysis was split into two parts, first examining the grid-dependence of the evaporation process of the liquid droplets (Sec. 5.2), and followed by a discussion of the effect of the cell size on the resolution of the gas-phase fields in the vicinity of the droplets, characterized by the mixture fraction variance (Sec. 5.3).

Focusing on the error of the evaporation rate and time of the liquid droplets, closed-form expressions were derived based on analytical solutions of simplified setups, whose universal validity has been subsequently validated. The main outcomes are as follows:

- The error of the evaporation rate and time is generally a function of four characteristic parameters: the length ratio $\Delta x/d_0$, the mass ratio φ representing the initial ratio of liquid to gaseous mass in the computational cell, the reference mass transfer number $B_{M,\mathrm{ref}}$, and the cell Péclet number $\mathrm{Pe}_{\Delta x}$. Further, it was shown that the effect of $B_{M,\mathrm{ref}}$ can be incorporated into a modified mass ratio φ^*, reducing the number of characteristic parameters to three.
- Assuming steady-state conditions, the error of the evaporation rate depends on only two parameters, $\Delta x/d$ and $\mathrm{Pe}_{\Delta x}$, and follows the relation given by Eq. (5.17).
- In the transient case, the error of the evaporation time is a function of all three parameters $\Delta x/d_0$, φ^* and $\mathrm{Pe}_{\Delta x}$, and can be described by Eq. (5.25).
- In the practically relevant case ($\Delta x/d_0 \lesssim 20$) and assuming a small relative velocity ($\mathrm{Pe}_{\Delta x} \lesssim 4$), the relation for the error of the evaporation time, Eq. (5.25), reduces to the simple relation $\epsilon_\tau = (\Delta x/d_0)^{-1}$, which states that the error is inversely proportional to the ratio of cell size to initial droplet diameter.

The error due to lack of resolution of the gaseous fields in the vicinity of the droplet was analyzed assuming steady-state conditions and pure mass transfer. First, the assumption of infinitely fast mixing within the computational cell as induced by the PSI-cell model was examined, followed by an investigation of the effect of the cell size on the resolved mixture fraction variance. The results can be summarized as follows:

- The characteristic mixing time near the droplet is fast compared to the resolved scales of the Eulerian field, justifying the use of the PSI-cell model, which implies infinitely fast mixing within the computational cell.
- The variance predicted by the PSI-cell model agrees well with the analytical solution for sufficiently large domain sizes $L/d \gtrsim 10$, and decays proportional to $(L/d)^{-2}$. For $L/d \lesssim 10$, the PSI-cell model overestimates the variance.
- The cell size was found to have no significant effect on the resolved variance, as the effects of distributing the source term to a larger volume and numerical discretization cancel each other out. Accordingly, the variance is accurately reproduced regardless of the computational cell size, provided that the characteristic volume of each droplet is resolved by the numerical grid.
- By distributing the source term to a given gas-phase volume larger than the cell size, the variance decreases exponentially and can be approximated by Eq. (5.32).

To conclude, the results of the analysis state that in order to minimize both the error of the evaporation rate and the error of the scalar variance, the cell size should be as large as possible but at the same time ensure that the inter-droplet space is still resolved by the numerical grid. However, it is not always possible to meet both criteria, and often a compromise must be made. Depending on the type of simulation, the following guidelines for performing grid-independent simulations using the PSI-cell model can be formulated:

- **CP-DNS:** Here, the largest possible cell size is usually determined by the resolution requirements of turbulence and chemistry, so that the error of the evaporation rate cannot be completely avoided. The derived error relations then allow for an estimate of the expected error prior to the simulation. The scalar variance around the droplets is reproduced by the PSI-cell model regardless of the cell size, provided that the inter-droplet space is resolved ($\Delta x < \Delta_L$), albeit overestimated for $\Delta_L/d \lesssim 10$.
- **LES/RANS:** These kind of simulations are characterized by larger cell sizes, so that the error of the evaporation rate is often not a problem. The inter-droplet space is usually not resolved by the numerical grid ($\Delta x > \Delta_L$), meaning that the variance of the individual droplets is not taken into account. Equation (5.32) with $\Delta = 0$ and $L = \Delta_L$ may help to assess the importance of the variance resulting from the individual droplets in order to decide whether modeling is required or not.
- **Lagrangian FDF methods:** Here, the variance resulting from the evaporating droplets is determined by the way how source terms are transferred to the notional particles and by the volume of each gas-phase particle. If the selected stochastic

particles receive source terms from only one droplet each (which is approximately fulfilled by the one-to-one coupling technique), Eq. (5.32) with $\Delta = (V^{sp})^{1/3}$ and $L = \Delta_L$ can be used to provide a simple estimate of the loss of variance compared to the reference value ($\Delta = 0$).

The effectiveness of the derived relations in practical simulations involving multiple droplets and including the effects of turbulence and chemistry is demonstrated in Appendix E.5 by comparing *a priori* estimates with *a posteriori* errors from Euler-Lagrange simulations, and the usage of the relations will also be addressed in the following chapters.

Chapter 6

A Comparative Study of Two-Phase Coupling Models

The present chapter provides a detailed a priori analysis of various two-phase coupling models in the context of dense and sparse particle methods based on the work published by Sontheimer et al. [198]. All required input data, including the evaporation rate, are extracted from the CP-DNS, with focus on the distribution of the source terms among the stochastic particles. After discussing the strengths and weaknesses of the different models, potential improvements for the sparse-Lagrangian two-phase coupling are presented by combining concepts of the SAT model with the one-to-one coupling technique. This eventually leads to the development of a time delay model, in which the source terms are transferred partially to the gas-phase particles using a characteristic mixing time.

6.1 Computational Setup

To assess the two-phase coupling models presented in Sec. 4.5, an idealized regime is considered where the entire spray has been atomized and the liquid phase can be represented by an ensemble of spherical droplets (cf. Fig. 2.2). The droplet distribution is assumed to be homogeneous as is the turbulence such that statistically homogeneous and isotropic turbulence can be used. This allows to examine the complex spray combustion phenomena by means of spatially averaged statistics, where the generation and destruction of variance is determined solely by the evaporation process and scalar dissipation, respectively (cf. Appendix B). The various two-phase coupling models are examined by using the *a priori* modeling strategy introduced in Sec. 4.7.3, where a CP-DNS provides LES-like input data to the Lagrangian FDF method.

The computational domain consists of a cubic box of length $L = 12\,\mathrm{mm}$ with

periodic boundary conditions. The initial gas is composed of nitrogen and oxygen with mass fractions $Y_{N_2} = 0.767$ and $Y_{O_2} = 0.233$ similar to those of air. The initial temperature is set to $T_0 = 1500\,\mathrm{K}$ to allow for spontaneous ignition once the evaporation and mixing process has started, and the initial pressure is $p_0 = 1\,\mathrm{atm}$. The chemistry is modeled using a global single-step reaction for ethanol combustion in air [228]. The velocity field is initialized with homogeneous isotropic turbulence, which was generated with a preceding non-reacting and incompressible simulation without droplets using the linear forcing method described in Carroll and Blanquart [21]. The corresponding Taylor Reynolds number is $\mathrm{Re}_\lambda = 40$ and the eddy turnover time has a value of $\tau_0 = 0.16\,\mathrm{ms}$. The chosen Reynolds number corresponds to fully developed turbulence and ensures that the largest and smallest relevant scales of fluid motion are well resolved on the computational mesh (more details will be given below). The droplets are composed of liquid ethanol and are distributed randomly in the domain with an initial diameter of $d_0 = 20\,\mu\mathrm{m}$ and an initial temperature of $T_{d,0} = 300\,\mathrm{K}$. The initial velocity of the droplets is equal to the local gas velocity, and the Stokes number is $\mathrm{St} = (\rho_l d_0^2)/(18\mu)/\tau_0 \approx 2.2$. Three droplet loading ratios are considered, covering dilute sprays as well as moderately dense sprays. The corresponding parameters are reported in Tab. 6.1.

For the CP-DNS, the computational domain is discretized by $N_x \times N_y \times N_z = 256 \times 256 \times 256 \approx 16.8\,\mathrm{M}$ uniform grid cells, resulting in a cell size of $\Delta x \approx 47\,\mu\mathrm{m}$. This grid resolution ensures sufficient resolution of the Kolmogorov length scale ($\Delta x/\eta \approx 1$), and resolves the inter-droplet space by at least five grid cells with a ratio of cell size to initial droplet diameter of $\Delta x/d_0 \approx 2.3$. The accurate resolution of the near-droplet fields conflicts with the requirement for a grid-independent estimation of the evaporation rate, as discussed in Ch. 5. According to the error relation given by Eq. (5.25), the cell size of the CP-DNS would result in errors of the order of 40 %, which is not justifiable. For this reason, appropriate far-field conditions are estimated by averaging the gas state within the characteristic volume of each droplet ($V = \Delta_L^3$), which largely eliminates the dependence of the evaporation rate on the computational cell size. Note that the evaporation source terms are still transferred to the cell that contains the droplet to capture the large gradients at the positions of the droplets. As demonstrated in Sec. 5.3, this will accurately reproduce the variance that is generated by the evaporation of each droplet (since $\Delta_L/\Delta x > 1$ and $\Delta_L/d_0 > 10$). LES-like input data required for the Lagrangian FDF method are obtained by post-filtering the CP-DNS data using an LES cell size of $\Delta_{\mathrm{LES}} = 8\Delta x$. The turbulent diffusivity is calculated from Eq. (4.20) assuming a turbulent Schmidt number of $\mathrm{Sc}_t = 0.4$, and the turbulent viscosity is obtained from the Smagorinsky model with $C_s = 0.1$. The different two-phase coupling

Table 6.1: Droplet loading ratios for the simulations of spray combustion in statistically homogeneous turbulence. The table lists the normalized nominal droplet distance Δ_L/d_0, the number of droplets N_d, the initial liquid volume fraction ϕ_d, the initial liquid-to-gas mass ratio $m_{l,0}/m_{g,0}$ and the global equivalence ratio Φ.

Case	Δ_L/d_0	N_d	ϕ_d	$m_{l,0}/m_{g,0}$	Φ
low	35	4913	$1.2 \cdot 10^{-5}$	0.04	0.4
mid	20	27 000	$6.5 \cdot 10^{-5}$	0.22	2.0
high	12	125 000	$3.0 \cdot 10^{-4}$	1.02	9.1

models presented in Secs. 4.5.2 and 4.5.3 are examined in the context of both dense and sparse particle methods. The dense particle simulations involve 20 particles per LES cell, giving a total of 655 360 stochastic particles, and the sparse particle simulations are performed with a particle number density of one particle per LES cell, resulting in 32 768 notional particles within the computational domain. To eliminate possible modeling errors associated with an evaluation of the evaporation rate based on the stochastic particle solution, the evaporation rate and the droplet heating term for the Lagrangian FDF method are extracted from the CP-DNS data. This allows for an unbiased comparison of the effects of the fuel droplets on the gas phase between the CP-DNS and the stochastic particle method.

The variance equation (see Appendix B for its derivation) reveals a strong interaction between mixing and evaporation, with the result that different two-phase coupling models may require different mixing models to yield the correct variance. The preferred approach for the analysis is to leave the mixing model unchanged and use the available conventional models that work well in single-phase flows, so that the performance of the Lagrangian FDF method is mainly determined by the two-phase coupling model. For the dense particle simulations, the continuous Curl model with a deterministic mixing extent is used (cf. Sec. 4.3.4), where the mixing time is given by Eq. (4.49) with $C_f = 0.1$. The sparse particle methods employ the MMC mixing model with the a-ISO mixing time scale using the model constants as reported in Sec. 4.4.3. A discussion of the mixing time modeling in spray flames will be given later in Sec. 6.2.3.

The MMC mixing model requires the specification of appropriate mixing parameters r_m and f_m, representing typical distances between the particles in physical and reference mixture fraction space, respectively. Due to the initial homogeneous mixture fraction field and the fact that different droplet loadings result in widely varying mixture fraction ranges, the isoscalar sliver relation (cf. Sec. 4.4.2) cannot be used for the present setup, and a different strategy is required. Here, the values for the mixing parameters are determined (iteratively) in such a way that the parameters match the real distances subsequently calculated from the simulation data.

Table 6.2: MMC parameters for the simulations of spray combustion in statistically homogeneous turbulence. The table lists values for the mixing parameters r_m and f_m as well as for the coupling parameters r_m^* and f_m^* required for the one-to-one coupling strategy based on the minimization of the effective square distance, Eq. (4.60).

Case	Mixing, Eq. (4.51)		Two-phase coupling, Eq. (4.60)	
	r_m (m)	f_m (-)	r_m^* (m)	f_m^* (-)
Low	$8.0 \cdot 10^{-4}$	$2.0 \cdot 10^{-4}$	$4.8 \cdot 10^{-4}$	$1.2 \cdot 10^{-4}$
Mid	$8.0 \cdot 10^{-4}$	$7.2 \cdot 10^{-4}$	$4.8 \cdot 10^{-4}$	$4.3 \cdot 10^{-4}$
High	$8.0 \cdot 10^{-4}$	$1.5 \cdot 10^{-3}$	$4.8 \cdot 10^{-4}$	$9.0 \cdot 10^{-4}$

Note that by changing the droplet loading, only the parameter f_m is changed, since the number of notional particles and thus the distances in physical space remain the same. The same procedure is used to find the values for the two-phase coupling parameters r_m^* and f_m^*, which are required for the one-to-one coupling strategy based on the minimization of the effective square distance between the fuel droplets and the stochastic particles, Eq. (4.60). The values found are reported in Tab. 6.2. The next chapter will provide details on how these parameters can be estimated prior to the simulation for practically relevant configurations with pre-evaporation.

The governing equations of the CP-DNS and the Lagrangian FDF are solved numerically using the OpenFOAM-based `mmcDropletDNSFoam` solver, as introduced in Sec. 4.7.3. To minimize the numerical dissipation, the solution of the Eulerian transport equations in the CP-DNS employs cubic interpolation schemes while using a TVD scheme for mixture fraction and species mass fractions to ensure boundedness, in combination with a second-order backward time discretization scheme (see Appendix D for details on the numerical schemes). Simulations are performed for two eddy turnover times, where the time step is adjusted dynamically to ensure a maximum Courant number of $\mathrm{CFL}_{\max} = 0.4$.

6.2 Analysis of the CP-DNS Data

6.2.1 Baseline Results

Fuel evaporates and mixes with the ambient gas, with auto-ignition of the mixture eventually leading to combustion in the gas phase, while turbulence decays over time. The amount of evaporated fuel and the combustion characteristics depend on the droplet loading, as illustrated in Fig. 6.1. With the lowest droplet loading (case *low*), mean mixture fraction values remain small and do not reach the stoichiometric value ($f_{\mathrm{st}} \approx 0.12$), and mainly isolated droplet burning with relatively low flame temperatures can be observed. For case *mid*, mixture fraction values are higher and close to the stoichiometric value, resulting in the highest temperatures. Due to the

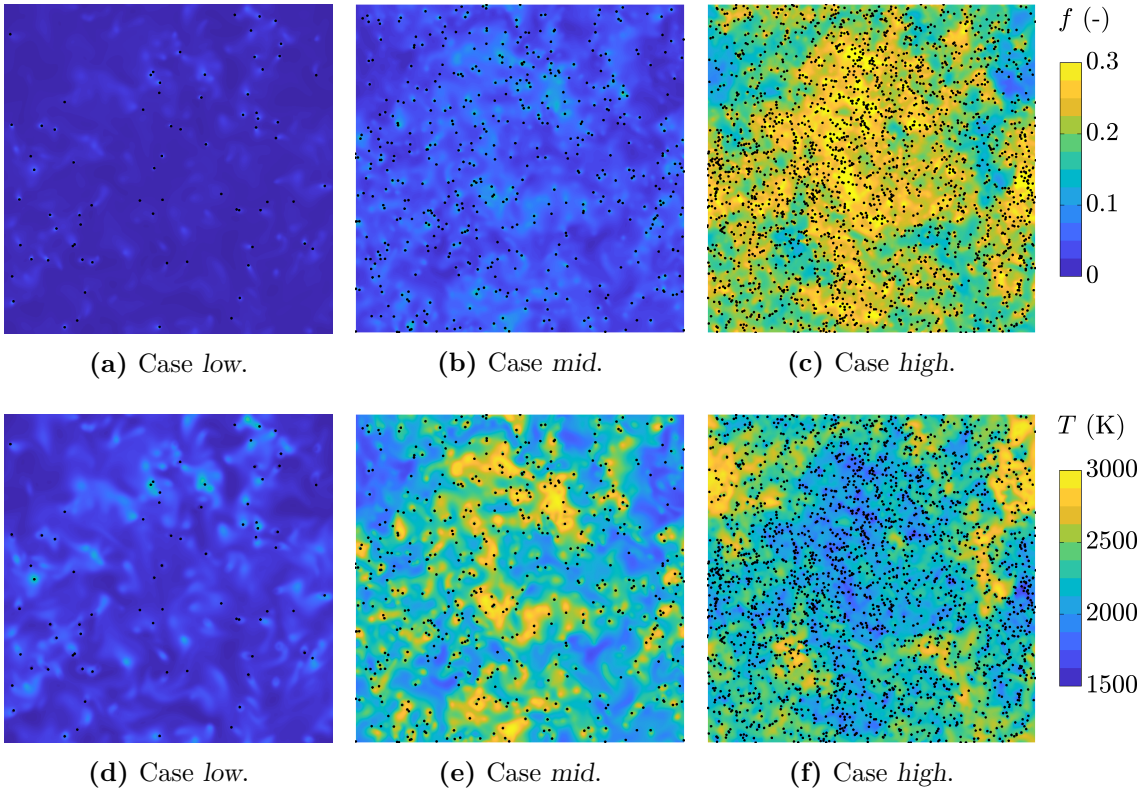

(a) Case *low*. **(b)** Case *mid*. **(c)** Case *high*.

(d) Case *low*. **(e)** Case *mid*. **(f)** Case *high*.

Figure 6.1: Contour plots (x-y slice for $z = L_z/2$) of mixture fraction (top) and temperature (bottom) of the CP-DNS at time $t = \tau_0$. The droplets (black dots) are magnified by a factor of 5.

reduced inter-droplet distance, isolated droplet burning as well as group combustion occurs. Finally, case *high* exhibits the highest mixture fraction values with both regions of stoichiometric and rich mixtures, where in the latter the excessive cooling of the droplets prevents combustion to take place.

The time evolution of the spatially averaged mixture fraction and temperature as well as the corresponding root-mean-square (rms) is plotted in Fig. 6.2 (solid lines). Both the mean and rms of the mixture fraction are proportional to the amount of evaporated fuel and increase once the evaporation process has started, but partially show a decline in the increase at later times as the fuel concentration in the domain rises. The mean temperature increases continuously for case *low* and *mid*, whereas for case *high* it increases strongly at the beginning but then declines after $t/\tau_0 \approx 0.6$. This is attributable to the fact that the high amount of evaporation leads to an early ignition of the gas mixture, followed by an intense combustion in which the available oxygen is almost completely consumed after a short time due to the high equivalence ratio (cf. Tab. 6.1). The rms of the temperature mainly follows the trends reported for the rms of the mixture fraction.

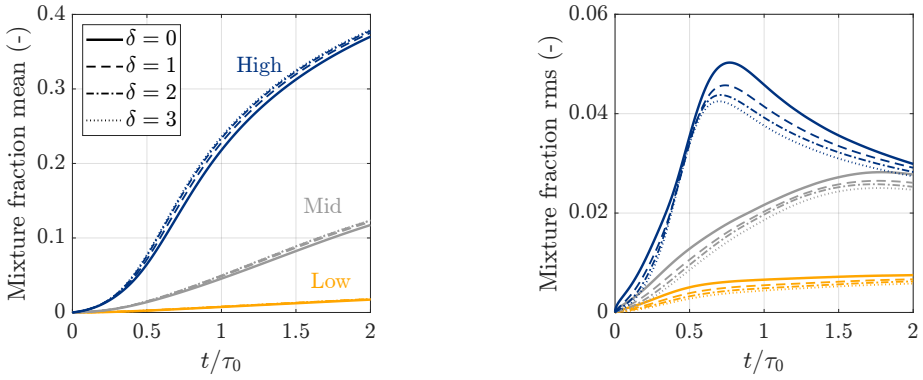

(a) Mixture fraction mean and rms.

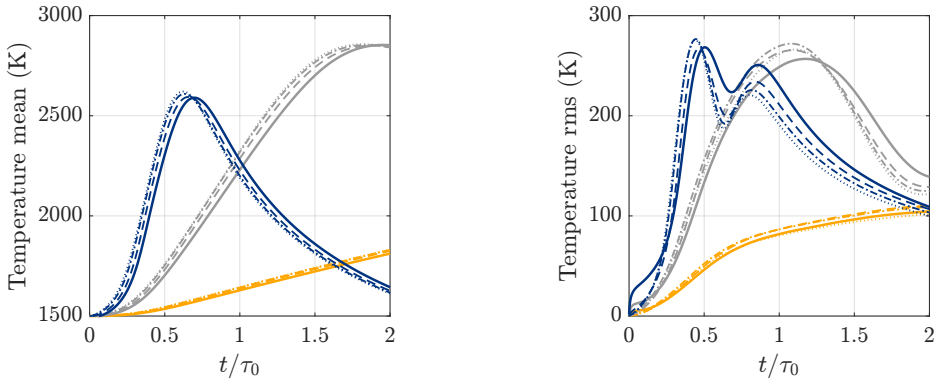

(b) Temperature mean and rms.

Figure 6.2: Temporal evolution of mean and rms of mixture fraction and temperature of the CP-DNS for different droplet loadings and source term distributions. The legend and color indication is the same in each subfigure. The reference case, where source terms are transferred entirely to the cell that contains the droplet, is given by $\delta = 0$.

6.2.2 Significance of the Near-Droplet Fields

To quantify the importance of the generation of variance by the individual droplets, additional simulations are performed in which the droplet source terms are gradually distributed to a larger volume of length $\Delta = (1 + 2\delta)\Delta x$ with parameter $\delta = 0, 1, 2, ...$, as explained in Sec. 5.3.3. This imposes artificial mixing in the surroundings of the droplets and shall emulate the effect of the source term distribution towards larger LES cells or stochastic particles in a sparse particle method. According to Eq. (5.32), which describes the variance of an individual droplet, a value of $\delta = 1$ reduces the variance to 58 % of the value associated with the reference solution ($\delta = 0$) for case *low*, to 35 % for case *mid*, and to 12 % for case *high*, while a value of $\delta = 3$ eliminates the variance of the individual droplets completely except for case *low*. Note that in simulations involving multiple droplets, the total variance does not drop to zero, as the inhomogeneous distribution of the evaporation source terms due to random droplet positions leads to the formation of large-scale structures, whose variance is not described by Eq. (5.32).

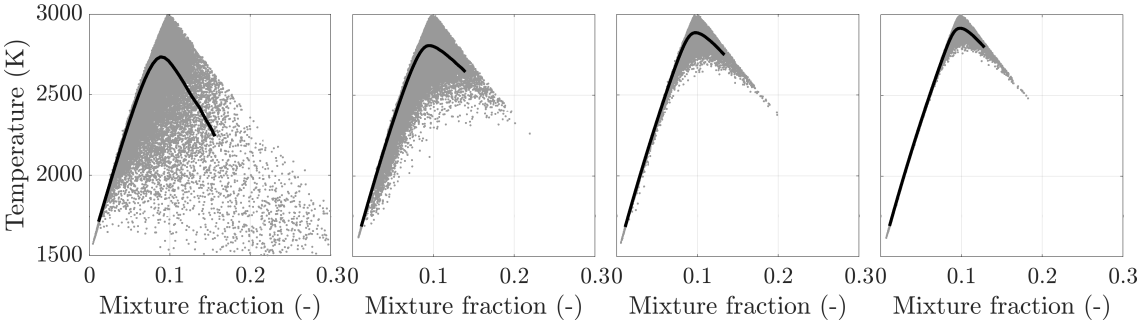

(a) $\delta = 0$ (reference). **(b)** $\delta = 1$. **(c)** $\delta = 2$. **(d)** $\delta = 3$.

Figure 6.3: Scatter plots of temperature versus mixture fraction obtained from the CP-DNS with different source term distributions (case *mid*, time $t = \tau_0$). For better clarity, the plots show only a sample of the simulation data. The black line denotes the conditional mean temperature.

The results of the simulations with different values of δ are shown in Fig. 6.2 along with the results of the reference case ($\delta = 0$). While the spatially averaged mixture fraction is almost unaffected, the rms of the mixture fraction field is reduced if source terms are distributed to a larger volume, as expected. The average temperature profiles shown in Fig. 6.2(b) exhibit a slightly higher mean temperature, which is because an increasing value of δ artificially increases the mixing in the surroundings of the droplet and thus enhances the reactions. Looking at the rms of the temperature, the effects are more complex and no clear trend of the parameter δ can be seen. On the one hand, a similar effect as for the rms of mixture fraction is expected, where a larger δ increasingly eliminates the large gradients at the droplet positions and thus reduces the variance. This effect can be observed at the very beginning of the simulation, where the reference solution ($\delta = 0$) exhibits a pronounced increase of the temperature rms due to the strong local cooling of the gas by the evaporating droplets, which no longer occurs if δ is increased. On the other hand, the complex interactions between evaporation and combustion can also lead to a temporary increase of the variance for a larger δ, as can be seen in Fig. 6.2(b) in particular for case *mid*.

Finally, Fig. 6.3 shows scatter plots of temperature versus mixture fraction at time $t/\tau_0 = 1$ exemplary for case *mid*. The reference case with $\delta = 0$ (Fig. 6.3(a)) indicates that a considerable amount of the gas-phase elements is not fully burning, which is attributable to the strong local cooling effect of the evaporating droplets, preventing the gas phase in the immediate vicinity of the droplets from ignition. With increasing δ, this scattering disappears as source terms are distributed across a larger volume, resulting in a more homogeneous distribution of fuel mass and temperature in the gas phase and thus producing more cells with an ignitable mixture. This trend can also be observed for the other droplet loadings considered here (not shown for brevity). Finally it should be noted that the region associated with

the source term distribution for $\delta = 3$ represents a volume similar to an LES cell. Therefore, it is expected that the dense particle method using the EQUAL model as well as the sparse particle method utilizing the one-to-one coupling model (assuming a particle number density of one particle per LES cell) will give similar results as shown in Fig. 6.3(d).

6.2.3 Assessment of Mixing Time Modeling in Spray Flames

The modeling of the mixing time scale for the Lagrangian FDF methods is based on an analogy with the time scale of the Eulerian subgrid scalar fluctuations that is given by $\tau_E = f_V/\widetilde{\chi}$ (cf. Sec. 4.3.4). Since the models for the mixture fraction subgrid variance and filtered scalar dissipation rate were derived in the context of single-phase flows, it is not clear whether the conventional models for the Lagrangian mixing time scale can be readily applied to spray flames.

The relationship between variance and scalar dissipation, taking into account the effect of droplet evaporation, is provided by the balance equation for the mixture fraction subgrid variance, which is derived in Appendix B. Focusing on the leading terms that are relevant for modeling of the mixing time, the equation can be expressed as

$$\frac{\partial(\bar{\rho} f_V)}{\partial t} = \underbrace{-\bar{\rho}\widetilde{\chi}}_{\text{Dissipation}} + \underbrace{2\left(\overline{f\dot{S}}_M - \widetilde{f}\overline{\dot{S}}_M\right) - \left(\overline{f^2\dot{S}}_M - \widetilde{f}^2\overline{\dot{S}}_M\right)}_{\text{Production due to evaporation}}. \tag{6.1}$$

The right-hand side contains the filtered scalar dissipation rate, which inherently reduces the variance, as well as the source terms due to droplet evaporation, which generally increase the variance. In stochastic particle methods, the mixing model replaces the scalar dissipation term, and the two-phase coupling model determines the evaluation of the evaporation sources and thus the amount of variance generated by the evaporating droplets. Due to the separate treatment of mixing and evaporation in modeling, the role of the mixing model is still to dissipate the scalar fluctuations. An inclusion of the evaporation source terms into the expression for the mixing time scale with the intention of counteracting the dissipation, as indicated by Eq. (6.1), is therefore not appropriate.

Despite the fact that evaporation is accounted for exclusively by the two-phase coupling model, mixing is implicitly affected by the evaporation process in terms of a modification of the subgrid variance and filtered scalar dissipation rate. This is demonstrated in Fig. 6.4, where predictions of the conventional models given by Eqs. (4.47) and (4.48), which were derived for single-phase flows, are compared to

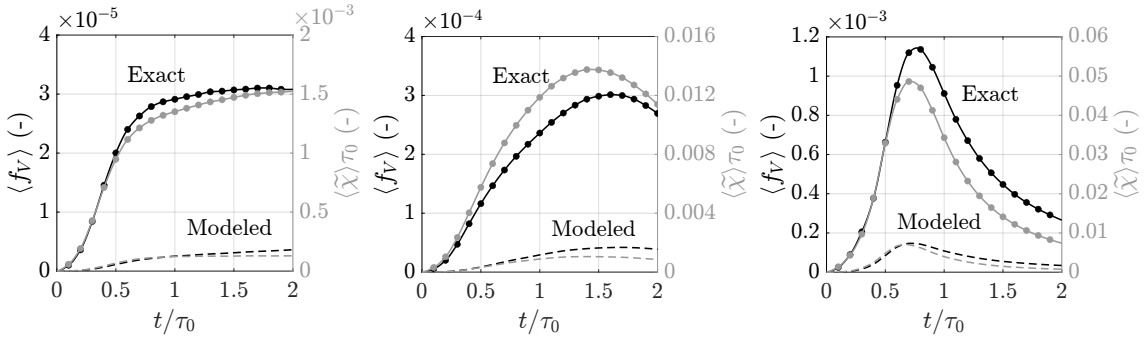

(a) Case *low*. **(b)** Case *mid*. **(c)** Case *high*.

Figure 6.4: Temporal evolution of spatially averaged subfilter variance $f_V = \widetilde{f^2} - \widetilde{f}^2$ and filtered scalar dissipation rate $\widetilde{\chi}$ normalized by the eddy turnover time. The exact quantities are extracted from the DNS data using explicit filtering, while the modeled quantities are determined using the standard models for single-phase flames given by Eqs. (4.47) and (4.48).

post-filtered data from the CP-DNS. Since the subgrid fluctuations resulting from the evaporating droplet field are not represented by these models, they lead to a significant underprediction of the subgrid variance and filtered dissipation rate. The discrepancies between the model predictions and the CP-DNS data are particularly large for the present configuration, since scalar fluctuations are generated exclusively at the smallest scales, resulting in relatively homogeneous filtered fields. Nevertheless, the models are able to reproduce the qualitative behavior correctly, so that an adjustment of the model constants can provide an adequate description for spray flames. It can also be seen that the droplets affect the variance and the dissipation rate to the same extent, so that the mixing time, which is defined as the ratio of both quantities, remains largely unaffected. Although the simulation data show that this is not equally true for all cases considered here, the present work refrains from a case-specific altering of the model constants in the present chapter, and employs the existing models without modification. Further, it should be noted that the model for the mixing time scale was found to have only a small effect on the results of the stochastic particle methods for the present setup, where variation of the modeling constant affects the unconditional fluctuations only moderately and the conditional fluctuations hardly at all.

6.3 Evaluation of the Two-Phase Coupling Models

6.3.1 Global Statistics

Figure 6.5 shows the temporal evolution of mixture fraction rms and temperature mean and rms predicted by the stochastic particle methods using different two-phase coupling models and compared to the CP-DNS data using the reference case with $\delta = 0$. Since the evaporation rate is taken from the CP-DNS, the mean mixture fraction is exactly reproduced by all models and is therefore not shown. In Fig. 6.5(a), the results of the sparse-Lagrangian MMC model utilizing a one-to-one coupling strategy between the droplets and the stochastic particles with particle selection conditional on the reference mixture fraction space is compared to the EQUAL model, which is the standard model in a dense particle method. While the EQUAL model is able to reproduce the evolution of the mean temperature (albeit temperatures are slightly too high), it consistently underestimates the rms of mixture fraction and temperature. This is because the evaporation source terms are distributed equally among the notional particles within the LES cell, preventing the generation of composition fluctuations at subgrid level. These results are consistent with the trends previously reported for the CP-DNS with source terms distributed to a larger volume (cf. Fig. 6.2). In contrast, the one-to-one coupling model that is used by the sparse-Lagrangian MMC-LES model shows overall very good agreement with the CP-DNS data for both mixture fraction and temperature. Although the distribution of source terms in the sparse-particle method is subject to the same volume as in the EQUAL model, the one-to-one coupling strategy shows much better agreement of the rms profile with the CP-DNS, although a slight deviation remains. This is attributable to the fact that the conditioning on the reference field causes some particles to be favored and thus receive more mass from the evaporating droplets, resulting in an inhomogeneous distribution of the evaporation source terms among the notional particles and thus increasing the variance in the stochastic particle field. Figure 6.6 quantifies this hypothesis, where the number of droplets per stochastic particle during two-phase coupling is shown for the three different droplet loadings. For case *mid* (Fig. 6.6(b)), which is chosen here for explanation, the number of droplets and stochastic particles is approximately the same (cf. Tab. 6.1), so that, without conditioning, each stochastic particle is paired on average with a single stochastic particle. This is indicated by the dashed line in Fig. 6.6. The conditioning of the particle selection now results in some particles receiving the source terms of more than one droplet, while about half of the particles receive none

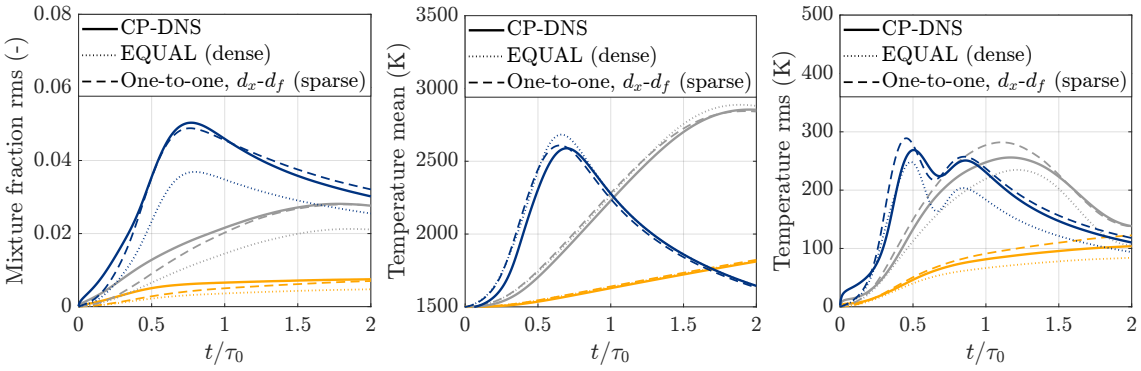

(a) EQUAL model (dense particle method) versus one-to-one coupling with particle selection conditional on the reference mixture fraction space in a sparse particle method.

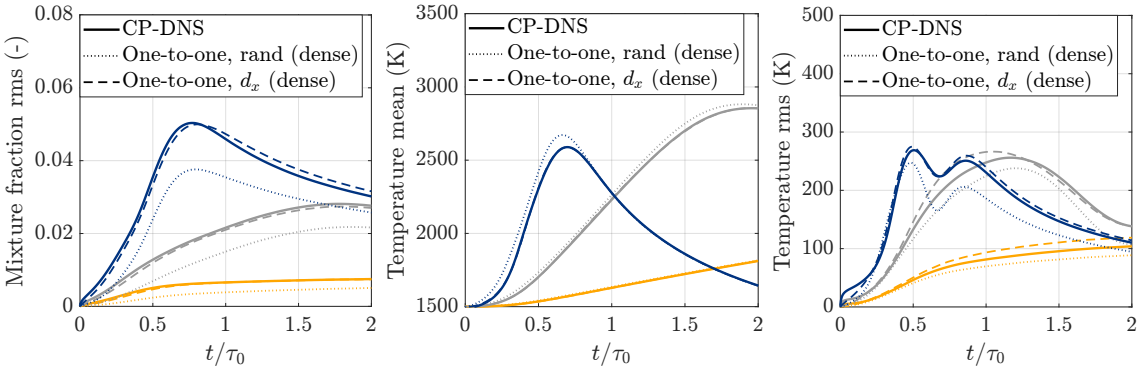

(b) One-to-one coupling in a dense particle method using either a random particle selection within the LES cell or a selection of the closest particle in physical space.

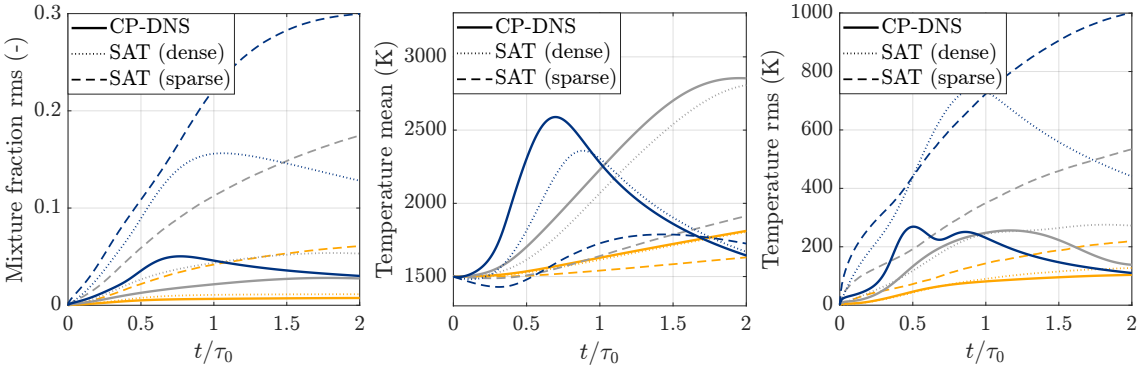

(c) SAT model in a dense and sparse particle method.

Figure 6.5: Temporal evolution of mixture fraction rms and temperature mean and rms obtained from the stochastic particle methods using different two-phase coupling models and compared to the CP-DNS data ($\delta = 0$). The color indication is the same as in Fig. 6.2.

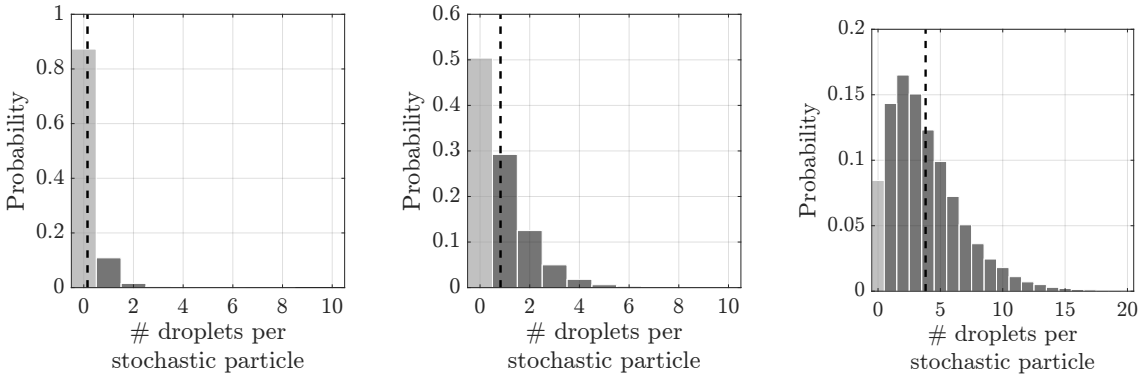

(a) Case *low*. **(b)** Case *mid*. **(c)** Case *high*.

Figure 6.6: Probability distribution for the number of droplets coupled per stochastic particle using the one-to-one coupling model with a sparse particle distribution at time $t = \tau_0$. The probability that a stochastic particle is not coupled with a droplet is marked in light gray. The dashed line indicates the average number of droplets per stochastic particle, corresponding to an equal distribution of the evaporation source terms among the stochastic particles.

at all, leading to an uneven distribution of source terms. Further, it was found that the assignment of the particles to the droplets is maintained for a certain time (until the random walk and the inertia of the droplet have caused them to drift away), which reflects real droplet evaporation and also contributes to variance generation. The non-uniform distribution of the source terms among the stochastic particles is also observed for the other droplet loadings, making the model independent of the droplet loading.

The capability of the one-to-one coupling strategy to predict an adequate amount of variance in a sparse particle method is now tested for a dense particle distribution, as this may overcome the limitations of the EQUAL model. Since a conditioning on the LES-filtered mixture fraction field is not reasonable in the case of a dense particle distribution, the assignment of the stochastic particles to the droplets is done either randomly within the LES cell or by selecting the closest particle in physical space ($\lambda_f = 0$). The corresponding mean and rms profiles of mixture fraction and temperature are shown in Fig. 6.5(b). For a random selection, the results are very similar to the EQUAL model. This is because a different particle is selected in each time step for each droplet, so that over time the source terms are distributed evenly among the stochastic particles in the LES cell, implying artificial mixing. In contrast, if the particle that is closest in physical space is selected to receive the source terms, each droplet is paired with the same particle for a certain period of time, while the remaining particles do not receive any mass. The model thus reflects the effects observed in the CP-DNS, where the fuel mass is initially transferred to a small gas volume (i.e., the DNS cell that contains the droplet) and is then mixed with the surrounding gas to produce an ignitable gas mixture. As

shown in Fig. 6.5(b), this produces a higher variance compared to the random selection, and leads to excellent agreement with the CP-DNS. However, it should be noted that the performance of the model may depend on the number of stochastic particles, as discussed in Sec. 4.5.4.

If the SAT model is used, in which source terms are distributed preferentially to particles near the saturation state, one obtains rms values that are clearly too high, and also the mean temperature deviates considerably from the CP-DNS, as shown in Fig. 6.5(c). This is a result of concentrating the evaporation source terms on a small number of gas-phase particles, resulting in high mixture fraction and low temperature values on these individual particles. Unlike dense particle methods, mixing and two-phase coupling are not restricted to the LES cell in a sparse particle method. In combination the larger volume represented by each gas-phase particle, this results in particles receiving source terms from a significantly larger number of droplets (several hundred for case *mid*), thus amplifying the effects. The large variance in the mixture fraction and temperature fields requires more mixing to be done by the mixing model, so improvements can be expected by adjusting the mixing time scale. However, this is not the objective of the present work, and Sec. 6.4.1 presents an alternative approach to overcome the high mixture fraction and low temperature values predicted by the SAT model in a sparse particle method.

6.3.2 PDFs of Mixture Fraction and Temperature

The two-phase coupling model should not only predict the correct global statistics but also accurately model the evolution of the higher moments, such as the distribution of mixture fraction and temperature within the domain. Figure 6.7 shows the PDFs of mixture fraction exemplary for case *mid*, which are obtained from the different two-phase coupling models and compared to the CP-DNS. Both the EQUAL model (Fig. 6.7(a)) and the one-to-one coupling technique with a random particle selection (Fig. 6.7(b)) using a dense particle distribution lead to reasonable predictions, but predict a slightly too thin shape of the mixture fraction PDF. This is a result of artificial mixing induced by the models, as mentioned earlier. The one-to-one coupling with a selection of the nearest particle in physical space (Fig. 6.7(c)) leads to slight improvements, but the shape of the PDF is still not correct. Excellent agreement with the CP-DNS data is obtained by the sparse particle method utilizing a one-to-one coupling technique conditional on the reference mixture fraction space (Fig. 6.7(d)), which shows that mixing of the fuel vapor with the ambient gas is accurately described by the model. In contrast, the SAT model leads to larger deviations from the CP-DNS, with mixture fraction values being generally too low.

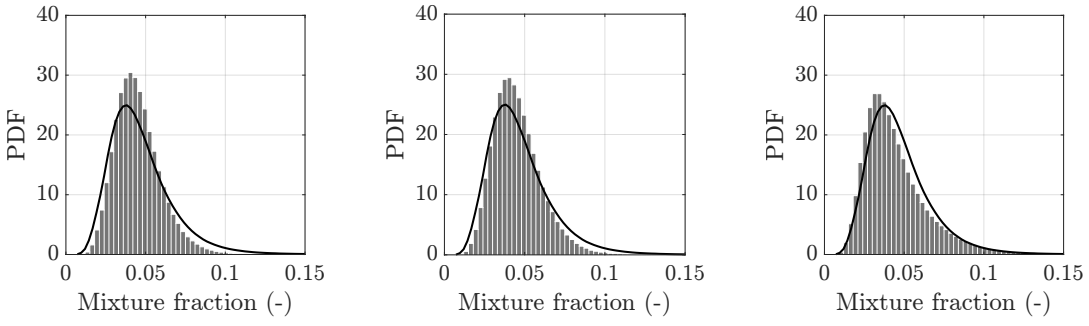

(a) EQUAL (dense). **(b)** One-to-one, rand (dense). **(c)** One-to-one, d_x (dense).

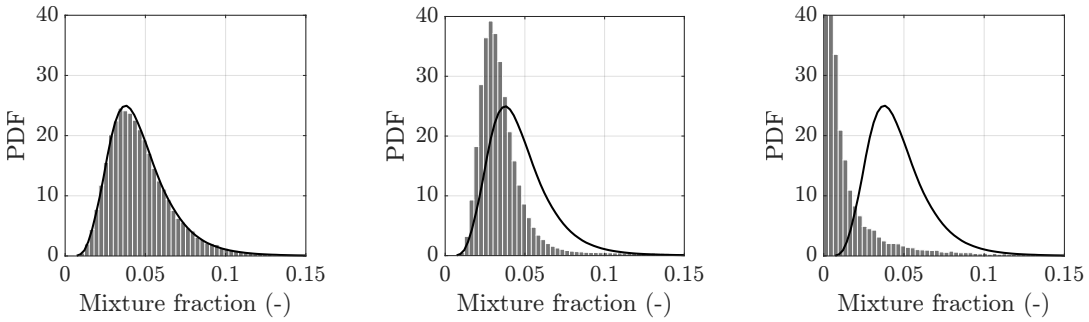

(d) One-to-one, d_x-d_f (sparse). **(e)** SAT (dense). **(f)** SAT (sparse).

Figure 6.7: PDF of mixture fraction obtained from the stochastic particle methods using different two-phase coupling models (case *mid*, time $t = \tau_0$). The black line denotes the CP-DNS.

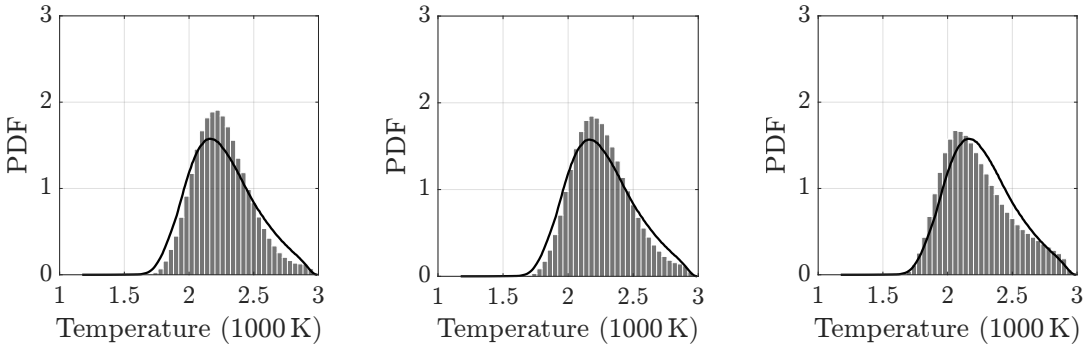

(a) EQUAL (dense). **(b)** One-to-one, rand (dense). **(c)** One-to-one, d_x (dense).

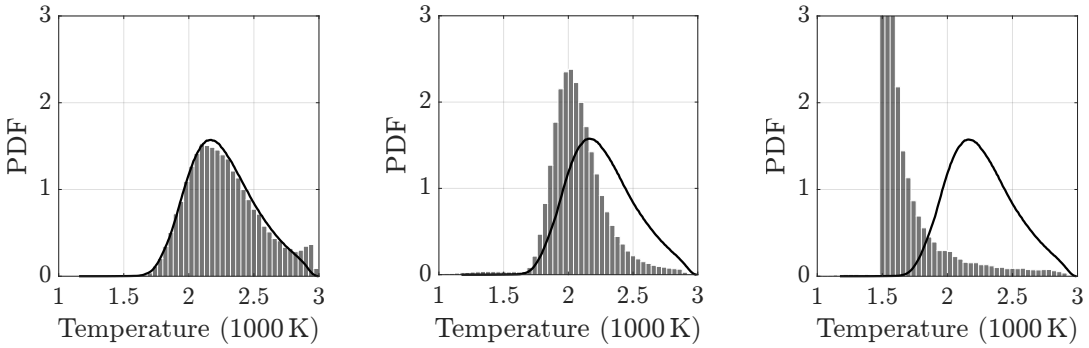

(d) One-to-one, d_x-d_f (sparse). **(e)** SAT (dense). **(f)** SAT (sparse).

Figure 6.8: PDF of temperature obtained from the stochastic particle methods using different two-phase coupling models (case *mid*, time $t = \tau_0$). The black line denotes the CP-DNS.

While the shape of the PDF is still reasonably well reproduced if a dense particle distribution is used (Fig. 6.7(e)), the sparse particle method predicts a completely incorrect shape of the PDF, where a significant portion of the particles is close to the initial state and thus not affected by the evaporation process (Fig. 6.7(f)). Note that the SAT model produces high mixture fraction values close to the saturation value for a few stochastic particles, but these are not visible in the PDF because their probability is low in relation to the overall PDF ($\mathcal{O}(10^{-3})$ for the dense particle method and $\mathcal{O}(10^{-1})$ for the sparse particle method).

The PDFs of the temperature, which are shown in Fig. 6.8, generally reveal the same trends as those reported for the mixture fraction. However, some models show a peak at higher temperatures, which is most pronounced in the one-to-one coupling model using a sparse particle distribution (Fig. 6.8(d)). This is attributable to the fact that the evaporation source terms are distributed over a larger volume, which implies artificial mixing and produces more particles with an ignitable mixture. This effect will be discussed in more detail in the following section.

6.3.3 Conditional Statistics

The correlation between mixture fraction and temperature predicted by the stochastic particle methods using different two-phase coupling models is shown in Fig. 6.9 exemplary for case *mid*. The corresponding reference solution provided by the CP-DNS is given by Fig. 6.3(a).

Using a dense particle distribution, both the EQUAL model and the one-to-one coupling model with a random particle selection significantly underestimate the conditional fluctuations, resulting in an overprediction of the conditional mean temperature, as indicated by the black line (Figs. 6.9(a) and 6.9(b)). This is because the evaporation source terms are effectively distributed over a larger gas volume, as mentioned earlier, reflecting the trends already observed in the CP-DNS study with variable source term distributions (cf. Fig. 6.3). In contrast, a considerable amount of conditional variance is generated if the closest particle in physical space is selected (Fig. 6.9(c)). Here, the distribution of the fuel mass to only a few selected particles within the LES cell in combination with the small volume of the gas-phase particles resulting from the dense particle distribution leads to a fuel-rich mixture and a low temperature on these particles, which prevents ignition. However, the agreement with the CP-DNS is only moderate, and the conditional mean temperature is still too high.

Although the one-to-one coupling in a sparse particle method shares similarities with the one-to-one coupling in a dense particle method in that it ensures pairing

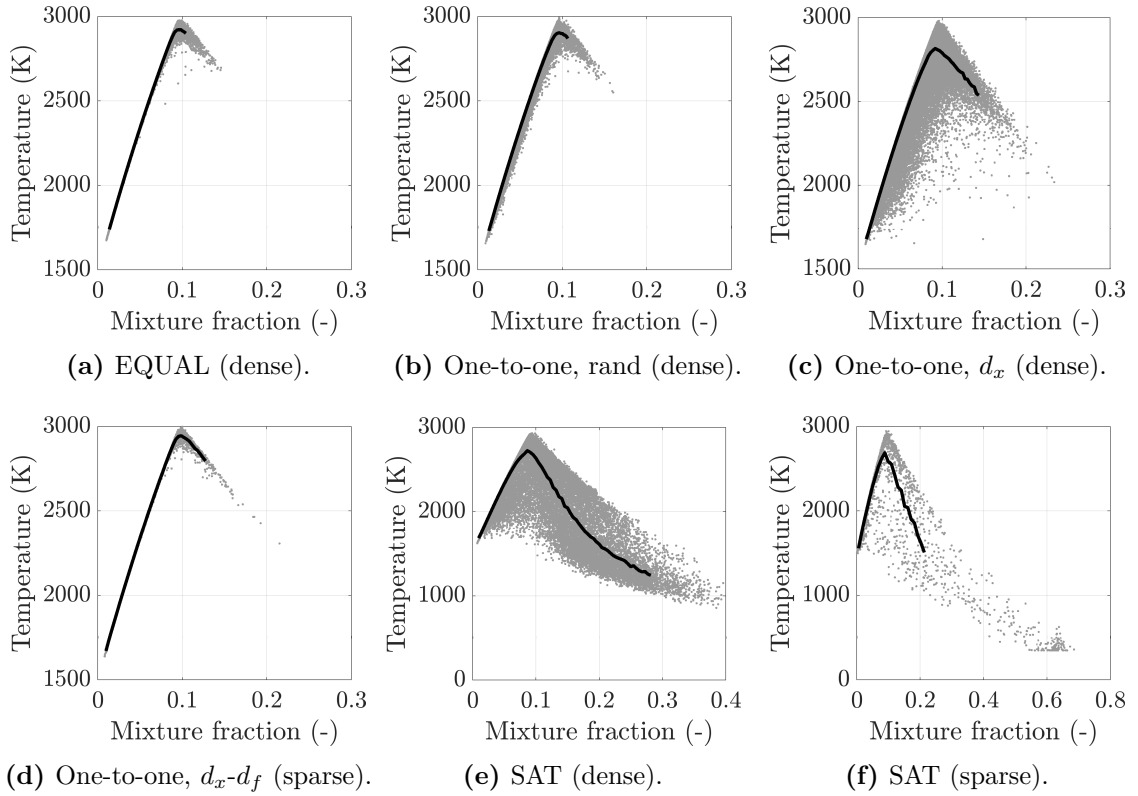

(a) EQUAL (dense). **(b)** One-to-one, rand (dense). **(c)** One-to-one, d_x (dense).

(d) One-to-one, d_x-d_f (sparse). **(e)** SAT (dense). **(f)** SAT (sparse).

Figure 6.9: Scatter plots of temperature versus mixture fraction obtained from the stochastic particle methods using different two-phase coupling models (case *mid*, time $t = \tau_0$). For better clarity, the plots show only a sample of the simulation data. The black line denotes the conditional mean temperature.

of the same particles and droplets for a certain time interval and generates a similar amount of unconditional variance, the corresponding scatter plot exhibits almost no conditional fluctuations (Fig. 6.9(d)). This is a result of the large gas volume represented by each particle in the sparse particle method, which causes only moderate changes in the gas-phase properties, in particular eliminating the locally strong cooling effect of the droplets, and thus produces too many burning particles.

The results obtained from the SAT model using dense and sparse particle distributions are shown in Figs. 6.9(e) and 6.9(f), respectively. In both cases, much higher mixture fraction and lower temperature values are produced than with the other models due to the concentration of the source terms on a small number of particles, where in particular the sparse particle method features a significant amount of gas-phase particles located near saturation conditions. These high mixture fraction and low temperature values cannot be observed in the CP-DNS (cf. Fig. 6.3(a)). Although the existence of values close to saturation is physical as they reflect the conditions at the droplet surface, it is not reasonable to expect such extreme values in the simulations since they are limited to the immediate vicinity of the droplets. As shown by Bilger [10], the probability for mixture fraction to take values at sat-

uration conditions is proportional to the volume fraction of the liquid droplets and thus often negligible in dilute sprays, which is also in agreement with the simple estimate presented in Sontheimer *et al.* [195]. For case *mid*, the analytical solution of Bilger for the mixture fraction PDF, evaluated at saturation conditions, predicts values of the order of 10^{-4}, whereas the PDF resulting from the SAT model is larger by a factor of ten for the dense particle distribution and by a factor of thousand for the sparse particle distribution. However, focusing on the mixture fraction range that is covered by the reference CP-DNS (Fig. 6.3(a)), the SAT model leads to a clearly more accurate approximation of the conditional temperature fluctuations than predicted by the EQUAL model and the one-to-one coupling strategy, with reasonable agreement of the conditional mean temperature.

6.4 Potential Improvements to Sparse-Lagrangian Two-Phase Coupling

In sparse particle methods, the one-to-one coupling strategy between the droplets and the stochastic particles has shown to slightly underestimate the unconditional fluctuations, while significantly underestimating the conditional fluctuations due to artificial mixing on the gas-phase particles. In contrast, the SAT model has demonstrated that pairing a larger number of droplets with a stochastic particle can provide an adequate description of the conditional fluctuations, but it significantly overestimates the conditions at the saturation state, resulting in a considerable deviation of the unconditioned variables. This suggests to combine concepts from both models in order to improve the existing two-phase coupling models in the framework of a sparse particle method, which is the focus of the present section. The results will only be reported for case *mid* in the following, but the trends are essentially the same for the other droplet loadings.

6.4.1 SAT Model With Restriction on Droplet Number

The generation of the excessively high mixture fraction and low temperature values by the SAT model in a sparse particle method can be avoided by artificially limiting the number of droplets that are paired with each stochastic particle in each time step. This prevents the gas-phase particles from reaching saturation conditions and leads to a more homogeneous distribution of the fuel mass and the temperature in the gas phase, as source terms are distributed to a larger number of stochastic particles. Note that a similar effect could be obtained by limiting the maximum distance in physical space between the droplets and the stochastic particles.

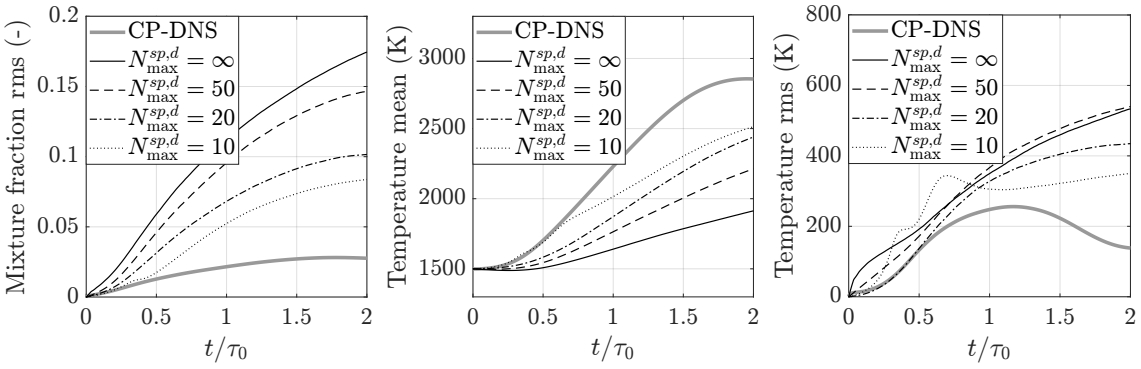

(a) Mixture fraction rms and temperature mean and rms.

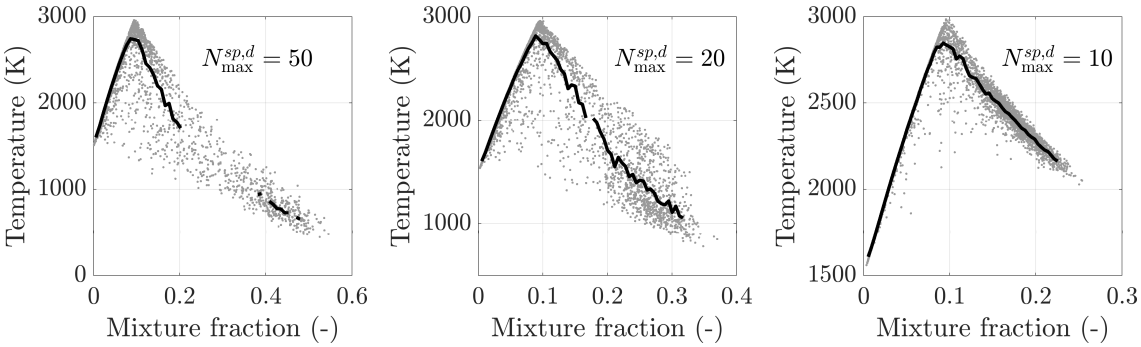

(b) Scatter plots of temperature versus mixture fraction at time $t = \tau_0$. The black line denotes the conditional mean temperature.

Figure 6.10: Results of the SAT model with a prescribed maximum number of droplets per stochastic particle using a sparse particle distribution (case *mid*).

Figure 6.10 shows the results that are obtained from the sparse particle method using the SAT model with different maximum numbers of droplets per stochastic particle. Without restriction (denoted as $N^{sp,d}_{\max} = \infty$), the SAT model leads to the pairing of several hundred droplets with each selected gas-phase particle for the given particle number density and droplet loading, resulting in a significant overprediction of the mixture fraction variance. From about $N^{sp,d}_{\max} \lesssim 50$, the variance is noticeably reduced, with the results of the stochastic particle methods increasingly approaching the CP-DNS data (Fig. 6.10(a)). The predictions for the mean temperature show essentially the same trend, where in particular the case with $N^{sp,d}_{\max} = 10$ leads to very good agreement with the CP-DNS at the beginning of the simulation ($t/\tau_0 \lesssim 0.6$). For the time history of the temperature rms, no clear trend can be seen, with $N^{sp,d}_{\max} = 20$ giving the best results at the earlier times. Scatter plots of temperature versus mixture fraction along with the conditional mean temperature are shown in Fig. 6.10(b). As expected, restricting the number of droplets per particle reduces the range of mixture fraction and temperature values, where $N^{sp,d}_{\max} = 10$ and $N^{sp,d}_{\max} = 20$ yield a similar range as observed in the CP-DNS (cf. Fig. 6.3(a)). The conditional mean temperature remains almost unaffected, and also the conditional fluctuations

remain on a similar level for $N_{\max}^{sp,d} \gtrsim 20$, but are reduced if the number of droplets is limited to $N_{\max}^{sp,d} = 10$.

The results show that in particular at the beginning of the simulation, where the one-to-one coupling model underestimates the variance, the coupling of a larger number of droplets with each stochastic particle can compensate for the larger volume of the notional particles, resulting in a larger variation of the gas-phase properties and preventing their ignition. Nevertheless, there are still significant deviations from the reference solution at later times, making the overall agreement unsatisfactory.

6.4.2 Blending Between One-To-One Coupling and SAT Model

Good predictions of unconditional averages and conditionally averaged quantities by the one-to-one coupling technique and the SAT model, respectively, suggest some potential for the combination of the two approaches. A relatively simple remedy is to introduce a weighted combination of the one-to-one coupling and the SAT model, and to control their respective influence by adjustment of the weighting factor. Figure 6.11 shows the mixture fraction rms for case *mid* using two different weighting factors for the SAT model. The term 10 % SAT indicates that 10 % of the evaporated mass of a droplet is distributed according to the SAT model, while the remaining mass is distributed using the one-to-one coupling technique. It can be seen that this approach allows to generate profiles between the pure one-to-one and SAT model, respectively, as a function of the weighting factor. A weighting of the SAT model by 10 % leads to good agreement with the CP-DNS at the beginning of the evaporation process, where the one-to-one coupling underpredicts the variances, but yields too large rms values at later times. Here, a time-dependent weighting factor would be required to achieve good agreement over the entire simulation time, which, however, is not easy to determine and not in the sense of a universally valid model. The same trends can also be observed for the mean and rms of the temperature (not shown). As can be seen from the scatter plots in Fig. 6.11(b), the increased variance is a result of the wider mixture fraction range that arises from the influence of the SAT model, but the probability of high mixture fraction values is much reduced compared to the pure SAT model. However, the conditional variance stays too low and the conditional mean temperature continues to be too high.

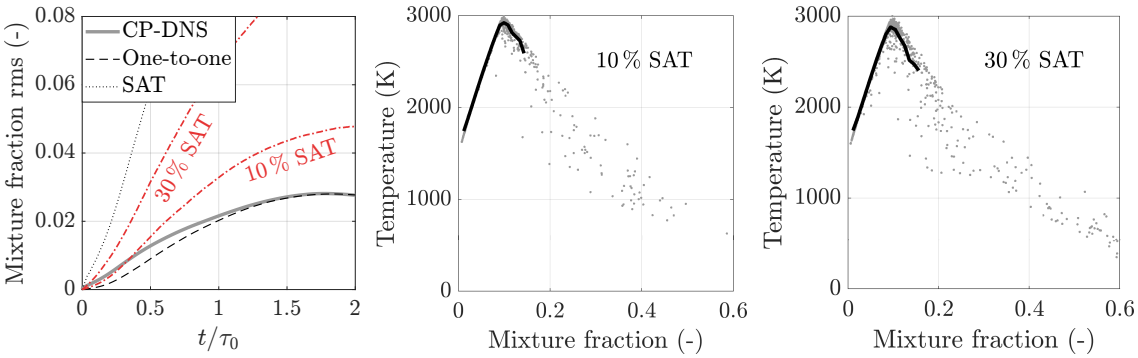

(a) Mixture fraction rms.

(b) Scatter plots of temperature versus mixture fraction at time $t = \tau_0$. The black line denotes the conditional mean temperature.

Figure 6.11: Results for a weighted combination of the one-to-one coupling strategy and the SAT model using a sparse particle distribution (case *mid*).

6.4.3 Inclusion of Saturation Space in the Effective Square Distance

Preferential mass transfer to particles with higher fuel vapor concentrations can also be effectuated for the one-to-one coupling strategy by extending the effective square distance between the droplets and the stochastic particles, Eq. (4.60), by the distance in saturation space (with all Boolean variables set to unity for simplicity),

$$\hat{d}^2_{d,sp} = \sum_{i=1}^{3} \left(\frac{d^{d,sp}_{x_i}}{r^*_m/\sqrt{3}} \right)^2 + \left(\frac{d^{d,sp}_f}{f^*_m} \right)^2 + \left(\frac{d^{d,sp}_s}{s^*_m} \right)^2 . \tag{6.2}$$

The distance in saturation space is represented here by the separation of the fuel mass fraction of the stochastic particle to the saturated fuel mass fraction associated with the conditions at the droplet surface, $d^{d,sp}_s = |Y_{F,s} - Y^{sp}_F|$, and s^*_m is a normalization parameter.

Figure 6.12(a) shows the time evolution of the mixture fraction rms for different values of parameter s^*_m. A small value of s^*_m leads to a strong weighting of the distance in saturation space and hence produces similar results as with the pure SAT model, whereas a larger value yields a low weighting of the distance in saturation space and thus reduces the effect of the preferential pairing with particles close to saturation conditions. In contrast to the simple weighting of both models that was discussed previously, one does not obtain results that lie in between the limits of the respective models. Instead, the results are equivalent to one-to-one coupling at the beginning, but start to diverge after a certain time, with the increase in variance being similar to the pure SAT model. This behavior can be explained as follows. At the beginning, all particles have a similar fuel mass fraction value and hence exhibit the same distance in saturation space. The selection of particles is therefore equivalent to the minimization of Eq. (4.60). However, due to irregular particle

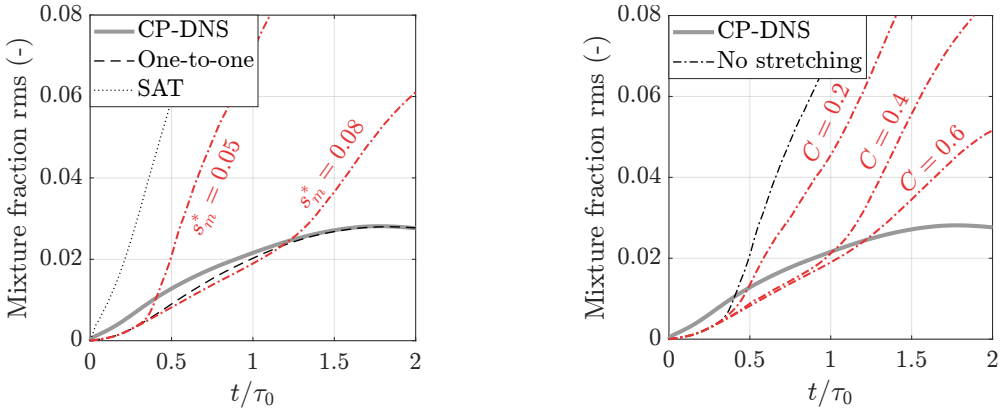

(a) Two-phase coupling based on Eq. (6.2).

(b) Two-phase coupling based on Eq. (6.2) with stretching function Eq. (6.3).

Figure 6.12: Results for a one-to-one coupling based on the minimization of the effective square distance with incorporation of the saturation space, Eq. (6.2), using a sparse particle distribution (case *mid*).

positions and turbulent dispersion, the coupling will eventually lead to an uneven distribution of the evaporated mass among the stochastic particles. As a result, some particles will have higher fuel mass fractions and are therefore closer to the saturation limit. These particles are then preferentially selected, increasing the fuel mass fraction even further, which in turn favors preferential selection. After a certain time, the same few particles are continuously selected and the model resembles the SAT model. The parameter s_m^* controls the weighting between the respective distances and only affects the time of transition from the one-to-one coupling to the SAT model. The use of Eq. (6.2) correctly reduces the high probability of large mixture fraction values close to saturation conditions but does not prevent their existence. The unconditional variance is still too high while the conditional variance continues to be too low.

To avoid the sudden transition from the one-to-one coupling model to the SAT model, a modification of the model is necessary. The modification should allow for enhancing the pairing of droplets with particles that have higher fuel mass fraction values (as this increases the conditional variance) but it should prevent pairing solely with particles at saturation conditions, as this generates the (unphysical) pronounced peak at high fuel mass fractions and strongly increases the unconditional variance. For these reasons, a stretching of the distance in saturation space is applied, i.e., $d_s^{d,sp}$ is replaced by $w \cdot d_s^{d,sp}$ in Eq. (6.2), where w is a stretching function. The stretching function must increase faster than d_s decreases when approaching the saturation limit. Accordingly, an exponential stretching of the form

$$w = \exp\left(C \frac{Y_F^{sp}}{d_s^{d,sp}}\right) \tag{6.3}$$

is suggested. This scaling ensures that small and moderate distances remain unaffected, while larger distances in saturation space are exponentially amplified, leading to a strong increase of the effective square distance and preventing selection of these particles for two-phase coupling. The constant in Eq. (6.3) controls the exponential increase and hence determines the position of the peak in the mixture fraction distribution that would otherwise occur at saturation conditions. Results with different values of C and using $s_m^* = 0.05$ are shown in Fig. 6.12(b). It is clear to see how a larger value of C reduces the variance, as the peak that would occur at saturation conditions is now shifted to lower mixture fraction values due to the scaling function, but a match with CP-DNS data that is clearly superior to the one-to-one coupling is still not achieved.

6.4.4 Time Delay Model

The main drawback of the one-to-one coupling strategy in a sparse particle method is the artificial mixing in the surroundings of the droplets, which is a result from distributing the evaporation source terms to the relatively large volume represented by each gas-phase particle. The model therefore cannot reproduce the local cooling effect of the droplets, leading to earlier ignition of the gas mixture and a lack of conditional fluctuations. A simple test provides insight into whether accounting for the local cooling effect of the droplets can improve the model predictions. To this end, a sparse-Lagrangian simulation with the one-to-one coupling model is performed, where in each time step the chemistry substep is not conducted for those particles that are selected to pair with a droplet. This should prevent the gas mixture that receives the evaporation source terms from ignition, and thus allow the droplets to cool down the gas state associated with the surroundings of the droplets, as is the case with real droplet evaporation. The results are shown in Fig. 6.13, demonstrating excellent agreement of the mean temperature with the CP-DNS data, and also slight improvements of the conditional statistics. While the case where chemistry is solved on all particles has exhibited almost no conditional fluctuations (cf. Fig. 6.9(d)), the scatter is now slightly increased, leading to a reduction of the conditional mean temperature. Although the agreement with the CP-DNS is not yet satisfactory, the test shows that a delay in chemistry yields the desired effects and is able to improve the model predictions. The conditional fluctuations can be further enhanced by increasing the delay time for the chemistry, where in general the delay time should be represented by the characteristic time scale describing the mixing of the fuel vapor with the ambient gas on the stochastic particles. Such a time delay model will be formulated in the following.

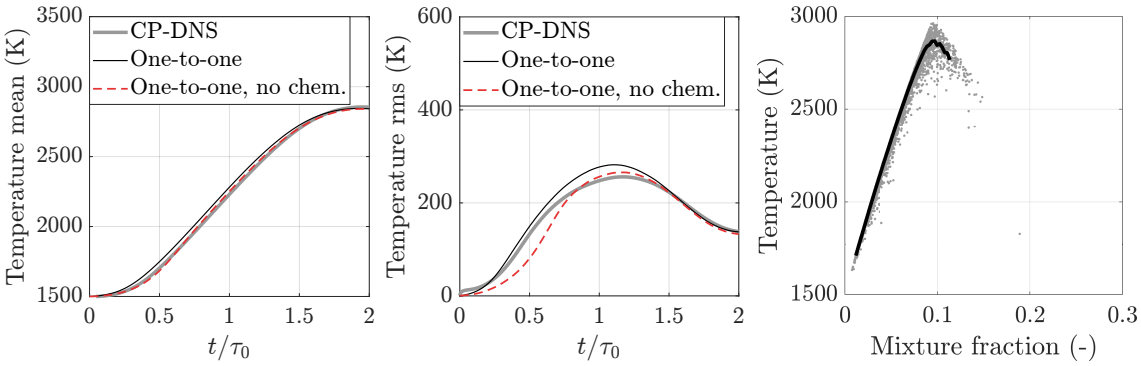

(a) Temperature mean and rms. The red line denotes the case where chemistry is not solved for particles coupled with droplets. **(b)** Scatter plot of temperature versus mixture fraction ($t = \tau_0$).

Figure 6.13: Results of the one-to-one coupling strategy (sparse particle method, case *mid*), whereby the chemistry substep is not performed during the particular time step for particles that are selected for pairing with a droplet.

The suppression of chemical reactions on the particles coupled with droplets represents a significant interference with the physics, and will therefore be replaced by a delayed (or partial) transfer of the source terms to the gas-phase particles. This shall account for a finite mixing time associated with the mixing of the evaporated fuel mass within the gas volume represented by the stochastic particles, and achieve the same effect as a delay in chemistry. The model requires to split the volume of the stochastic particle into two subvolumes, where one subvolume receives the source terms from the droplets, thus reflecting the high fuel concentrations at the droplet position, while the other subvolume represents the gas state in the surroundings of the droplet where chemical reactions take place. Between the two subvolumes there is an exchange of heat and mass, representing the mixing of the fuel vapor with the ambient gas. Accordingly, the model shares similarities with the eddy dissipation concept that is used in (pure gas-phase) combustion modeling (cf. Sec. 2.2). The division of the volume raises a number of modeling issues that need to be addressed, such as the definition of a suitable ratio between the two subvolumes. Therefore, a simplified version of the model will be used within the present work, in which the volume associated with the source terms is assumed to be infinitely small. This is motivated by the fact that the size of the droplets is small in relation to the volume that is represented by a stochastic particle. The evaporation source terms are stored in additional fields on the stochastic particles and are accumulated over time, where in each time step a portion of the total sources is mixed with the gas phase. Note that these additional fields must be taken into account for the mass and energy balance between the droplets and the gas phase.

The partial transfer of the source terms to the gas phase is subject to the following requirements:

- The amount of transferred heat and mass should depend on the total size of the accumulated source terms. The larger the source terms are, the more fuel mass should be mixed with the gas phase.
- Further, the amount of transferred heat and mass must depend on the computational time step.
- It must be ensured that no more heat and mass is transferred to the gas phase than is stored in the source terms.
- The transfer of heat and mass is modeled using a characteristic time scale that describes the mixing of the fuel vapor with the ambient gas.

Based on these requirements, the following model is suggested. The amount of mass and heat that is transferred in each time step to a stochastic particle is given by

$$\delta m = \gamma m_{\text{total}}, \qquad \delta H = \gamma H_{\text{total}}, \tag{6.4}$$

where m_{total} and H_{total} are the accumulated source terms of the stochastic particle for mass and heat (expressed in terms of enthalpy), respectively, and $\gamma \in [0,1]$ denotes the fraction of the total source term that is transferred to the gas phase at the current time step. This fraction is modeled similarly to the mixing extent in the particle interaction model, and is given by

$$\gamma = 1 - \exp\left(-\frac{\Delta t}{\tau_{\text{mix}}^{d,sp}}\right), \tag{6.5}$$

where $\tau_{\text{mix}}^{d,sp}$ is the characteristic time scale that describes the mixing of the fuel vapor originating from the droplet with the ambient gas represented by the stochastic particle. For $\Delta t = 0$ and $\tau \to \infty$, the expression yields $\gamma = 0$, resulting in no mass and heat being transferred to the gas phase, while $\Delta t \to \infty$ and $\tau \to 0$ lead to $\gamma = 1$ and thus source terms are transferred entirely to the gas phase during the time step. In Sec. 5.3.2, a mixing time based on an isolated droplet in a quiescent environment was derived (Eq. (5.30)). An alternative choice for the mixing time, which takes into account the effect of turbulent mixing, is given by Eq. (4.49). To account for both laminar and turbulent mixing, the minimum of the two time scales is taken,

$$\tau_{\text{mix}}^{d,sp} = \min\left(C_{\text{lam}}\frac{d(V^{sp})^{1/3}}{\mathcal{D}}, C_{\text{turb}}\frac{(V^{sp})^{2/3}}{\mathcal{D}_{\text{eff}}}\right), \tag{6.6}$$

where the characteristic length has been replaced by the cube root of the volume represented by the stochastic particle and given by $V^{sp} = m^{sp}/\rho^{sp}$. Values for the modeling constants C_{lam} and C_{turb} can be found by comparison with the original models. The analytical solution derived in Sec. 5.3.2 leads to a value of the order of $C_{\text{lam}} \approx 0.1$ for the laminar mixing time, and using the standard value for the

modeling constant in Eq. (4.49) results in $C_{\mathrm{turb}} = 0.05$ for the turbulent mixing time. Whether these theoretical values are also suitable for the time delay model must be verified by simulations.

Figure 6.14 shows the results of the time delay model used in combination with the one-to-one coupling strategy with particle selection conditional on the reference mixture fraction space. Simulations have been performed with different values for the modeling constants. Using the default values $C_{\mathrm{lam}} = 0.1$ and $C_{\mathrm{turb}} = 0.05$, the laminar time scale determines the overall mixing time according to Eq. (6.6), and a value of approximately $\gamma \approx 0.1$ is obtained, meaning that only 10 % of the total source term is transferred to the gas phase in each time step. Nevertheless, the effects on the mean mixture fraction are rather small (not shown). This is due to the fact that the assignment between the droplets and the stochastic particles changes over time, so there are time steps in which a particle does not receive source terms, which then allows the remaining heat and mass stored on the particle to be transferred to the gas phase. The rms of mixture fraction and temperature as well as the spatially averaged temperature become slightly smaller if the time delay model is used (Fig. 6.14(a)). While this increases the deviation from the CP-DNS for the mixture fraction rms, it leads to slightly better agreement of the temperature predictions. An increasing value of C_{lam} increases the mixing time and thus the delay time for the transfer of the source terms to the gas phase, thus causing a further decrease of the rms values and the mean temperature. For $C_{\mathrm{lam}} = 1$, the laminar and turbulent time scales are about the same size, while for $C_{\mathrm{lam}} = 10$ solely the turbulent time scale determines the mixing time. Consequently, there is no significant difference in the results between $C_{\mathrm{lam}} = 1$ and $C_{\mathrm{lam}} = 10$. Looking at the scatter plots shown in Fig. 6.14(b), the effect of the time delay model is rather small and does not lead to significant improvements. The conditional mean temperature remains on a too high level, while there are hardly any conditional fluctuations. In fact, the conditional fluctuations are even slightly reduced if a larger value for C_{lam} and thus a larger delay time is used.

The unsatisfactory results require a reassessment of the time delay model. While the partial transfer of the source terms to the gas-phase particles is able to slightly delay the chemistry, it cannot solve the problem of artificial mixing, since source terms are still transferred to a larger volume. As a result, the droplets cause only moderate changes in the gas-phase properties and do not produce significant conditional fluctuations. To overcome this issue, source terms need to be transferred to a smaller volume, which could be realized by using two subvolumes on the particles, as discussed earlier. However, this would require a complete revision of the time delay model, with additional modeling challenges to overcome.

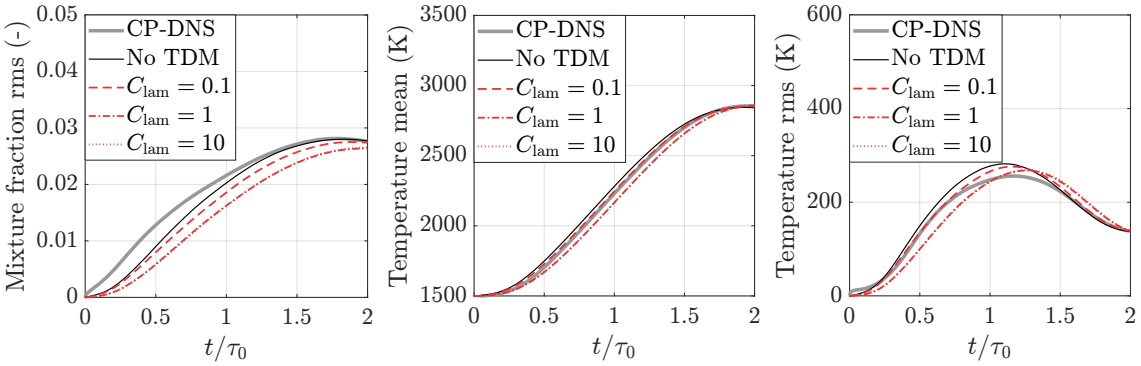

(a) Mixture fraction rms and temperature mean and rms.

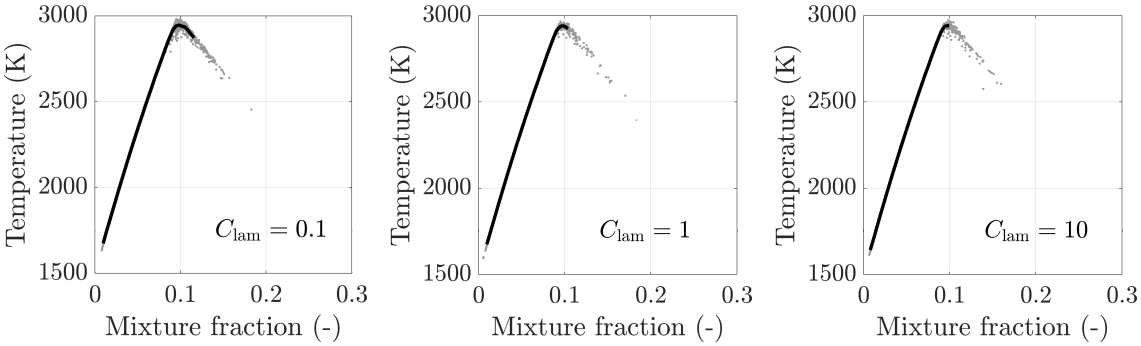

(b) Scatter plots of temperature versus mixture fraction at time $t = \tau_0$. The black line denotes the conditional mean temperature.

Figure 6.14: Results of the time delay model (TDM) with different modeling constants in combination with the one-to-one coupling strategy in a sparse particle method. (case *mid*). The simulations with $C_{\mathrm{lam}} = 1$ and $C_{\mathrm{lam}} = 10$ lead to almost identical results.

6.5 Summary and Discussion

The performance of various two-phase coupling models in the context of dense and sparse particle methods was evaluated by comparison with CP-DNS data using statistically homogeneous and decaying turbulence with varying droplet loadings. The EQUAL model used in dense particle methods has led to good agreement of the mean temperature, but unconditional and conditional variances were consistently too low as the model does not generate any composition fluctuations at subgrid scale. The sparse-Lagrangian MMC-LES model employing a one-to-one coupling between the droplets and the stochastic particles showed good agreement of unconditional mean and rms and is superior to the EQUAL model in predicting the mixture fraction variance and PDF, since source terms are not distributed evenly among the gas-phase particles but preferentially to individual particles. However, the model also suffers from the fact that the conditional variance is too low, which is attributable to the relatively large particle volume resulting from the sparse particle distribution, implying artificial mixing and thus enhancing chemical reactions. The

one-to-one coupling strategy was also applied to a dense particle method, where a selection of the closest particle in physical space has led to significant improvements compared to the EQUAL model for both unconditional and conditional statistics. Nevertheless, due to the smaller volume of gas-phase particles, the performance of the model is expected to exhibit a dependence on the number of stochastic particles. Naud's SAT model, which was originally derived for dense particle methods, provides alternative coupling and was applied to the sparse-Lagrangian MMC model for the first time. It has produced a reasonable match of the conditional statistics, but significantly overestimated the unconditional variances, as source terms are concentrated on a small number of gas-phase particles, resulting in an overprediction of the conditions at the saturation state. If was found that these effects are enhanced by the sparse particle number, so that the model cannot be recommended to be used in combination with the MMC-LES model.

To improve the model predictions in the context of a sparse particle method, possible modifications and combinations of the one-to-one coupling strategy with the SAT model were proposed. Limiting the number of droplets coupled with a stochastic particle could decrease the overpredicted range of mixture and temperature values, thus reducing the unconditional variance, but significant deviations from the CP-DNS data remained. A simple blending between the one-to-one coupling and the SAT model allowed to generate arbitrary variances in between the two models, giving partial improvement of the results in particular at the beginning of the simulation, but generally requires a time-dependent weighting factor to achieve agreement throughout the entire simulation. A model extension that is more consistent with the MMC philosophy was obtained by adding the distance in saturation space to the effective square distance for two-phase coupling. However, this model produced results similar to the SAT model after a certain transitional period, as the preferential selection of particles close to saturation conditions was amplified during the evaporation process. To overcome the artificial mixing induced by the large particle volume, a time delay model was proposed, where source terms are transferred partially instead of entirely to the gas-phase particles using a finite mixing time. Although the results showed that chemistry was slightly delayed, leading to minor improvements of the unconditional temperature predictions, the present model formulation could not solve the problem of artificial mixing on the gas-phase particles, as source terms are still transferred to the entire volume of the particles.

An ideal two-phase coupling should predict both the correct amount of unconditional variance and the conditional fluctuations resulting from the interaction between evaporation and chemistry. The results presented in this chapter have shown that for a sparse particle distribution the latter can be taken into account by

either coupling a larger number of droplets with a stochastic particle (which significantly increases the unconditional fluctuations), or by distributing the evaporated mass to a smaller volume (which is not trivial in a sparse particle method). Two possible solutions should be mentioned here. First, one could introduce a set of smaller gas-phase particles that are selected to receive the source terms, with the fuel mass subsequently transferred gradually to the larger particles by mixing. This could reflect the locally high fuel concentrations found at the droplet positions, while the unconditional variance would not be biased due to low mass of these particles. Secondly, a revision of the time delay model using two subvolumes and incorporating ideas from the eddy dissipation concept (EDC) could achieve a similar effect, since evaporation and combustion take place in separate subvolumes. However, none of these approaches is easy to implement, and introduces additional complexity to the MMC-LES model. Accordingly, the one-to-one coupling technique appears to be the most appropriate closure for the sparse-Lagrangian MMC-LES model at present due to its simplicity and similarity with the MMC mixing pair selection. Further, the next chapter will show that the model limitations identified here often play a minor role in practical applications.

Chapter 7

A Priori Testing of the Two-Phase MMC-LES Model

The following chapter provides an in-depth a priori analysis and validation of the sparse-Lagrangian two-phase MMC-LES model using a temporally evolving droplet-laden double shear layer. The analysis is based on the work published by Sontheimer et al. [197], but is adapted and extended to the current state of research. Since the previous chapter has demonstrated the superior performance of the one-to-one coupling strategy, the method is further examined here, where the focus is now on the selection of suitable gas-phase particles to evaluate the conditional evaporation rate. Results are presented for different conditioning variables with the intention of enforcing localness in composition space of the two-phase coupling, introducing also the concept of double conditioning. Furthermore, the sensitivity of the two-phase MMC-LES model towards MMC modeling parameters is evaluated.

7.1 Computational Setup

7.1.1 Description of the CP-DNS

A temporally evolving droplet-laden double shear layer is considered, as illustrated in Fig. 7.1, which approximates the spatial evolution of a turbulent planar spray flame. The central fuel jet carries the liquid droplets and is surrounded by two oxidizer streams consisting of air and streaming in the opposite direction. The initial velocity and mixture fraction fields are based on the setup of Hawkes *et al.* [78] (case L), with length and velocity scales altered to adjust the characteristic flow time scale to the time scales of evaporation and combustion while keeping the Reynolds number constant. The computational domain extends across $L_x \times L_y \times L_z = 12H \times 14H \times 8H$ with $H = 2.88\,\mathrm{mm}$ being the height of the central

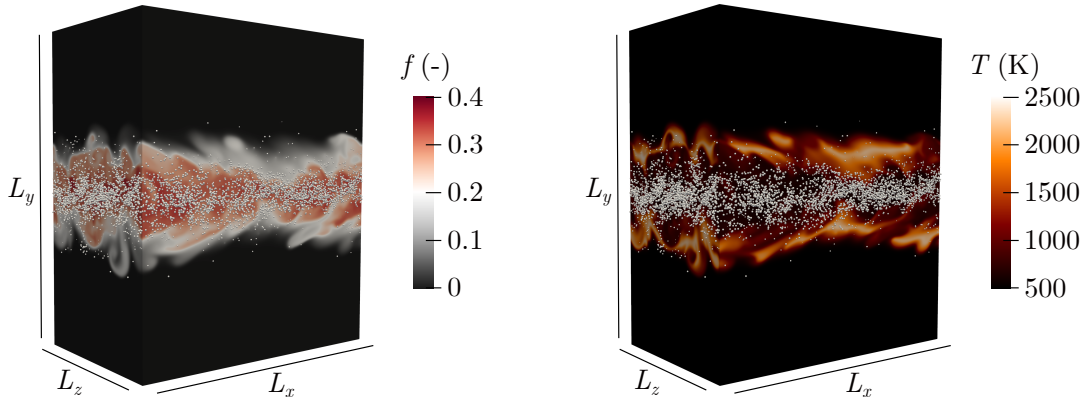

(a) Mixture fraction. **(b)** Temperature.

Figure 7.1: Visualization of the temporally evolving droplet-laden double shear layer at time $t/t_j = 30$, showing the instantaneous mixture fraction (left) and temperature (right) field of the CP-DNS as well as the liquid fuel droplets (gray dots, scaled by a factor of ten for better visibility).

jet. The characteristic jet velocity, describing the relative difference between the fuel and the oxidizer streams, is $U = U_{\mathrm{Fu}} - U_{\mathrm{Ox}} = 30\,\mathrm{m/s}$, corresponding to a cold-jet Reynolds number of $\mathrm{Re} = UH/\nu_{\mathrm{Fu}} = 2510$, and the characteristic jet time scale is $t_j = H/U = 96\,\mu\mathrm{s}$. Turbulent fluctuations with an integral length scale of $l_{\mathrm{int}} = H/3$ and a turbulence intensity of $I = 5\,\%$ are superimposed on the mean velocity field in the jet region in order to trigger the evolution of shear-generated turbulence (cf. Fig. 7.2(a)). The gaseous part of the central fuel jet is composed of nitrogen and pre-evaporated ethanol with a temperature of $T_{\mathrm{Fu}} = 500\,\mathrm{K}$ and an initial mixture fraction of two times the stoichiometric value ($f_{\mathrm{Fu}} = 2f_{\mathrm{st}} \approx 0.23$). The oxidizer stream is composed of pure air with mass fractions $Y_{\mathrm{N_2}} = 0.724$ and $Y_{\mathrm{O_2}} = 0.276$ and a temperature of $T_{\mathrm{Ox}} = 500\,\mathrm{K}$. The spatial distribution of the species mass fractions and the temperature is initialized using a laminar flamelet solution, leading to the existence of a thin laminar flame in the shear region to ignite the gas mixture once the two streams have mixed. The resulting initial mixture fraction and temperature profiles are shown in Fig. 7.2(b). Chemistry is governed by a global single-step mechanism for ethanol combustion in air [228], and the pressure is set to the atmospheric value.

The liquid droplets consist of pure ethanol and are randomly distributed within the central jet with $-0.5H \leq y_{d,0} \leq 0.5H$. The droplets have an initial diameter of $d_0 = 30\,\mu\mathrm{m}$ and an initial velocity equal to the local gas velocity. The initial droplet temperature is chosen to match the wet-bulb temperature according to the initial jet conditions and is set to $T_{d,0} = 315\,\mathrm{K}$. The number of droplets in the jet is $N_d \approx 80\,000$, corresponding to an overall equivalence ratio of $\Phi = 0.5$ and an initial nominal droplet distance of $\Delta_L/d_0 \approx 10$.

The computational domain is discretized by $N_x \times N_y \times N_z = 288 \times 336 \times$

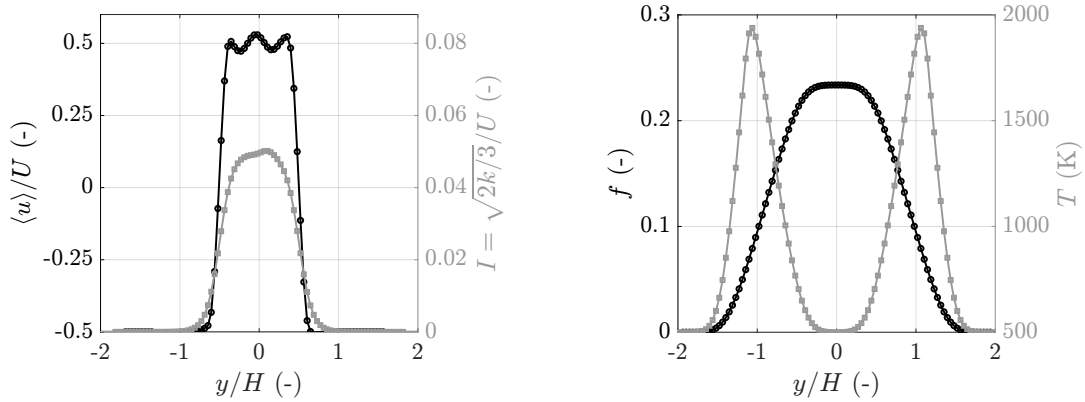

(a) Mean axial velocity and turbulence intensity. **(b)** Mixture fraction and temperature.

Figure 7.2: Initial profiles of the droplet-laden double shear layer configuration, plotted versus the normalized cross-stream direction. Symbols denote the cell values of the DNS mesh.

$192 \approx 18.6\,\mathrm{M}$ grid cells, resulting in a uniform cell size of $\Delta x = 120\,\mu\mathrm{m}$. This grid resolution has proven to be sufficient for the original single-phase configuration [40, 217, 218], and a grid convergence study for the present droplet-laden configuration has revealed little effect of the mesh on the unconditional and conditional statistics (cf. Appendix F). Periodic boundary conditions are applied in streamwise (x) and spanwise (z) directions, and non-reflecting boundary conditions are used in the cross-stream (y) direction. An additional LES mesh is defined for post-filtering the CP-DNS data to provide input data for the MMC-LES model. The LES cell size is set to $\Delta_{\mathrm{LES}} = 4\Delta x$, which ensures that 80 % of the turbulent kinetic energy is resolved by the LES field throughout the entire simulation time, as is common in LES [163, 164]. The calculation of the turbulent diffusivity, which is required for the mixing model, from the post-filtered DNS fields follows the same procedure as described in Sec. 6.1. As shown in Fig. 7.3, this leads to reasonable agreement between the models and the exact data extracted from the CP-DNS, where the discrepancies are largest in the central jet region and attributed to the effect of the droplets.

Simulations are run for 40 characteristic jet time scales, where the time step is adjusted dynamically to ensure a maximum Courant number of $\mathrm{CFL}_{\mathrm{max}} = 0.4$. The numerical solver and the discretization schemes are the same as described in Sec. 6.1, and computing times are reported in Appendix F.

7.1.2 Description of the MMC-LES Model

The sparse-Lagrangian MMC-LES model is used in combination with the a-ISO model for the mixing time scale and the one-to-one coupling strategy for two-phase coupling according to Eq. (4.60). In contrast to Ch. 6, where the evaporation rate for

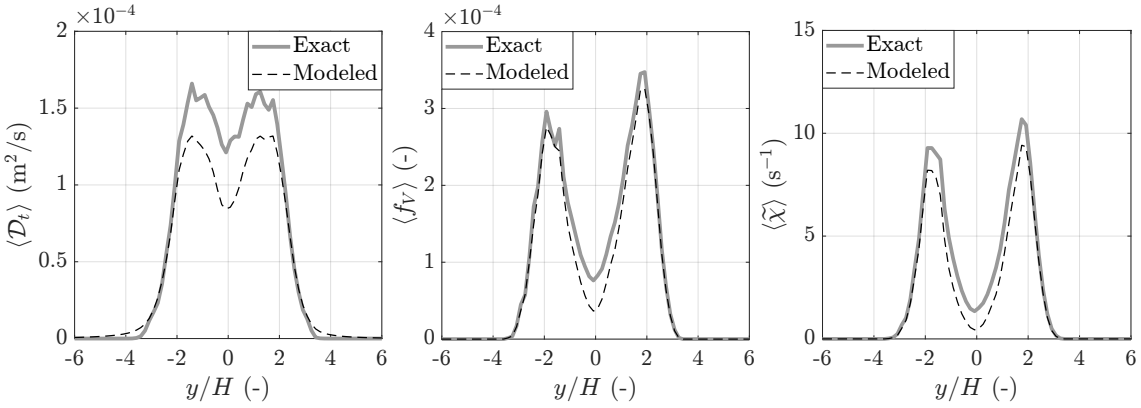

(a) Turbulent diffusivity. **(b)** Mixture fraction subgrid variance. **(c)** Filtered scalar dissipation rate.

Figure 7.3: Comparison of modeled and exact turbulent diffusivity, mixture fraction subgrid variance and filtered scalar dissipation rate at time $t/t_j = 30$. The data are averaged in homogeneous directions x and z and plotted versus the normalized cross-stream coordinate y/H. The modeled quantities are calculated using the models presented in Ch. 4, while the exact data are extracted from the CP-DNS using explicit filtering.

the stochastic particle solution was extracted from the CP-DNS, it is now calculated based on the properties of the stochastic particles, as described in Sec. 4.5. This allows for a comparison of the evaporation quantities predicted by the stochastic particle method with those of the CP-DNS, as explained in Sec. 4.7.3, thus enabling further validation of the two-phase MMC-LES model. The stochastic particles are distributed uniformly across the entire domain with a particle number of $N^{sp} = 36\,288$, which corresponds to one (Lagrangian) particle per eight (Eulerian) LES cells and is denoted as 1L/8E. This resolution was found to provide sufficient data to obtain convergent statistics while representing a sparse particle distribution that generally requires conditioning. The effect of the stochastic particle number density will be discussed later in Sec. 7.3.1.

The MMC mixing model requires the specification of suitable mixing parameters r_m and f_m, representing characteristic distances between mixing particles in physical and reference mixture fraction space, respectively. Previous works [60, 60, 70, 89, 205, 218] have established $f_m = 0.03$ as a standard parameter for single-phase flows, where mixture fraction ranges from zero to one. In flows involving droplet evaporation, mixture fraction is below unity (cf. Sec. 4.1.2), resulting in a smaller separation of the mixing pairs in mixture fraction space. For this reason, a scaling of f_m is suggested in order to keep the relative weighting between distances in physical and mixture fraction space unchanged (cf. Eq. (4.51)). Assuming a maximum mixture fraction of about $f_{\mathrm{max}} \approx 0.4$ for the present setup (cf. Fig. 7.4(a)), scaling of the standard value yields $f_m = 0.012$. The corresponding value $r_m = 1\,\mathrm{mm}$ is calculated from the isoscalar sliver relation, which is given by Eq. (4.52) and evaluated

using the maximum filtered gradient of the initial mixture fraction field. Analysis of the simulation results will show whether these parameters are appropriately chosen, and the effect of f_m will be examined in more detail later in Sec. 7.3.2.

Similar to the MMC mixing model, the two-phase coupling based on Eq. (4.60) requires the specification of suitable coupling parameters r_m^* and f_m^*, which represent characteristic distances between the droplets and the stochastic particles in physical and reference mixture fraction space, respectively. Appendix C provides a detailed analysis of distances between particles of two independent particle clouds, with the result that the average distance between the fuel droplets and the stochastic particles is identical to the mean inter-particle distance of the stochastic particle cloud. This generally allows to use the same parameters for two-phase coupling (r_m^*, f_m^*) as used for mixing (r_m, f_m). However, since different algorithms are employed for the minimization of the respective effective square distances (Eqs. (4.51) and (4.60)), the real mean inter-particle distances are different. As demonstrated in Appendix C, a direct search method, which is used for two-phase coupling, yields on average smaller distances between droplets and stochastic particles than the k-d-tree algorithm, which is used to form mixing pairs, would provide. Accordingly, the two-phase coupling parameters are estimated based on the relation $r_m/r_m^* = f_m/f_m^* = 1.66$, where the specific ratio was found by numerical calculations assuming a four-dimensional space comprised of physical space and mixture fraction space (see Appendix C for details). This scaling, which results in $f_m^* = 0.0072$ and $r_m^* = 0.6\,\mathrm{mm}$, will be confirmed later by comparison of the two-phase coupling parameters with real distances calculated from the simulation data (cf. Sec. 7.3.2).

7.2 Detailed Analysis of the Sparse-Lagrangian Two-Phase Coupling

7.2.1 Two-Phase Coupling Conditional on Mixture Fraction

The conditional evaporation rate that appears in the transport equations of the stochastic particles (Eqs. (4.38) and (4.39)) is evaluated by minimizing the effective square distance between the droplets and the stochastic particles in physical and reference mixture fraction space (Eq. (4.60)). To assess the importance of conditioning the droplet-particle pairing on the composition space, additional simulations are performed using a particle selection in either pure physical space ($\lambda_f = 0$) or pure reference mixture fraction space ($\lambda_x = 0$), the latter of which was used in the

two-phase MMC-LES model of Khan *et al.* [102]. The three cases are denoted as $(x, 0)$ for a particle selection in pure physical space, $(x, \widetilde{f})$ for a particle selection in both physical and reference mixture fraction space, and $(0, \widetilde{f})$ for a particle selection in pure reference mixture fraction space. Note that only the particle selection for the two-phase coupling is changed, but not the selection of particle pairs for the MMC mixing model, which is always based on physical and reference mixture fraction space according to Eq. (4.51).

Figure 7.4 shows the mean and root-mean-square (rms) of temperature and mixture fraction predicted by the stochastic particle method and compared to the CP-DNS at different times. The data are averaged in homogeneous directions x and z and plotted versus the normalized cross-stream coordinate y/H (cf. Fig. 7.1). There is very good agreement of the MMC model predictions with the CP-DNS data for the mean and rms of mixture fraction, and the profiles are hardly affected by the particle assignment. Only the particle selection in pure reference mixture fraction space, case $(0, \widetilde{f})$, shows a slight reduction of the peak maximum mixture fraction, and an explanation will be given later. The good agreement of the mixture fraction rms in the jet region indicates that the variance generated by the evaporating droplets is accurately reproduced, as was discussed in detail in the previous chapter. Looking at the temperature predictions shown in Figs. 7.4(c) and 7.4(d), some differences between the stochastic particle results can be observed. In all three simulations, the maximum mean temperature is underpredicted by about 100 K to 200 K, where again case $(0, \widetilde{f})$ exhibits the largest deviations from the CP-DNS. Possible reasons for the consistent underprediction of the temperatures will be discussed in more detail in the following. It is noteworthy that a particle selection in pure physical space, $(x, 0)$, leads to similar predictions of the unconditional averages as a particle selection conditional on physical and reference mixture fraction spaces, $(x, \widetilde{f})$, so that conditioning does not seem to be necessary here. However, typical MMC applications often have an even lower particle number density, and therefore a particle selection without conditioning is not always expected to be successful.

Scatter plots of temperature versus mixture fraction along with the conditional mean temperature are shown in Fig. 7.5 at time $t/t_j = 30$, indicating a considerable amount of local flame extinction and re-ignition. Both the conditional mean temperature and the amount of conditional fluctuations are adequately represented in all three cases, although a particle selection in pure reference mixture fraction space produces a slightly lower conditional mean temperature and thus more gas-phase particles well below the equilibrium temperature. It should be noted that the consistent underprediction of the conditional fluctuations that was reported in Ch. 6 and attributed to the large particle volume cannot be observed here, which is a

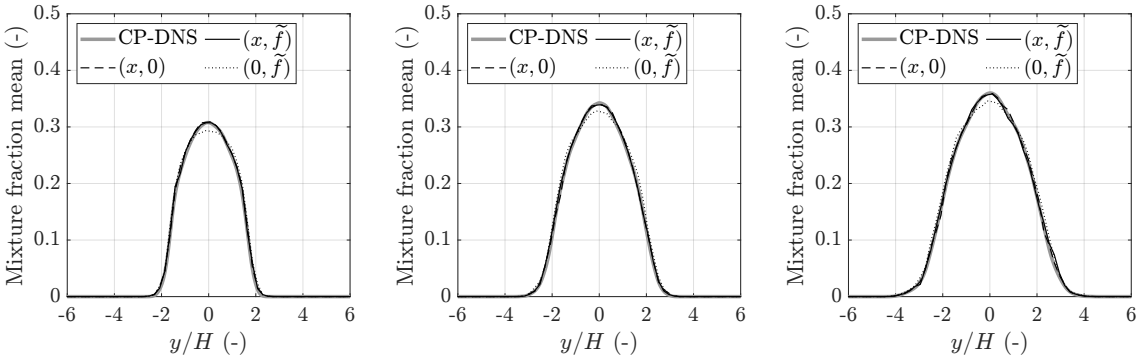

(a) Mixture fraction mean at times $t/t_j = \{20, 30, 40\}$ (from left to right).

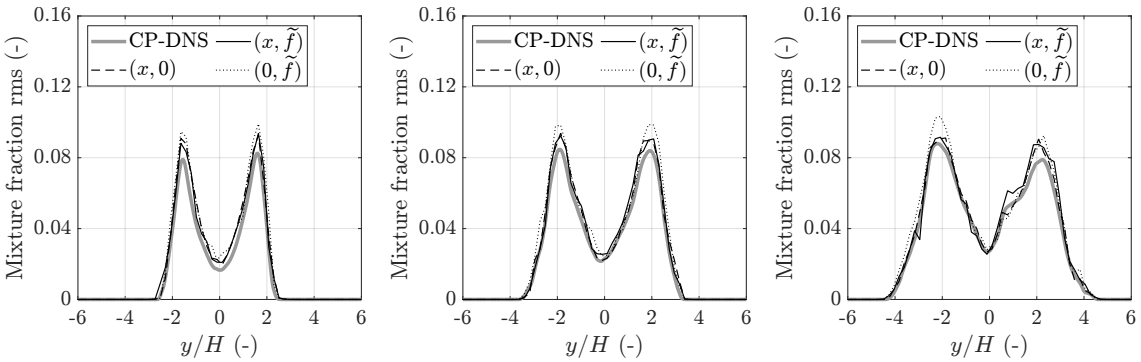

(b) Mixture fraction rms at times $t/t_j = \{20, 30, 40\}$ (from left to right).

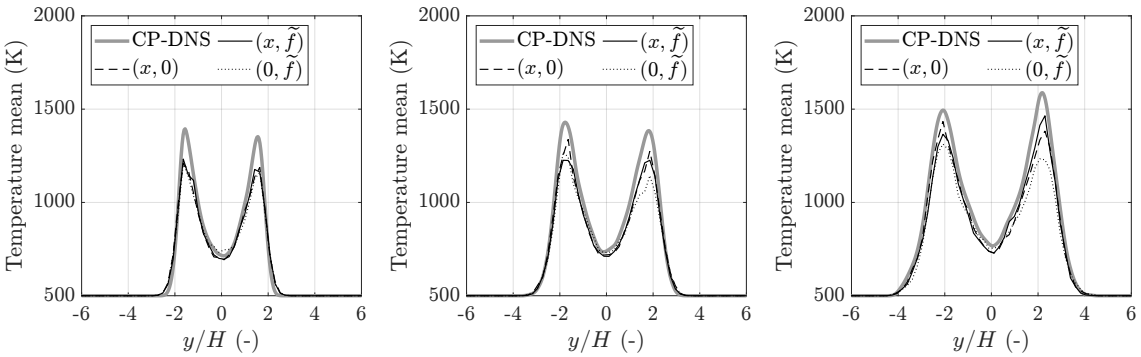

(c) Temperature mean at times $t/t_j = \{20, 30, 40\}$ (from left to right).

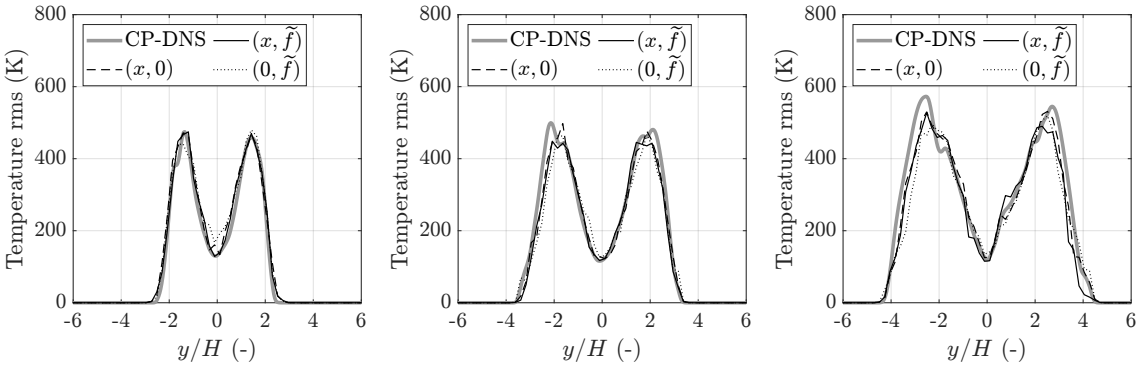

(d) Temperature rms at times $t/t_j = \{20, 30, 40\}$ (from left to right).

Figure 7.4: Mean and rms of mixture fraction and temperature obtained from the sparse-Lagrangian MMC-LES model using the one-to-one coupling strategy and a particle number density of 1L/8E.

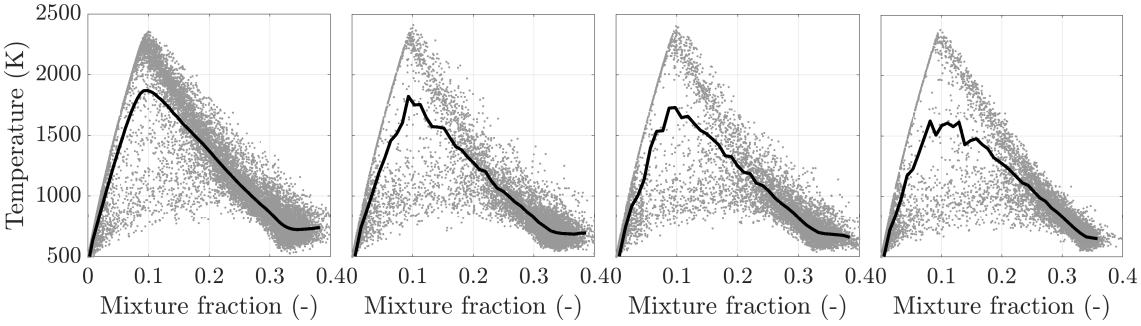

(a) CP-DNS. **(b)** $(x, 0)$. **(c)** $(x, \widetilde{f})$. **(d)** $(0, \widetilde{f})$.

Figure 7.5: Scatter plots of temperature versus mixture fraction at time $t/t_j = 30$ obtained from the sparse-Lagrangian MMC-LES model using the one-to-one coupling strategy and a particle number density of 1L/8E. For better clarity, the plots show only a sample of the simulation data. The black line denotes the conditional mean temperature.

result of the different physical configurations. While Ch. 6 assumed a homogeneous distribution of turbulence and droplets, with combustion occurring in the immediate vicinity of the droplets, the present double shear layer configuration exhibits a distinct separation between evaporation, which takes place in the central jet, and combustion, which occurs in the shear region. As a result, most of the droplets do not interact with the flame, and the conditional fluctuations in the present configuration are mainly caused by the interactions between turbulence and chemistry.

A comparison of droplet properties obtained from the stochastic particle methods and the CP-DNS is depicted in Fig. 7.6 by showing the PDF of the droplet diameter at different times. It can be seen that a particle selection in pure reference mixture fraction space leads to a larger deviation from the CP-DNS with a more narrow distribution of droplet diameters. In contrast, particle selections that take into account the distance in physical space, i.e., cases $(x, 0)$ and $(x, \widetilde{f})$, give very good agreement, which shows that the evaporation process is accurately reproduced by the sparse particle method.

Analysis of the two-phase coupling relations between the fuel droplets and the gas-phase particles provides explanations for the trends described above. Figure 7.7 visualizes the two-phase coupling relations for the three simulations in a two-dimensional slice, showing the filtered reference mixture fraction field superimposed by the fuel droplets and the stochastic particles, with lines indicating the assignments of the droplets to the stochastic particles. If particles are selected in pure physical space, as shown in Fig. 7.7(a), each droplet is paired with its nearest gas-phase particle, resulting in the smallest distances in physical space. For sufficiently high particle number densities, proximity in physical space also implies proximity in composition space. However, the particle selection in pure physical space cannot prevent coupling of droplets with gas-phase particles across the flame

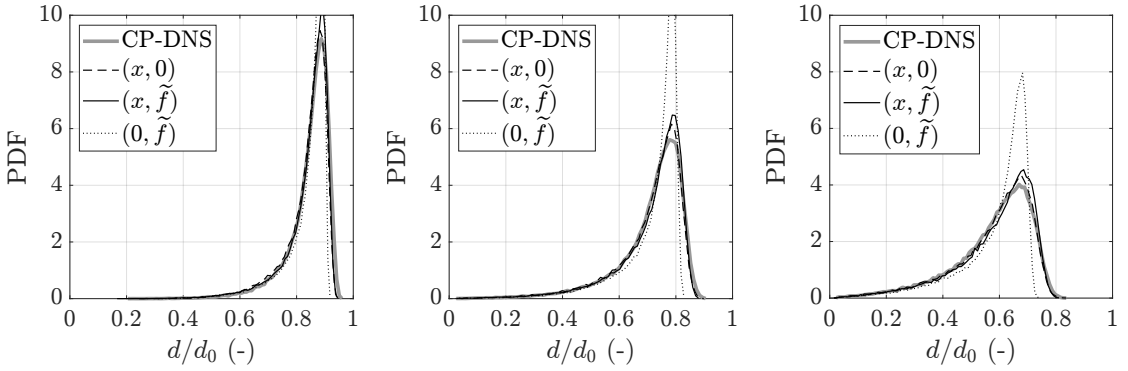

(a) $t/t_j = 20$. **(b)** $t/t_j = 30$. **(c)** $t/t_j = 40$.

Figure 7.6: PDF of the droplet diameter obtained from the sparse-Lagrangian MMC-LES model using the one-to-one coupling strategy and a particle number density of 1L/8E.

(highlighted by the blue circle in Fig. 7.7(a)), with the result that the gas compositions found at the position of the droplet and that represented by the stochastic particle may differ greatly. A particle selection that explicitly minimizes distances in both physical and reference mixture fraction space according to Eq. (4.60) is shown in Fig. 7.7(b). The coupling relations generally look similar to the particle selection in pure physical space (Fig. 7.7(a)), but a closer look reveals some differences. As the distance in mixture fraction space is taken into account, droplets are often no longer paired with their nearest gas-phase particles, which increases the distances in physical space (but still keeps them moderate). Furthermore, the minimization of the effective square distance is able to largely prevent droplets from being paired with particles across the flame. Finally, Fig. 7.7(c) shows the coupling relations for a particle selection in pure reference mixture fraction space. This leads to significantly increased distances in physical space, which are limited only by the underlying super mesh (cf. Sec. 4.7.2). Moreover, it can be observed that droplets are primarily coupled with the particles in the streamwise direction, but not in the cross-stream direction, where the gradients of mixture fraction are large. Finally, it should be noted that in all three cases some particles are coupled with a larger number of droplets, while some particles are not coupled with any droplet even if they are located in the central jet region. In Fig. 7.7, the number of droplets per particle is indicated by the size of the red dots, while particles that are not coupled with a droplet are marked by red crosses. This inhomogeneity leads to an increase of the scalar variance in the stochastic particle field, as discussed earlier (cf. Fig. 6.6).

An alternative visualization of the coupling relations is obtained by plotting them in the composition space, as shown in Fig. 7.8. It can be seen that the two-phase coupling mainly takes place at high mixture fraction and low temperature values, which are associated with the jet conditions. However, some droplets are

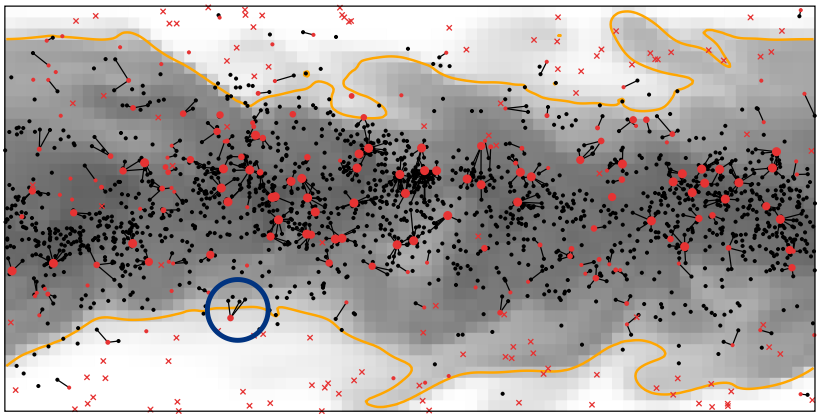

(a) Two-phase coupling with particle selection in pure physical space. The blue circle marks unphysical coupling across the flame.

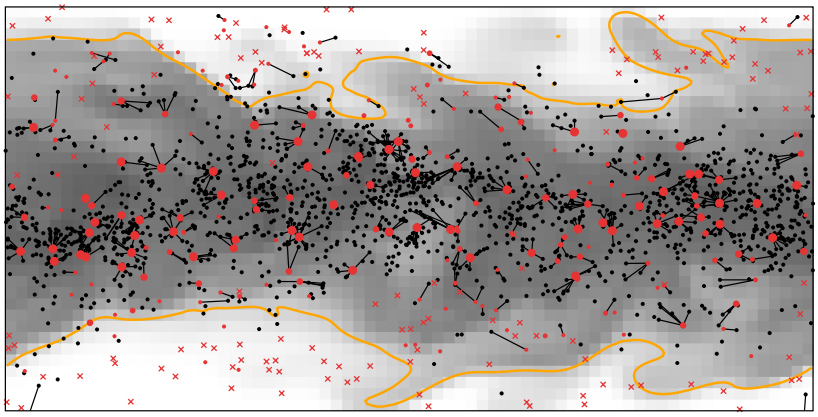

(b) Two-phase coupling with particle selection in physical and reference mixture fraction space.

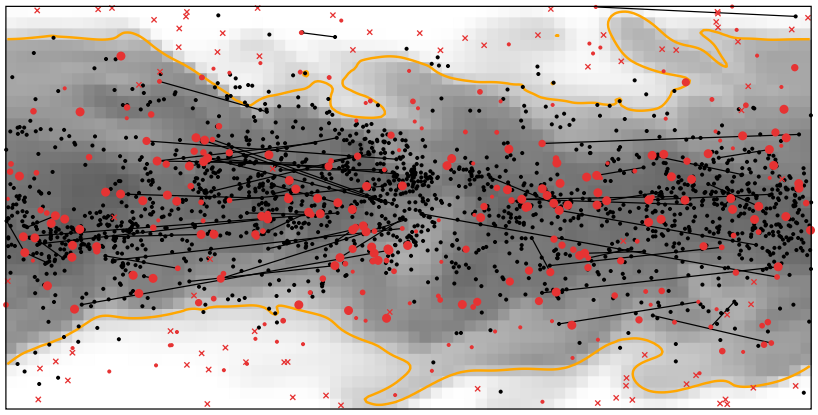

(c) Two-phase coupling with particle selection in pure reference mixture fraction space.

Figure 7.7: Visualization of the two-phase coupling relations at time $t/t_j = 30$ using the one-to-one coupling strategy and a particle number density of 1L/8E. The background shows the cell values of the filtered reference mixture fraction field in the x-y slice through the origin, and the orange line indicates the flame position (stoichiometric mixture fraction value). Black dots mark the droplets and red symbols the stochastic particles, both of which are shown within the layer $-\Delta_{\mathrm{LES}}/2 \leq y \leq \Delta_{\mathrm{LES}}/2$. Stochastic particles are scaled by the number of droplets coupled with them, or indicated by a cross if no droplets are coupled with them. Black lines indicate the droplet-particle pairs if both are inside the specified layer (not every droplet shown is connected to a gas-phase particle, as the coupling partner can also be found outside the specified layer).

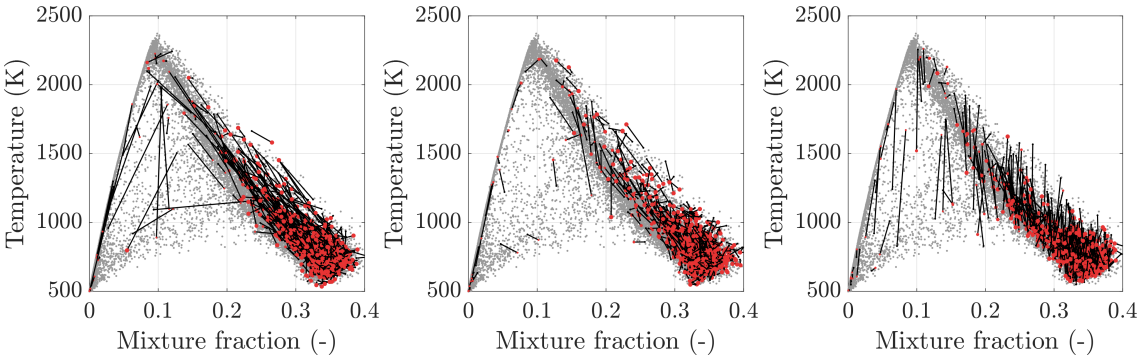

(a) $(x, 0)$. **(b)** $(x, \widetilde{f})$. **(c)** $(0, \widetilde{f})$.

Figure 7.8: Visualization of the two-phase coupling relations in composition space at time $t/t_j = 30$ using the one-to-one coupling strategy and a particle number density of 1L/8E. The black lines show a random selection of droplets (black dots) coupled with stochastic particles (red dots), which are plotted using their interpolated LES values. Gray dots in the background show the scatter plot of the CP-DNS for reference (Fig. 7.5(a)).

also located in regions with lower mixture fraction values, where the different particle selections show qualitative differences. A selection of gas-phase particles in pure physical space (Fig. 7.8(a)) can result in large distances in both mixture fraction and temperature space, since it does not enforce localness in composition space. The increased separation in composition space can be largely reduced by using a particle selection that minimizes distances in both physical and reference mixture fraction spaces (Fig. 7.8(b)). In contrast, if particles are selected in pure mixture fraction space (Fig. 7.8(c)), large distances in temperature space (up to 1000 K) can be observed between the droplets and the gas-phase particles. This is due to a lack of correlation between mixture fraction and temperature caused by the effect of local extinction. As a result, the same mixture fraction value may be associated with different temperatures, so that minimizing distances in pure mixture fraction space does not necessarily imply localness in composition space. The coupling of droplets, which are typically located in regions of low temperature, with hot gas-phase particles can lead to flame extinction, thus reducing the unconditionally and conditionally averaged temperatures (cf. Figs. 7.4(c) and 7.5(d)), as well as to an enhanced evaporation process, which explains the deviation of the PDF of the droplet diameter (cf. Fig. 7.6).

7.2.2 Double Conditioning on Mixture Fraction and Temperature

Improvements may be obtained by introducing additional conditioning variables for the two-phase coupling. As the evaporation process is mainly controlled by the gas-phase temperature and mixture fraction does not perfectly correlate with

it, a conditioning of the particle selection on both Eulerian mixture fraction and temperature is introduced,

$$\hat{d}^2_{d,sp} = \underbrace{\underbrace{\lambda_x \sum_{i=1}^{3} \left(\frac{d^{d,sp}_{x_i}}{r^*_m/\sqrt{3}} \right)^2 + \lambda_f \left(\frac{d^{d,sp}_f}{f^*_m} \right)^2}_{\text{Single conditioning}} + \lambda_T \left(\frac{d^{d,sp}_T}{T^*_m} \right)^2}_{\text{Double conditioning}}, \tag{7.1}$$

which is referred to as double conditioning. Here, $d^{d,sp}_T = |\widetilde{T}(\mathbf{x}_d) - \widetilde{T}(\mathbf{x}^{sp})|$ denotes the distance between the droplets and the stochastic particles in the temperature space, with temperature being interpolated from the filtered Eulerian field to the respective particle positions, and T^*_m is a suitable normalization parameter analogous to f^*_m. The parameter could in principle be determined using an equivalent isoscalar sliver relation based on the characteristic temperature gradient, or alternatively using an analogy between the characteristic temperature and mixture fraction ranges. Both approaches have shown to yield similar values, with $T^*_m = 40\,\mathrm{K}$ used in the present work. It should be noted that the additional reference variable will alter the coupling distances and thus their relative weighting, so that an adjustment of the coupling parameters is generally required (see Straub *et al.* [202] for a discussion). However, for simplicity, the values determined on the basis of single conditioning are retained in the present work. Again, boolean variables λ_x, λ_f and λ_T are used to realize different particle selections, e.g., a particle selection in pure mixture fraction and temperature space, which is denoted as $(0, \widetilde{f}, \widetilde{T})$.

Figures 7.9 and 7.10 show the unconditionally and conditionally averaged mixture fraction and temperature that are obtained with the proposed double conditioning using different combinations of the effective square distance, and the PDF of the droplet diameter is shown in Fig. 7.11(a). The results with single conditioning on the filtered reference mixture fraction field, case $(x, \widetilde{f}, 0)$, are also shown for comparison. Although slight improvements are obtained for the evaporation process, particularly if conditioning on physical space is omitted (Fig. 7.11(a)), the temperatures remain too low and at a similar level as that obtained with single conditioning on mixture fraction alone.

An explanation can be found by looking at the temperatures that are "seen" by the droplets, and which mainly determine the evaporation rate. In the CP-DNS the ambient temperature for the evaporation model is given by the local cell value, whereas in the stochastic particle method it is given by the temperature of the stochastic particle that is coupled with the droplet. Figure 7.12 shows a comparison of both quantities for different conditioning variables. If particles are selected conditionally on the reference mixture fraction field (Fig. 7.12(a)) there is only a weak

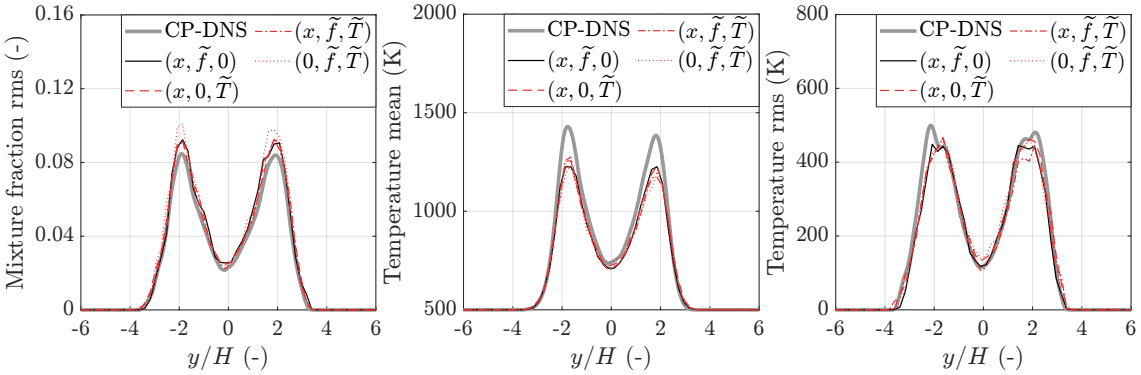

(a) Mixture fraction rms. **(b)** Temperature mean. **(c)** Temperature rms.

Figure 7.9: Mixture fraction rms and temperature mean and rms at time $t/t_j = 30$ obtained from the sparse-Lagrangian MMC-LES model (1L/8E) using the one-to-one coupling strategy with double conditioning on the Eulerian mixture fraction and temperature. The mean mixture fraction is not significantly affected and therefore not shown.

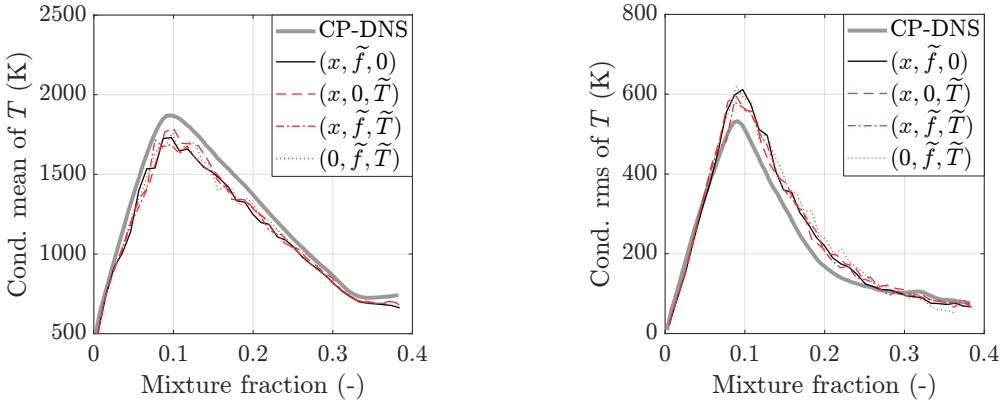

(a) Conditional mean of temperature. **(b)** Conditional rms of temperature.

Figure 7.10: Conditional mean and rms of temperature at time $t/t_j = 30$ obtained from the sparse-Lagrangian MMC-LES model (1L/8E) using the one-to-one coupling strategy with double conditioning on the Eulerian mixture fraction and temperature.

correlation between the two temperatures, as indicated by the strong scatter around the conditional mean. This is attributable to the insufficient correlation between mixture fraction and temperature, as shown in Fig. 7.5. If the Eulerian temperature is used for the particle selection, Fig. 7.12(b), the correlation is slightly improved, but strong dispersion persists. This shows that there is no clear correlation between the temperatures solved in the CP-DNS and on the stochastic particles, which makes a conditioning on the Eulerian temperature field questionable. It should be noted that this is mainly an effect that occurs if MMC is coupled with DNS, where two independent solutions for the gas-phase temperature exist. In real MMC-LES, the gas-phase temperature is calculated exclusively on the stochastic particles and subsequently mapped to the Eulerian field, which leads to an improved correlation between the two temperatures.

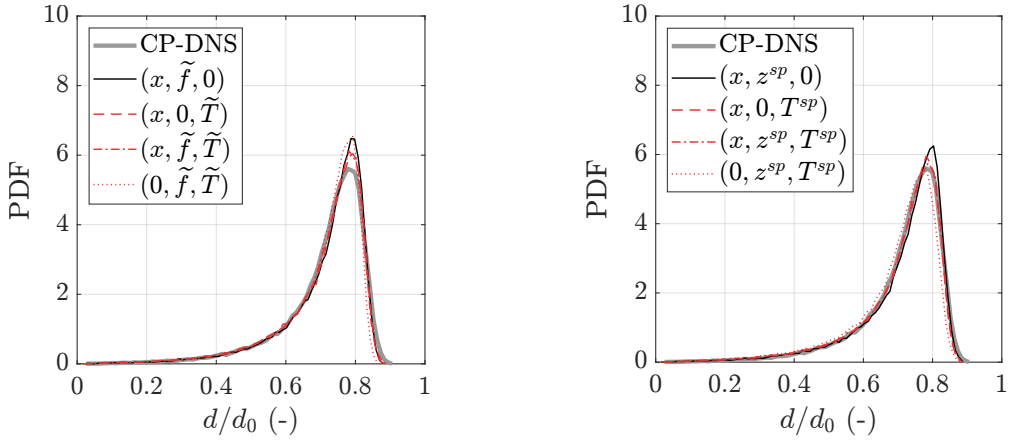

(a) Using Eulerian fields for conditioning.

(b) Using stochastic particle properties for conditioning.

Figure 7.11: PDF of the droplet diameter at time $t/t_j = 30$ obtained from the sparse-Lagrangian MMC-LES model (1L/8E) using the one-to-one coupling strategy with double conditioning on either Eulerian fields or stochastic particle properties.

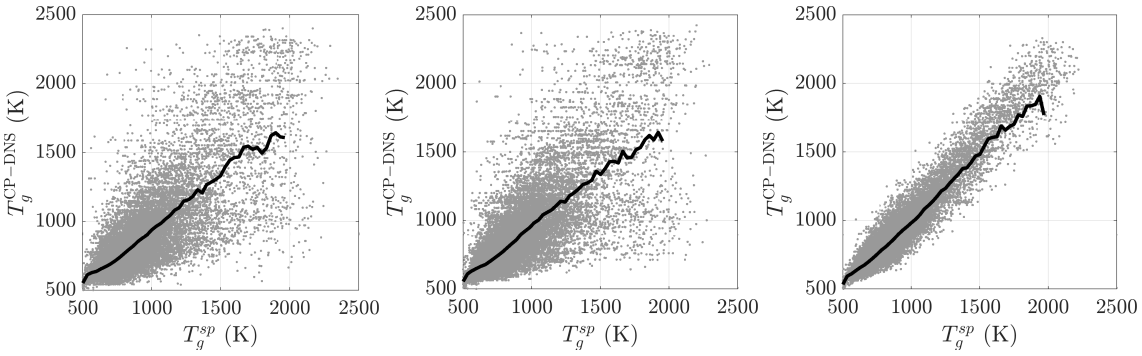

(a) $(x, \widetilde{f}, 0)$.

(b) $(x, 0, \widetilde{T})$.

(c) $(x, 0, T^{sp})$.

Figure 7.12: Scatter plots of temperature "seen" by the droplets in the CP-DNS and the MMC using different conditioning variables for two-phase coupling at time $t/t_j = 30$. The black line denotes the conditional mean.

7.2.3 Conditioning on Stochastic Particle Properties

As the droplet interacts with the gas phase that is represented by the stochastic particle, the properties of the stochastic particle may be better suited as conditioning variables. Accordingly, a new conditioning procedure is proposed that is based on the distance between the filtered Eulerian temperature at the droplet position and the temperature of the stochastic particle, i.e., using $d_f^{d,sp} = |\widetilde{f}(\mathbf{x}_d) - z^{sp})|$ and $d_T^{d,sp} = |\widetilde{T}(\mathbf{x}_d) - T^{sp})|$ in Eq. (7.1). As shown in Fig. 7.12(c), this yields a much improved correlation between the temperatures "seen" by the droplets, and thus eliminates a decorrelation of the evaporation rates in the CP-DNS and the stochastic particle solution. The remaining scatter is due to differences between the resolved temperature that is used to calculate the evaporation rate in the CP-DNS and the

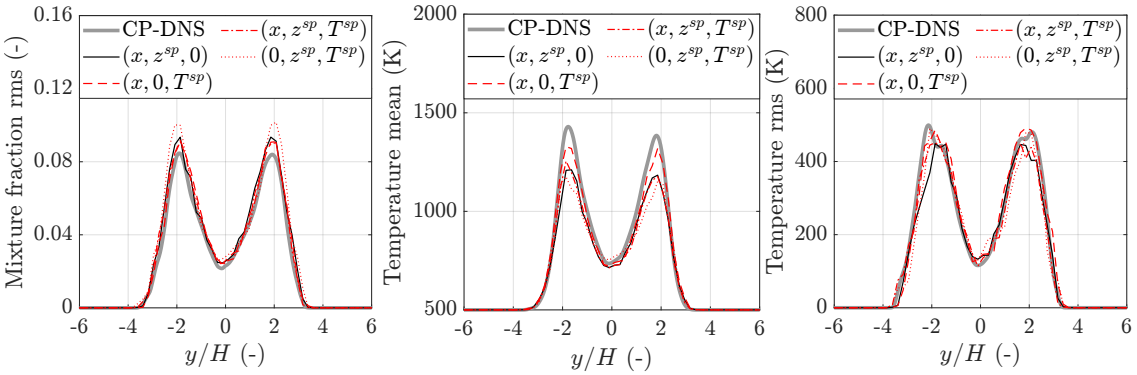

(a) Mixture fraction rms. **(b)** Temperature mean. **(c)** Temperature rms.

Figure 7.13: Mixture fraction rms and temperature mean and rms at time $t/t_j = 30$ obtained from the sparse-Lagrangian MMC-LES model (1L/8E) using the one-to-one coupling strategy with double conditioning on the stochastic particle mixture fraction and temperature. The mean mixture fraction is not significantly affected and therefore not shown.

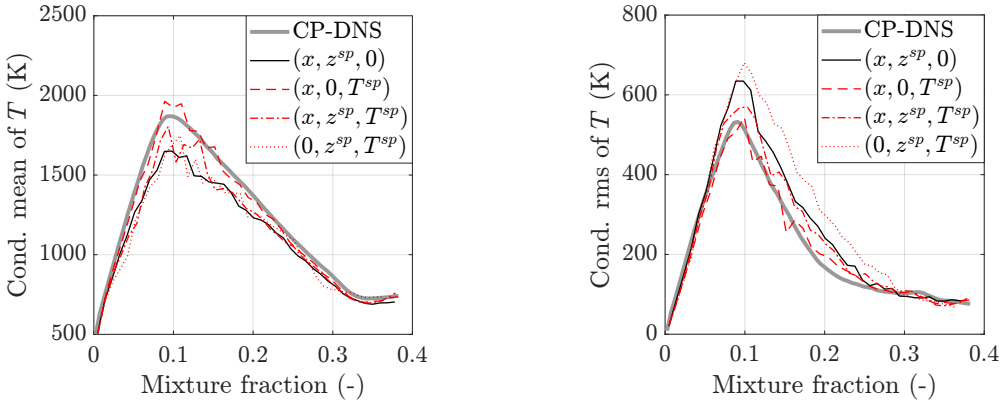

(a) Conditional mean of temperature. **(b)** Conditional rms of temperature.

Figure 7.14: Conditional mean and rms of temperature at time $t/t_j = 30$ obtained from the sparse-Lagrangian MMC-LES model (1L/8E) using the one-to-one coupling strategy with double conditioning on the stochastic particle mixture fraction and temperature.

filtered temperature that is interpolated to the droplet positions and used for the particle selection.

Mean and rms profiles of temperature and mixture fraction as well as conditional averages are shown in Fig. 7.13 and Fig. 7.14, respectively, and the PDF of the droplet diameter is shown in Fig. 7.11(b). As expected, the conditioning on stochastic particle properties leads to further improvements of the evaporation process, where in particular case $(x, 0, T^{sp})$ gives excellent agreement with the CP-DNS. Looking at the temperature predictions, it is apparent that conditioning on the mixture fraction leads to a persistent underestimation of the temperature field for the reasons stated above. In contrast, the conditioning on the stochastic particle temperature yields remarkable improvements of the unconditionally and conditionally averaged temperature, giving reasonable agreement with the CP-DNS data.

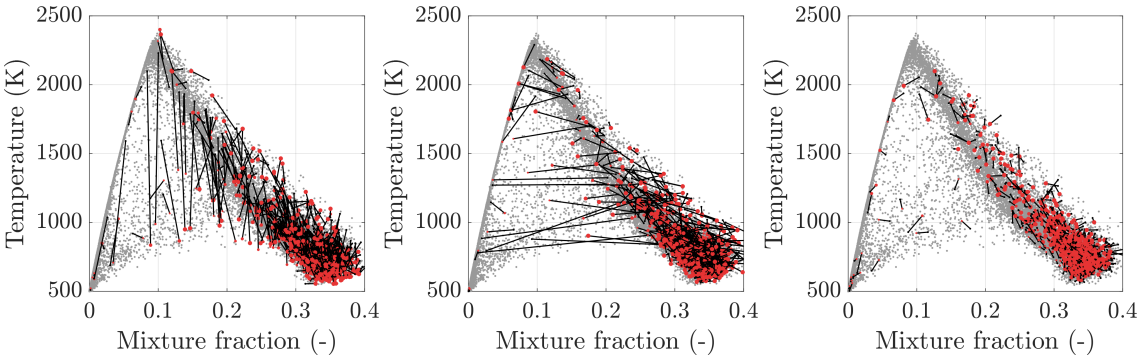

(a) $(x, z^{sp}, 0)$. **(b)** $(x, 0, T^{sp})$. **(c)** $(0, z^{sp}, T^{sp})$.

Figure 7.15: Visualization of the two-phase coupling relations in composition space at time $t/t_j = 30$ using the one-to-one coupling strategy with double conditioning on stochastic particle mixture fraction and temperature (1L/8E). The black lines show a random selection of droplets (black dots) coupled with stochastic particles (red dots), where droplets are plotted using their interpolated LES values and stochastic particles are plotted based on their particle properties. Gray dots in the background show the scatter plot of the CP-DNS for reference (Fig. 7.5(a)).

The double conditioning on mixture fraction and temperature does not lead to improvements compared to conditioning on mixture fraction alone, and the results remain almost unchanged. This might be due to the fact that the two-phase coupling parameters were estimated based on single conditioning and require further adjustment for the case of double conditioning, as mentioned earlier.

Finally, Fig. 7.15 shows a visualization of the coresponding two-phase coupling relations in the composition space. It is clear to see how a particle selection in pure mixture fraction space (Fig. 7.15(a)) minimizes the separation between the droplets and the particles in mixture fraction space, but results in large distances in the temperature space. The opposite is the case with a particle selection in pure temperature space (Fig. 7.15(b)). The best proximity in composition space is achieved by selecting particles in both mixture fraction and temperature space, as depicted in Fig. 7.15(c). Accordingly, this should minimize the error resulting from the two-phase coupling model. However, the persistent discrepancy in the temperature predictions indicates that there may be additional errors resulting from the MMC modeling, which will be examined in more detail in the following section.

7.3 Influence of the MMC Modeling Parameters

7.3.1 Effect of the Stochastic Particle Number

While in intensive particle methods the number of stochastic particles is usually sufficiently high to keep the stochastic error low and to ensure an accurate representation of the local flame structures, this is not necessarily the case if a sparse

particle distribution is used. For this reason, the influence of the particle number density will now be investigated. The simplest and most obvious approach is to increase the particle number globally. While this reduces the stochastic error and improves the flame resolution, the Monte Carlo solution progressively converges to an intensive particle method as the number of particles is increased, thus making the conditioning of mixing and two-phase coupling questionable above a certain particle number density. In sparse particle methods, numerical convergence is defined by increasing the number of particles in a way that preserves the sparse character of the mixing model [107, 205]. There are several techniques to achieve this numerically, such as the method suggested by Sundaram *et al.* [205] and used by Vo *et al.* [218], in which the ensemble of notional particles is divided into smaller subgroups for mixing in order to keep the mixing distances constant and sparse, with the number of subgroups given by the factor by which the number of particles is increased compared to the base case. In the following, both approaches (increasing the particle number globally and using multiple clouds) will be used to examine the effect of the stochastic particle number.

First, the numerical convergence of the two-phase MMC-LES model is evaluated by increasing the number of particles while preserving the sparse character of mixing and two-phase coupling. If the method proposed by Sundaram *et al.* [205] is applied to two-phase flows, several issues arise that need to be addressed. First, not only the mixing model but also the two-phase coupling model requires that the ensemble of particles is divided into subgroups in order to preserve the sparse character of both mixing and two-phase coupling. Second, the smaller volume of each particle resulting from a higher particle number density introduces a dependence of the evaporation process on the number of stochastic particles (cf. Sec. 5.2), and prevents the Monte Carlo solution from convergence if the number of particles is increased. Therefore, an alternative approach is used here, in which the number of particles is increased by introducing additional particle clouds. Each cloud contains the number of particles of the base case and is solved independently, which preserves the sparse character of the mixing model. The same strategy is used for the fuel droplets, i.e., for each particle cloud an additional set of droplet mass and temperature is introduced (see Sec. 4.7.3). Accordingly, each cloud represents an independent realization of the turbulent composition field, with mixing and two-phase coupling distances kept constant and sparse in each cloud. For the calculation of unconditional and conditional averages the data of all clouds is used, which reduces the stochastic error as the number of clouds is increased. Figures 7.16 and 7.17 show the results that are obtained for an increasing number of particle clouds using case $(x, \widetilde{f})$ with a particle number density of 1L/8E as base case. The equivalent

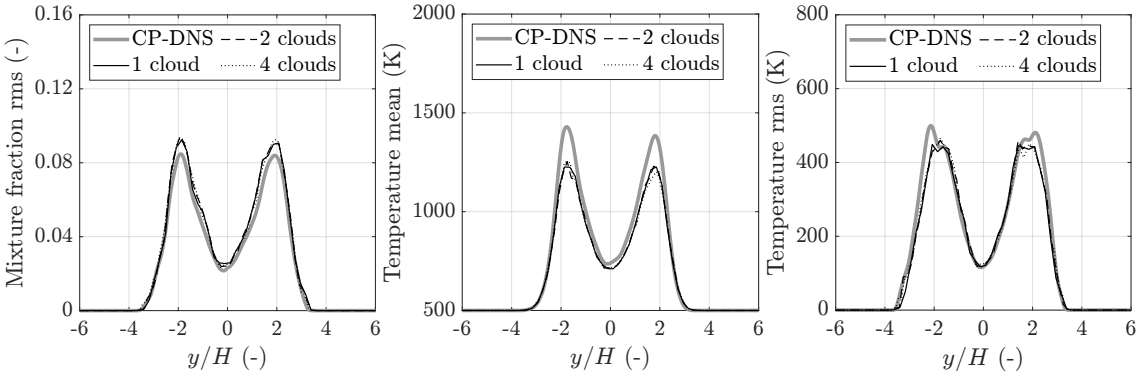

(a) Mixture fraction rms. **(b)** Temperature mean. **(c)** Temperature rms.

Figure 7.16: Mixture fraction rms and temperature mean and rms at time $t/t_j = 30$ obtained from the sparse-Lagrangian MMC-LES model using multiple particle clouds (case $(x, \widetilde{f})$ with 1L/8E per cloud).

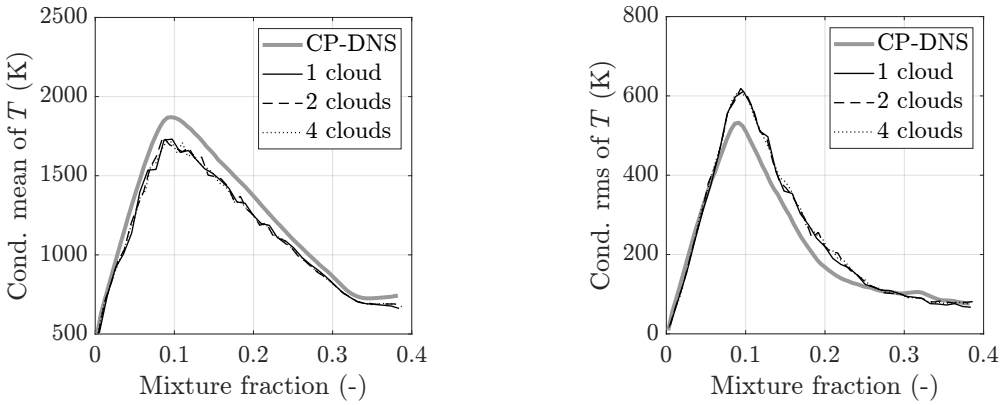

(a) Conditional mean of temperature. **(b)** Conditional rms of temperature.

Figure 7.17: Conditional mean and rms of temperature at time $t/t_j = 30$ obtained from the sparse-Lagrangian MMC-LES model using multiple particle clouds (case $(x, \widetilde{f})$ with 1L/8E per cloud).

particle number densities, calculated with the total number of particles, are given by 1L/4E and 1L/2E if two and four clouds are used, respectively. Remarkably, the results do not show any influence of the number of clouds, which proves that the particle number density of the base case is sufficiently high to keep the stochastic error low. As an alternative to using multiple clouds one could expand the domain size in the homogeneous directions, which would also increase the total number of particles while keeping the distances for mixing and two-phase coupling constant. The results obtained with this method reveal the same trends (not shown).

The previous approach has demonstrated that the stochastic error is small, but it does not indicate whether the local flame structure is accurately represented, since each cloud exhibits the same sparse particle distribution. For this reason, the particle number is now increased globally, making the particle method less sparse.

Table 7.1: MMC parameters for the simulations of the droplet-laden temporally evolving double shear layer using different particle number densities. The table lists values for the mixing parameters r_m and f_m as well as for the two-phase coupling parameters r_m^* and f_m^* as a function of the number of stochastic particles.

N^{sp}	N^{sp} per LES cell	Mixing, Eq. (4.51)		Two-phase coupling, Eq. (4.60)	
		r_m (m)	f_m (-)	r_m^* (m)	f_m^* (-)
36 288	1L/8E	$1.0 \cdot 10^{-3}$	0.012	$6.0 \cdot 10^{-4}$	0.0072
72 576	1L/4E	$7.4 \cdot 10^{-4}$	0.012	$4.5 \cdot 10^{-4}$	0.0072
145 152	1L/2E	$5.5 \cdot 10^{-4}$	0.012	$3.3 \cdot 10^{-4}$	0.0072
290 304	1L/1E	$4.1 \cdot 10^{-4}$	0.012	$2.5 \cdot 10^{-4}$	0.0072

Starting with a particle number density of 1L/8E the number of particles is increased by a factor of two, resulting in particle number densities of 1L/4E, 1L/2E and 1L/1E. Note that even the highest particle number density considered here is still much lower than in a conventional intensive particle method [208], so all simulations can be considered to be sparse. The change in the stochastic particle number density requires an adjustment of the mixing and two-phase coupling parameters, where the mixing parameters are calculated based on the isoscalar sliver relation presented in Sec. 4.4.2 and the two-phase coupling parameters are scaled accordingly, as discussed in Sec. 7.1.2. For two simulations with identical flow properties but different numbers of particles, denoted as N_1^{sp} and N_2^{sp}, the isoscalar sliver relation can be written as

$$\frac{r_{m,1}}{r_{m,2}} = \left(\frac{\Delta_{L,1}}{\Delta_{L,2}}\right)^{3/D_f} = \left(\frac{N_2^{sp}}{N_1^{sp}}\right)^{3/D_f}, \tag{7.2}$$

where parameter f_m is kept constant. The values for the mixing parameters r_m and f_m as well as for the corresponding two-phase coupling parameters r_m^* and f_m^* of the simulations with different particle numbers are reported in Tab. 7.1. The results shown in Figs. 7.18 and 7.19 reveal a strong effect of the number of particles on the temperature predictions, whereas the mixture fraction profiles are hardly affected (mean profile does not show an effect and is therefore not shown). It can be seen that an increase in the particle number results in higher temperatures, where case 1L/4E leads to almost perfect agreement with the CP-DNS data, while larger particle number densities overestimate the temperatures and underpredict the conditional fluctuations. This trend is attributable to the ambiguity of the correlation between mixture fracture and temperature, where a low number of particles can lead to global extinction due to nonlocal mixing, while the statistical significance of inadequate mixing decreases as the number of particles is increased [205]. The fact that the case with 1L/4E gives the best agreement with the CP-DNS is therefore rather coincidental, and a further increase in the number of particles seems to produce a converged solution, the accuracy of which may depend on additional parameters

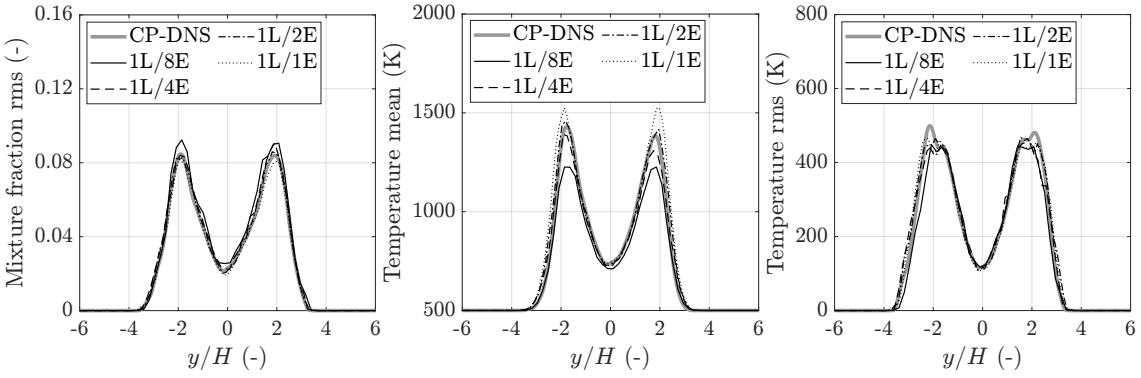

(a) Mixture fraction rms. **(b)** Temperature mean. **(c)** Temperature rms.

Figure 7.18: Mixture fraction rms and temperature mean and rms at time $t/t_j = 30$ obtained from the sparse-Lagrangian MMC-LES model (case $(x, \widetilde{f})$ with 1L/8E) using a varying number of stochastic particles.

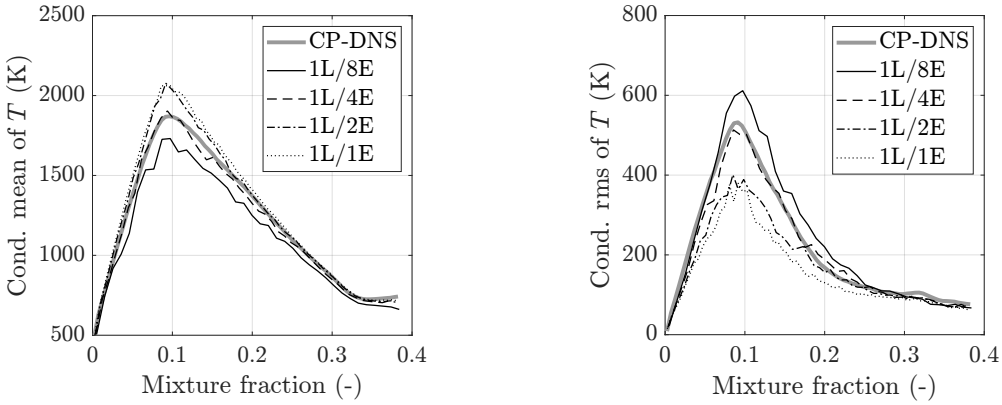

(a) Conditional mean of temperature. **(b)** Conditional rms of temperature.

Figure 7.19: Conditional mean and rms of temperature at time $t/t_j = 30$ obtained from the sparse-Lagrangian MMC-LES model (case $(x, \widetilde{f})$ with 1L/8E) using a varying number of stochastic particles.

such as the model for the mixing time scale. This effect will be investigated later. Note that an improved resolution of the local flame structures could in principle also be achieved by using a non-uniform super mesh, in which particles are concentrated in the shear region where combustion takes place. However, if the MMC-LES model is coupled with the CP-DNS, such a grid stretching is not readily realizable, since three meshes are involved (DNS mesh, LES mesh, super mesh) whose cell faces must coincide.

7.3.2 Sensitivity Towards f_m

In Sec. 7.1.2 a scaling of the standard value $f_m = 0.03$ was suggested to account for the smaller mixture fraction range in two-phase flows. This scaling will now be verified by performing simulations of case $(x, \widetilde{f})$ using different values of f_m. In

Table 7.2: MMC parameters for evaluating the sensitivity towards f_m. The table lists values for the mixing parameters r_m and f_m as well as for the two-phase coupling parameters r_m^* and f_m^* using a particle number density of 1L/8E.

Mixing, Eq. (4.51)		Two-phase coupling, Eq. (4.60)	
r_m (m)	f_m (-)	r_m^* (m)	f_m^* (-)
$1.5 \cdot 10^{-3}$	0.0048	$8.6 \cdot 10^{-4}$	0.0029
$1.0 \cdot 10^{-3}$	0.012	$6.0 \cdot 10^{-4}$	0.0072
$6.8 \cdot 10^{-4}$	0.03	$4.1 \cdot 10^{-4}$	0.0181

addition to the default value $f_m = 0.03$ and the scaled value $f_m = 0.012$, a simulation with a further reduced value of $f_m = 0.0048$ (applying the same ratio) is also performed. The corresponding values for r_m are calculated based on the isoscalar sliver relation, Eq. (4.52), and are reported in Tab. 7.2 along with the corresponding two-phase coupling parameters. Although the previous section has demonstrated that a higher particle number is required to improve the model predictions, the particle number density is kept at 1L/8E here, since conditioning and thus the effect of f_m becomes less important at higher particle numbers. Figure 7.20 shows the results for the unconditional averages, while the conditional averages are plotted in Fig. 7.21. The results indicate that there is a considerable dependence of the results on the parameter f_m, in particular for the temperature predictions. The standard value for single-phase combustion, $f_m = 0.03$, gives quite good agreement with the CP-DNS for both unconditional and conditional averages, while the smaller values for f_m underestimate the temperatures. In general, a smaller value of f_m enforces smaller distances in reference mixture fraction space, thus amplifying the effect of conditioning. However, due to the insufficient correlation between mixture fracture and temperature, a particle selection in reference mixture fraction space causes flame extinction by pairing the wrong particles with each other and with the droplets, and is thus responsible for the underpredicted temperatures. In contrast, a larger value of f_m reduces the effect of the conditioning and thus prefers particles that are close in physical space, which may provide better proximity in composition space. Note that a variation of f_m affects both the particle selection for mixing and for two-phase coupling, and therefore different trends are obtained here compared to Sec. 7.2.1, where only the particle selection for two-phase coupling was changed. In fact, the results show only a weak dependence if only the two-phase coupling parameters r_m^* and f_m^* are changed while the mixing parameters r_m and f_m are kept constant, which is consistent with the trends reported in Sec. 7.2.1.

To assess whether the proposed scaling of f_m is reasonable, the mixing parameters are compared with the real mixing distances that are calculated from the simulation data. Figure 7.22 shows instantaneous values for the distances $d_x^{p,q}$ and

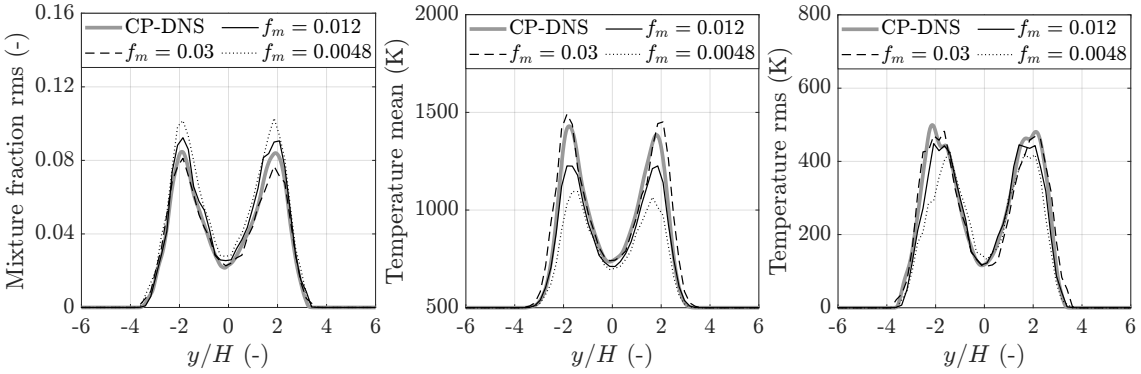

(a) Mixture fraction rms. **(b)** Temperature mean. **(c)** Temperature rms.

Figure 7.20: Mixture fraction rms and temperature mean and rms at time $t/t_j = 30$ obtained from the sparse-Lagrangian MMC-LES model (case $(x, \widetilde{f})$ with 1L/8E) using different values of f_m for both mixing and two-phase coupling.

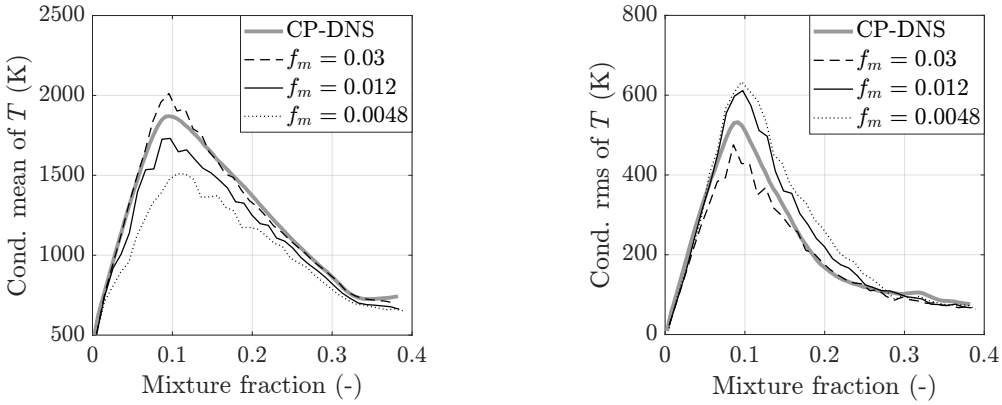

(a) Conditional mean of temperature. **(b)** Conditional rms of temperature.

Figure 7.21: Conditional mean and rms of temperature at time $t/t_j = 30$ obtained from the sparse-Lagrangian MMC-LES model (case $(x, \widetilde{f})$ with 1L/8E) using different values of f_m for both mixing and two-phase coupling.

$d_f^{p,q}$ between mixing particles, normalized by the corresponding mixing parameters r_m and f_m, along with their spatial averages (thick black solid line) and plotted versus the normalized cross-stream coordinate. A value of $d_x^{p,q}/r_m = 1$ and $d_f^{p,q}/f_m = 1$ (marked by the thin black line) indicates that the parameters are consistent with the real distances and thus appropriately chosen. Looking at the plots obtained from the default value $f_m = 0.03$, it can be seen that the average distance in physical space is approximately constant and larger than the parameter r_m, while the average distance in reference mixture fraction space is smaller than the prescribed parameter $f_m = 0.03$. In fact, one finds that the average distance in physical space agrees well with the distance that results from a particle selection in pure physical space (marked by the black dashed line, see Appendix C for details), which reveals that the conditioning of the mixing pair selection is ineffective. This indicates the

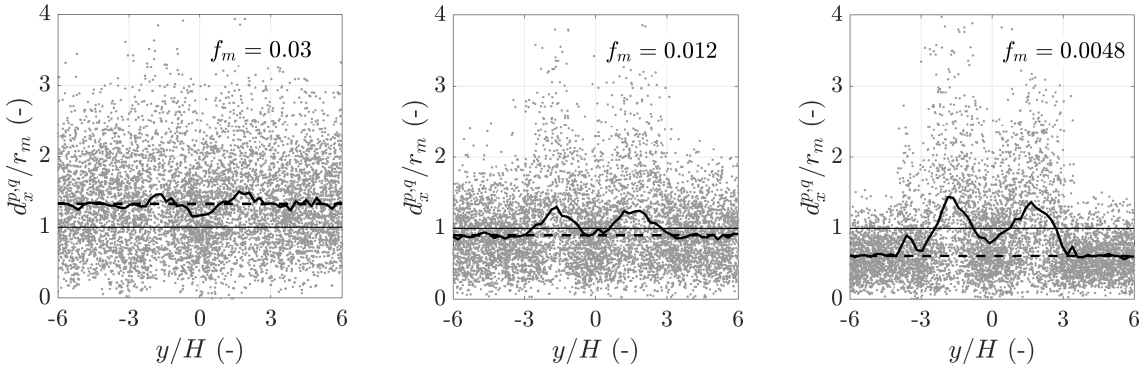

(a) Distances in physical space.

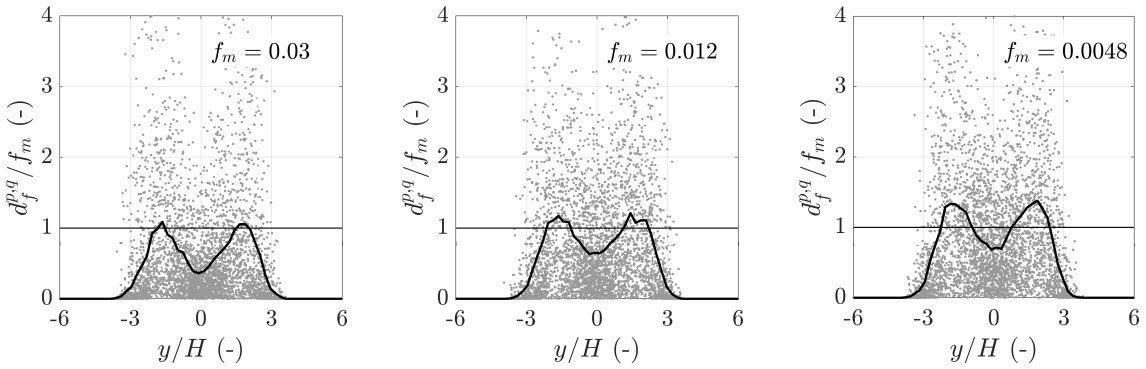

(b) Distances in reference mixture fraction space.

Figure 7.22: Distances between mixing particles in physical space and reference mixture fraction space, normalized by the mixing parameters, at time $t/t_j = 30$ (case $(x, \widetilde{f})$ with 1L/8E). Gray dots show the instantaneous particle data (random subset), while the thick black solid line denotes the average distance. The black dashed line marks the physical distance corresponding to a particle selection in pure physical space. The thin black line indicates an optimal choice of parameters.

that the mixing parameters are not chosen consistently. If the value of f_m is decreased, the conditioning in mixture fraction space becomes more important, which leads to an increase of distances in physical space, in particular in the shear region, where gradients of mixture fraction are largest and thus particles must be selected from a wider range to maintain the prescribed distances. Note that the parameter r_m that results from the isoscalar sliver relation is also increased, and therefore the normalized distances do not increase. For $f_m = 0.012$ the effect of a conditional particle selection is still relatively small, whereas for $f_m = 0.0048$ a significant increase in the shear region can be observed. In both cases, the normalized distances in mixture fraction space remain relatively unchanged (while the actual distances decrease) and show good agreement with the mixing parameter f_m. This demonstrates that a scaling of the standard value for f_m is indeed necessary for two-phase flows, with the reported results suggesting even further reduction of f_m than used in the present work.

Similar to the mixing distances between the stochastic particles, Fig. 7.23 shows

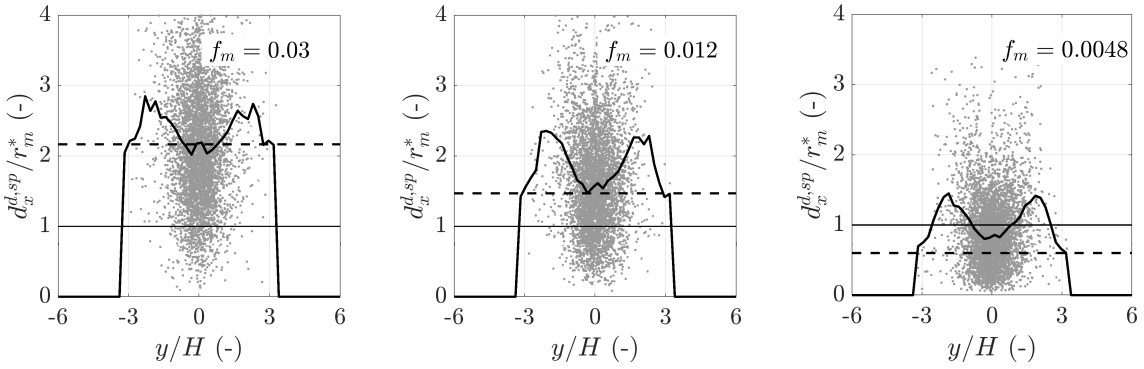

(a) Distances in physical space.

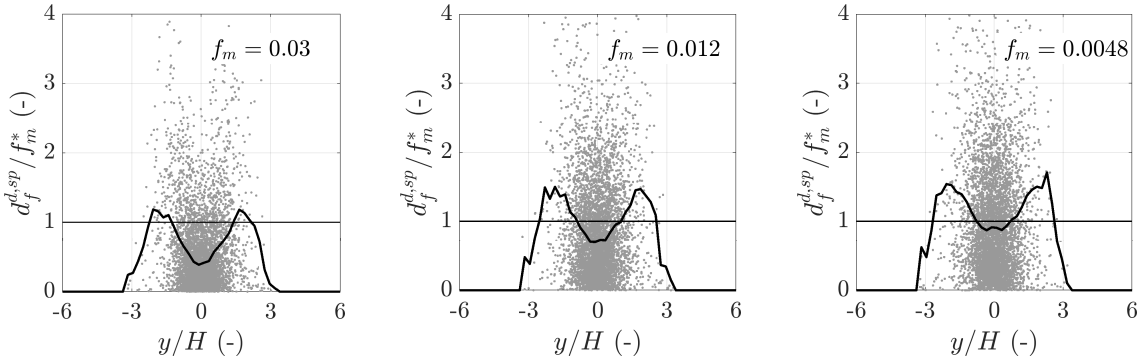

(b) Distances in reference mixture fraction space.

Figure 7.23: Distances between droplets and stochastic particles in physical space and reference mixture fraction space, normalized by the mixing parameters, at time $t/t_j = 30$ (case $(x, \widetilde{f})$ with 1L/8E). Gray dots show the instantaneous particle data (random subset), while the thick black solid line denotes the average distance. The black dashed line marks the physical distance corresponding to a particle selection in pure physical space. The thin black line indicates an optimal choice of parameters.

a comparison of the two-phase coupling parameters with the real distances between droplets and stochastic particles calculated from the simulation data. Here, essentially the same trends are observed as reported earlier for the mixing distances. For $f_m = 0.03$, the real distances in physical space are larger than the corresponding coupling parameter r_m^* and agree well with the distances resulting from a particle selection in pure physical space (dashed line), which is due to the fact that f_m and thus f_m^* is chosen too large. With decreasing value for f_m, the physical distances approach the coupling parameter r_m^*, while $d_f^{d,sp}/f_m^*$ remains approximately constant. The results demonstrate the analogy between mixing distances and two-phase coupling distances and confirm the estimation of suitable coupling distances between the droplets and the stochastic particles, as derived in Appendix C.

7.3.3 Effect of the Mixing Time Scale

The analysis of mixing times on the basis of the CP-DNS data, as was presented in Sec. 6.2.3, has demonstrated that the conventional models derived for single-phase flames can also be used for spray flames, although some uncertainty remained with respect to the modeling constants. For this reason, the effect of mixing time scale modeling will now be discussed. To this end, simulations of case $(x, \widetilde{f})$ with a particle number density of 1L/8E are performed using different values of the model constant C_f in combination with either the anisotropic (a-ISO) model, which has been used in all previous simulations, or the Cleary and Klimenko (C&K) model. For details on the model formulations the reader is referred to Sec. 4.4.3. Based on the default value $C_f = 0.1$, the model constant is decreased and increased by a factor of two, resulting in $C_f = 0.05$ and $C_f = 0.2$, respectively. Note that the same effect could be achieved by variation of the constant in the model for the turbulent diffusivity, but changing C_f provides a more direct control of the mixing time.

Results for the a-ISO model are shown in Figs. 7.24 and 7.25. While the effects on the mixture fraction are rather small (mean profile is not affected and therefore not shown), the averaged temperature profile shows a clear influence of the model constant. Here, a smaller value of C_f, corresponding to a smaller mixing time and thus enhanced mixing (cf. Eq. (4.54)), produces higher temperatures, with in particular the value $C_f = 0.05$ leading to remarkably good agreement with the CP-DNS data. This is in agreement with the results shown in Fig. 7.3, as a smaller value for C_f is equivalent to the use of a larger turbulent diffusivity (cf. Eq. (4.54)). The conditional profiles (Fig. 7.25) show essentially the same trends, where again $C_f = 0.05$ gives the best agreement with the CP-DNS. Minor further improvements for the temperature predictions are achieved if a particle selection conditional on the stochastic particle temperature is employed (not shown).

Results obtained from the C&K model using different values of C_f are shown in Figs. 7.26 and 7.27. In contrast to the a-ISO model, the C&K model shows only a weak dependence on the model constant. However, both the unconditionally and conditionally averaged temperatures are overpredicted, while the conditional fluctuations are significantly underestimated. This is due to the significantly lower mixing time scales produced by the C&K model. Note that the same underprediction of conditional variance of the C&K model was found by Vo *et al.* [218, 219] for single-phase flames using both MMC coupled to DNS [218] and MMC in combination with a real LES [219], as well as by Sharma and De [184] in MMC-LES of dilute spray flames.

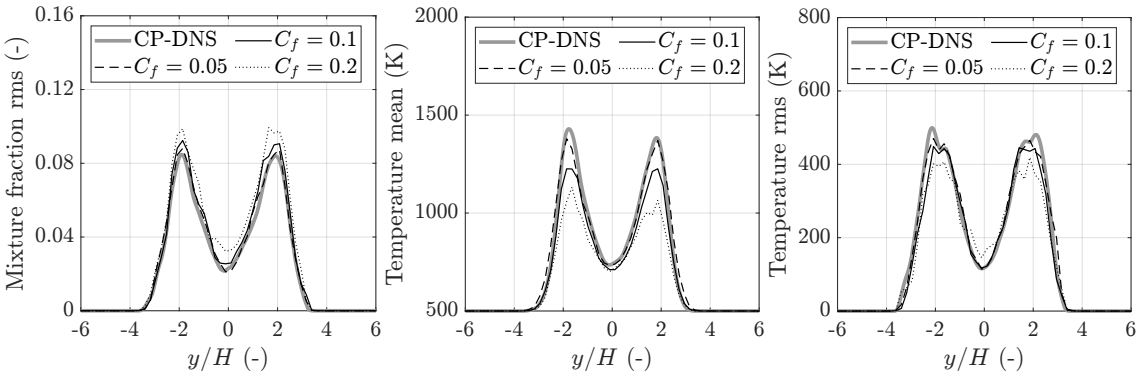

(a) Mixture fraction rms. **(b)** Temperature mean. **(c)** Temperature rms.

Figure 7.24: Mixture fraction rms and temperature mean and rms at time $t/t_j = 30$ obtained from the sparse-Lagrangian MMC-LES model (case $(x, \widetilde{f})$ with 1L/8E) using different values of C_f in the a-ISO mixing time scale model.

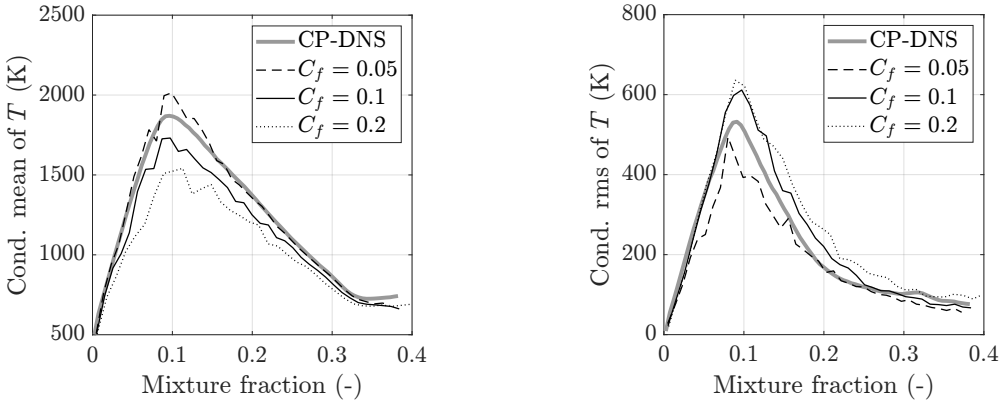

(a) Conditional mean of temperature. **(b)** Conditional rms of temperature.

Figure 7.25: Conditional mean and rms of temperature at time $t/t_j = 30$ obtained from the sparse-Lagrangian MMC-LES model (case $(x, \widetilde{f})$ with 1L/8E) using different values of C_f in the a-ISO mixing time scale model.

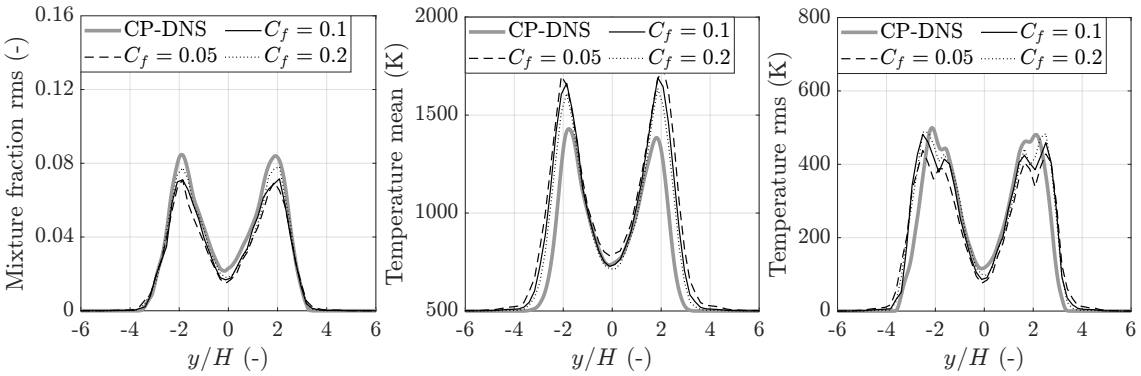

(a) Mixture fraction rms. **(b)** Temperature mean. **(c)** Temperature rms.

Figure 7.26: Mixture fraction rms and temperature mean and rms at time $t/t_j = 30$ obtained from the sparse-Lagrangian MMC-LES model (case $(x, \widetilde{f})$ with 1L/8E) using different values of C_f in the C&K mixing time scale model.

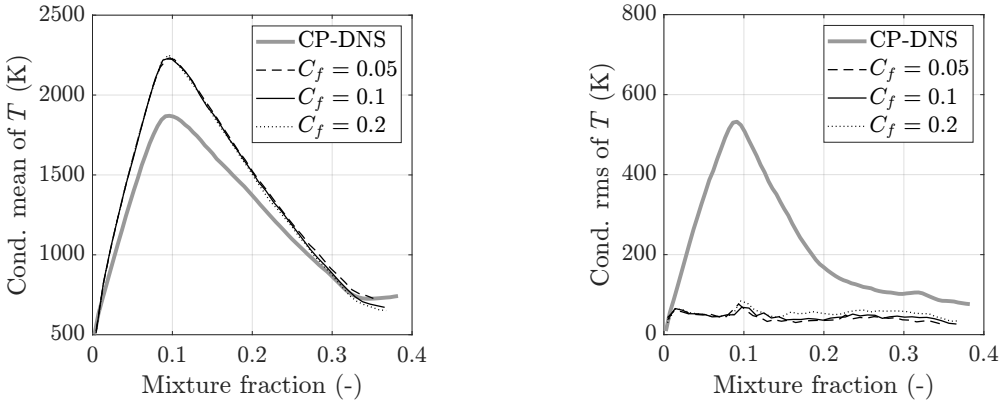

(a) Conditional mean of temperature. **(b)** Conditional rms of temperature.

Figure 7.27: Conditional mean and rms of temperature at time $t/t_j = 30$ obtained from the sparse-Lagrangian MMC-LES model (case $(x, \widetilde{f})$ with 1L/8E) using different values of C_f in the C&K mixing time scale model.

7.4 Summary and Discussion

The sparse-Lagrangian two-phase MMC-LES model was tested using an *a priori* strategy based on a temporally evolving droplet-laden double shear layer. The two-phase coupling between the droplets and the gas-phase particles was realized by utilizing the one-to-one coupling technique with particle selection conditional on a set of suitable reference variables. Using the filtered mixture fraction as a conditioning variable, as is conventional in MMC-LES modeling of non-premixed flames, good agreement was achieved for the mean and rms of mixture fraction, whereas the unconditionally and conditionally averaged temperatures were underestimated by about 100 K to 200 K. No significant differences were found between a particle selection in pure physical space and in physical and mixture fraction space. In contrast, a particle selection in pure reference mixture fraction space has led to somewhat larger deviations, in particular for the evaporation process. This was due to a lack of correlation between mixture fraction and temperature, with the latter being the predominant driving force for evaporation. The introduction of temperature as an additional conditioning variable for two-phase coupling has given improved predictions of evaporation rates and droplet size distributions, and partial improvements were also obtained for the temperature predictions. Further, it was outlined that there is not always a good correlation between the temperature in the Eulerian field, which is used for conditioning, and the temperature that is transported by the stochastic particles, and therefore conditioning on the stochastic particle mixture fraction and temperature was proposed. While this has improved the localness of the two-phase coupling in the DNS-based analysis, the importance of this approach is likely to be smaller in stand-alone LES, where the gas-phase temperature is solved exclusively on the stochastic particles.

Subsequent analysis of the influence of the MMC modeling parameters revealed a strong effect on the unconditional and conditional temperature predictions. Similar to the two-phase coupling, the reference mixture fracture field does not provide sufficient localness of the mixing operator, which can cause excessive flame extinction due to unphysical mixing. Increasing the stochastic particle number density and increasing the value for f_m have both led to improved temperature predictions. This is attributable to the fact that the importance of conditioning is reduced and particles are increasingly selected in pure physical space, which may provide better localness, in particular at high particle numbers. Further, a comparison of mixing and coupling parameters with distances calculated from the simulation data has demonstrated that a scaling of the standard value $f_m = 0.03$ is required to account for the smaller mixture fraction range in two-phase flows. Results with different

models for the mixing time scale have established that the a-ISO model provides a reasonable mixing time for spray flames, but requires an adjustment of the model constant to account for the effect of the evaporating droplets. In contrast, the C&K model has led to large discrepancies between the predicted conditional fluctuations and the CP-DNS data.

Based on the findings of the present chapter, two major refinements of the MMC mixing model are required to obtain reliable predictions for dilute spray flames with a significant amount of extinction and re-ignition. First, the concept of double conditioning should also be applied to the MMC mixing pair selection to ensure localness of the mixing operator, where the reaction progress variable or alternatively the temperature could be used as an additional reference variable [202]. Second, further research is required to incorporate the effect of droplet evaporation into the model for the mixing time scale. Alternatively, the a-ISO model combined with a dynamic procedure for estimating the model constant may be used to provide sufficiently accurate predictions for spray flames [184, 186].

Chapter 8

MMC-LES of an Evolving Droplet-Laden Double Shear Layer

The following chapter presents results of the sparse-Lagrangian two-phase MMC-LES model coupled with a stand-alone LES. The computational setup is the same as used in the previous chapter, but now additionally involves the effects of LES modeling of the turbulent flow field and density coupling from the stochastic particles back to LES. The results of this a posteriori study are compared with the CP-DNS data as well as with the model predictions of MMC coupled with the CP-DNS.

8.1 Computational Setup

The physical configuration is the same as used in Ch. 7 and describes the temporal evolution of a droplet-laden double shear layer. LES is used to compute the turbulent flow field, which requires additional modeling of the subgrid fluctuations. Here, the σ-model with $C_\sigma = 1.5$ is used (cf. Sec. 4.2.3), which has been shown to provide a more accurate description of the turbulent flow field compared to the Smagorinsky model and has exhibited a low dependence on the model constant. In *a posteriori* LES testing, a major challenge arises in determining an appropriate grid resolution [210]. On the one hand, the mesh must be fine enough to accurately represent the larger turbulent motions, where a resolution of about 80 % of the turbulent kinetic energy is recommended for LES [163]. On the other hand, the mesh should be sufficiently coarse in order to be able to draw reliable conclusions about the performance of the subgrid combustion model. Tests have shown that a mesh resolution of $N_x \times N_y \times N_z = 72 \times 84 \times 48 = 290\,304$ grid cells (i.e., the same resolution as used for filtering in the *a priori* analysis) provides qualitatively good predictions of the averaged velocity and reference mixture fraction profiles, while a lower grid resolution was not able to capture the larger turbulent motions and

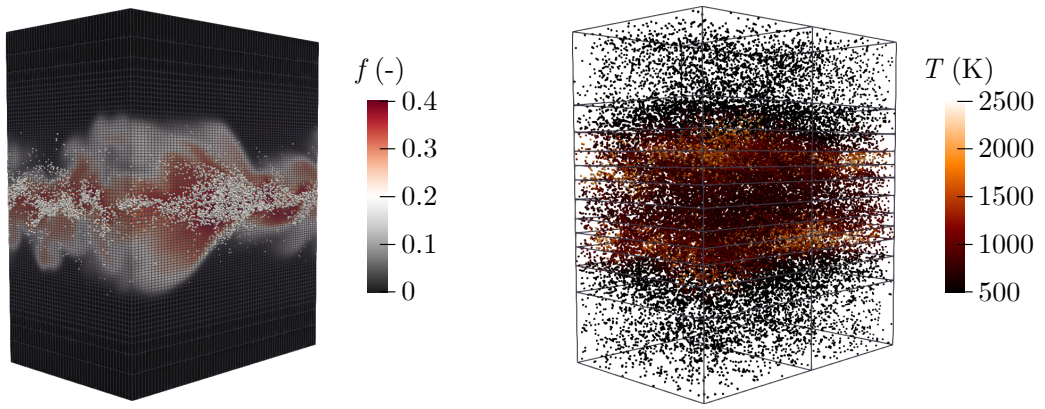

(a) Reference mixture fraction field and fuel droplets (scaled by a factor of ten).

(b) Stochastic particle field colored by the temperature of the particles.

Figure 8.1: Illustration of the MMC-LES setup for the temporally evolving droplet-laden double shear layer at time $t/t_j = 30$. The gray lines indicate the LES cells (left) and super cells (right).

resulted in a significantly delayed jet breakup. Note that the same mesh resolution has been used in previous LES studies of a similar configuration [219, 235]. A grid stretching in cross-stream direction is applied, where the cell sizes of the LES mesh and the super mesh are reduced in the jet region and increased towards the domain boundaries, as depicted in Fig. 8.1. This improves the resolution of the gradients in the shear region, in particular at the beginning of the simulation. Furthermore, the use of a non-uniform super mesh enables a higher particle number density in the flame zone, where a particle number control algorithm is employed to keep the particle number approximately constant within each super cell. The LES passes the velocity, the turbulent diffusivity and the reference mixture fraction to the stochastic particles, which in turn feed back their density to the Eulerian LES using the coupling method described in Sec. 4.6. The total number of stochastic particles within the domain is set to $N^{sp} = 36\,288$, corresponding to an average particle number density of 1L/8E. Although the clustering of stochastic particles towards the shear region leads to locally higher particle number densities, the globally determined values for the mixing and two-phase coupling parameters, as reported in Tab. 7.1, are retained for the present MMC-LES. Unless otherwise stated, the a-ISO mixing time with $C_f = 0.1$ is used, and the two-phase coupling utilizes a particle selection in physical and reference mixture fraction space according to Eq. (4.60).

The simulations are performed using the two-phase MMC-LES solver called `mmcDropletFoam`, which is described in Sec. 4.7.2. Linear interpolation schemes are used, as is common in LES, in combination with the `backward` method for time discretization. The MMC-LES simulations require about 35 CPUh on a workstation with 24 cores, which is a reduction of the computing time of the CP-DNS by a factor of more than 50 (cf. Tab. F.1).

8.2 Results

Accurate predictions of the MMC model for the reactive scalars require an accurate representation of the jet breakup by the LES subgrid model. To this end, the temporal evolution of the reference mixture fraction field that is obtained from the LES is compared with the CP-DNS data from the previous chapter. As shown in Fig. 8.2(a), there is very good agreement throughout the entire simulation. This indicates that the LES predicts the correct jet breakup, which enables comparability between the present MMC-LES predictions and the results of the DNS-based analysis that were presented in the previous chapter. A slight deviation exists at later times, which may be due to differences in the temperature fields in combination with density-weighted averaging or due to differences in the evaporation process, both of which will be examined later. Good agreement is also obtained for the mean streamwise velocity (not shown). Differences can be observed by looking at the turbulent kinetic energy, which is shown in Fig. 8.2(b). Here, the LES leads to larger turbulent fluctuations despite the lower grid resolution and the lack of subgrid fluctuations. The rms of reference mixture fraction is also overpredicted, albeit not

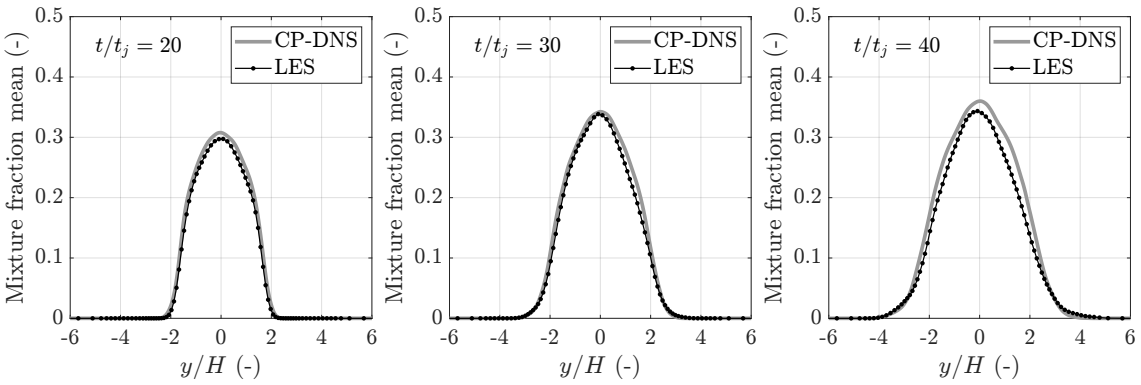

(a) Mixture fraction mean at different times.

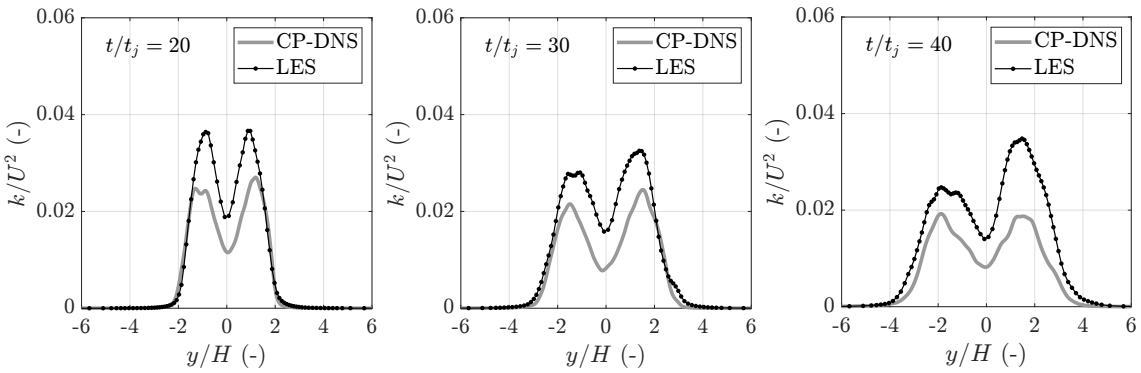

(b) Turbulent kinetic energy at different times.

Figure 8.2: Mean of the Eulerian reference mixture fraction and turbulent kinetic energy obtained from the LES and compared to the CP-DNS. Black dots mark the cell values.

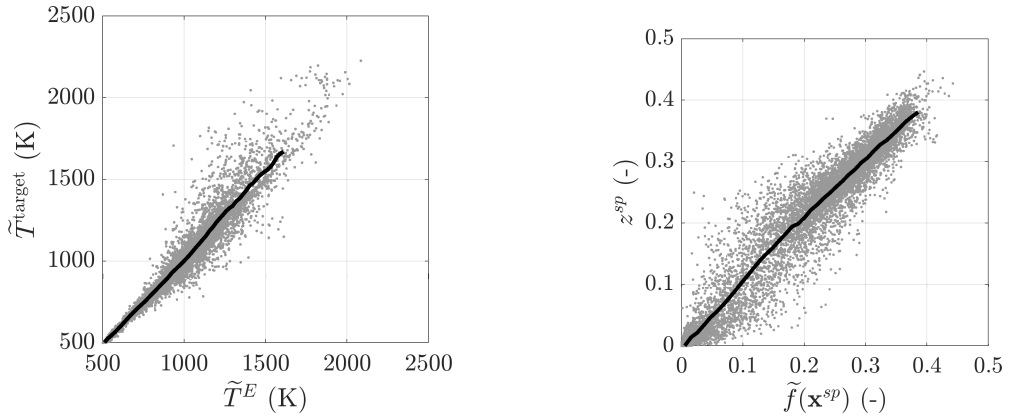

(a) Scatter plot of target temperature $\widetilde{T}^{\text{target}}$ versus equivalent temperature $\widetilde{T}^{E}$ in the LES.

(b) Scatter plot of particle mixture fraction z^{sp} versus filtered reference mixture fraction $\widetilde{f}(\mathbf{x}^{sp})$.

Figure 8.3: Proof of consistency between the stochastic particle field and the Eulerian LES at time $t/t_j = 30$. The black line denotes the conditional mean.

as strongly (not shown). This is attributable to the efficiency of the subgrid model, whose role is to emulate the dissipation of the resolved turbulent fluctuations in the absence of subfilter fluctuations. Obviously, the dissipation is not high enough, despite the fact that the mean profiles show good agreement.

Next, the consistency between the stochastic particle field and the Eulerian LES is demonstrated. Figure 8.3(a) shows a scatter plot of the instantaneous target temperature, which is obtained by mapping the stochastic particle temperature to the Eulerian field using the method described in Sec. 4.6, versus the equivalent temperature, which is obtained from the solution of an additional transport equation that applies a relaxation towards the target temperature and which is used to evaluate the density and thermophysical properties in the LES. There is a good linear correlation between the two temperatures with a low level of fluctuations, which verifies the density coupling between the stochastic particle field and the Eulerian LES. Figure 8.3(b) shows the correlation between the mixture fraction solved on the stochastic particles and the reference mixture fraction solved in the LES and interpolated to the particle positions. Again, there is a clear correlation, which is required for conditioning of the mixing operator to ensure localness in composition space. The scatter in the $\widetilde{f}$-z correlation is due to the stochastic movement of the particles and reflects subfilter fluctuations, which are not resolved by the reference mixture fraction field.

Figure 8.4 provides a comparison of results obtained from the stand-alone MMC-LES with the CP-DNS data and with results obtained from MMC coupled with the CP-DNS, which were presented in the previous chapter and are here denoted as MMC-DNS. Note that the MMC-DNS uses exactly the same MMC mod-

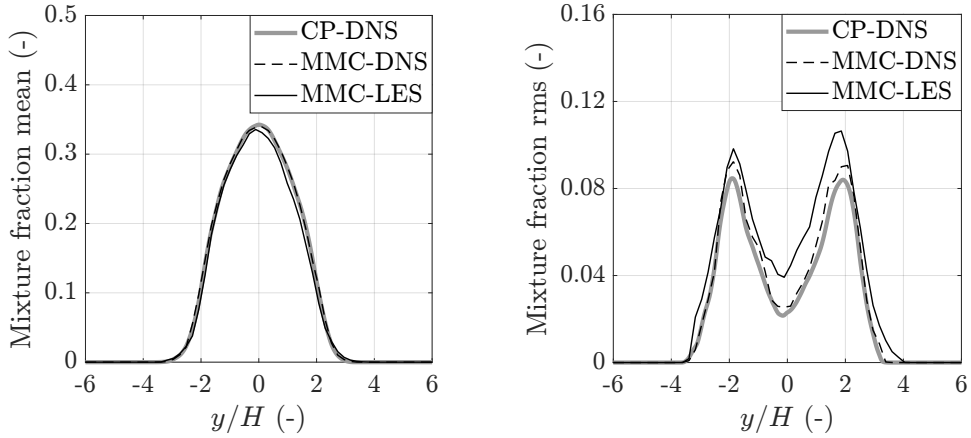

(a) Mean and rms of mixture fraction.

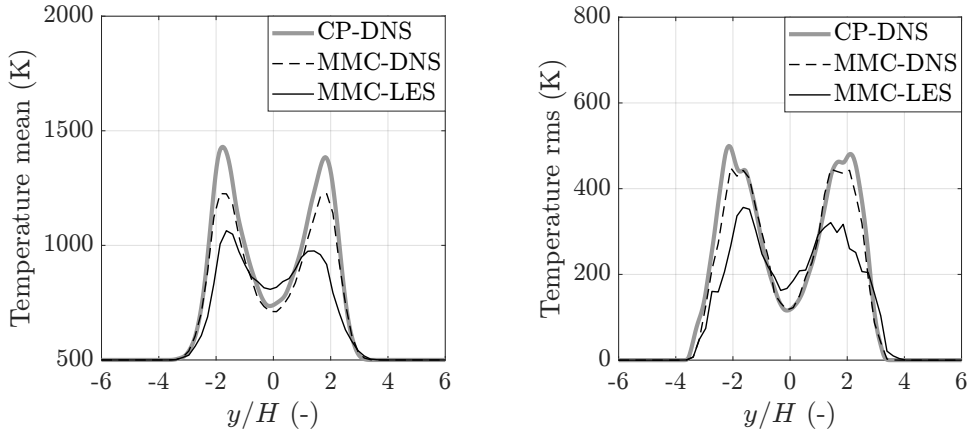

(b) Mean and rms of temperature fraction.

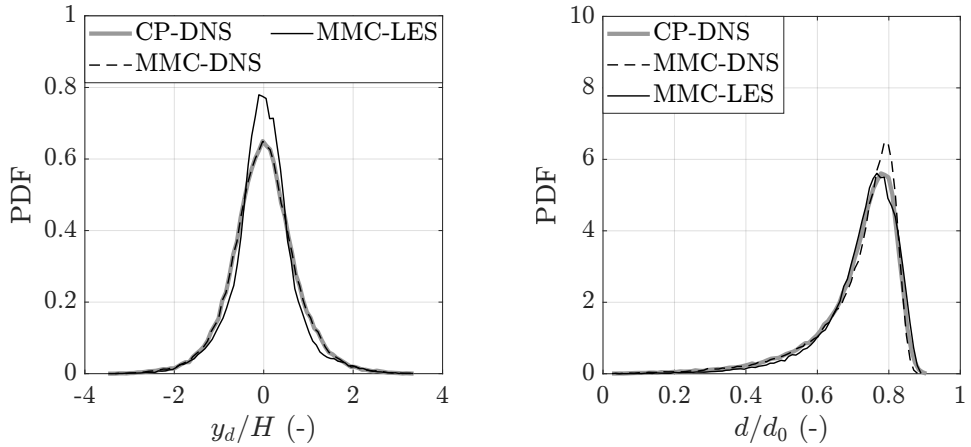

(c) PDF of the droplet positions (y-direction) and the droplet diameter.

Figure 8.4: Comparison of results obtained from the CP-DNS, MMC coupled with the CP-DNS (denoted as MMC-DNS), and the stand-alone MMC-LES. All results are shown at time $t/t_j = 30$.

eling parameters as the present MMC-LES to ensure comparability of the results. The mean mixture fraction profile is accurately predicted by the MMC-LES, while fluctuations are somewhat too large (Fig. 8.4(a)). This is due to the insufficient dissipation of the subgrid model, as mentioned above, and is therefore an effect of the LES subgrid model and not the MMC model. In contrast, the gas-phase temperatures are significantly underestimated by the MMC-LES, where the deviations to the CP-DNS are larger than in the MMC-DNS (Fig. 8.4(b)). As discussed in the previous chapter, this may be attributable to an inadequate mixing time scale, where the effects are amplified in the stand-alone MMC-LES due to the additional modeling of the turbulent diffusivity. Furthermore, the increased fluctuations result in intensified mixing of the cold gas of the central jet with the hot gas of the shear region, as indicated by the overpredicted temperature mean and rms in the center of the domain (Fig. 8.4(b)), which additionally contributes to flame extinction. A comparison of droplet properties is shown in Fig. 8.4(c). It can be seen that the droplet dispersion is slightly smaller in the MMC-LES, which is due to the lack of subgrid fluctuations in the LES. The PDF of the droplet diameter shows very good agreement with the CP-DNS, although the temperatures, which substantially determine the evaporation rate, have exhibited a considerable deviation from the CP-DNS. Obviously, the effects of a higher temperature in the jet region and a lower temperature in the shear region cancel each other, so that the evaporation rate takes on average similar values as in the CP-DNS.

Using double conditioning on mixture fraction and temperature for the two-phase coupling did not lead to significant improvements of the results (not shown for brevity), which suggests that the deviations of the temperature predictions are attributable to the mixing model, as discussed in Sec. 7.3. For this reason, the influence of the MMC mixing parameters on the MMC-LES model predictions will be briefly discussed. The results are shown in Fig. 8.5 exemplary for the conditional mean temperature, but the trends are essentially the same for the unconditionally averaged temperature, while mixture fraction is not significantly affected. Figure 8.5(a) shows results obtained using an varying number of stochastic particles. In contrast to the MMC-DNS, the number of stochastic particles has no influence here, as the grid stretching leads to a sufficiently high particle number density in the flame region even with the lowest particle number. A variation of the mixing parameter f_m (Fig. 8.5(b)) and the constant C_f in the mixing time scale (Figs. 8.5(c) and 8.5(d)) generally shows the same trends as reported in Sec. 7.3. It can be seen that both the scaled value $f_m = 0.012$ and the default value $f_m = 0.03$ can reproduce the conditional mean temperature of the CP-DNS, provided that the modeling constant C_f is adjusted properly. Using $f_m = 0.012$, the best match

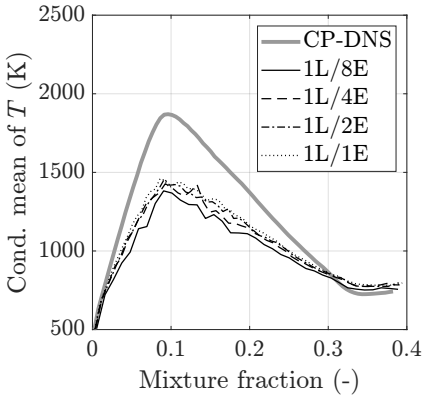

(a) Effect of stochastic particle number.

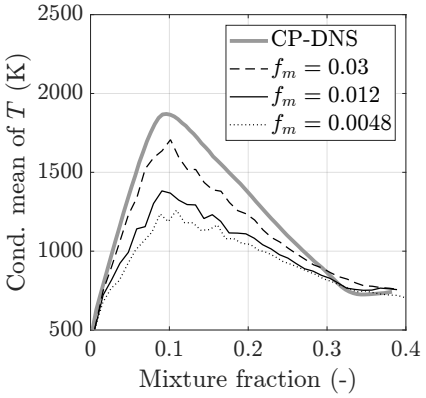

(b) Effect of parameter f_m.

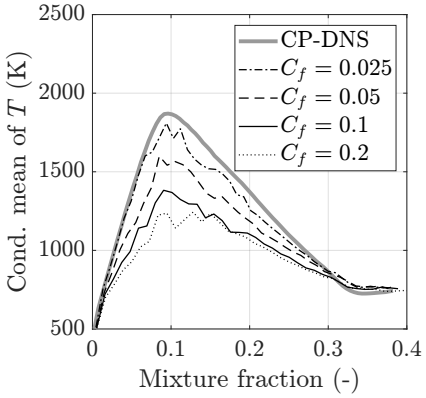

(c) Effect of constant C_f using $f_m = 0.012$.

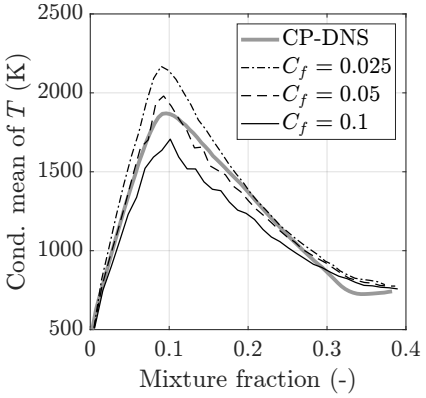

(d) Effect of constant C_f using $f_m = 0.03$.

Figure 8.5: Effect of the MMC modeling parameters on the conditional mean temperature at time $t/t_j = 30$.

with the CP-DNS data is obtained for $C_f = 0.025$ (cf. Fig. 8.5(c)), while a value of $C_f = 0.05$ is required for $f_m = 0.03$ (cf. Fig. 8.5(d)). A final comparison of the CP-DNS and the MMC-LES using these two sets of "tuned" modeling parameters is provided in Fig. 8.6, which shows the corresponding scatter plots of temperature versus mixture fraction at time $t/t_j = 30$. In both cases, the MMC-LES shows qualitatively good agreement of the conditional mean temperature and the conditional fluctuations with the CP-DNS, which demonstrates the good predictive capabilities of the two-phase MMC-LES model for spray flames with extinction and re-ignition if adjusted parameters are used.

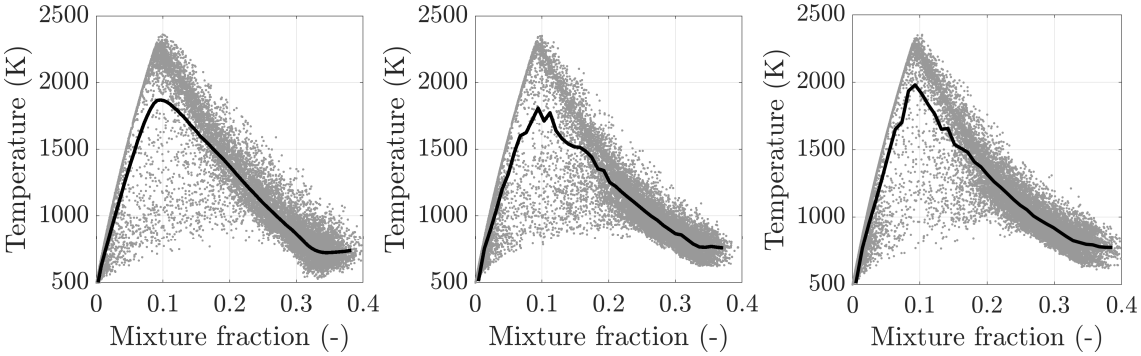

(a) CP-DNS. **(b)** $f_m = 0.012$, $C_f = 0.025$. **(c)** $f_m = 0.03$, $C_f = 0.05$.

Figure 8.6: Comparison of scatter plots obtained from the CP-DNS and the MMC-LES with adjusted modeling parameters f_m and C_f at time $t/t_j = 30$.

8.3 Summary and Discussion

A stand-alone MMC-LES of the droplet-laden double shear layer configuration was performed, and the results were compared with the CP-DNS data and with results obtained from MMC coupled with the CP-DNS. Emphasis was made on the importance of accurately predicting the jet breakup to ensure comparability of the results, which was achieved by utilizing a grid stretching in the cross-stream direction. In addition, the grid stretching has led to a local increase in particle number density in the flame zone. The MMC-LES has shown good predictions of the mean mixture fraction and the evaporation process, but significantly underestimated the temperatures. The deviations were larger than in the MMC-DNS, which was attributed to additional modeling errors associated with subgrid modeling in stand-alone MMC-LES. Analysis of the sensitivity of the MMC-LES model towards the modeling parameters has essentially revealed the same trends as reported earlier for the DNS-based analysis, where in particular an adjustment of the mixing time constant has eventually led to excellent agreement with the CP-DNS. This again points out the need for further studies regarding the modeling of the mixing time in spray flames in order to achieve accurate prediction of the reactive scalars.

Chapter 9

Conclusions and Outlook

9.1 Summary and Conclusions

The present work has performed an in-depth analysis and validation of the sparse-Lagrangian two-phase MMC-LES model for dilute spray flames. The model employs an Eulerian LES for the turbulent flow field and reference mixture fraction field, a Monte Carlo particle method for the reactive scalars, and a Lagrangian solver for the liquid fuel droplets. While the chemical source term is closed in this approach, molecular diffusion is not and is represented by a mixing model. The MMC model utilizes the concept of localness of the mixing operator by conditioning the particle selection on the reference mixture fraction space, which allows the number of stochastic particles to be significantly reduced compared to a conventional particle method. While this is a key benefit to the efficiency of the model, the sparse representation of the gas phase poses a challenge in coupling the droplets with the stochastic particles. In the present work, a one-to-one coupling strategy with particle selection conditional on a set of suitable conditioning variables was proposed in order to ensure localness in composition space. This two-phase coupling was further examined and validated by comparison with a reference solution provided by a CP-DNS using *a priori* and *a posteriori* strategies.

In the first part of the thesis, the grid dependence of the two-phase coupling in conventional Euler-Lagrange simulations based on the PSI-cell model has been extensively studied, which is of direct relevance for the CP-DNS to serve as an accurate reference solution. Based on an isolated droplet in an infinite environment, relations were derived that describe the effect of the cell size on the evaporation rate and time as well as on the resolved mixture fraction variance. The second part of the thesis was devoted to the analysis and validation of the two-phase coupling in a sparse particle method. The analysis was organized in three steps, where each step extended the analysis by additional modeling aspects, such as the modeling

of the conditional evaporation rate on the stochastic particles or the modeling of turbulence in the Eulerian field. In a first step, a rather simple configuration with homogeneous turbulence and droplet distribution was considered, where all input data for the two-phase MMC-LES model, such as velocity, turbulent diffusivity and evaporation rate, were extracted from the CP-DNS. This allowed for an unbiased comparison of different techniques to distribute the evaporation source terms among the stochastic particles and to focus on the immediate effects on variance generation and combustion. In addition, the predictions of the sparse-Lagrangian MMC model were compared with results obtained from conventional intensive particle methods. The second step added the evaluation of the conditional evaporation rate to the stochastic particle solution, and focused on the identification of suitable conditioning variables for the two-phase coupling using a temporally evolving droplet-laden double shear layer. Further, the influence of the MMC modeling parameters was discussed. Finally, in the third step, a stand-alone MMC-LES of the same configuration was performed to establish the findings from the DNS-based analysis.

The scientific contributions of this work can be formulated as answers to the key questions posed in Sec. 1.3.

- **How can the error of the evaporation rate and time be estimated prior to the simulation?**
  Based on an isolated droplet in an infinite environment, it was shown that the error of the steady-state evaporation rate depends on only two parameters, namely the ratio of cell size to droplet diameter, $\Delta x/d$, and the cell Péclet number defined as $\mathrm{Pe}_{\Delta x} = u_\infty \Delta x/\mathcal{D}_F$. The specific relationship for the error of the steady-state evaporation rate is given by

$$\epsilon_{\dot{m}} = \min\left[\left(1+\frac{2}{3}\frac{\Delta x}{d}\right)^{-1}, \left(1+\frac{1}{\pi}\frac{\mathrm{Pe}_{\Delta x}}{\mathrm{Sh}^*}\frac{\Delta x}{d}\right)^{-1}\right].$$

  The error of the evaporation time additionally depends on the modified mass ratio φ^*, which is defined as $\varphi^* = (m_{d,0}/m_{g,0})/\ln(1+B_{M,\mathrm{ref}})$ with $m_{d,0} = \frac{\pi}{6}\rho_l d_0^3$ and $m_{g,0} = \rho_\infty \Delta x^3$, and follows the relation

$$\epsilon_\tau = \min\left[\left(\frac{\Delta x}{d_0}\right)^{-1}, 0.6\varphi^*, \frac{2\pi}{3}\left(\frac{\mathrm{Pe}_{\Delta x}}{\mathrm{Sh}^*}\right)^{-1}\left(\frac{\Delta x}{d_0}\right)^{-1}\right].$$

  In the practically relevant case of $\Delta x/d_0 \lesssim 20$ and assuming a small relative velocity with $\mathrm{Pe}_{\Delta x} \lesssim 4$, the relation for the error of the evaporation time simplifies to $\epsilon_\tau = (\Delta x/d_0)^{-1}$, which provides a very convenient way to estimate the error of the evaporation time prior to the simulation.

- **How does a lack of resolution of the near-droplet fields affect the mixture fraction variance?**
  Contrary to expectations, the variance of a single droplet has been found to be accurately reproduced by the PSI-cell model regardless of the cell size, provided that the inter-droplet space is resolved by the numerical mesh (albeit overestimated for $\Delta_L/d \lesssim 10$). This is because the effects of discretization and distributing source terms to a larger volume cancel each other. In contrast, if the source term is distributed to a larger volume while the mesh remains unchanged, the variance decays exponentially, as expected.
- **What is a suitable mixing time scale for dilute spray flames?**
  The mixing time is usually modeled by analogy with the Eulerian time scale, which is defined as the ratio of scalar subgrid variance to filtered dissipation rate. Analysis of the mixture fraction subgrid variance and dissipation rate by means of CP-DNS data has shown that the conventional models derived for single-phase flames also lead to qualitatively correct predictions for spray flames, but may require an adjustment of the model constants. Consistent with this, the a-ISO model with adjusted model constant has led to an accurate description of the conditional temperature fluctuations and thus provides a reasonable mixing time also for spray flames.
- **How can the evaporated mass be distributed among stochastic particles in order to mimic real evaporation?**
  A one-to-one coupling strategy between the droplets and the stochastic particles, where each droplet is coupled with a single gas-phase particle that provides the ambient conditions and receives the source terms, has been shown to fulfill most of the properties of an ideal two-phase coupling model. The mutual interaction of droplets and gas-phase particles prevents the occurrence of unphysical values and the approach is able to generate the correct amount of scalar variance. To avoid a dependence on numerical parameters, the coupling must not be random in each time step but subject to a specific rule, e.g., by selecting the closest particle in physical space, which ensures pairing with the same particle for a certain period of time. The method is not confined to sparse particle methods and can equally be applied to intensive particle methods.
- **How does the relative performance of the sparse-Lagrangian MMC-LES model compare to conventional intensive particle methods?**
  MMC combined with the one-to-one coupling strategy for two-phase coupling was superior to the conventional particle methods in both efficiency and accuracy. The mixture fraction predictions were in excellent agreement with the CP-DNS data, while the EQUAL model has underestimated the variance due the even

distribution of source terms among the particles in the computational cell, and the SAT model, which distributes source terms preferably to particles close to saturation conditions, has significantly overestimated the scalar fluctuations. The temperature predictions were comparable to that of the EQUAL model, since source terms are transferred to a relative large gas volume represented by each particle in a sparse particle method, which implies artificial mixing. This gives rise to further improvements, which will be outlined in the next section.

- **How can the evaporation rate be determined if the gas phase is represented by a sparse distribution of stochastic particles?**
  A particle selection conditional on a set of suitable conditioning variables, which is realized by adopting the concept of minimizing the effective square distance, can provide localness of the two-phase coupling, and thus overcome the difficulties associated with a sparse representation of the gas phase where a particle is not always present close to the droplet. In MMC-LES of non-premixed flames, the reference mixture fraction is usually used as a proxy for localness in composition space, and the simulations have shown that it also serves as an adequate conditioning variable for two-phase coupling in spray flames. It was outlined that the inclusion of the distance in physical space is beneficial and thus recommended. For sprays with a considerable amount of extinction, double conditioning is required, which was presented here based on temperature. Further, it was argued that conditioning on stochastic particle properties may provide better localness if there is not sufficient correlation between the stochastic particle properties and their Eulerian equivalents.
- **How robust is the two-phase MMC-LES model with respect to the modeling parameters?**
  The two-phase coupling based on the one-to-one coupling strategy showed little dependence on the MMC modeling parameters, while the MMC mixing model showed a strong influence of the parameters, such as the number of particles and the mixing parameter f_m. This was attributed to the lack of correlation between mixture fracture and temperature, and is therefore case-dependent and not universally valid.

In summary it can be said that the sparse-Lagrangian two-phase MMC-LES model combined with the one-to-one coupling strategy provides a powerful and efficient prediction method for dilute spray flames. The present work has provided valuable insights into the two-phase coupling in dense and sparse-Lagrangian FDF methods and has made major contributions to the DNS-based model validation.

9.2 Outlook

In the following, proposals are presented for future analyses and to further improve the existing two-phase coupling between the droplets and the stochastic particles:

- **Configuration for future *a priori* analyses**
  The droplet-laden double shear layer has proven to be a suitable setup for the *a priori* analysis of the two-phase MMC-LES model, as it reproduces the essential effects of a real spray while keeping the computational effort manageable. For future simulations, it is recommended to calculate the turbulent diffusivity required by the mixing time scale model directly, i.e., based on Eqs. (4.14) and (4.19), instead of using a turbulence model. This eliminates the dependence on the specific form of the model used, which may have limited validity for spray flames, and the influence of the associated modeling parameters. Further, it is recommended to use a higher Reynolds number in order to increase the relevance of subfilter fluctuations, where the other cases presented in Hawkes *et al.* [78] could serve as suitable baseline configurations. Another limitation of the present setup may be the use of single-step chemistry, which should be extended to a reduced mechanism involving multiple reaction equations as well as intermediate species. To reduce the computational cost of the CP-DNS, one could use tabulation techniques [34, 162], which are available in both the base distribution of OpenFOAM and the MMC libraries.
- **Time delay model**
  To overcome the artificial mixing that results from the distribution of the evaporation source terms to the larger volume represented by each stochastic particle, a time delay model was suggested in Sec. 6.4.4 that transfers the source terms to the particles with a certain delay. However, no significant improvements were obtained, which is attributable to the simplicity of the model formulation used in the present work. Therefore, additional work is required to revise the model, e.g., by splitting the volume into two subvolumes using concepts from the eddy dissipation concept (EDC), as discussed in Sec. 6.5.
- **Improved particle selection algorithm**
  The minimization of the effective square distance between the droplets and the stochastic particles is realized using a direct search algorithm, in which the computational cost increases proportional to $N_d \cdot N^{sp}$. While this was not a shortcoming in the CP-DNS, where the chemistry calculation and the solution of the Eulerian transport equations was the most time-consuming part, the LES showed that a significant amount of computing time can be spent on minimizing the distances between the droplets and the particles, especially when a higher particle

number was used. It is therefore recommended to implement an optimized algorithm. A possible implementation could be to divide the set of stochastic particles into smaller subgroups using a k-d tree algorithm [57] similar to the mixing pair selection. Knowing the subgroup in which a droplet is located, one only needs to search for the nearest particle in that subgroup (and, if required, also in the adjacent subgroups). With such an approach, significantly fewer distances need to be computed, thus reducing the computing time. Note that the droplet-particle pairs found (and thus the distances between droplets and gas-phase particles) are generally the same as those obtained with a direct search algorithm.

To improve the performance of the sparse-Lagrangian mixing model in spray flames with a significant amount of extinction and re-ignition, the following recommendations are made:

- **Double conditioning for MMC mixing pair selection**
  The present droplet-laden double shear layer configuration has shown a considerable amount of extinction, which can also be observed in real spray flames [74]. Under these conditions, a single reference variable such as mixture fraction may not provide adequate localness in composition space and cause excessive flame extinction due to unphysical mixing. This problem has been addressed in the present work by introducing a double conditioning approach for the two-phase coupling, and further improvements may be obtained by adopting the same strategy to the mixing operator using the reaction progress variable (or temperature) as a second reference variable, as outlined by Straub *et al.* [202].
- **Mixing time modeling in dilute spray flames**
  The present work has shown that the a-ISO model generally provides a suitable mixing time scale for MMC-LES of dilute spray flames. However, some uncertainty exists regarding the model constant, and an adjustment was required to improve the model predictions. This gives rise to the use of a dynamic procedure for estimating the model constant in the mixing time scale [186], which eliminates the need to adjust the model constant in two-phase flows and thus may provide the desired amount of mixing. Such a dynamic procedure in combination with the a-ISO model was used recently by Sharma and De [184] for a series of dilute spray flames, where improved results were obtained compared to the static a-ISO model. However, such an approach cannot be expected to represent all of the physical effects associated with the evaporation process, and therefore a detailed analysis of how to incorporate the effects of the evaporating droplets into the model for the mixing time scale is still required. Inspiration for the development of a new model could be provided by the work of Pera *et al.* [147]. Validation

requires extraction of the "exact" mixing time from the CP-DNS data, which has not yet been demonstrated for the sparse-Lagrangian MMC model with mixing conditional on the reference space.

Suggestions for further implementations that extend the applicability of the two-phase MMC-LES model are provided below:

- **Spray modeling**
  The simulation of a real spray requires additional modeling of the breakup and atomization processes along with the incorporation of droplet collisions and coalescence (cf. Fig. 2.2). These aspects have not been covered in the present work, since only the dilute region has been considered. Due to the high volume fraction of the liquid phase in the region close to the nozzle, the breakup of the fuel jet is more properly described using an Eulerian approach. The incorporation of such an approach into the sparse-Lagrangian MMC model would then require a new model for the coupling between the Eulerian solver for the liquid phase and the stochastic particles representing the gas phase.
- **Application to real spray flames**
  In the present work, the sparse-Lagrangian two-phase MMC-LES model has been validated based on rather simple configurations at relatively low Reynolds numbers. The next step should be to apply the model to real spray flames at high Reynolds numbers and to compare the results with experimental data, such as the Sydney piloted spray flame series [74]. There are already applications of the two-phase MMC-LES model to spray flames [102, 103, 184, 185], but they mostly use the model formulation of Khan *et al.* [102]. The present work has elaborated further improvements such as the double conditioning and the findings may help to improve the model predictions.
- **Extension to coal and biomass combustion**
  The numerical modeling of the combustion of pulverized solid fuels, particularly coal and biomass, uses similar concepts as for spray combustion in that the fuel particles are treated as point particles. Accordingly, the two-phase MMC-LES model can be readily applied to solid fuels by extending the models describing the evolution of the fuel particles by the effects of devolatilization and char conversion. There is already work on this topic [240], and the present study may provide valuable insights for modeling the coupling between the fuel particles and the stochastic particles. Furthermore, the analysis of the cell-size dependence of the PSI-cell model provides guidelines for deriving equivalent error relations for solid fuel particles, which is particularly important since the size of pulverized solid fuel particles is typically larger than that of droplets in spray combustion applications.

Appendix A

Derivation of the Evaporation Source Terms

A.1 Evaporation Source Terms in the Eulerian Transport Equations

The expressions for the evaporation source terms in the Eulerian transport equations of the carrier gas are derived based on the conservation of mass, momentum and energy between a finite gas volume and the liquid droplets. For the derivation it is assumed that the conserved quantities (mass, momentum and energy) only change due to the evaporation process, which is equivalent to the assumption of a closed system. Accordingly, the equations of the gas phase reduce to their zero-dimensional form, containing only the time derivative and the evaporation source term. Furthermore, only a single droplet is considered for the sake of simplicity. For systems with multiple droplets, the total source terms are simply obtained by performing a summation over all droplets within the volume under consideration. Droplet properties are marked with subscript d, while properties of the gas phase are written without index.

The conservation of total mass states that the temporal change of the sum of gaseous mass and droplet mass is zero,

$$\frac{\mathrm{d}m_{\mathrm{total}}}{\mathrm{d}t} = \frac{\mathrm{d}(\rho V)}{\mathrm{d}t} + \frac{\mathrm{d}m_d}{\mathrm{d}t} = 0, \tag{A.1}$$

where V is the gas volume. Solving the equation for the time derivative of density gives the expression for the mass source term,

$$\frac{\mathrm{d}\rho}{\mathrm{d}t} = \dot{S}_M = -\frac{1}{V}\frac{\mathrm{d}m_d}{\mathrm{d}t}. \tag{A.2}$$

Since only single-component liquids are considered within the present work, the change of gaseous fuel mass is equal to the change of droplet mass, while the change

of the gaseous masses of the remaining species is zero,

$$\frac{\mathrm{d}(\rho Y_k)}{\mathrm{d}t} = \dot{S}_{M,k} = \begin{cases} \dot{S}_M, & k = F, \\ 0, & k \neq F. \end{cases} \tag{A.3}$$

Momentum is a vector quantity, where in a closed system the momentum is conserved in each physical direction. Accordingly, the conservation of the total momentum vector $\mathbf{I}_{\mathrm{total}}$ can be expressed component-wise,

$$\frac{\mathrm{d}I_{\mathrm{total,i}}}{\mathrm{d}t} = \frac{\mathrm{d}(\rho u_i V)}{\mathrm{d}t} + \frac{\mathrm{d}(m_d u_{d,i})}{\mathrm{d}t} = 0, \tag{A.4}$$

resulting in

$$\frac{\mathrm{d}(\rho u_i)}{\mathrm{d}t} = \dot{S}_{u,i} = -\frac{1}{V}\frac{\mathrm{d}(m_d u_{d,i})}{\mathrm{d}t}. \tag{A.5}$$

The conservation of energy is expressed in terms of absolute enthalpy $H = mh$, meaning that the sum of absolute enthalpy of the gas and the liquid droplet remains constant. By differentiating with respect to time one obtains

$$\frac{\mathrm{d}H_{\mathrm{total}}}{\mathrm{d}t} = \frac{\mathrm{d}(\rho h V)}{\mathrm{d}t} + \frac{\mathrm{d}(m_d h_d)}{\mathrm{d}t} = 0. \tag{A.6}$$

The corresponding evaporation source term is then given by

$$\frac{\mathrm{d}(\rho h)}{\mathrm{d}t} = \dot{S}_h = -\frac{1}{V}\frac{\mathrm{d}(m_d h_d)}{\mathrm{d}t}. \tag{A.7}$$

The expression for the evaporation source term in the balance equation for sensible enthalpy is obtained by inserting the decomposition of absolute enthalpy into enthalpy of formation and sensible enthalpy. Using Eqs. (3.6) and (3.7), the absolute enthalpy can be written as

$$h = \sum_{k=1}^{N_s} Y_k h_k = \sum_{k=1}^{N_s} Y_k h_{f,k}^{\circ} + \sum_{k=1}^{N_s} Y_k h_{s,k} = \sum_{k=1}^{N_s} Y_k h_{f,k}^{\circ} + h_s. \tag{A.8}$$

The time derivative of absolute enthalpy can then be expressed as

$$\frac{\mathrm{d}(\rho h)}{\mathrm{d}t} = \frac{\mathrm{d}(\rho h_s)}{\mathrm{d}t} + \frac{\mathrm{d}}{\mathrm{d}t}\left(\rho \sum_{k=1}^{N_s} Y_k h_{f,k}^{\circ}\right) = \frac{\mathrm{d}(\rho h_s)}{\mathrm{d}t} + \sum_{k=1}^{N_s} h_{f,k}^{\circ}\frac{\mathrm{d}(\rho Y_k)}{\mathrm{d}t}. \tag{A.9}$$

Inserting Eqs. (A.2) and (A.3) results in

$$\frac{\mathrm{d}(\rho h)}{\mathrm{d}t} = \frac{\mathrm{d}(\rho h_s)}{\mathrm{d}t} + h_{f,F}^{\circ}\dot{S}_M = \frac{\mathrm{d}(\rho h_s)}{\mathrm{d}t} - h_{f,F}^{\circ}\frac{1}{V}\frac{\mathrm{d}m_d}{\mathrm{d}t}. \tag{A.10}$$

Using Eq. (A.7), the evaporation source term in the sensible enthalpy equation finally takes the form

$$\frac{\mathrm{d}(\rho h_s)}{\mathrm{d}t} = \dot{S}_{h_s} = -\frac{1}{V}\left(\frac{\mathrm{d}(m_d h_d)}{\mathrm{d}t} - h_{f,F}^{\circ}\frac{\mathrm{d}m_d}{\mathrm{d}t}\right). \tag{A.11}$$

The expression for the source term in the energy equation based on temperature is derived from Eq. (A.11) by inserting the expression for the sensible enthalpy, Eq. (3.7). The time derivative of sensible enthalpy can be written as

$$\frac{\mathrm{d}(\rho h_s)}{\mathrm{d}t} = \frac{\mathrm{d}}{\mathrm{d}t}\left(\sum_{k=1}^{N_s} \rho Y_k h_{s,k}\right) = \sum_{k=1}^{N_s} h_{s,k}\frac{\mathrm{d}(\rho Y_k)}{\mathrm{d}t} + \sum_{k=1}^{N_s} \rho Y_k \frac{\mathrm{d}h_{s,k}}{\mathrm{d}t}. \tag{A.12}$$

Using the chain rule and the first fundamental theorem of calculus, the time derivative of the sensible enthalpy of the species is given by

$$\frac{\mathrm{d}h_{s,k}}{\mathrm{d}t} = \frac{\mathrm{d}}{\mathrm{d}t}\left(\int_{T_\mathrm{ref}}^{T} c_{p,k}\mathrm{d}T'\right) = \frac{\mathrm{d}}{\mathrm{d}T}\left(\int_{T_\mathrm{ref}}^{T} c_{p,k}\mathrm{d}T'\right)\frac{\mathrm{d}T}{\mathrm{d}t} = c_{p,k}\frac{\mathrm{d}T}{\mathrm{d}t}, \tag{A.13}$$

where $c_{p,k}$ is evaluated at temperature T. With this relation and by inserting the expression for the species mass source term, Eq. (A.3), one obtains

$$\frac{\mathrm{d}(\rho h_s)}{\mathrm{d}t} = \sum_{k=1}^{N_s} h_{s,k}\dot{S}_{m,k} + \sum_{k=1}^{N_s} \rho Y_k c_{p,k}\frac{\mathrm{d}T}{\mathrm{d}t} = h_{s,F}\dot{S}_M + \rho c_p \frac{\mathrm{d}T}{\mathrm{d}t}. \tag{A.14}$$

For the time derivative of temperature the following relation holds:

$$\frac{\mathrm{d}(\rho T)}{\mathrm{d}t} = \rho\frac{\mathrm{d}T}{\mathrm{d}t} + T\frac{\mathrm{d}\rho}{\mathrm{d}t} \quad \Rightarrow \quad \rho\frac{\mathrm{d}T}{\mathrm{d}t} = \frac{\mathrm{d}(\rho T)}{\mathrm{d}t} - T\frac{\mathrm{d}\rho}{\mathrm{d}t} = \frac{\mathrm{d}(\rho T)}{\mathrm{d}t} - T\dot{S}_M. \tag{A.15}$$

With this relation the temporal change of sensible enthalpy can be expressed as

$$\frac{\mathrm{d}(\rho h_s)}{\mathrm{d}t} = h_{s,F}\dot{S}_M + c_p\frac{\mathrm{d}(\rho T)}{\mathrm{d}t} - c_p T\dot{S}_M. \tag{A.16}$$

Solving the equation for the time derivative of temperature and inserting the expressions for the mass source term, Eq. (A.2), and sensible enthalpy source term, Eq. (A.11), finally gives

$$\begin{aligned} c_p\frac{\mathrm{d}(\rho T)}{\mathrm{d}t} = \dot{S}_T &= \frac{\mathrm{d}(\rho h_s)}{\mathrm{d}t} - (h_{s,F} - c_p T)\dot{S}_M \\ &= -\frac{1}{V}\left(\frac{\mathrm{d}(m_d h_d)}{\mathrm{d}t} - (h^\circ_{f,F} + h_{s,F} - c_p T)\frac{\mathrm{d}m_d}{\mathrm{d}t}\right) \\ &= -\frac{1}{V}\left(\frac{\mathrm{d}(m_d h_d)}{\mathrm{d}t} - (h_F - c_p T)\frac{\mathrm{d}m_d}{\mathrm{d}t}\right). \end{aligned} \tag{A.17}$$

The derived expressions are validated by solving the Lagrangian droplet equations along with the zero-dimensional equations of the gas phase, where the source terms account for mass, momentum and heat transfer between the liquid phase and the gas phase. The setup is identical to case ETH-1500K as described in Tab. 3.1, and the volume of the gas is set to $V = (15d_0)^3$. As shown in Fig. A.1, the total mass, momentum and absolute enthalpy remain constant versus time, which confirms the derived expressions for the evaporation source terms. The mass of the individual species is also conserved (not shown). Note that the results are independent of the energy variable that is used in the energy equation for the gas phase (absolute enthalpy, sensible enthalpy or temperature).

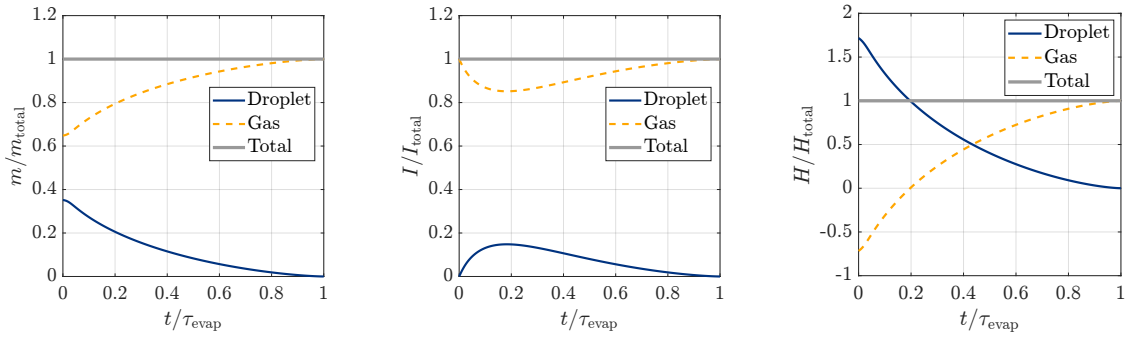

(a) Mass conservation. **(b)** Momentum conservation. **(c)** Enthalpy conservation.

Figure A.1: Proof of conservation of mass, momentum and absolute enthalpy based on a single droplet in a finite gas environment for the Eulerian fields. The initial conditions are given by case ETH-1500K (see Tab. 3.1), and the gas volume is $V = (15d_0)^3$. The results are independent of the energy variable in the energy equation (absolute enthalpy, sensible enthalpy or temperature).

A.2 Evaporation Source Terms in the Stochastic Particle Equations

The derivation of the closed-form expressions for the evaporation source terms in the stochastic particle equations is based on the assumption that the assignment of the fuel droplets to the stochastic particles is known as part of the two-phase coupling model, such that the conditional evaporation source term can be replaced by an instantaneous evaluation. Accordingly, the stochastic particle equations, considering only the evaporation substep, are given by (cf. Eqs. (4.38) and (4.39)),

$$\mathrm{d}\phi_\alpha^{sp} = (\Pi_\alpha^{sp} - \phi_\alpha^{sp}\Pi_F^{sp})\,\mathrm{d}t, \tag{A.18}$$

$$\mathrm{d}m^{sp} = m^{sp}\Pi_F^{sp}\mathrm{d}t, \tag{A.19}$$

with the composition vector $\boldsymbol{\phi}^{sp} = (\mathbf{Y}^{sp}, h^{sp})^\mathsf{T}$ containing the species mass fractions and absolute enthalpy. In analogy to the derivation of the source terms for the Eulerian solution, the pairing of a single droplet with a single stochastic particle is considered, with the change of mass and enthalpy of the droplet within a certain time interval given by $\mathrm{d}m_d$ and $\mathrm{d}(m_d h_d)$, respectively.

By substituting the expression for the generalized source term Π_F^{sp}, which can be expressed as (cf. Secs. 3.1.1, 3.1.4 and 3.2.4)

$$\Pi_F^{sp} = \frac{1}{\rho^{sp}}\dot{S}_M^{sp} = -\frac{1}{\rho^{sp}V^{sp}}\frac{\mathrm{d}m_d}{\mathrm{d}t} = -\frac{1}{m^{sp}}\frac{\mathrm{d}m_d}{\mathrm{d}t}, \tag{A.20}$$

the equation for the mass of the stochastic particle, Eq. (A.19), reduces to

$$\mathrm{d}m^{sp} = -\mathrm{d}m_d. \tag{A.21}$$

As expected, the change in the stochastic particle mass is equal to the negative change in the droplet mass, which preserves the total mass. Equation (A.18), evaluated for the fuel mass fraction, $\phi_\alpha^{sp} = Y_F^{sp}$, takes the form

$$\mathrm{d}Y_F^{sp} = (\Pi_F^{sp} - Y_F^{sp}\Pi_F^{sp})\,\mathrm{d}t = (1 - Y_F^{sp})\Pi_F^{sp}\mathrm{d}t. \tag{A.22}$$

Inserting the expression for Π_F^{sp}, Eq. (A.20), the equation for the fuel mass fraction finally becomes

$$\mathrm{d}Y_F^{sp} = -\frac{1}{m^{sp}}(1 - Y_F^{sp})\mathrm{d}m_d. \tag{A.23}$$

Note that the same equation is obtained from the condition $\mathrm{d}(m^{sp}Y_F^{sp}) = -\mathrm{d}m_d$, which provides an alternative way for the derivation. In a similar way one obtains the following equation for the non-evaporating species,

$$\mathrm{d}Y_k^{sp} = -\frac{1}{m^{sp}}(0 - Y_k^{sp})\mathrm{d}m_d, \qquad k \neq F. \tag{A.24}$$

Finally, using the expression for the generalized enthalpy source term Π_h^{sp}, which is given by

$$\Pi_h^{sp} = \frac{1}{\rho^{sp}}\dot{S}_h^{sp} = -\frac{1}{\rho^{sp}V^{sp}}\frac{\mathrm{d}(m_d h_d)}{\mathrm{d}t} = -\frac{1}{m^{sp}}\frac{\mathrm{d}(m_d h_d)}{\mathrm{d}t}, \tag{A.25}$$

the equation for the absolute enthalpy of the stochastic particle, Eq. (A.18) with $\phi_\alpha^{sp} = h^{sp}$, takes the form

$$\mathrm{d}h^{sp} = -\frac{1}{m^{sp}}\left(\mathrm{d}(m_d h_d) - h^{sp}\mathrm{d}m_d\right). \tag{A.26}$$

Again, it is possible to achieve the same expression with the condition $\mathrm{d}(m^{sp}h^{sp}) = -\,\mathrm{d}(m_d h_d)$.

Khan *et al.* [102] adopted a different notation for their two-phase MMC-LES formulation, in which the enthalpy source term, Eq. (A.25), is split according to

$$\Pi_h^{sp} = -\frac{1}{m^{sp}}\left(\underbrace{m_d c_l \frac{\mathrm{d}T_d}{\mathrm{d}t}}_{=\dot{Q}_d} + h_d \underbrace{\frac{\mathrm{d}m_d}{\mathrm{d}t}}_{=-m^{sp}\Pi_F^{sp}}\right). \tag{A.27}$$

The first term can be identified with the right-hand side of the droplet temperature equation (droplet heating term, cf. Eq. (3.25)), while the second term is related to the mass source term. By introducing a droplet heating term per unit evaporative mass, $q_d = \dot{Q}_d/\dot{m}$, the enthalpy source term can be expressed as a function of the fuel mass source term,

$$\Pi_h^{sp} = (h_d - q_d)\Pi_F^{sp}. \tag{A.28}$$

This allows further generalization, since now all components of the composition vector contain the fuel mass source term in the expression for the evaporation source term. The equation for the composition vector, Eq. (A.18), can then be written as

$$\mathrm{d}\phi_\alpha^{sp} = (\phi_{\alpha,d}^{*} - \phi_\alpha^{sp})\Pi_F^{sp}\mathrm{d}t, \tag{A.29}$$

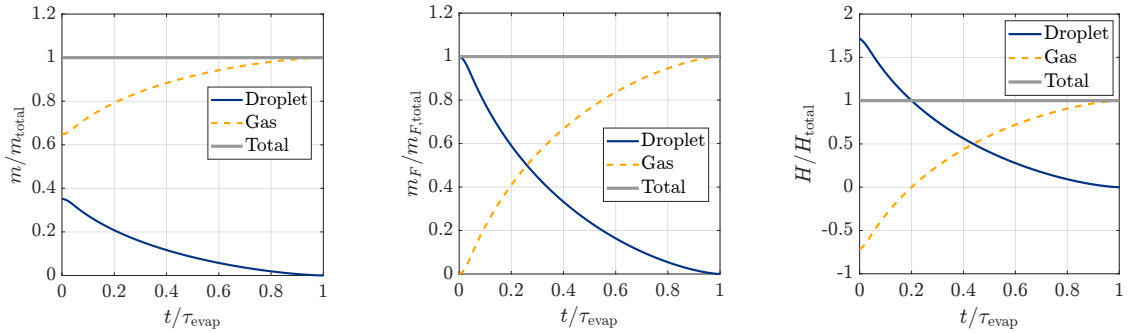

(a) Total mass conservation. **(b)** Fuel mass conservation. **(c)** Enthalpy conservation.

Figure A.2: Proof of conservation of total mass, fuel mass and absolute enthalpy based on the coupling between a single droplet and a single stochastic particle. The initial conditions are given by case ETH-1500K (see Tab. 3.1, the gas velocity is set to zero here), and the volume of the stochastic particle is $V^{sp} = (15d_0)^3$.

with $\phi^*_{\alpha,d} = \phi_{\alpha,d}$ for $\phi_\alpha \in \mathbf{Y}$, and $\phi^*_{\alpha,d} = h_d - q_d$ for $\phi^{sp}_\alpha = h^{sp}$. Note that the droplet heating term per unit evaporative mass (q_d) is not defined if the evaporation rate becomes zero (pure heat transfer), which may cause numerical difficulties.

The derived expressions are validated using the setup from the previous section but with the gas velocity set to zero, as momentum transfer is not part of the two-phase coupling between the Lagrangian fields (cf. Fig. 4.1). As shown in Fig. A.2, total mass, species mass and absolute enthalpy are conserved between the droplet and the stochastic particle. It should be noted that the numerical discretization of the presented equations is not necessarily mass and energy conserving, as the composition vector includes the variables in non-conservative form (i.e., Y_k instead of ρY_k). Using the explicit Euler method, the discretized form of the fuel mass fraction equation, Eq. (A.23), is given by

$$Y_F^{sp}(t+\Delta t) = \frac{(m^{sp}(t) + \mathrm{d}m_d)Y_F^{sp}(t) - \mathrm{d}m_d}{m^{sp}(t)}. \tag{A.30}$$

A discretely mass-conserving formulation follows from the discretization of the condition $\mathrm{d}(m^{sp}Y_F^{sp}) = -\mathrm{d}m_d$ and is given by

$$Y_F^{sp}(t+\Delta t) = \frac{m^{sp}(t)Y_F^{sp}(t) - \mathrm{d}m_d}{m^{sp}(t) - \mathrm{d}m_d}. \tag{A.31}$$

The two expressions differ by the prefactor of the fuel mass fraction at the old time level and by the denominator. Note that this error also occurs if another numerical method is used. Since the evaporated mass per time step is usually several orders of magnitude smaller than the mass of the stochastic particle, the error is negligible and both expressions can be used equivalently in practice (the absolute error in Fig. A.2 at $t = \tau_{\text{evap}}$ is 0.04 % for the fuel mass and 0.07 % for the absolute enthalpy).

Appendix B

Mixture Fraction Variance Equation

B.1 Variance Definition

The balance equation for the mixture fraction variance is derived here in the LES context, where the variance is associated with the subgrid-scale variance, but is equally valid in the RANS context if the filter operator is replaced by an averaging operator. The variance is typically defined as the mean square of the fluctuations. However, as discussed in Cook *et al.* [35] and Jiménez *et al.* [98], the application of this definition to LES, $f_V = \widetilde{f''^2}$, was found to cause problems in practical calculations. Therefore, the subgrid-scale variance is usually defined as the filtered-mean-of-the-square minus the square-of-the-filtered-mean,

$$f_V = \widetilde{f^2} - \widetilde{f}^2. \tag{B.1}$$

This definition is also consistent with the filtered density function approach [98]. Note that for Reynolds operators, for which $\tilde{\tilde{f}} = \tilde{f}$, both definitions are equivalent.

B.2 Derivation of the Variance Equation

B.2.1 Exact Form

Starting with the instantaneous transport equation for mixture fraction, which is given by Eq. (4.4) and repeated here for the sake of completeness,

$$\frac{\partial(\rho f)}{\partial t} + \frac{\partial(\rho u_j f)}{\partial x_j} = \frac{\partial}{\partial x_j}\left(\rho \mathcal{D} \frac{\partial f}{\partial x_j}\right) + \dot{S}_M, \tag{B.2}$$

transport equations for the filtered squared mixture fraction, $\widetilde{f^2}$, and the squared filtered mixture fraction, $\widetilde{f}^2$, are derived in order to obtain the balance equation for

the subgrid-scale variance according to the variance definition, Eq. (B.1). Using the following relations,

$$\frac{\partial(\rho f^2)}{\partial t} = 2f\frac{\partial(\rho f)}{\partial t} - f^2\frac{\partial \rho}{\partial t}, \tag{B.3a}$$

$$\frac{\partial(\rho u_j f^2)}{\partial x_j} = 2f\frac{\partial(\rho u_j f)}{\partial x_j} - f^2\frac{\partial(\rho u_j)}{\partial x_j}, \tag{B.3b}$$

$$\frac{\partial}{\partial x_j}\left(\rho\mathcal{D}\frac{\partial f^2}{\partial x_j}\right) = 2f\frac{\partial}{\partial x_j}\left(\rho\mathcal{D}\frac{\partial f}{\partial x_j}\right) + 2\rho\mathcal{D}\frac{\partial f}{\partial x_j}\frac{\partial f}{\partial x_j}, \tag{B.3c}$$

the multiplication of the instantaneous mixture fraction equation by $2f$ and incorporating the continuity equation, Eq. (3.1), yields the transport equation for the squared mixture fraction,

$$\underbrace{\frac{\partial(\rho f^2)}{\partial t}}_{\text{Temporal change}} + \underbrace{\frac{\partial(\rho u_j f^2)}{\partial x_j}}_{\text{Convection}} = \underbrace{\frac{\partial}{\partial x_j}\left(\rho\mathcal{D}\frac{\partial f^2}{\partial x_j}\right)}_{\text{Diffusion}} \underbrace{- 2\rho\mathcal{D}\frac{\partial f}{\partial x_j}\frac{\partial f}{\partial x_j}}_{\text{Dissipation}} + \underbrace{(2f - f^2)\dot{S}_M}_{\text{Evaporation source}} . \tag{B.4}$$

Compared to the transport equation for the mixture fraction, Eq. (B.2), the balance equation for the squared mixture fraction contains an additional dissipation term, which is linked to the scalar dissipation rate,

$$\chi = 2\mathcal{D}\frac{\partial f}{\partial x_j}\frac{\partial f}{\partial x_j}, \tag{B.5}$$

with unit s^{-1}. Note that the scalar dissipation rate is always positive, making the term in Eq. (B.4) a dissipation term due to the negative sign. The evaporation source term appears with a prefactor that is between zero and one since mixture fraction is below unity. By applying the density-weighted filter operator to the transport equation for the squared mixture fraction, Eq. (B.4), one obtains

$$\frac{\partial(\bar{\rho}\widetilde{f^2})}{\partial t} + \frac{\partial(\bar{\rho}\widetilde{u}_j\widetilde{f^2})}{\partial x_j} = \frac{\partial}{\partial x_j}\left(\bar{\rho}\mathcal{D}\frac{\partial\widetilde{f^2}}{\partial x_j}\right) - \bar{\rho}\widetilde{\chi} - \frac{\partial}{\partial x_j}\left(\bar{\rho}\widetilde{u_j f^2} - \bar{\rho}\widetilde{u}_j\widetilde{f^2}\right) + 2\overline{f\dot{S}}_M - \overline{f^2\dot{S}}_M. \tag{B.6}$$

Similar to the derivation of the transport equation for the non-filtered squared mixture fraction described above, an equation for the squared filtered mixture fraction can be derived. Starting from the exact transport equation for the filtered mixture fraction given by Eq. (4.13), one obtains

$$\frac{\partial(\bar{\rho}\widetilde{f}^2)}{\partial t} + \frac{\partial(\bar{\rho}\widetilde{u}_j\widetilde{f}^2)}{\partial x_j} = \frac{\partial}{\partial x_j}\left(\bar{\rho}\mathcal{D}\frac{\partial\widetilde{f}^2}{\partial x_j}\right) - \bar{\rho}\breve{\chi} - 2\widetilde{f}\frac{\partial}{\partial x_j}\left(\bar{\rho}\widetilde{u_j f} - \bar{\rho}\widetilde{u}_j\widetilde{f}\right) + (2\widetilde{f} - \widetilde{f}^2)\bar{\dot{S}}_M, \tag{B.7}$$

where the scalar dissipation rate appears here as a function of filtered variables,

$$\breve{\chi} = 2\mathcal{D}\frac{\partial\widetilde{f}}{\partial x_j}\frac{\partial\widetilde{f}}{\partial x_j}. \tag{B.8}$$

The balance equation for the subgrid-scale variance of mixture fraction is finally obtained by subtracting Eq. (B.7) from Eq. (B.6), leading to

$$\begin{aligned}\frac{\partial(\bar{\rho}f_V)}{\partial t}+\frac{\partial(\bar{\rho}\widetilde{u}_j f_V)}{\partial x_j} &= \frac{\partial}{\partial x_j}\left(\bar{\rho}\mathcal{D}\frac{\partial f_V}{\partial x_j}\right)-\underbrace{\bar{\rho}(\widetilde{\chi}-\check{\chi})}_{(1)}\\ &\quad-\underbrace{\frac{\partial}{\partial x_j}\left(\bar{\rho}\widetilde{u_j f^2}-\bar{\rho}\widetilde{u}_j\widetilde{f^2}\right)}_{(2)}+\underbrace{2\widetilde{f}\frac{\partial}{\partial x_j}\left(\bar{\rho}\widetilde{u_j f}-\bar{\rho}\widetilde{u}_j\widetilde{f}\right)}_{(3)}\\ &\quad+\underbrace{2\left(\overline{f\dot{S}}_M-\widetilde{f}\overline{\dot{S}}_M\right)}_{(4)}-\underbrace{\left(\overline{f^2\dot{S}}_M-\widetilde{f}^2\overline{\dot{S}}_M\right)}_{(5)}.\end{aligned} \tag{B.9}$$

This equation describes the temporal change of the subgrid-scale mixture fraction variance due to the effects of resolved convection and molecular diffusion, dissipation and production, subgrid-scale turbulent fluxes, and evaporation sources. There are five unclosed terms in Eq. (B.9) denoted as (1) to (5), which require modeling. The evaporation sources, terms (4) and (5), appear with both positive and negative sign and thus lead to variance production and destruction. Typically, term (5) has a smaller absolute value than term (4) and can often be neglected [147]. Accordingly, evaporation generally leads to an increase of the subgrid-scale variance.

If the filter operator is replaced by an averaging operator in a homogeneous system, where the mean gradients vanish, the variance equation reduces to

$$\frac{\partial(\bar{\rho}f_V)}{\partial t}=-\bar{\rho}\widetilde{\chi}+2\left(\overline{f\dot{S}}_M-\widetilde{f}\overline{\dot{S}}_M\right)-\left(\overline{f^2\dot{S}}_M-\widetilde{f}^2\overline{\dot{S}}_M\right). \tag{B.10}$$

This equation clearly shows the destruction and generation of variance due to the mechanisms of scalar dissipation and evaporation, respectively. Note that this equation is often approximately fulfilled also in inhomogeneous systems, since the scalar dissipation term and the evaporation source terms are typically the dominant terms in the variance equation.

B.2.2 Modeled Form

The subgrid-scale turbulent fluxes, terms (2) and (3), are closed by the classical gradient diffusion model using a turbulent diffusivity [98],

$$-\frac{\partial}{\partial x_j}\left(\bar{\rho}\widetilde{u_j f^2}-\bar{\rho}\widetilde{u}_j\widetilde{f^2}\right)=\frac{\partial}{\partial x_j}\left(\bar{\rho}\mathcal{D}_t\frac{\partial\widetilde{f^2}}{\partial x_j}\right), \tag{B.11}$$

and

$$2\widetilde{f}\frac{\partial}{\partial x_j}\left(\bar{\rho}\widetilde{u_j f}-\bar{\rho}\widetilde{u}_j\widetilde{f}\right)=-2\widetilde{f}\frac{\partial}{\partial x_j}\left(\bar{\rho}\mathcal{D}_t\frac{\partial\widetilde{f}}{\partial x_j}\right)=-\frac{\partial}{\partial x_j}\left(\bar{\rho}\mathcal{D}_t\frac{\partial\widetilde{f^2}}{\partial x_j}\right)+2\bar{\rho}\mathcal{D}_t\frac{\partial\widetilde{f}}{\partial x_j}\frac{\partial\widetilde{f}}{\partial x_j}, \tag{B.12}$$

where Eq. (B.3c) was used to reformulate the resolved diffusion term. By inserting these models into the balance equation for the subgrid-scale mixture fraction variance, Eq. (B.9), the following modeled balance equation is obtained,

$$\begin{aligned}\frac{\partial(\bar{\rho}f_V)}{\partial t}+\frac{\partial(\bar{\rho}\widetilde{u}_j f_V)}{\partial x_j} &= \frac{\partial}{\partial x_j}\left(\bar{\rho}(\mathcal{D}+\mathcal{D}_t)\frac{\partial f_V}{\partial x_j}\right)\\ &\quad -\bar{\rho}\widetilde{\chi}+2\bar{\rho}(\mathcal{D}+\mathcal{D}_t)\frac{\partial\widetilde{f}}{\partial x_j}\frac{\partial\widetilde{f}}{\partial x_j}\\ &\quad +2\left(\overline{f\dot{S}}_M-\widetilde{f}\bar{\dot{S}}_M\right)-\left(\overline{f^2\dot{S}}_M-\widetilde{f}^2\bar{\dot{S}}_M\right). \end{aligned} \tag{B.13}$$

The remaining terms that need modeling are the filtered scalar dissipation rate $\widetilde{\chi}$ and the evaporation source terms. The common model for the filtered scalar dissipation rate that is given by Eq. (4.48) cannot be used for closure of the variance equation, as it is based on local equilibrium between dissipation and production (in the absence of evaporation sources), and thus the variance equation would reduce to a convection-diffusion equation in which the subgrid-scale variance is conserved. Instead, the filtered scalar dissipation rate is often modeled in terms of a characteristic mixing time scale that is assumed to be proportional to the characteristic turbulent time scale, as proposed by Jiménez *et al.* [98]. The modeling of the evaporation source terms is discussed in Pera *et al.* [147], where an algebraic model for term (4) in Eq. (B.9) is derived using dimensional arguments, while term (5) is neglected.

B.3 Some Remarks on the Numerical Evaluation

Care must be taken when analyzing the magnitude of the terms in the variance equation, e.g., by using post-filtered DNS data. The final form of the variance equation is based on reformulations of the spatial derivatives as given by Eqs. (B.3b) and (B.3c), which require a smooth and differentiable mixture fraction field to be valid. In Euler-Lagrange simulations of dilute sprays, the two-way coupling between the liquid droplets and the gas phase typically produces discrete source terms leading to large gradients at the droplet positions, which can cause numerical inaccuracies in the evaluation of the spatial derivatives. As a result, the derived variance equation, Eq. (B.9), may not be fulfilled by the numerical method.

To demonstrate the possible inconsistency of the variance equation if the terms are evaluated using numerical data, a simplified mixture fraction equation is considered, neglecting the effect of convection and assuming a constant density and diffusion coefficient,

$$\frac{\partial f}{\partial t}=\mathcal{D}\frac{\partial^2 f}{\partial x_j^2}+\dot{S}, \tag{B.14}$$

where $\dot{S} = \dot{S}_M/\rho$ is the evaporation source term. Multiplication of the equation by $2f$ gives the equation for the squared mixture fraction,

$$\frac{\partial f^2}{\partial t} = 2\mathcal{D} f \frac{\partial^2 f}{\partial x_j^2} + 2f\dot{S}. \tag{B.15}$$

Note that the reformulation of the diffusion term according to Eq. (B.3c) is not yet applied. The corresponding balance equation for the mixture fraction variance, $f_V = \overline{f^2} - \bar{f}^2$, then takes the form

$$\frac{\partial f_V}{\partial t} = \overline{2\mathcal{D} f \frac{\partial^2 f}{\partial x_j^2}} - 2\mathcal{D}\bar{f}\frac{\partial^2 \bar{f}}{\partial x_j^2} + \mathcal{S}^+, \tag{B.16}$$

where the term $\mathcal{S}^+$ is used for the evaporation source to indicate that it has a positive sign,

$$\mathcal{S}^+ = 2\left(\overline{f\dot{S}} - \bar{f}\bar{\dot{S}}\right). \tag{B.17}$$

Note that the second evaporation source, term (5) in Eq. (B.9), which has a negative sign, does not appear here because density is assumed to be constant and convection is neglected, eliminating the need for the continuity equation. By applying the reformulation of the diffusion term given by Eq. (B.3c), the usual form of the variance equation is obtained,

$$\frac{\partial f_V}{\partial t} = \mathcal{D}\frac{\partial^2 f_V}{\partial x_j^2} - \overline{2\mathcal{D}\frac{\partial f}{\partial x_j}\frac{\partial f}{\partial x_j}} + 2\mathcal{D}\frac{\partial \bar{f}}{\partial x_j}\frac{\partial \bar{f}}{\partial x_j} + \mathcal{S}^+. \tag{B.18}$$

Note that both variance equations, Eqs. (B.16) and (B.18) are mathematically equivalent, but their numerical evaluation may be different, as will be shown shortly. To further simplify the problem, a homogeneous system is considered, where the mean gradients vanish. This yields the following equivalent equations for the mixture fraction variance,

$$\frac{\mathrm{d}f_V}{\mathrm{d}t} = -\bar{\chi}^* + \mathcal{S}^+, \qquad \bar{\chi}^* = -\overline{2\mathcal{D} f \frac{\partial^2 f}{\partial x_j^2}}, \tag{B.19a}$$

$$\frac{\mathrm{d}f_V}{\mathrm{d}t} = -\bar{\chi} + \mathcal{S}^+, \qquad \bar{\chi} = \overline{2\mathcal{D}\frac{\partial f}{\partial x_j}\frac{\partial f}{\partial x_j}}. \tag{B.19b}$$

Figure B.1 compares the magnitude of the terms on the right-hand side of the two variance equations with the time derivative of the mixture fraction variance based on a cubic domain filled with evaporating droplets and utilizing the particle-source-in-cell approach (cf. Sec. 3.2.4). First, the case is considered where the evaporated mass is transferred to the cell that contains the droplet, which results in discrete source terms that are non-zero only at the droplet positions. As shown in Fig. B.1(a), the usual form of the variance equation, Eq. (B.19b), produces an inconsistency between

the right-hand side of the equation and the time derivative of the variance. This is because the mixture fraction field is non-smooth due to discrete source terms, and therefore the reformulation of the diffusion term is not valid. In contrast, the evaluation of the right-hand side of the original form of the variance equation, Eq. (B.19a), coincides with the time derivative of the variance. If the source terms are distributed to a larger volume around each droplet in a way to produce a smooth mixture fraction field (see Sec. 5.3.3 for details), the right-hand side and the left-hand side of both variance equations agree, as shown in Fig. B.1(b). Although the exact form of the mixture fraction variance equation is often not fulfilled by the numerical method due to the occurrence of non-smooth source terms, it can still be used to study the different mechanisms of variance production and dissipation.

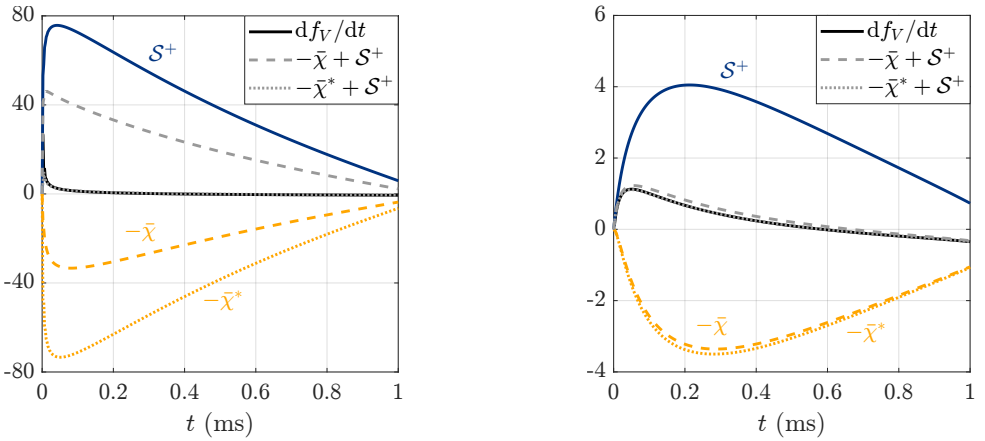

(a) Discrete source terms. **(b)** Smooth source terms.

Figure B.1: Proof of validation of the variance equation based on evaporating droplets in a cubic domain (closed system) considering only mass transfer. The nominal droplet distance is $\Delta_L/d_0 = 20$, and the cell size is $\Delta x/d_0 = 2$. Droplets evaporate according to the volume-averaged mixture fraction of the gas phase, and the evaporated mass is either transferred to the cell that contains the droplet (a) or distributed over a larger volume to create smooth fields (b).

Appendix C

Inter-Particle Distances: Direct Search vs. k-d Tree Algorithm

C.1 Description of the Problem

The estimation of appropriate mixing and coupling parameters for the two-phase MMC-LES model requires knowledge of the expected mean distances between the stochastic particles and the droplets, which result from the minimization of the effective square distances (cf. Eqs. (4.51) and (4.60)). In Sec. 4.4.2, the isoscalar sliver relation was presented, which provides a relation between the mixing distances r_m and f_m in physical and reference space, respectively. However, it does not contain information about the absolute values of the mixing parameters as well as the numerical algorithm used to find the nearest neighbors. Furthermore, there is no such relationship for estimating the two-phase coupling parameters. Therefore, the following questions arise, which will be clarified in the present chapter:

(1) What is the average mutual distance between randomly distributed particles that results from the use of a direct search method?
(2) What is the average mutual distance between randomly distributed particles that results from the use of the k-d tree algorithm (as used in MMC)?
(3) What is the average distance between two independent particle clouds (as required for two-phase coupling between the droplets and the notional particles)?

To answer these questions, a random distribution of particles in a multidimensional space is considered, with $\nu = \{1, 2, 3, ...\}$ denoting the dimension of the space. Note that dimensions higher than three can be associated with the MMC reference variables that are used for the particle selection in addition to the three-dimensional physical space. A key quantity to characterize the particle distribution is the particle

number density, which specifies the number of particles per unit volume,

$$n = \frac{N}{V}, \tag{C.1}$$

where N is the number of particles and $V = L^\nu$ is the volume occupied by the particles with L being the length of the domain in each dimension. From the particle number density the nominal particle distance is derived,

$$\Delta_L = n^{-1/\nu} = \left(\frac{V}{N}\right)^{1/\nu}, \tag{C.2}$$

which represents the distance between the particles in a regular arrangement. Since the particles have random positions, the nominal particle distance does not reflect the real distances between the particles, but serves as a reference length. The distance between a particle p and its nearest neighbor q is denoted as $d^{p,q}$, and by taking the average over all particle pairs the mean inter-particle distance $\langle d^{p,q} \rangle$ is obtained. A closed-form expression for the mean inter-particle distance of randomly distributed particles exists, which is given by [23, 81]

$$\frac{\langle d^{p,q} \rangle}{\Delta_L} = \frac{1}{\sqrt{\pi}} \left[\Gamma\left(\frac{\nu}{2} + 1\right)\right]^{1/\nu} \Gamma\left(1 + \frac{1}{\nu}\right), \tag{C.3}$$

where Γ denotes the gamma function. The corresponding values for dimensions $\nu = 1$ to $\nu = 5$ are reported in Tab. C.1. It can be seen that the ratio $\langle d^{p,q} \rangle / \Delta_L$ increases with increasing dimension, but is smaller than one for practical cases ($\nu \leq 14$).

When solving the nearest neighbor search problem with a computer code, the simplest solution is to calculate for each point the distance to every other point and keep the minimum distance found. This algorithm, which is referred to as direct search, reproduces the analytical solution given by Eq. (C.3). However, it is not suitable for high particle numbers, as the computing time increases quadratically with the particle number.

C.2 The k-d Tree Algorithm

C.2.1 Properties of the k-d Tree Algorithm

The MMC mixing model uses an approximate nearest neighbor search method [31] based on the k-d tree [57] to minimize the effective square distance between the stochastic particles, which is referred to as k-d tree algorithm in the present work. As illustrated in Fig. C.1, the k-d tree algorithm differs from a direct search by the following properties:

- Particles are grouped in unique pairs, which is desirable for pairwise mixing, in an attempt to minimize the mean inter-particle distance (in MMC this is the effective square distance), whereas a direct search can lead to chain-like assignments. As a result, not every particle can be paired with its nearest neighbor, such that the mean inter-particle distance is larger compared to a direct search.
- The algorithm features an approximately linear scaling of the computing time with the number of particles and is therefore much more efficient than a direct search, in particular for higher particle numbers.

C.2.2 How the Algorithm Works

The procedure of selecting particle pairs for mixing based on the k-d tree algorithm is described in Cleary *et al.* [31]. The implementation in C++ makes use of pointers and recursive function calls, and can be summarized as follows:

1. Calculate the scaled spans of each dimension. For the effective square distance given by Eq. (4.51) the scaled spans are given by
$$l_{x_i} = \frac{\max(x_i^{sp}) - \min(x_i^{sp})}{r_i}, \qquad l_f = \frac{\max(f^{sp}) - \min(f^{sp})}{f_m}, \tag{C.4}$$
where f^{sp} denotes the reference mixture fraction at the particle positions.
2. Sort the particles along the direction of the dimension that has the largest span.
3. Divide the sorted list of particles into two sections of equal size, where the number of particles in at least one section must be divisible by two.

These steps are repeated for each section until the number of particles in each section is equal to or lower than two.

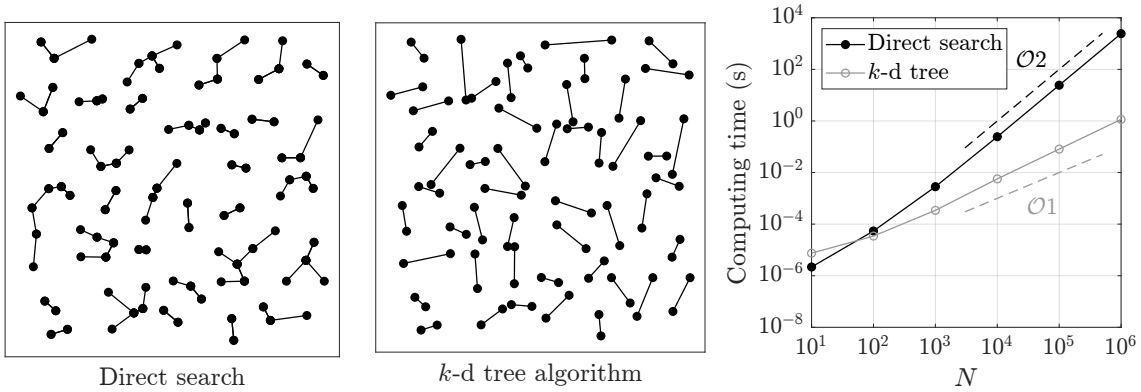

(a) Nearest neighbors, connected by a line, in a 2D domain obtained from direct search and the k-d tree algorithm.

(b) Computing time versus number of particles in a 3D domain.

Figure C.1: Comparison of direct search and k-d tree algorithm for finding the nearest neighbors in a random distribution of particles.

C.2.3 Mean Inter-Particle Distances

In order to find the mean inter-particle distances obtained from the k-d tree algorithm, a multidimensional space of dimension ν with length $L = 1$ per dimension is considered and filled with N particles at random positions. The k-d tree algorithm is then used to divide the set of particles into pairs minimizing the mutual distances. For each pair the inter-particle distance $d^{p,q}$ is calculated and the average of all pairs, $\langle d^{p,q} \rangle$, is taken. The results of the calculations with different numbers of particles and dimensions are shown in Fig. C.2. For small numbers of particles ($N \lesssim 10^4$), there are larger fluctuations ($\pm 10\,\%$), which decrease as the number of particles is further increased. In contrast to the one-dimensional case, where the mean inter-particle distance converges to a single value, there is no convergence in the higher dimensions and the mean inter-particle distance shows a wave pattern as a function of the number of particles. For each dimension investigated here, the average value of the mean inter-particle distance is calculated using the results with $N > 10^5$. The corresponding values are reported in Tab. C.1, where they are compared to the results of the direct search method. It can be seen that the k-d tree algorithm yields mean inter-particle distances close to the nominal particle distance and thus larger than those obtained from a direct search. In a one-dimensional space the mean inter-particle distance determined by the k-d tree algorithm is exactly equal to the nominal particle distance, whereas it is slightly smaller in two- and three-dimensional problems and slightly larger in higher dimensions. The trend that the mean inter-particle distance increases with increasing dimension is the same as for the direct search. By calculating the ratio of the respective mean inter-particle distances, one obtains a value that is almost constant and close to 5/3, except for the one-dimensional case, where it is two.

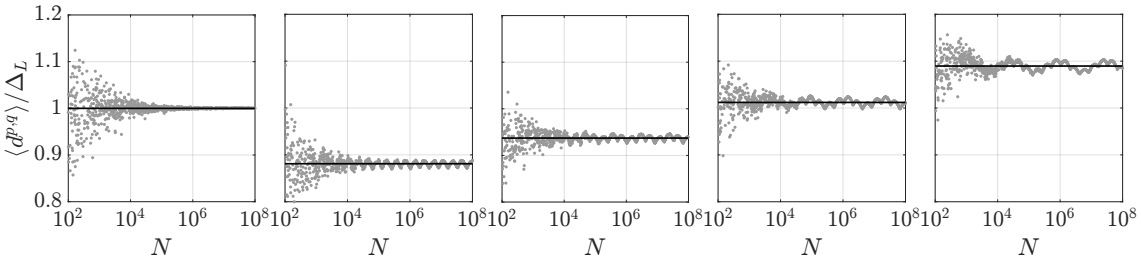

(a) $\nu = 1$ **(b)** $\nu = 2$ **(c)** $\nu = 3$ **(d)** $\nu = 4$ **(e)** $\nu = 5$

Figure C.2: Mean inter-particle distances obtained from the k-d tree algorithm, normalized by the nominal particle distance and plotted versus the number of particles, for different dimensions ν. The solid line marks the average value that is calculated using the results with $N > 10^5$.

Table C.1: Mean inter-particle distances for different dimensions ν obtained from direct search and k-d tree algorithm.

	$\nu = 1$	$\nu = 2$	$\nu = 3$	$\nu = 4$	$\nu = 5$
$\langle d^{p,q} \rangle / \Delta_L$, direct search, Eq. (C.3)	0.5000	0.5000	0.5540	0.6081	0.6587
$\langle d^{p,q} \rangle / \Delta_L$, k-d tree algorithm	1.0000	0.8811	0.9372	1.0119	1.0896
Ratio k-d tree algorithm to direct search	2.00	1.76	1.69	1.66	1.65

C.3 Distances Between Two Particle Clouds

The two-phase coupling between the fuel droplets and the stochastic particles based on a one-to-one coupling strategy involves the determination of minimum distances between two independent particle clouds (cf. Sec. 4.5.3). In order to find appropriate coupling parameters, knowledge of the expected distances between the droplets and the notional particles is required. Therefore, the present investigation is extended by a second particle cloud, where only direct search will be considered in the following. Both particle clouds occupy the same volume, but may have different numbers of particles, denoted as N_1 and N_2. As illustrated in Fig. C.3, four different inter-particle distances can be defined: $d_{1,1}^{p,q}$ and $d_{2,2}^{p,q}$ are the inter-particle distances of cloud 1 and 2, respectively, considering only one cloud each (Figs. C.3(a) and C.3(b)), $d_{1,2}^{p,q}$ denotes the distance between a particle from cloud 1 and its nearest neighbor in cloud 2 (Fig. C.3(c)), and $d_{2,1}^{p,q}$ denotes the reverse case (Fig. C.3(d)). The figure suggests that the average distance $\langle d_{1,2}^{p,q} \rangle$ is comparable to $\langle d_{2,2}^{p,q} \rangle$, and $\langle d_{2,1}^{p,q} \rangle$ to $\langle d_{1,1}^{p,q} \rangle$. This assumption is verified by comparing the PDFs of the aforementioned inter-particle distances, as shown in Fig. C.4(a), and its validity is generalized by numerical calculations with varying particle numbers N_1 and N_2 (cf. Fig. C.4(b)) and different dimensions (not shown). Consequently, the average distance between a particle from cloud 1 and its nearest neighbor in cloud 2 is equivalent to the mean inter-particle distance of cloud 2, and does not depend on the mean inter-particle distance of cloud 1. The application of this finding to the MMC two-phase coupling indicates that the distance between the droplets and the stochastic particles is in principle the same as the inter-particle distance of the stochastic particles, and does not depend on the number of droplets. However, as the two-phase coupling employs a direct search while the MMC mixing pair selection utilizes the k-d tree algorithm, the distances differ by a constant factor as given by Tab. C.1.

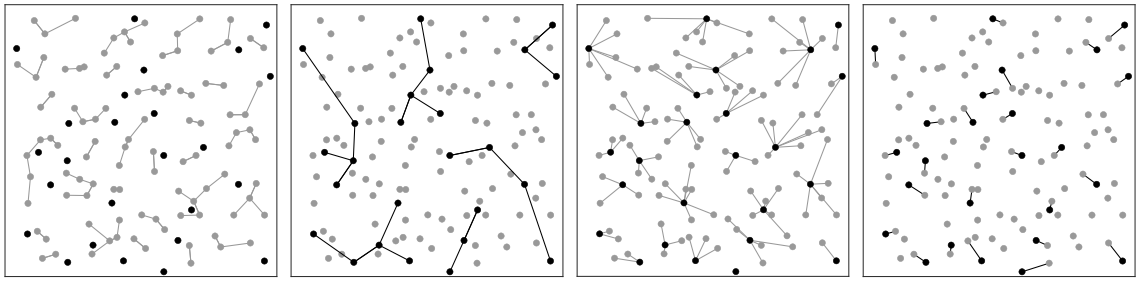

(a) $d_{1,1}^{p,q}$ **(b)** $d_{2,2}^{p,q}$ **(c)** $d_{1,2}^{p,q}$ **(d)** $d_{2,1}^{p,q}$

Figure C.3: Nearest neighbor search within and between two particle clouds (cloud 1 is marked in gray, and cloud 2 in black) using direct search. The term $d_{\alpha,\beta}^{p,q}$ denotes the distance of a particle p in cloud α to its nearest neighbor q in cloud β.

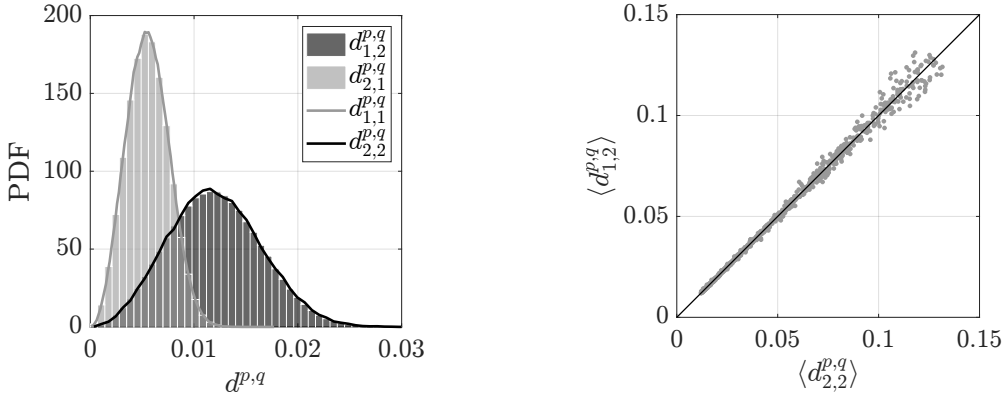

(a) PDFs of inter-particle distances within and between two clouds denoted as 1 and 2, with particle numbers $N_1 = 10^6$ and $N_2 = 10^5$.

(b) Relation between mean inter-particle distances $\langle d_{1,2}^{p,q} \rangle$ and $\langle d_{2,2}^{p,q} \rangle$ for different particle numbers N_1 and N_2.

Figure C.4: Analysis of inter-particle distances within and between two particle clouds using direct search in a three-dimensional domain with length $L = 1$.

Appendix D

Quasi-DNS Capabilities of OpenFOAM for Reacting Flows

D.1 Background

OpenFOAM [75, 95, 227] is one of the most widely used open-source libraries for computational fluid dynamics and offers a variety of well-established solvers for a wide range of applications, including simple incompressible flows as well as complex multiphase flows with turbulence and chemical reactions. Although OpenFOAM is conceived for RANS and LES, its great flexibility also makes OpenFOAM attractive as a tool for the direct numerical simulation (DNS). A DNS generally requires high-order (third order or higher [225]) schemes, whereas the ability of OpenFOAM to handle arbitrary meshes limits its accuracy to second order. However, if simple configurations with structured meshes are considered, OpenFOAM provides a higher-order interpolation scheme (referred to as `cubic`), which minimizes the numerical dissipation, though without increasing the overall order. In this context, the term quasi-DNS is often used, which refers to a model-free simulation that does not fulfill the strict requirements of a DNS but is accurate enough [243]. Although several studies have confirmed the quasi-DNS capabilities of OpenFOAM for both non-reacting flows [3, 27, 110, 111, 116] and reacting flows [125, 217, 218, 222, 224, 238, 243], a detailed quantification of the numerical accuracy of OpenFOAM with focus on turbulent reacting flows was not available until now [244].

The numerical accuracy and parallel performance of OpenFOAM and its reacting flow extension `EBIdnsFoam` [238] have recently been evaluated by Zirwes *et al.* [244] using the benchmark suite of Abdelsamie *et al.* [1] and comparing OpenFOAM with well-established high-fidelity DNS solvers. The purpose of the present chapter is to provide complementary investigations that are not included in the paper, whereby single studies are repeated to ensure completeness of the present chapter.

The outline is as follows. First, the accuracy of OpenFOAM's spatial discretization schemes is evaluated using simple validation cases with analytical solutions. This is followed by a detailed analysis of the operator splitting technique used to evaluate the reaction rates in OpenFOAM. Finally, more complex benchmark cases involving turbulence-like motion and combustion are presented, providing a direct comparison between OpenFOAM and a high-order DNS solver.

D.2 Accuracy of OpenFOAM's Discretization Schemes

D.2.1 Overview and Properties of the Numerical Schemes

OpenFOAM employs an implicit solution of the governing equations based on the finite volume method, where the partial differential equations are discretized in their integral form to enforce conservation of mass, momentum and energy. Volume integrals are converted to surface integrals using the divergence theorem, where an interpolation scheme is required for the evaluation of the fluxes at the faces of each computational cell. The interpolation schemes available in OpenFOAM are summarized in Tab. D.1 along with their basic properties, and can be mainly classified into the three groups of central schemes, upwind-based schemes and total variation diminishing (TVD) schemes.

The central schemes are usually the most accurate schemes due to their low dissipative error, but they can lead to stability problems, in particular if large gradients occur. In addition to the linear interpolation, which is often the default method, OpenFOAM provides a cubic interpolation scheme that makes use of explicitly calculated gradients in the adjacent cells (see Zirwes *et al.* [243, 244] for implementation details).

Upwind-based schemes take the flow direction into account during interpolation and thus have a higher stability compared to the central schemes especially for strong convective flows, but they exhibit a larger dissipative and dispersive error. OpenFOAM offers here the classical first-order `upwind` scheme and a second-order accurate `linearUpwind` scheme, which applies an explicit correction to the first-order upwind scheme based on the gradient in the upstream cell.

TVD schemes are designed to produce solutions that are free of oscillations, which is achieved by introducing a flux limiter function to preserve monotonicity, but they lead to a higher dissipative error and decrease to first-order accuracy in regions of large gradients and at local extrema. In addition to the classical flux limiter functions (`vanLeer`, `Minmod`, `SuperBee`, ...), OpenFOAM offers TVD-

Table D.1: Surface interpolation schemes in OpenFOAM along with their strengths and weaknesses.

Central schemes	Upwind-based schemes	TVD schemes
`linear`, `cubic`	`upwind`, `linearUpwind`	`limitedLinear`, `limitedCubic`, `QUICK`, `MUSCL`, `vanLeer`, `Minmod`, `SuperBee`, ...
⊕ Low dissipative error ⊖ Dispersive error ⊖ Potential stability problems	⊕ Higher stability ⊖ Dissipative error ⊖ Dispersive error	⊕ Solution remains bounded ⊕ No spurious oscillations ⊕ Low dispersive error ⊖ Dissipative error ⊖ Problems with local extrema

versions of the central interpolation schemes, which are known as `limitedLinear` and `limitedCubic`. These schemes basically employ a linear and cubic interpolation, respectively, but afterwards limit the interpolated value to satisfy the TVD property.

An alternative to TVD schemes are weighted essentially non-oscillating (WENO) schemes, which have been recently implemented in OpenFOAM [65, 126]. Gärtner *et al.* [65] showed that the WENO scheme leads to improved results if the flow contains discontinuities or if unstructured meshes are used, whereas the accuracy on structured meshes, which are usually used for DNS, is not better than for the central interpolation schemes. For this reason and because of the higher computational cost, the WENO scheme is not considered in the present work.

Transient problems additionally require a discretization of the time derivative term, where OpenFOAM offers the first-order Euler method, the Crank-Nisolson method and a second-order multistep method referred to as `backward` method. While the first-order Euler method generally provides higher stability, a second-order discretization must be used for an accurate time-resolved simulation. It was found that both the `backward` discretization and the Crank-Nicolson method generally produce similar results, and therefore the time discretization schemes will not be examined here. For more details on the spatial and temporal discretization schemes the reader is referred to the text books [55, 137, 214].

D.2.2 One-Dimensional Transport of a Sine Wave

The first validation case is the one-dimensional transport of a sine wave with constant velocity and periodic boundaries, which involves only the solution of the transport equation of a passive scalar. The domain size is set to $L = 1\,\mathrm{m}$ with a velocity of $u = 1\,\mathrm{m/s}$, and the initial field is given by $f(x) = \sin(\kappa x)$ with wavenumber $\kappa = 2\pi\,\mathrm{m}^{-1}$. The diffusivity is set to zero so that the convection term is the only

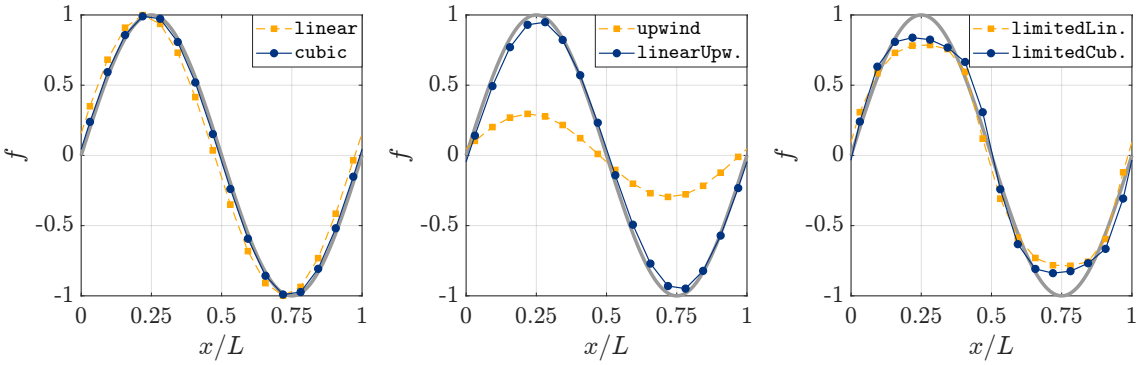

(a) Central schemes. **(b)** Upwind-based schemes. **(c)** TVD schemes.

Figure D.1: Numerical solution of the one-dimensional transport of a sine wave after one cycle over the domain using different discretization schemes. The number of grid cells is $N_x = 16$ and the Courant number is CFL $= 0.1$. The gray line denotes the exact solution.

spatial term that requires a discretization. The cell size is given by $\Delta x = L/N_x$, and a small time step is used in order to eliminate the error resulting from the time discretization method. Simulations are run for one cycle over the domain using the OpenFOAM solver `scalarTransportFoam`, with the exact solution given by the initial field.

The numerical solutions that are obtained after one cycle over the domain are shown in Fig. D.1 for different spatial discretization schemes. The `linear` scheme has almost no dissipative error but shows a dispersive error, while the `cubic` scheme minimizes both errors due to the use of a higher-order interpolation polynomial (Fig. D.1(a)). The first-order `upwind` scheme is clearly too dissipative, which makes it useless for practical problems (Fig. D.1(b)). In contrast, the second-order `linearUpwind` scheme leads to quite good predictions but exhibits a slight dissipative and dispersive error. The TVD schemes `limitedLinear` and `limitedCubic` have a low dispersive error, but significantly flatten the local extrema, since the limiter function reduces the solution there to first-order accuracy (Fig. D.1(c)). The `limitedCubic` scheme is slightly less dissipative, but the differences to the `limitedLinear` scheme are relatively small.

Figure D.2 shows the calculated L_2 errors obtained from different grid resolutions and discretization schemes. In Fig. D.2(a), the `linear` interpolation scheme is compared with the `cubic` interpolation scheme. It can be seen that the `cubic` scheme leads to smaller errors, but still shows a second-order convergence of the error, although the interpolation has a formal order of four. This has generally two reasons. First, the overall order of accuracy of the numerical solution is limited by the second order of the face flux integration, which, however, is irrelevant in the one-dimensional case. Second, the `cubic` scheme uses an interpolation polynomial that is based on point values, whereas the finite-volume discretization is based on

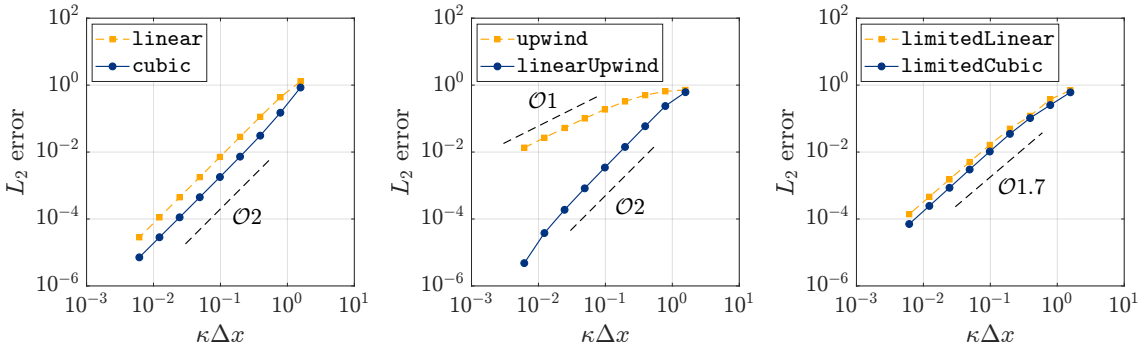

(a) Central schemes. **(b)** Upwind-based schemes. **(c)** TVD schemes.

Figure D.2: L_2 error obtained from the numerical solution of the one-dimensional transport of a sine wave after one cycle over the domain using different discretization schemes and plotted versus the cell size.

cell values. This inconsistency results in the discretization of the convection term being only second-order accurate. It is possible to achieve a fourth-order discretization of the convection term by modifying the coefficients for the `cubic` interpolation scheme, but test have shown that in three-dimensional simulations involving a pressure-velocity coupling the overall order is still two due to the aforementioned reason, so no improvements are obtained. The results of the upwind-based schemes are shown in Fig. D.2(b), where the simple `upwind` scheme reflects a first-order accuracy, while the `linearUpwind` scheme shows a second-order convergence with an accuracy comparable to the `cubic` scheme. Finally, Fig. D.2(c) shows the results of the TVD schemes, where the `limitedLinear` scheme is compared with the `limitedCubic` scheme. Due to the effect of the limiter function, the order of accuracy is no longer two but takes a value between one and two (here 1.7) depending on the smoothness of the solution.

D.2.3 Two-Dimensional Taylor-Green Vortex

The second validation case is an incompressible two-dimensional Taylor-Green vortex at a Reynolds number of Re = 1600, which requires the coupled solution for velocity and pressure while still featuring an analytical solution. The setup is described in Abdelsamie *et al.* [1] and in Zirwes *et al.* [244] and is not repeated here. Simulations are run for ten characteristic time scales with a Courant number of CFL = 0.03 using the incompressible solver `pimpleFoam`. The L_2 errors of the velocity (x-component) are shown in Fig. D.3. Again, the `upwind` scheme shows a first-order convergence of the error, while the `limitedLinear` scheme exhibits almost second-order accuracy. In contrast, the results obtained from the `linear` and `cubic` schemes do not show a clear trend. For coarse to moderate meshes, both

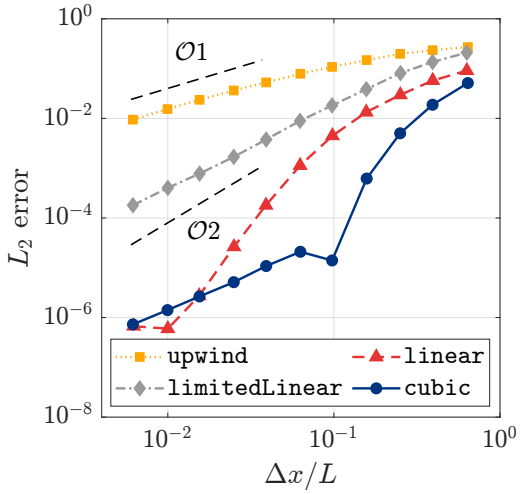

Figure D.3: L_2 error of the velocity (x-component) obtained from the numerical solution of the incompressible two-dimensional Taylor-Green vortex using different discretization schemes and plotted versus the cell size.

schemes exhibit a convergence order of more than second order, while the `cubic` scheme shows only a first-order convergence if the mesh is sufficiently fine. These trends are attributable to the pressure-velocity coupling and the iterative solution of the equation system, which also affects the convergence of the error. In fact, it was found that the convergence behavior of the `linear` and `cubic` schemes depends not only on the numerical parameters (e.g., time step width, matrix solver), but also on the flow parameters (e.g., domain size, characteristic velocity, Reynolds number). This sensitivity also explains the differences to the trends reported in Zirwes *et al.* [244]. However, it can still be observed that the `cubic` scheme leads to overall much smaller errors than obtained with the `linear` scheme and thus provides a more accurate solution of the flow field.

D.3 Operator Splitting Technique for Evaluating the Reaction Rates

D.3.1 Description of the Splitting Methods

In turbulent reacting flows, the characteristic chemical time scales are typically orders of magnitude smaller than the characteristic time scales of the flow and turbulence, which makes a coupled solution of the flow and chemistry with a direct evaluation of the reaction rates infeasible. For this reason, an operator-splitting technique is usually applied, which decouples the evaluation of the chemical reaction rates from the solution of the flow equations, enabling the use of optimized numerical

methods and time steps for each subproblem and thus reducing the computational cost. However, the splitting approach also introduces an error, which often reduces the numerical discretization to first-order accuracy.

The Classical Operator Splitting Methods

The discretized form of a scalar transport equation with a chemical source term is represented here by the general ordinary differential equation (ODE) given by

$$\frac{\mathrm{d}q}{\mathrm{d}t} + \mathcal{F}(q) = \mathcal{R}(q), \tag{D.1}$$

where q denotes the solution variable, $\mathcal{F}$ is the operator that results from the discretization of the spatial terms (i.e., the convection and diffusion terms), and $\mathcal{R}$ denotes the chemical source term.

The application of the classical first-order operator-splitting method, sometimes also known as "Godunov splitting" [118], to Eq. (D.1) is given by the sequential solution of the following subproblems:

$$\text{Substep 1:} \qquad \frac{\mathrm{d}q}{\mathrm{d}t} = \mathcal{R}(q), \qquad q^n \xrightarrow{\Delta t} q^*, \tag{D.2a}$$

$$\text{Substep 2:} \qquad \frac{\mathrm{d}q}{\mathrm{d}t} + \mathcal{F}(q) = 0, \qquad q^* \xrightarrow{\Delta t} q^{n+1}. \tag{D.2b}$$

Both subproblems are solved over one full time step using standard methods for each subproblem (i.e., a stiff ODE solver in substep 1 and the finite volume method in substep 2), where q^* represents an intermediate solution. One can show that this method is generally first-order accurate no matter how well each step is approximated, since the splitting method introduces an error proportional to the time step if operators $\mathcal{F}$ and $\mathcal{R}$ do not commute [118].

A slight modification of the above splitting technique yields a second-order accurate splitting method (provided that each subproblem is solved with a method of at least second-order accuracy) [118]:

$$\text{Substep 1:} \qquad \frac{\mathrm{d}q}{\mathrm{d}t} = \mathcal{R}(q), \qquad q^n \xrightarrow{\Delta t/2} q^*, \tag{D.3a}$$

$$\text{Substep 2:} \qquad \frac{\mathrm{d}q}{\mathrm{d}t} + \mathcal{F}(q) = 0, \qquad q^* \xrightarrow{\Delta t} q^{**}, \tag{D.3b}$$

$$\text{Substep 3:} \qquad \frac{\mathrm{d}q}{\mathrm{d}t} = \mathcal{R}(q), \qquad q^{**} \xrightarrow{\Delta t/2} q^{n+1}. \tag{D.3c}$$

This method is called "Strang splitting" and is often the preferred splitting approach due to its second-order accuracy for general problems. The order of solving the individual subproblems is in principle arbitrary, but it is advantageous to solve the flow equations only once in the second step, since the computational cost for

evaluating the operator $\mathcal{F}$, representing the spatial discretization of the transport equations, is proportional to the number of grid points, whereas the time integration of the chemical source term solely depends on the time interval (which is the same if the integration is performed over two half time steps or one full time step). Note that multistep methods, i.e., methods that use values of previous time steps such as OpenFOAM's `backward` method, cannot be used for these kind of splitting methods, as different equations are solved in each substep. More details will be given later.

Another possibility to obtain higher-order splitting methods are iterative splitting methods, where the individual subproblems are solved sequentially and iteratively until a converged state is reached [71]. However, such an iterative procedure is not practical in the context of chemically reacting flows due to the high computational cost of each subproblem.

Operator Splitting Technique in OpenFOAM

In OpenFOAM, a different splitting technique is used to decouple the chemistry calculation from the solution of the transport equations. The first substep is equivalent to the classical first-order splitting method, solving the pure chemistry problem,

$$\text{Substep 1:} \qquad \frac{\mathrm{d}q}{\mathrm{d}t} = \mathcal{R}(q), \qquad q^n \xrightarrow{\Delta t} q^*. \tag{D.4}$$

In the second substep, the full transport equation is solved, where the chemical source term is approximated by its time-averaged value resulting from the solution of the first substep,

$$\text{Substep 2:} \qquad \frac{\mathrm{d}q}{\mathrm{d}t} + \mathcal{F}(q) = \frac{q^* - q^n}{\Delta t}, \qquad q^n \xrightarrow{\Delta t} q^{n+1}. \tag{D.5}$$

Note that the initial value for substep 2 is given here by the value at the beginning of the time step, in contrast to the classical splitting methods, which use the intermediate solution of the previous substep. As will be shown in the next section, the splitting technique used by OpenFOAM is first-order accurate and allows to use multistep methods for the discretization of the transport equation without compromising consistency. In the special case that the implicit Euler method is used to discretize substep 2, the method reproduces the classical first-order splitting method.

D.3.2 Detailed Analysis of the Splitting Methods

Model Equation and Numerical Discretization

To analyze the accuracy and consistency of the operator splitting methods using different time discretization methods, a simplified model equation is considered with

constant coefficients α and β,

$$\frac{\mathrm{d}q}{\mathrm{d}t} = \alpha q + \beta q. \tag{D.6}$$

The exact solution of this ODE after one time step is given by

$$q^{n+1} = q^n \exp((\alpha + \beta)\Delta t), \tag{D.7}$$

and the corresponding characteristic polynomial, expressed as a Taylor series, is given by

$$P = \frac{q^{n+1}}{q^n} = 1 + (\alpha + \beta)\Delta t + \frac{1}{2}(\alpha + \beta)^2\Delta t^2 + \frac{1}{6}(\alpha + \beta)^3\Delta t^3 + ... \tag{D.8}$$

An operator splitting method treats the two terms on the right-hand side of Eq. (D.6) separately, resulting in subproblems A and B, respectively. Subproblem A, which is given by $\mathrm{d}q/\mathrm{d}t = \alpha q$ and which represents the solution of the transport equation, is discretized by either the second-order trapezoidal rule,

$$\frac{q^{n+1} - q^n}{\Delta t} = \frac{1}{2}\left(\alpha q^n + \alpha q^{n+1}\right), \tag{D.9}$$

or a second-order implicit multistep method,

$$\frac{3q^{n+1} - 4q^n + q^{n-1}}{2\Delta t} = \alpha q^{n+1}. \tag{D.10}$$

Both schemes are available in OpenFOAM and are referred to as `CrankNicolson` and `backward`. For subproblem B, which is given by $\mathrm{d}q/\mathrm{d}t = \beta q$ and which represents the evaluation of the chemical reaction rates, the analytical solution is used, which can be seen as a "perfect" ODE integration. Accordingly, the error of the numerical solution results solely from the splitting method and the discretization of the first subproblem.

Unsplit Method

If the full equation is solved without the use of an operator splitting method, the discretization of Eq. (D.6) based on the trapezoidal rule results in the following characteristic polynomial,

$$P = \frac{2 + (\alpha + \beta)\Delta t}{2 - (\alpha + \beta\Delta t)} = 1 + (\alpha + \beta)\Delta t + \frac{1}{2}(\alpha + \beta)^2\Delta t^2 + \frac{1}{4}(\alpha + \beta)^3\Delta t^3 + ... \tag{D.11}$$

Using the multistep method, one obtains the following expression,

$$P = \frac{2 + \sqrt{1 + 2(\alpha + \beta)\Delta t}}{3 - 2(\alpha + \beta)\Delta t} = 1 + (\alpha + \beta)\Delta t + \frac{1}{2}(\alpha + \beta)^2\Delta t^2 + \frac{1}{2}(\alpha + \beta)^3\Delta t^3 + ..., \tag{D.12}$$

where the relations $q^{n+1} = P^2 q^{n-1}$ and $q^n = P q^{n-1}$ have been used. By comparing the characteristic polynomial of the numerical discretizations with the analytical solution given by Eq. (D.8), one finds that the $\mathcal{O}(\Delta t)$ and $\mathcal{O}(\Delta t^2)$ terms are reproduced correctly, making the discretizations second-order accurate.

Classical First-Order Splitting

Subproblem B (representing the chemistry evaluation) is solved first using an analytical integration over one full time step, which gives an intermediate value of

$$q^* = q^n \exp(\beta \Delta t). \tag{D.13}$$

Afterwards, subproblem A is solved using either the trapezoidal rule or the multistep method. Combining the two substeps, the trapezoidal rule leads to

$$\begin{aligned} P = \frac{2+\alpha\Delta t}{2-\alpha\Delta t}\exp(\beta\Delta t) = 1 + (\alpha+\beta)\Delta t + \frac{1}{2}(\alpha+\beta)^2\Delta t^2 \\ + \frac{1}{12}(3\alpha^3 + 6\alpha^2\beta + 6\alpha\beta^2 + 2\beta^3)\Delta t^3 + ... \end{aligned} \tag{D.14}$$

For the present model equation with scalar coefficients, the method exhibits a second-order accuracy, although it is first-order accurate for general problems due to the splitting error [118]. Using the multistep method, one obtains the following expression for the characteristic polynomial

$$\begin{aligned} P &= \frac{2\exp(\beta\Delta t) + \sqrt{4\exp(2\beta\Delta t) - (3 - 2\alpha\Delta t)}}{3 - 2\alpha\Delta t} \\ &= 1 + (\alpha + 2\beta)\Delta t + \frac{1}{2}(\alpha^2 - 2\beta^2)\Delta t^2 + ... \end{aligned} \tag{D.15}$$

In contrast to the trapezoidal rule, the multistep method does not lead to a consistent discretization, which has a formal order of zero. This shows that discretizations that use values from previous time steps cannot be used in combination with the classical splitting methods, as different equations are solved in each substep.

Strang Splitting

The Strang splitting method consists of three steps, where the analytical integration of subproblem B will be used in the second step. Utilizing the trapezoidal rule to discretize subproblem A one finally obtains

$$\begin{aligned} P &= \left(\frac{4+\alpha\Delta t}{4-\alpha\Delta t}\right)\exp(\beta\Delta t) \\ &= 1 + (\alpha+\beta)\Delta t + \frac{1}{2}(\alpha+\beta)^2\Delta t + \frac{1}{48}(9\alpha^3 + 24\alpha^2\beta + 24\alpha\beta^2 + 8\beta^3)\Delta t^3 + ... \end{aligned} \tag{D.16}$$

This discretization is second-order accurate, but since the third-order term is very similar to the exact solution given by Eq. (D.8) it is to be expected that the numerical error is small. Again, the multistep method does not lead to a consistent discretization and is therefore not reported here.

OpenFOAM Splitting

Similar to the classical first-order splitting, subproblem B is solved first using an analytical integration, which results in the expression given by Eq. (D.13). Afterwards, the full equation is solved using an approximation for subproblem B,

$$\frac{\mathrm{d}q}{\mathrm{d}t} = \alpha q + \frac{q^* - q^n}{\Delta t}. \tag{D.17}$$

If the trapezoidal rule is used to discretize the equation, one finally finds

$$P = \frac{2\exp(\beta\Delta t) + \alpha\Delta t}{2 - \alpha\Delta t} = 1 + (\alpha+\beta)\Delta t + \frac{1}{2}(\alpha^2 + \alpha\beta + \beta^2)\Delta t^2 + \frac{1}{12}(3\alpha^3 + 3\alpha^2\beta + 3\alpha\beta^2 + 2\beta^3)\Delta t^3 + ... \tag{D.18}$$

The discretization is first-order accurate even for the linear problem, although the error may be small as the second-order term is similar to the exact solution. Using the multistep method, the characteristic polynomial takes the following form,

$$P = \frac{(\exp(\beta\Delta t) + 1) + \sqrt{(\exp(\beta\Delta t) + 1)^2 - (3 - 2\alpha\Delta t)}}{3 - 2\alpha\Delta t} = 1 + (\alpha+\beta)\Delta t + \frac{1}{2}\alpha^2\Delta t^2 + \frac{1}{6}(3\alpha^3 + 6\alpha^2\beta + 9\alpha\beta^2 + 4\beta^3)\Delta t^3 + ... \tag{D.19}$$

In contrast to the classical splitting techniques, the multistep method leads here to a consistent discretization, which is first-order accurate.

D.3.3 Validation

Linear ODE

The theoretical findings will now be validated by numerical calculations utilizing the discretization and splitting methods discussed in the previous section. The coefficients of the model equation, Eq. (D.6), are set to $\alpha = -1$ and $\beta = -0.5$, and the solution is calculated until a time of $t = 1$ with an initial value of $q_0 = 1$.

The results are shown in Fig. D.4, showing the L_2 error plotted versus the time step. If the trapezoidal rule is used to discretize subproblem A (Fig. D.4(a)), both the classical and the Strang splitting methods lead to a second-order convergence of the error, whereas the OpenFOAM splitting technique shows a first-order accuracy,

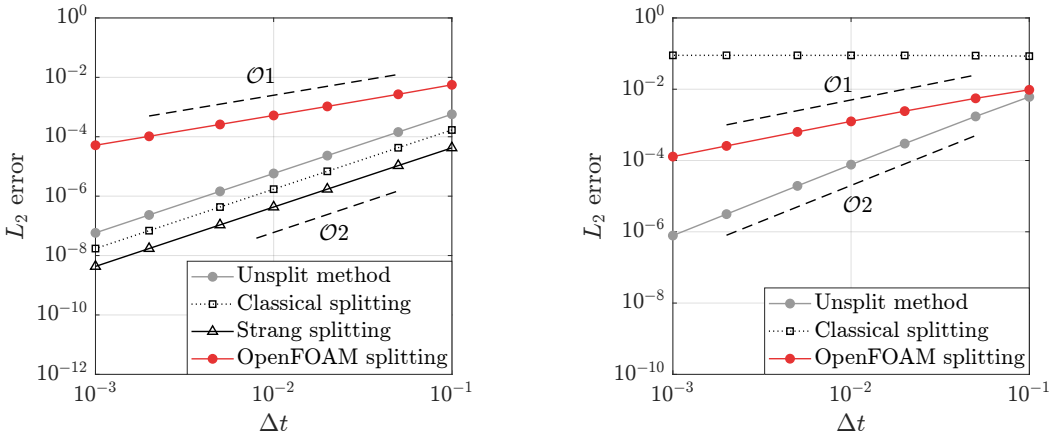

(a) Trapezoidal rule (`CrankNicolson`). **(b)** Multistep method (`backward`).

Figure D.4: L_2 error obtained from the numerical solution of the linear model equation, Eq. (D.6), using different time discretization methods and operator splitting techniques.

which is in agreement with the theoretical findings. It is noticeable that the classical splitting and the Strang splitting methods result in smaller errors than the unsplit method, which can be attributed to the fact that the corresponding error term is closer to the exact solution than that of the unsplit method. If the multistep method is used for time discretization (Fig. D.4(b)), the classical splitting method exhibits a constantly high error (zero-order accuracy), whereas the splitting technique of OpenFOAM still shows a first-order convergence of the error.

One-Dimensional Diffusion Flame

While the linear ODE has allowed for an analytical proof of the accuracy and consistency of the different splitting techniques, it does not exhibit a splitting error and is therefore not suitable for an universal validation. For this reason, a more complex text case based on a one-dimensional diffusion flame is now considered. The chemically reacting system is described in Mitarai *et al.* [133, 134] and is governed by the mixture fraction and a normalized temperature. Here, only molecular diffusion and chemical reactions are considered, with the diffusion coefficient set to $\mathcal{D} = 0.01$. The reaction parameters take the values that are reported in Mitarai *et al.* [133, 134] (case $r = 8$), with the pre-exponential factor set to $A = 7.5 \cdot 10^4$. The physical domain has a length of $L = 1$ with periodic boundaries. Mixture fraction is initialized using a smoothed top-hat profile (hyperbolic tangent profile) such that fuel and oxidizer are initially in separated regions, and the temperature is initially taken to be in chemical equilibrium. As time progresses, molecular diffusion induces mixing of the fuel and the oxidizer, resulting in spatial propagation of the flame. The mixture fraction and temperature equations are discretized by

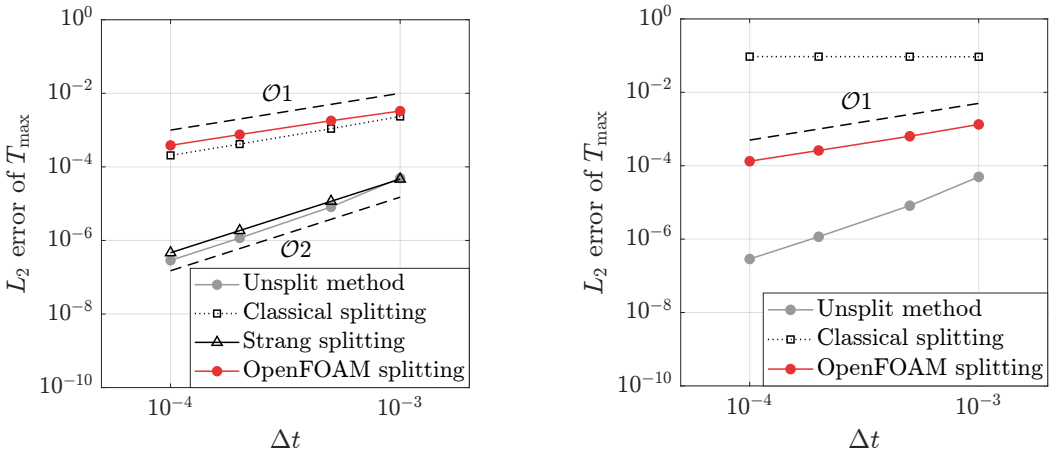

(a) Trapezoidal rule (`CrankNicolson`). **(b)** Multistep method (`backward`).

Figure D.5: L_2 error obtained from the numerical solution of the one-dimensional diffusion flame using different time discretization methods and operator splitting techniques.

a finite difference method using $N_x = 200$ grid points in combination with either the trapezoidal rule or the multistep method for time integration. The integration of the chemical source term is performed using a stiff ODE solver. The reference solution that is required to calculate the error is generated using a coupled solution with a sufficiently small time step.

Figure D.5 shows the L_2 error of the maximum temperature at time $t = 1$ as a function of the computational time step using different time discretization methods and splitting techniques. If the trapezoidal rule is used for time integration (Fig. D.5(a)), the Strang splitting is the only splitting method that exhibits a second-order convergence with an accuracy comparable to the unsplit method. The classical splitting method shows a first-order convergence, since the splitting error is not zero here. The OpenFOAM splitting technique also exhibits a first-order convergence of the error, with similar accuracy than the classical splitting method. If the multistep method is used (Fig. D.5(b)), again only the splitting technique used by OpenFOAM gives a consistent first-order discretization, whereas the classical splitting technique exhibits a constantly large error.

D.3.4 Further Remarks

Besides the issue with multistep methods, there are further situations in which an operator splitting technique must be used with caution. One example is the calculation of steady-state solutions (e.g., flamelet curves) by employing a time-marching method until a steady-state is reached. The steady state results from a balance between two dynamic processes (e.g., diffusion and chemistry), which are treated separately if an operator splitting method is used. This can cause

oscillations around the correct solution and, in the worst case, prevent convergence. Furthermore, the use of a splitting technique results in a dependence of the steady-state solution on the computational time step even in the converged state. Often, the size of the time step is chosen relatively large to enable faster convergence, making the splitting error, which is directly proportional to the time step width if a first-order splitting method is used, the dominant error and resulting in an inaccurate solution.

Another example is the use of an operator splitting method in combination with the PIMPLE loop for pressure-velocity coupling (cf. Fig. 4.4). Since chemistry is handled separately from the solution of the flow field, the reaction rates must be evaluated outside the PIMPLE loop to achieve a consistent discretization, and must not be updated within the iterative pressure-velocity coupling. An evaluation of the reaction rates outside the PIMPLE loop and thus once per time step is also preferable since it reduces the computational cost.

D.4 Comparison With a High-Order DNS Solver

D.4.1 Description of the DNS Solver

A high-order finite difference solver was developed to provide a reference solution when evaluating the quasi-DNS capabilities of OpenFOAM's standard solvers. The DNS solver employs a solution of the three-dimensional compressible Navier-Stokes equations in their conservative form using a density-based fully explicit solution procedure. Spatial derivatives are approximated by central finite differences of 8th-order accuracy for all derivatives, and time integration is performed using an explicit 4-stage low-storage Runge-Kutta method [100]. While the lack of dissipation of central differences is desirable for the accuracy of turbulent simulations, these schemes are not stable for an explicit time integration method without some form of damping, since the nonlinear terms in the Navier-Stokes equations generate higher harmonics that cause instabilities. To ensure a stable solution without affecting the resolved flow field, a compact 8th-order filter [59] is applied to the conserved variables at the end of each time step in order to remove the unresolved high-wavenumber structures.

The DNS solver is written in Fortran 90 and is parallelized using OpenMPI and the concept of domain decomposition, where each process is assigned to one subdomain. To reduce the excessive data communication that would result from the iterative solution required by the compact filter formulation, the boundary points of the subdomains are treated in an explicit way, which allows all subdomains to be solved simultaneously and independently once the data has been exchanged at the

beginning of the filter substep.

Two versions of the DNS solver exist, one for non-reacting flows and one for reacting flows. The non-reacting flow solver solves the compressible Navier-Stokes equations assuming a calorically perfect gas with constant heat capacities and transport properties. The reacting flow solver employs the solution of additional transport equations for the species mass fractions, as described in Sec. 3.1, and involves the calculation of the chemical reaction rates based on a fully coupled approach. A single-step reaction equation with five species is used, and all thermophysical properties are assumed to be constant assuming unity Lewis numbers.

D.4.2 Non-Reacting Flows

A three-dimensional Taylor-Green vortex is considered, which represents a canonical test case to study vortex dynamics, the decay of turbulence and the energy dissipation process [42, 225]. It is characterized by a simple setup with well-defined initial conditions while featuring several effects of real turbulent flows, making it to an excellent benchmark case for the evaluation of numerical discretization schemes. The computational domain is a cubic box with size $-\pi L \leq \{x, y, z\} \leq \pi L$, where all boundaries are periodic. The initial velocity field is given by

$$u(x, y, z) = U_0 \sin\left(\frac{x}{L}\right) \cos\left(\frac{y}{L}\right) \cos\left(\frac{z}{L}\right), \tag{D.20}$$

$$v(x, y, z) = -U_0 \cos\left(\frac{x}{L}\right) \sin\left(\frac{y}{L}\right) \cos\left(\frac{z}{L}\right), \tag{D.21}$$

$$w(x, y, z) = 0, \tag{D.22}$$

and the pressure is initialized according to

$$p(x, y, z) = p_0 + \frac{\rho_0 U_0^2}{16} \left[\cos\left(\frac{2x}{L}\right) + \cos\left(\frac{2y}{L}\right) \right] \left[\cos\left(\frac{2z}{L}\right) + 2 \right]. \tag{D.23}$$

The initial temperature field is assumed to be constant and the density is calculated using the equation of state. The gas constant is set to $\mathcal{R} = 300\,\mathrm{J/kgK}$ and the heat capacity is $c_p = 1000\,\mathrm{J/kgK}$. The reference temperature and pressure are given by $T_0 = 300\,\mathrm{K}$ and $p_0 = 10^5\,\mathrm{Pa}$, respectively, and the dynamic viscosity is $\mu = 1.8 \cdot 10^{-5}\,\mathrm{kg/ms}$ with a Prandtl number of $\mathrm{Pr} = 0.7$. The characteristic length is set to $L = 7.2 \cdot 10^{-4}\,\mathrm{m}$ and the characteristic velocity is $U_0 = 36\,\mathrm{m/s}$, leading to a characteristic flow time scale of $t_c = L/U_0 = 2 \cdot 10^{-5}\,\mathrm{s}$. The Reynolds number is $\mathrm{Re} = \rho_0 U_0 L/\mu = 1600$, which is a typical value for this benchmark, and the Mach number is $M_0 = 0.1$ so that the flow can be assumed to be incompressible. Simulations are performed up to a time of $t = 20\,tc$.

When dealing with the Taylor-Green vortex benchmark case, primary interest is on the kinetic energy dissipation rate. The volume-averaged kinetic energy within the domain is given by

$$\langle E_k \rangle = \frac{1}{\rho_0 V} \int_V \frac{\rho}{2} \|\mathbf{u}\|^2 \mathrm{d}V, \tag{D.24}$$

and the dissipation rate of kinetic energy is obtained by calculating the time derivative of the volume-averaged kinetic energy,

$$\varepsilon(E_k) = -\frac{\mathrm{d}\langle E_k \rangle}{\mathrm{d}t}. \tag{D.25}$$

For incompressible flows, it can be shown that the kinetic energy dissipation rate is related to the volume-averaged enstrophy $\langle \varsigma \rangle$,

$$\varepsilon(\varsigma) = \frac{2\mu}{\rho_0} \langle \varsigma \rangle, \qquad \langle \varsigma \rangle = \frac{1}{\rho_0 V} \int_V \frac{\rho}{2} \|\boldsymbol{\omega}\|^2 \mathrm{d}V, \tag{D.26}$$

with $\boldsymbol{\omega}$ denoting the vorticity. For compressible flows, there is an additional pressure dilatation-based dissipation rate, which, however, is negligible for flows at low Mach numbers [42]. Theoretically, Eqs. (D.25) and (D.26) should give identical results, but in practice they will differ due to the effect of the numerical dissipation. While the total dissipation rate given by Eq. (D.25) is a result of both the physical and the numerical dissipation, the enstrophy-based dissipation rate given by Eq. (D.26) only includes the physical dissipation based on the resolved velocity field. Accordingly, the comparison of both quantities provides an estimation of the dissipation introduced by the numerical method.

The OpenFOAM simulations are performed using the incompressible solver `pimpleFoam`, and the results are compared with the high-order DNS solver and with a reference solution that is generated by a de-aliased pseudo-spectral code on a 512^3 grid [225]. Different grid resolutions with 64^3, 128^3, 256^3 and 512^3 grid cells are considered, where for the OpenFOAM simulations either the `linear` or `cubic` interpolation scheme is used in combination with a `backward` time discretization.

Figure D.6 shows the time evolution of the flow field obtained from the high-order DNS solver on the finest mesh, which is visualized using iso-surfaces of the vorticity that are colored by the velocity magnitude. Starting with the initial field, the large and well-shaped vortices begin to evolve and roll up. With advancing time, the smooth vortical structures become smaller and change their structure. At $t/t_c \approx 9$, the coherent structures break down and the flow becomes more irregular, exhibiting a pseudo-turbulent behavior. Beyond this point, the dissipation causes the structures to slowly decay until the flow comes to rest.

The time evolution of the volume-averaged kinetic energy that is obtained from the OpenFOAM simulations and the high-order DNS solver is shown in Fig. D.7 for

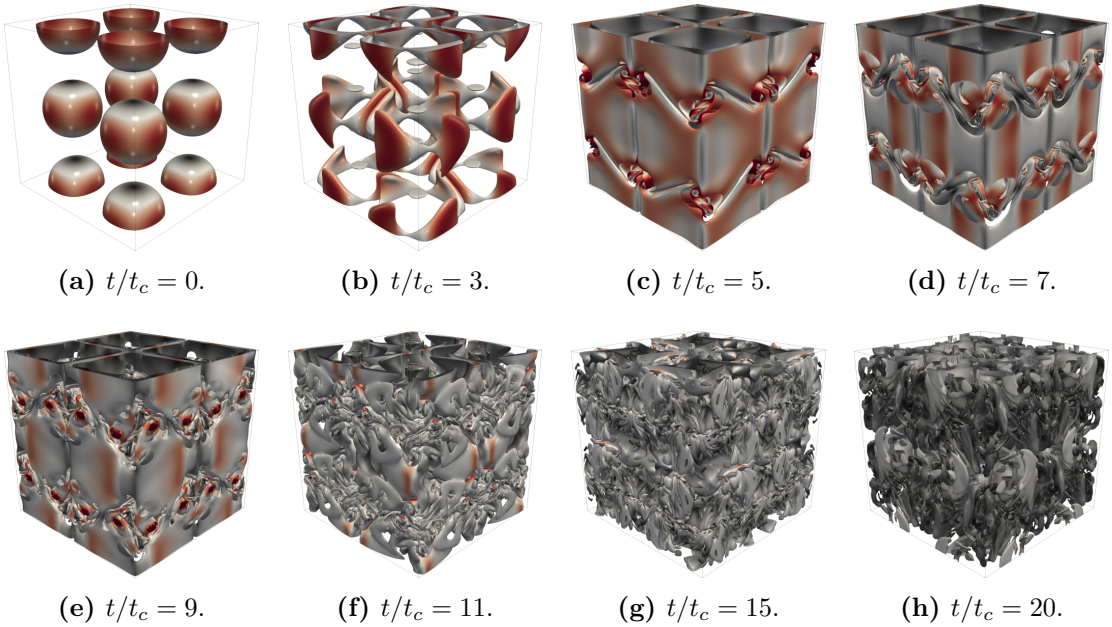

(a) $t/t_c = 0$. **(b)** $t/t_c = 3$. **(c)** $t/t_c = 5$. **(d)** $t/t_c = 7$.

(e) $t/t_c = 9$. **(f)** $t/t_c = 11$. **(g)** $t/t_c = 15$. **(h)** $t/t_c = 20$.

Figure D.6: Time evolution of the flow field of the three-dimensional Taylor-Green vortex, visualized by iso-surfaces of the z-component of vorticity colored by the velocity magnitude.

different grid resolutions and compared to the reference solution provided by the pseudo-spectral code. Overall there is quite good agreement, and only the `linear` scheme on the coarsest mesh shows larger deviations. A closer look at $5 \lesssim t/t_c \lesssim 10$ reveals that the coarser the mesh, the less kinetic energy is contained due to an increased numerical dissipation. The accurate prediction of the time history of the kinetic energy implies that the directly calculated dissipation rate, Eq. (D.25), is also adequately reproduced (not shown). In contrast, the enstrophy-based dissipation rate given by Eq. (D.26) and shown in Fig. D.8, which is associated with the resolved dissipation, shows qualitative differences between the different discretization schemes and grid resolutions. In general, it can be observed that for coarse grids the predicted dissipation rate is too low but converges to the reference solution as the grid is refined. This indicates that the turbulent structures are not fully resolved on coarse to moderate meshes, with numerical dissipation contributing substantially to the total dissipation. While the OpenFOAM simulations utilizing the `linear` interpolation scheme do not match the reference solution even at the highest grid resolution (Fig. D.8(a)), the `cubic` scheme leads to very good results already at a grid resolution of 256^3 and provides excellent agreement on the finest mesh (Fig. D.8(b)). A direct comparison reveals that the `linear` scheme requires about twice the grid resolution to achieve an accuracy comparable to the `cubic` scheme. The results obtained from the high-order DNS solver are shown in Fig. D.8(c) for comparison. It is remarkable that, despite the considerably higher discretization order, a similar accuracy to the `cubic` scheme is achieved, which is also reported

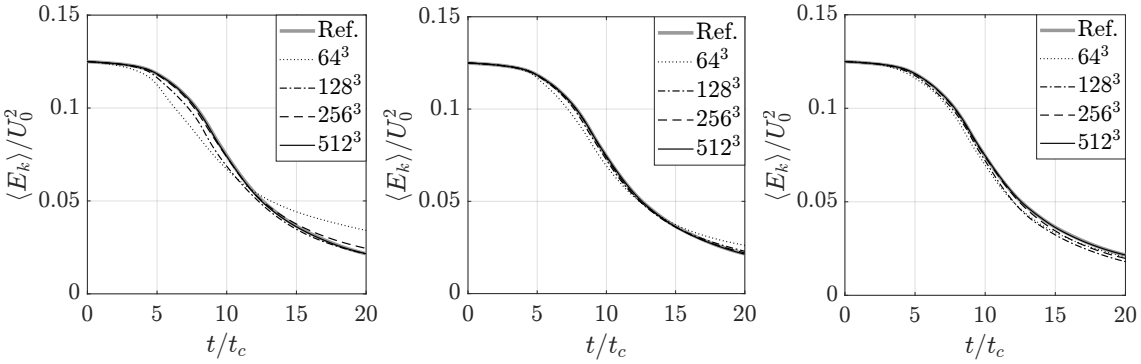

(a) OpenFOAM, `linear`. **(b)** OpenFOAM, `cubic`. **(c)** High-order DNS solver.

Figure D.7: Time evolution of the volume-averaged kinetic energy obtained from OpenFOAM and the high-order DNS solver using different grid resolutions. The reference solution is given by a pseudo-spectral code on a 512^3 grid [225].

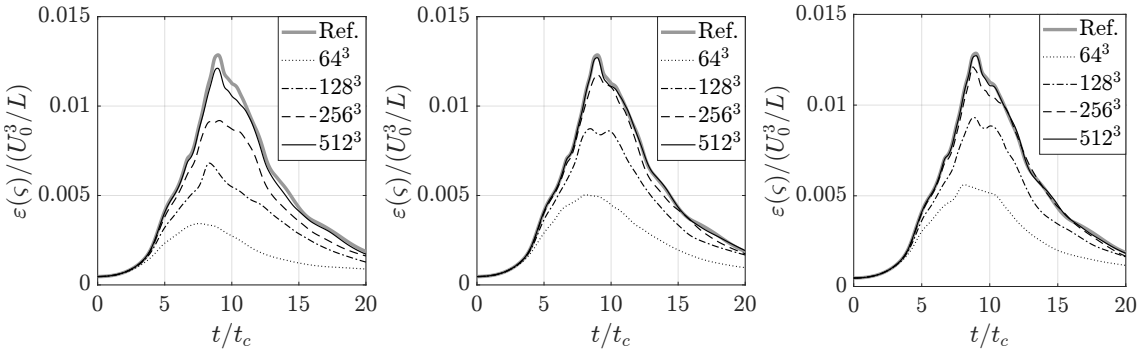

(a) OpenFOAM, `linear`. **(b)** OpenFOAM, `cubic`. **(c)** High-order DNS solver.

Figure D.8: Time evolution of the enstrophy-based dissipation rate obtained from OpenFOAM and the high-order DNS solver using different grid resolutions. The reference solution is given by a pseudo-spectral code on a 512^3 grid [225].

in Zirwes *et al.* [244] by comparison with a different high-order DNS solver. In the present DNS solver, the numerical dissipation can be directly related to the spatial filter, which selectively adds dissipation to damp the high-wavenumber structures. As the mesh is refined, more and more structures are resolved by the mesh and the effect of the filter decreases, reducing the numerical dissipation. In OpenFOAM, no spatial filter is required, as the implicit solution procedure introduces the desired amount of numerical dissipation required to stabilize the simulation.

Figure D.9 shows instantaneous contour lines of the normalized vorticity magnitude predicted by OpenFOAM and compared to the reference solution. There is a reasonable agreement for the 256^3 mesh, but the structures are jagged and not well defined. If the mesh is refined, the structures become smoother and more defined and converge to the reference solution. While the `linear` scheme still shows minor deviations on the 512^3 mesh, the `cubic` scheme leads to excellent agreement with the reference solution, which is consistent with the trends reported in Fig. D.8.

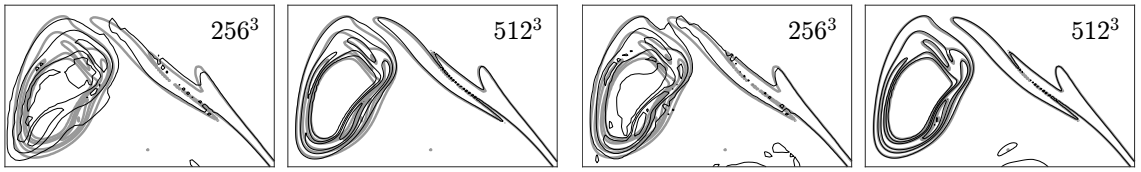

(a) OpenFOAM, `linear` scheme. **(b)** OpenFOAM, `cubic` scheme.

Figure D.9: Contour lines of the normalized vorticity magnitude $\|\boldsymbol{\omega}\|t_c = \{1, 5, 10, 20, 30\}$ on the y-z plane through $x/L = -\pi$ in the region $0 \leq y/L \leq \frac{\pi}{2}$ and $\frac{\pi}{2} \leq z/L \leq \frac{4\pi}{5}$ at time $t/t_c = 8$. Black lines denote the OpenFOAM results, and the thick gray line marks the reference solution given by the pseudo-spectral code on a 512^3 grid [225].

The ability of OpenFOAM to resolve the entire range of turbulent structures is evaluated by looking at the kinetic energy spectra, which are shown in Fig. D.10 for a grid resolution of 256^3. At time $t/t_c = 10$ (Fig. D.10(a)), the energy in the smallest scales is maximum, whereas at later times (Fig. D.10(b)) the energy decays for all wavenumbers [42]. Overall, there is very good agreement of the OpenFOAM results with the reference solution in the entire range of wavenumbers. Slight differences between the results can be observed at the highest wavenumbers, which are associated with the smallest structures of the flow. Here, the `linear` scheme provides excellent agreement with the reference solution up to the maximum wavenumber resolved by the numerical grid, whereas the `cubic` scheme slightly overestimates the kinetic energy of the highest wavenumbers due to its low dissipation. In contrast, the high-order DNS solver increasingly dampens the highest wavenumbers due to the effect of the spatial filter (here from about $\kappa\Delta x \gtrsim 2$, corresponding to $\kappa L \gtrsim 80$), which results in a slight deviation of the spectrum from the reference solution, but at the same time produces smoother fields and thus increases the stability.

Having demonstrated that OpenFOAM can accurately reproduce the entire range of wavenumbers in a turbulent flow, the question arises as to which cell size is required for an accurate simulation. To this end, the Kolmogorov length scale is calculated from the reference data and compared with the grid resolutions of the respective simulations. As shown in Fig. D.11, the Kolmogorov length decreases strongly at the beginning and reaches its minimum at $t/t_c \approx 9$, where the dissipation rate is highest (cf. Fig. D.8), and then increases again as the flow decays. If the `cubic` scheme is used, excellent agreement is achieved on the 512^3 mesh (cf. Fig. D.8(b)), corresponding to $\Delta x/\eta_{\min} \approx 1$. However, good predictions are also obtained at half the grid resolution, resulting in $\Delta x/\eta_{\min} \approx 2$. This confirms that the usual criterion of $\Delta x \lesssim 2\eta$ [55] is also valid for OpenFOAM despite the lower discretization order. However, if the `linear` scheme is used, the accuracy is reduced, and $\Delta x/\eta_{\min} \lesssim 1$ is required for an accurate simulation.

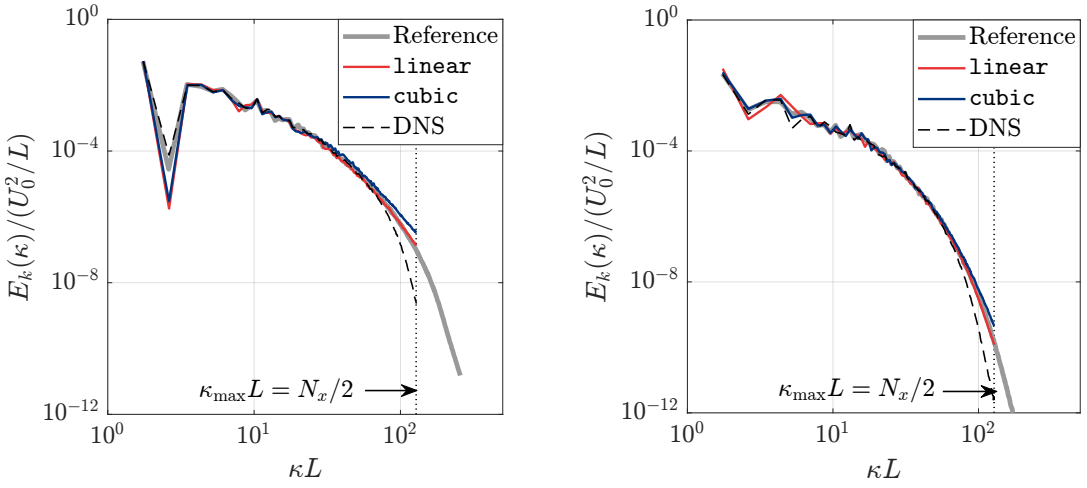

(a) $t/t_c = 10$. **(b)** $t/t_c = 20$.

Figure D.10: Kinetic energy spectrum $E_k(\kappa)$ as a function of the wavenumber κ normalized by the reference length L for a mesh resolution of 256^3 at times $t/t_c = 10$ and $t/t_c = 20$. The reference solution was generated with the DNS solver on the 512^3 mesh. The dotted line marks the maximum wavenumber resolved by the grid, which is given by $\kappa_{\max} = \pi/\Delta x$.

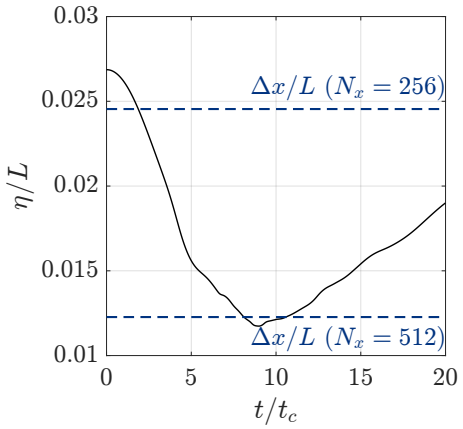

Figure D.11: Temporal evolution of the Kolmogorov length for the three-dimensional Taylor-Green vortex. The Kolmogorov length is calculated as $\eta = (\nu^3/\varepsilon)^{1/4}$, where the dissipation rate ε is given by the solution of the pseudo-spectral code on a 512^3 grid [225] (cf. Fig. D.8).

D.4.3 Reacting Flows

The DNS of chemically reacting flows involving realistic chemistry requires an accurate modeling of molecular transport coefficients in a multicomponent mixture as well as a computationally efficient time integration of the chemical reaction rates. The standard reacting solvers available in OpenFOAM often do not fulfill these requirements and rely on additional modeling assumptions such as the assumption of unity Schmidt or Lewis numbers, so that in general custom solvers that are coupled with external chemistry libraries are required. Such a reacting flow extension is given by the custom solver `EBIdnsFoam` [238], which couples OpenFOAM's functionality to solve partial differential equations with the open-source library Cantera [73] for

calculating detailed thermophysical and transport properties, in combination with an optimized computation of the chemical reaction rates. The accuracy and performance of the reacting flow extension `EBIdnsFoam` is investigated in detail in Zirwes *et al.* [244] based on the benchmark suite of Abdelsamie *et al.* [1], where the results are compared with four well-established high-fidelity low-Mach combustion solvers. For non-reacting conditions, excellent agreement is found between OpenFOAM and the other solvers, while some discrepancies remain in the reacting case, which are attributable to differences between low-Mach and compressible solvers and uncertainties in the calculation of thermophysical properties. For this reason, the present analysis further simplifies the validation benchmark of Abdelsamie *et al.* [1] in order to eliminate the additional uncertainties and provides an unbiased comparison of two compressible solvers, namely OpenFOAM's standard reacting solver `reactingFoam` and the reacting flow extension of the compressible high-order DNS solver introduced in Appendix D.4.1. Since both solvers rely on exactly the same mathematical equations, discrepancies between the results are directly attributable to the underlying numerical method.

A two-dimensional domain of size $-\pi L \leq \{x, y\} \leq \pi L$ with characteristic length $L = 1\,\mathrm{mm}$ and periodic boundaries is considered. The velocity field is initialized using a Taylor-Green vortex solution,

$$u(x,y) = U_0 \sin\left(\frac{x}{L}\right)\cos\left(\frac{y}{L}\right), \tag{D.27}$$

$$v(x,y) = -U_0 \cos\left(\frac{x}{L}\right)\sin\left(\frac{y}{L}\right), \tag{D.28}$$

with characteristic velocity $U_0 = 10\,\mathrm{m/s}$, resulting in a characteristic flow time scale of $t_c = L/U_0 = 10^{-4}\,\mathrm{s}$. The reacting scalars are initialized based on a mixture-fraction-like variable given by

$$f(x,y) = \frac{1}{2} + \frac{1}{2}\tanh\left(\frac{H/2 - |x|}{\delta}\right), \tag{D.29}$$

which separates the initial gas field into an oxidizer and a fuel region. The width and thickness of the fuel region are set to $H = 1.5\,L$ and $\delta = 0.15\,H$, respectively, and the initial mass fraction fields are calculated according to

$$Y_k(x,y) = Y_{k,\mathrm{Ox}} + (Y_{k,\mathrm{Fu}} - Y_{k,\mathrm{Ox}})f(x,y), \qquad k = 1, ..., N_s, \tag{D.30}$$

where N_s is the number of species. A single-step reaction equation with five species is used [228], where the fuel is n-heptane. The conditions of the oxidizer and the fuel stream are given by

$$\begin{aligned}
\mathrm{Ox}: &\quad Y_{\mathrm{C_7H_{16}}} = 0, &\quad Y_{\mathrm{O_2}} = 0.25, &\quad Y_{\mathrm{CO_2}} = 0, &\quad Y_{\mathrm{H_2O}} = 0, &\quad Y_{\mathrm{N_2}} = 0.75.\\
\mathrm{Fu}: &\quad Y_{\mathrm{C_7H_{16}}} = 0.2, &\quad Y_{\mathrm{O_2}} = 0, &\quad Y_{\mathrm{CO_2}} = 0, &\quad Y_{\mathrm{H_2O}} = 0, &\quad Y_{\mathrm{N_2}} = 0.8.
\end{aligned}$$

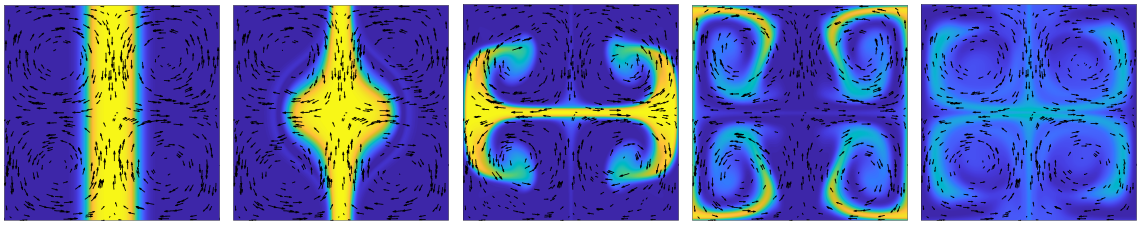

(a) Fuel mass fraction $Y_F \in [0, 0.2]$ at times $t/t_c = \{0, 1, 5, 10, 20\}$ (from left to right).

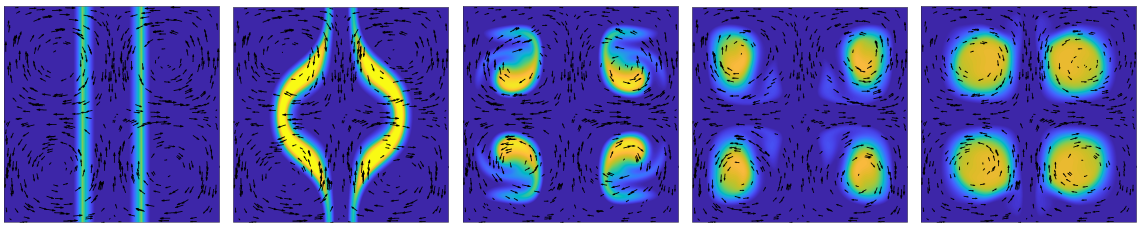

(b) Temperature $T \in [500\,\mathrm{K}, 2500\,\mathrm{K}]$ at times $t/t_c = \{0, 1, 5, 10, 20\}$ (from left to right).

Figure D.12: Visualization of the temporal evolution of the two-dimensional reacting Taylor-Green vortex. The plots show contours of the fuel mass fraction and the temperature at different times, and arrows indicate the flow field.

The temperature field is initialized by calculating the chemical equilibrium assuming constant enthalpy and constant pressure and using the initial mass fraction fields and a temperature and pressure of $T = 300\,\mathrm{K}$ and $p = 10^5\,\mathrm{Pa}$, respectively. Note that the initial mass fractions are not adjusted to chemical equilibrium to trigger the ignition of the gas mixture. The specific heat is set to $c_p = 1500\,\mathrm{J/kgK}$ for all species and the viscosity is $\mu = 1.8 \cdot 10^{-5}\,\mathrm{kg/ms}$, assuming a constant Prandtl number $\mathrm{Pr} = 0.7$ and equal diffusion coefficients with $\mathrm{Le} = 1$.

The OpenFOAM simulations are performed using the solver `reactingFoam`, which employs a pressure-based solution and utilizes the operator splitting technique for evaluating the chemical reaction rates as described in Appendix D.3.2. Note that the solver is modified here to satisfy $\mathrm{Pr} = 0.7$ (in its default version the solver assumes $\mathrm{Sc} = \mathrm{Pr} = 1$). Unless otherwise stated, the `cubic` interpolation scheme is used for spatial discretization while the corresponding TVD scheme `limitedCubic` is employed for reactive scalars, in combination with the `backward` scheme for time discretization. Simulations are performed using different grid resolutions up to a time of $t/t_c = 20$, where the time step is adjusted dynamically to ensure a maximum Courant number of $\mathrm{CFL}_{\mathrm{max}} = 0.3$. The reference solution is generated on a 512^2 mesh using the high-order finite difference solver as described in Appendix D.4.1, which employs a fully explicit and coupled solution of the flow and the chemistry.

The time evolution of the reacting Taylor-Green vortex is visualized in Fig. D.12, showing the instantaneous fuel mass fraction and temperature fields at different times. The initially rectangular fuel layer is distorted by the flow field and pushed

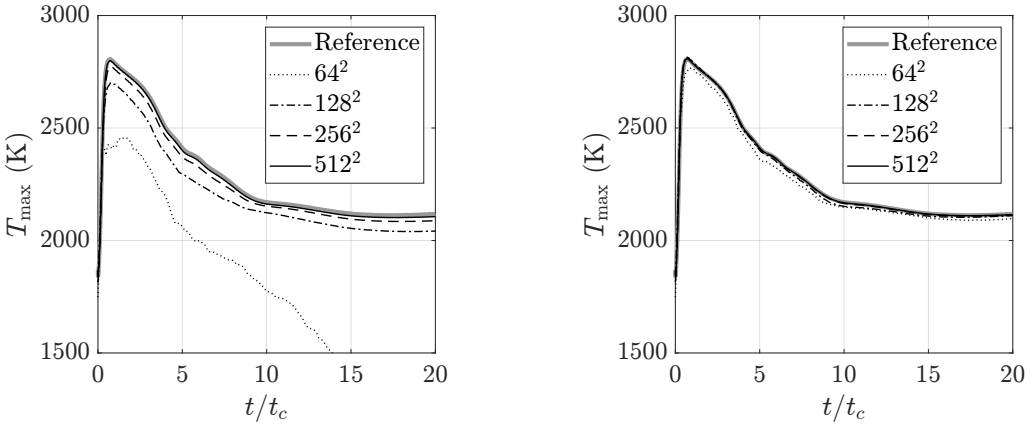

(a) With multivariate convection scheme. **(b)** No multivariate convection scheme.

Figure D.13: Time evolution of the maximum temperature in the domain for the reacting Taylor-Green vortex. The plots show results obtained using different grid resolutions with and without the multivariate convection scheme for the reactive scalars utilizing the `limitedCubic` scheme for the reactive scalars.

outward, where it eventually moves with the vortices. During the transport process, molecular diffusion causes the fuel to mix with the ambient air, resulting in ignition and combustion in the gas mixture.

By default, OpenFOAM uses a multivariate convection scheme for the discretization of the species mass fraction equations and the energy equation, which applies the same limiter to all reactive scalars using the strongest limiter. The time history of the maximum temperature obtained with the multivariate convection scheme is shown in Fig. D.13(a) for different grid resolutions. While the coarsest grid resolution shows significant deviations from the reference solution, a refinement of the grid resolution improves the agreement, but a very good match is not achieved even with the finest grid considered here. Note that these trends are also observed for non-reacting conditions (not shown). For this reason, simulations are repeated but without the multivariate convection scheme, where each transport equation is now discretized separately and independently. It should be noted that the multivariate convection scheme is implemented directly in the application solver and cannot be disabled by an entry in the input files, and disabling thus requires a modification of the solver. As shown in Fig. D.13(b), the calculation of separate limiters for each scalar leads to significant improvements of the results and to largely independence from the grid. Even the coarsest grid resolution now gives good agreement with the reference solution, and an excellent match is achieved on the 256^2 and 512^2 meshes.

Finally, the use of TVD schemes for the reactive scalars will be investigated. Figure D.14 shows contour plots of fuel mass fraction and temperature at time $t/t_c = 5$ obtained from different schemes used for the discretization of the scalar transport

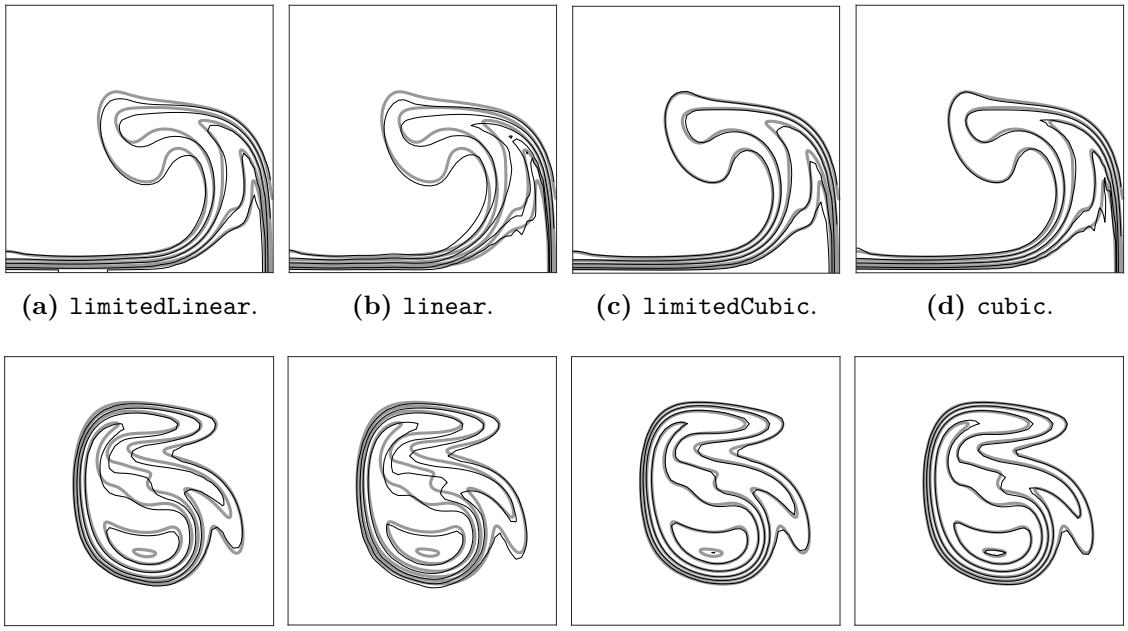

(a) `limitedLinear`. **(b)** `linear`. **(c)** `limitedCubic`. **(d)** `cubic`.

(e) `limitedLinear`. **(f)** `linear`. **(g)** `limitedCubic`. **(h)** `cubic`.

Figure D.14: Contour plots of fuel mass fraction (top) and temperature (bottom) in the region $0 \leq \{x, y\} \leq \pi L$ at time $t/t_c = 5$ obtained from OpenFOAM using different interpolation schemes for the reactive scalars (black lines) and compared to the reference solution (thick gray line). The contour levels for the fuel mass fraction are $Y_F = \{0.05, 0.1, 0.15, 0.18, 0.19\}$ and for the temperature $T = \{600, 800, 1100, 1600, 2200, 2400\}$. The grid resolution is $N_x \times N_y = 100 \times 100$, and no multivariate convection scheme is used.

equations. The grid resolution is set to $N_x \times N_y = 100 \times 100$, which gives sufficiently accurate results while still showing an effect of the numerical discretization. The best accuracy is obtained when the `cubic` interpolation scheme is used for all terms including the reacting scalars (Figs. D.14(d) and D.14(h)), but it also produces slight instabilities if the fields are not well resolved. Although the `cubic` interpolation scheme is not bounded, no unphysical values occur since the mass fractions are limited to their physical range after solving the transport equations (however, the artificial truncation may affect the calculation of the inert species). The use of the TVD scheme `limitedCubic` for the reactive scalars gives similar results, but does not produce spurious oscillations and is therefore preferable (Figs. D.14(c) and D.14(g)). The `linear` and `limitedLinear` schemes exhibit essentially the same trends but are less accurate and therefore show some larger deviations from the reference solution for the present grid resolution. As the mesh is refined, the agreement is improved, where already the 128^2 grid leads to an almost perfect agreement with the reference solution. For the 256^2 and 512^2 grid resolutions, there is no apparent difference in the contour plots regardless of the discretization scheme.

D.5 Conclusions

A detailed analysis of OpenFOAM's quasi-DNS capabilities for turbulent reactive flows using structured meshes with hexahedral cells was performed, focusing on low Mach number flows as often encountered in combustion applications. The analysis provides complementary investigations to the work of Zirwes *et al.* [244] and contained three steps. First, simple validation cases with analytical solutions were considered to examine the accuracy and order of OpenFOAM's discretization schemes. Afterwards, a detailed analysis of the operator splitting technique used to evaluate the reaction rates was presented. Finally, results of OpenFOAM's standard solvers were compared to a high-order DNS solver using more complex validation cases involving turbulence and combustion. The following conclusions were made:

- The `cubic` interpolation scheme offers the highest accuracy in OpenFOAM, which is often comparable to that achieved with a high-order DNS solver, and should therefore be used for DNS on structured meshes by default.
- For bounded scalars, such as mixture fraction or mass fractions, the TVD scheme `limitedCubic` is recommended, which employs a cubic interpolation but limits the value afterwards to satisfy the TVD property. It was found that the scheme does not contaminate the results and only slightly reduces the accuracy.
- The overall formal order of accuracy of OpenFOAM is two, although the `cubic` scheme employs an interpolation that is fourth-order accurate. In some cases, a convergence order higher than two can occur due to the pressure-velocity coupling.
- The central interpolation schemes (`linear`, `cubic`) provide an accurate solution down to the smallest scales without damping of the highest wavenumbers.
- For an accurate simulation, the `cubic` scheme requires a cell size of $\Delta x \lesssim 2\eta$, which reflects the usual criteria, whereas the `linear` scheme requires $\Delta x \lesssim \eta$.
- The DNS of chemically reacting flows usually requires a modification of the standard solvers to account for proper species transport. The use of the multivariate convection scheme for scalars is not recommended, as it introduces additional dissipation and leads to a stronger grid dependence.
- The operator splitting technique used in OpenFOAM to evaluate the reaction rates was shown to be first-order accurate and fully compatible with the `backward` time discretization. The calculation of the reaction rates should be done once before the PIMPLE loop is entered, and not within the iterative solution.
- Provided the initial conditions and thermophysical models are exactly known, OpenFOAM can lead to excellent agreement with high-fidelity solvers for both non-reacting and reacting conditions.

In summary, following these guidelines, OpenFOAM is well suited to be used as a

tool for the DNS of non-reacting and reacting flows at low Mach numbers and using hexahedral cells. For the cases investigated here, the lower discretization order of OpenFOAM was not a significant constraint, leaving the mesh resolution requirements equivalent to those of a high-order DNS solver. It should be noted that other situations than those considered here, such as simulations on unstructured meshes or simulations of flows involving discontinuities (e.g., multiphase flows or transonic flows), do not allow the use of the `cubic` interpolation scheme and thus require further extensions to perform DNS. Here, the recently developed WENO library for OpenFOAM [65, 126] could provide the required higher-order alternative to the `cubic` interpolation scheme. Finally, there are situations in which a high-order discretization is strictly required, such as the transport of vortices over large distances (e.g., computational aeroacoustics), where the mesh resolution requirement for a second-order method makes the simulation too expensive [225].

Appendix E

Supplementary Material to Chapter 5

E.1 Discretization of the Spherically Symmetric Gas-Phase Equations

For the case of quiescent environments, the gas-phase equations are solved in their one-dimensional spherically symmetric formulation. In order to be able to accurately represent numerical errors of real CFD in the analysis, the cell that contains the droplet is treated as a cube of length Δx, while the surrounding cells are assumed to be spherical, as illustrated in Fig. E.1. The importance of the correct treatment of the cell containing the droplet is demonstrated in Fig. E.2, which compares results obtained from a fully three-dimensional Cartesian solution (which would be the standard approach in CFD) with results that are obtained from one-dimensional solutions in a spherical coordinate system. Both, spheres with the same volume (dotted line) and spheres with the same surface area (dashed line) as the Cartesian cell, can lead to significant deviations of the fuel mass fraction in the cell containing the droplet (Fig. E.2(a)), and thus the evaporation time (including the associated error) is notably different (Fig. E.2(b)). In contrast, if the droplet cell is treated as a cube (solid line), the one-dimensional solution leads to results very similar to the Cartesian solution.

The discretized form of the gas-phase equations is obtained by performing a volume integration over the computational cell and applying Gauss's theorem to convert volume integrals into surface integrals. Using the equation for the fuel mass fraction given by Eq. (5.11) as an example, the discretized equation for the inner

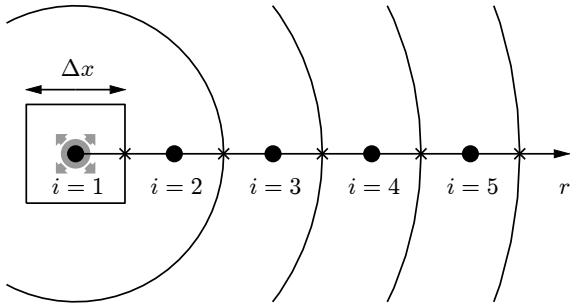

Figure E.1: Sketch of the numerical grid for the one-dimensional solution of the spherically symmetric problem (quiescent environments) with Cartesian treatment of the droplet cell. The gray dot denotes the evaporating droplet, which is placed in the origin, while cell centers are marked by black dots and cell faces by crosses.

grid cells in a spherically symmetric coordinate system is expressed as

$$\frac{\mathrm{d}(\rho Y_F)_i}{\mathrm{d}t} = -\frac{1}{V_{\mathrm{cell},i}}\left[\mathcal{F}_{i+\frac{1}{2}} S_{i+\frac{1}{2}} - \mathcal{F}_{i-\frac{1}{2}} S_{i-\frac{1}{2}}\right], \qquad i = 2, ..., N-1, \tag{E.1}$$

where $V_{\mathrm{cell},i}$ is the volume of the cell, $S_{i\pm\frac{1}{2}}$ denotes the surface area of the cell faces, and $\mathcal{F}_{i\pm\frac{1}{2}}$ is the face flux, which is given by

$$\mathcal{F}_{i\pm\frac{1}{2}} = \left[\rho u_r Y_F - \rho \mathcal{D}_F \frac{\mathrm{d}Y_F}{\mathrm{d}r}\right]_{i\pm\frac{1}{2}}, \tag{E.2}$$

with u_r being the radial velocity obtained from the continuity equation. Note that the equation for the inner grid cells does not contain a source term, since these cells do not contain any droplets. Quantities at the cell faces, denoted as $i \pm \frac{1}{2}$, are obtained by linear interpolation, and the gradient is approximated using central differences of second-order accuracy. For the cell that contains the droplet, the discretized equation becomes

$$\frac{\mathrm{d}(\rho Y_F)_i}{\mathrm{d}t} = -\frac{1}{V_{\mathrm{cell},i}} \mathcal{F}_{i+\frac{1}{2}} S_{i+\frac{1}{2}} + \dot{S}_M, \qquad i = 1. \tag{E.3}$$

Note that this formulation is also valid if the cell that contains the droplet is assumed to be a cube of length Δx, as shown in Fig. E.1, since the approximation of the surface integral using the midpoint rule reduces the summation of three-dimensional surface fluxes to a one-dimensional flux in radial direction. The volume and surface area of the cubic cell are given by $V_{\mathrm{cell}} = \Delta x^3$ and $S = 6\Delta x^2$, respectively. If the cell is treated as a sphere with radius $\Delta r/2$, the corresponding values are $V_{\mathrm{cell}} = \frac{\pi}{6}\Delta r^3$ and $S = \pi \Delta r^2$. The boundary condition at $r \to \infty$ is realized by applying an exponential grid stretching and using a fixed-value boundary condition.

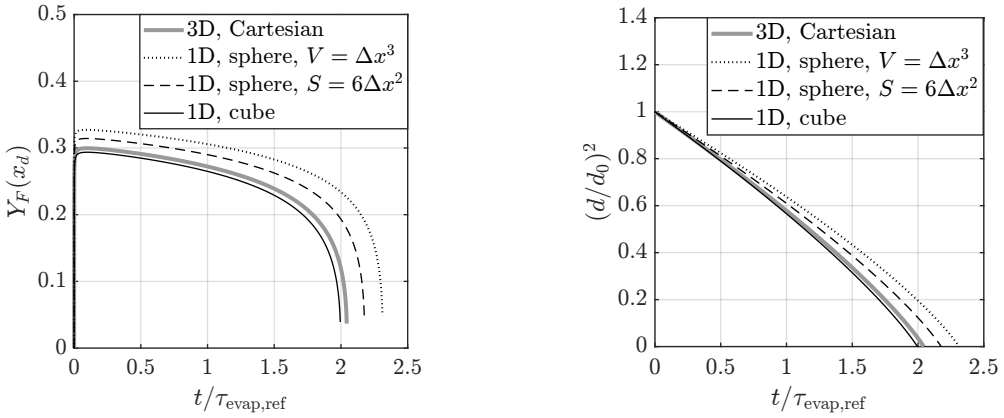

(a) Fuel mass fraction in the droplet cell.

(b) Squared droplet diameter.

Figure E.2: Comparison of the three-dimensional Cartesian solution with one-dimensional solutions in a spherical coordinate system using different treatments of the cell containing the droplet. The plots show the time evolution of (a) fuel mass fraction in the cell containing the droplet and (b) squared droplet diameter for a ratio of $\Delta x/d_0 = 1$.

E.2 Impact of the Evaporation Model on the Error Analysis

To study the dependence of the error analysis on the specific form of the evaporation model, calculations are repeated using representative evaporation models from a list presented in Miller *et al.* [132]. These models include non-equilibrium effects and a non-uniform droplet temperature, and the reader is referred to that reference for further details. Results are presented here for the case of transient droplet evaporation with heat and mass transfer, as this is the most relevant case for practical spray calculations and implicitly includes the relations obtained from steady-state solutions. Figure E.3 shows that the actual form of the evaporation model has only a very moderate influence on the error, and the general trends are still valid. The simplest model that does not involve any heat transfer correction due to evaporation (classical rapid mixing model, "M1") leads to an increased scatter compared to the other models. In contrast, the more advanced Langmuir-Knudsen models that include non-equilibrium effects ("M7" and "M8") and a non-uniform droplet temperature ("M8") yield very similar errors as the Abramzon and Sirignano model that has been used in the present error analysis (cf. Fig. 5.7(c)). Therefore, it can be concluded that the derived relationships are largely independent of the evaporation model and respect all the essential physical effects that are captured by the different forms of the models.

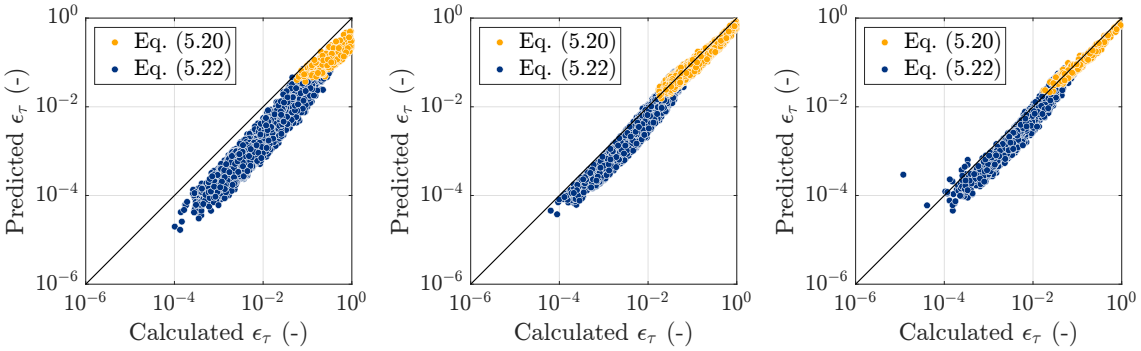

(a) Classical rapid mixing model (M1).

(b) Langmuir-Knudsen (M7).

(c) Langmuir-Knudsen with non-uniform droplet temperature (M8).

Figure E.3: Comparison of predicted and calculated errors for transient droplet evaporation with heat and mass transfer in quiescent environments using different evaporation models (fuel is *n*-heptane). The model implementations and names are taken from Miller *et al.* [132]. For more details on the legend see the caption of Fig. 5.7.

E.3 Modified Relations for Node-Wise Source Term Distribution

If a finite difference method is used where the flow variables are stored at grid points instead of grid cells, the source terms are distributed to the surrounding grid points using the same geometrical weighting factors as used for interpolation of the ambient conditions [168]. As a consequence, the error can be smaller, since the effective cell volume for the droplet is increased. This is illustrated in Fig. E.4, which shows the relative error of the steady-state evaporation rate as a function of the droplet position relative to the grid nodes. The maximum error is obtained if the droplet coincides with one of the grid points, resulting in source terms being distributed entirely to the corresponding node. In that special case, the derived relations can be used without modification. With increasing distance between the droplet and the grid nodes the error is reduced, as the source term is increasingly evenly distributed among the neighboring grid points. In the following the case is considered in which the droplet is located in the center between the grid points, and modified error relations are presented, which then allows to predict the minimum and maximum error.

The governing equations are solved in their three-dimensional form using a finite difference method of second-order accuracy, and trilinear interpolation is used to determine the geometrical weighting factors. All gas and droplet properties are varied within a wide range of typical values, where the same ranges are used as described in the main text. Assuming steady-state conditions, one finds that the error of the evaporation rate is still governed by the known error relation, but with

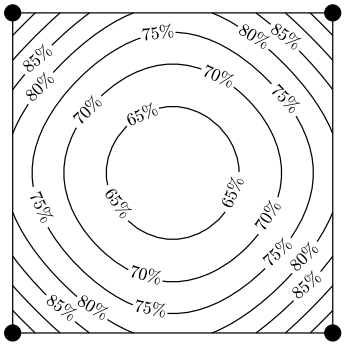

Figure E.4: Relative error of the steady-state evaporation rate as a function of the droplet position relative to the surrounding grid nodes (black dots). The error is obtained from a finite-difference solution of the three-dimensional equations with $\Delta x/d = 2$ and is normalized by the maximum error that occurs for droplets coinciding with the grid nodes.

the actual cell size being replaced by an effective cell size,

$$\epsilon_{\dot{m}} = \min\left[\left(1+\frac{2}{3}\frac{\Delta x_{\text{eff}}}{d}\right)^{-1}, \left(1+\frac{1}{\pi}\frac{\text{Pe}_{\Delta x_{\text{eff}}}}{\text{Sh}^*}\frac{\Delta x_{\text{eff}}}{d}\right)^{-1}\right], \tag{E.4}$$

with $\Delta x_{\text{eff}} = \sqrt{8}\Delta x \approx 2.8\Delta x$. This prefactor results from the fact that the geometrical weighting factor of the source term (which is 1/8 if the source term is distributed to the eight surrounding grid points) can equivalently also be included in the surface integrals. For the case of transient droplet evaporation, the modified version of the error relation is given by

$$\epsilon_\tau = \min\left[\left(\frac{\Delta x_{\text{eff}}}{d_0}\right)^{-1}, 0.6\varphi^*(2\Delta x), \frac{2\pi}{3}\left(\frac{\text{Pe}_{\Delta x_{\text{eff}}}}{\text{Sh}^*}\right)^{-1}\left(\frac{\Delta x_{\text{eff}}}{d_0}\right)^{-1}\right]. \tag{E.5}$$

The effective cell size is the same as in Eq. (E.4), with the exception of the relation for the closed system, which must be evaluated using twice the cell size, which is denoted by $\varphi^*(2\Delta x)$. This is because the underlying equations do not contain any surface integrals and only the volume is relevant in that case.

E.4 Details on the Derivations of the Error Relations

E.4.1 Relation for Convective Environments (Steady-State)

The derivation of the error relation given by Eq. (5.16) is based on the assumption that convective fluxes dominate over diffusive fluxes, which implies a large cell Péclet number. Furthermore, pure mass transfer with constant density and constant

properties is considered to allow for an analytical solution. A fuel mass balance for the cell that contains the droplet is formulated, assuming a one-dimensional flow aligned with the x-axis. Fresh gas with the conditions of the free stream enters the cell, and inside the cell fuel mass is released due to the evaporation of the liquid droplet, resulting in the outflow containing a higher fuel mass fraction equal to the conditions inside the cell. Accordingly, the fuel mass balance is expressed as

$$\underbrace{\rho u_\infty \Delta x^2 Y_{F,\infty}}_{\text{Inflow}} + \underbrace{\dot{m}}_{\text{Evaporation}} = \underbrace{\rho u_\infty \Delta x^2 Y_F}_{\text{Outflow}}. \tag{E.6}$$

Note that the velocity of the outflow is equal to the velocity of the inflow, neglecting the effect of the droplet on the momentum balance. The evaporation rate is given by Eq. (3.55) and evaluated using the cell value Y_F,

$$\dot{m} = \pi d \rho \mathcal{D}_F \mathrm{Sh}^* \ln(1 + B_M), \qquad B_M = \frac{Y_{F,s} - Y_F}{1 - Y_{F,s}}. \tag{E.7}$$

By inserting the expression for the evaporation rate into the fuel mass balance one obtains

$$\ln(1 + B_M) = \frac{1}{\pi} \frac{1}{\mathrm{Sh}^*} \underbrace{\frac{u_\infty \Delta x}{\mathcal{D}_F}}_{=\mathrm{Pe}_{\Delta x}} \frac{\Delta x}{d} (Y_F - Y_{F,\infty}). \tag{E.8}$$

An analytical solution for the unknown cell value Y_F is possible by assuming a small mass transfer number, which implies $Y_{F,s} \ll 1$ and leads to $\ln(1 + B_M) \approx B_M \approx Y_{F,s} - Y_F$. Using the approximation and assuming a constant modified Sherwood number, a closed-form expression for the local cell value Y_F that determines the error of the evaporation rate is obtained,

$$Y_F = \frac{Y_{F,s} + C Y_{F,\infty}}{1 + C}, \qquad C = \frac{1}{\pi} \frac{\mathrm{Pe}_{\Delta x}}{\mathrm{Sh}^*} \frac{\Delta x}{d}. \tag{E.9}$$

This solution is now inserted into the equation for the evaporation rate (using the approximation for the mass transfer number from above), leading to

$$\dot{m} = \pi d \rho \mathcal{D}_F \mathrm{Sh}^* (Y_{F,s} - Y_F) = \underbrace{\pi d \rho \mathcal{D}_F \mathrm{Sh}^* (Y_{F,s} - Y_{F,\infty})}_{=\dot{m}_{\mathrm{ref}}} \frac{C}{1 + C}, \tag{E.10}$$

where the reference evaporation rate is determined by the conditions of the fresh gas. Finally, the relative error of the evaporation rate, as defined by Eq. (5.2), can be calculated, where $\dot{m} < \dot{m}_{\mathrm{ref}}$ and therefore

$$\epsilon_{\dot{m}} = 1 - \frac{\dot{m}}{\dot{m}_{\mathrm{ref}}} = 1 - \frac{C}{1 + C} = \frac{1}{1 + C}. \tag{E.11}$$

By inserting the expression for the constant C, the error relation presented in Sec. 5.2.3 is obtained,

$$\epsilon_{\dot{m}} = \left(1 + \frac{1}{\pi} \frac{\mathrm{Pe}_{\Delta x}}{\mathrm{Sh}^*} \frac{\Delta x}{d} \right)^{-1}. \tag{E.12}$$

E.4.2 Relation for Quasi-Steady Processes (Transient Case)

Assuming quasi-steady conditions, knowledge of the error allows the instantaneous evaporation rate to be calculated from the reference evaporation rate,

$$\epsilon_{\dot{m}} = 1 - \frac{\dot{m}}{\dot{m}_{\mathrm{ref}}} \qquad \Rightarrow \qquad \dot{m} = (1 - \epsilon_{\dot{m}})\dot{m}_{\mathrm{ref}}, \tag{E.13}$$

where it was assumed that $\dot{m} < \dot{m}_{\mathrm{ref}}$. Inserting the error relation for the steady-state evaporation rate, which is given by Eq. (5.12), results in

$$\dot{m} = f_1 \dot{m}_{\mathrm{ref}}, \qquad f_1 = \frac{\alpha(\Delta x/d)}{1 + \alpha(\Delta x/d)}. \tag{E.14}$$

The factor $f_1 < 1$ can be seen as a correction to the evaporation in an infinite environment and reduces the evaporation rate, thus leading to an increase in the evaporation time. The time evolution of the droplet mass is then given by

$$\frac{\mathrm{d}m_d}{\mathrm{d}t} = -f_1 \dot{m}_{\mathrm{ref}}, \tag{E.15}$$

and can be transformed into an equation for the squared droplet diameter,

$$\frac{\mathrm{d}d^2}{\mathrm{d}t} = -\frac{4 f_1 \dot{m}_{\mathrm{ref}}}{\pi \rho_l d}. \tag{E.16}$$

By inserting the reference evaporation rate given by $\dot{m}_{\mathrm{ref}} = 2\pi d \rho \mathcal{D}_F \ln(1 + B_{M,\mathrm{ref}})$, one finally obtains

$$\frac{\mathrm{d}d^2}{\mathrm{d}t} = -f_1 K_{\mathrm{ref}}, \qquad K_{\mathrm{ref}} = \frac{8\rho\mathcal{D}_F}{\rho_l} \ln(1 + B_{M,\mathrm{ref}}). \tag{E.17}$$

Assuming constant thermodynamic properties, the evaporation constant K_{ref} is a constant, whereas the correction factor f_1 depends on the instantaneous droplet diameter, which makes an analytical solution complicated. Therefore, the correction factor is approximated by a suitable average value determined from the mean droplet diameter based on the d^2-law. Note that the d^2-law is not strictly fulfilled if the evaporation rate is evaluated using the local cell value, but can still provide a suitable approximation for the correction factor. Assuming d^2-law behavior, the droplet diameter evolves according to [211]

$$d(t) = d_0 \sqrt{1 - t/\tau_{\mathrm{evap}}}, \tag{E.18}$$

and its time averaged value is given by $\langle d \rangle = \frac{2}{3} d_0$. The approximation of the correction factor is then given by an evaluation using the time averaged droplet diameter,

$$f_1 \approx \frac{\alpha(\Delta x/\langle d \rangle)}{1 + \alpha(\Delta x/\langle d \rangle)} = \frac{\frac{3}{2}\alpha(\Delta x/d_0)}{1 + \frac{3}{2}\alpha(\Delta x/d_0)} = \mathrm{const.} \tag{E.19}$$

Using the average of d to approximate f_1 instead of averaging f_1 directly utilizing Eq. (E.18) results in a much simpler expression with a maximum deviation of about 3.7 % for $\Delta x/d_0 \geq 1$. With the right-hand side being a constant now, Eq. (E.17) can be solved analytically, resulting in the following expression for the evaporation time,

$$\tau_{\text{evap}} = \frac{d_0^2}{f_1 K_{\text{ref}}}. \tag{E.20}$$

With the reference evaporation time given by $\tau_{\text{evap,ref}} = d_0^2/K_{\text{ref}}$, the relative error of the evaporation time is found to be

$$\epsilon_\tau = \frac{\tau_{\text{evap}}}{\tau_{\text{evap,ref}}} - 1 = \frac{1}{f_1} - 1 = \frac{2}{3\alpha}\left(\frac{\Delta x}{d_0}\right)^{-1}. \tag{E.21}$$

E.4.3 Relation for a Closed System (Transient Case)

Pure Mass Transfer

A single droplet in a finite environment with volume V is considered. There is no net flux across the boundaries, representing a closed system, and inside the volume a homogeneous distribution is assumed. Following the procedure in Sec. 5.2, only mass transfer is considered in a first step, and later the analysis is extended to the case of combined heat and mass transfer. Note that for a closed system the density must be variable to satisfy mass conservation. According to these assumptions, the governing equations reduce to a set of coupled ordinary differential equations,

$$\frac{\mathrm{d}\rho}{\mathrm{d}t} = \dot{S}_M, \tag{E.22}$$

$$\frac{\mathrm{d}Y_F}{\mathrm{d}t} = (1 - Y_F)\dot{S}_M/\rho, \tag{E.23}$$

$$\frac{\mathrm{d}m_d}{\mathrm{d}t} = -\dot{m}, \tag{E.24}$$

with the source term providing the coupling between the gas phase and the liquid droplet via $\dot{S}_M = -\frac{1}{V}\frac{\mathrm{d}m_d}{\mathrm{d}t}$. Note that the equation for the fuel mass fraction has been reformulated using the continuity equation. The evaporation rate is given by $\dot{m} = 2\pi d\rho\mathcal{D}_F \ln(1 + B_M)$, where the mass transfer number is evaluated using the instantaneous fuel mass fraction of the finite environment. Although the gas density is allowed to change, a constant $\rho\mathcal{D}_F$ is assumed in the expression for the evaporation rate to simplify the problem. As the system is closed, total mass is conserved, so that knowledge of either liquid or gaseous mass can be used to directly infer the other. It is therefore only necessary to solve for one variable. In analogy to the d^2-law, the squared droplet diameter is chosen as solution variable, with the time

evolution given by

$$\frac{\mathrm{d}d^2}{\mathrm{d}t} = -\frac{8\rho\mathcal{D}_F}{\rho_l}\ln(1+B_M). \tag{E.25}$$

As mentioned before, the density that appears on the right-hand side of Eq. (E.25) is assumed to be constant, so that only the mass transfer number is a function of time. Using the initial droplet diameter and the evaporation time in an infinite environment equal to the initial state as reference length and time, respectively, the equation can be normalized, yielding

$$\frac{\mathrm{d}\hat{d}^2}{\mathrm{d}\hat{t}} = -\frac{\ln(1+B_M)}{\ln(1+B_{M,0})}, \tag{E.26}$$

with $\hat{d} = d/d_0$ and $\hat{t} = t/\tau_{\mathrm{evap,ref}}$. By formulating balance equations for the total mass and the fuel mass in the system according to

$$\rho_0 V + m_{d,0} = \rho V + m_d, \qquad \rho_0 Y_{F,0} V + m_{d,0} = \rho Y_F V + m_d, \tag{E.27}$$

the fuel mass fraction can be expressed as

$$Y_F = \frac{Y_{F,0} + \varphi(1-\hat{d}^3)}{1+\varphi(1-\hat{d}^3)}, \tag{E.28}$$

where $\varphi = m_{d,0}/(\rho_0 V)$ denotes the initial ratio of droplet mass to gaseous mass in the system. Using this expression it is possible to express the instantaneous mass transfer number as a function of the normalized droplet diameter,

$$1 + B_M = \frac{1+B_{M,0}}{1+\varphi(1-\hat{d}^3)}. \tag{E.29}$$

By inserting this relation into Eq. (E.26) one obtains

$$\frac{\mathrm{d}\hat{d}^2}{\mathrm{d}\hat{t}} = -1 + \frac{\ln(1+\varphi(1-\hat{d}^3))}{\ln(1+B_{M,0})}. \tag{E.30}$$

The first term on the right-hand side reflects the d^2-law for an infinite environment, while the second term acts as a correction factor to account for the effect of the finite environment. It increases with increasing mass ratio φ and decreasing mass transfer number $B_{M,0}$, and counteracts the evaporation process (positive sign). By separating the variables in Eq. (E.30) and performing an integration, an expression for the normalized evaporation time is found,

$$\hat{\tau}_{\mathrm{evap}} = \int_0^1 \left(1 - \frac{\ln(1+\varphi(1-s^{3/2}))}{\ln(1+B_{M,0})}\right)^{-1} \mathrm{d}s. \tag{E.31}$$

The integration variable indicates the third power of the non-dimensional droplet diameter, $s = \hat{d}^3$, and the integration is performed from the initial state ($s = 1$)

to complete evaporation ($s = 0$). Note that the integration limits are flipped to give the integrand a positive sign. The integral contains a singularity for $\varphi = B_{M,0}$ where the evaporation time approaches infinity. This corresponds to the case when the environment reaches saturation conditions and thus complete evaporation is no longer possible. Using the definition of the error given by Eq. (5.1), which can be expressed as $\epsilon_\tau = \hat{\tau}_{\text{evap}} - 1$, one finally obtains the expression for the relative error of the evaporation time,

$$\epsilon_\tau = \int_0^1 \left(\frac{\ln(1 + B_{M,0})}{\ln(1 + \varphi(1 - s^{3/2}))} - 1 \right)^{-1} \mathrm{d}s. \tag{E.32}$$

The integral has no analytical solution and must be solved numerically. However, an approximate solution can be found by introducing a Taylor series expansion of the integrand assuming small φ,

$$\left(\frac{\ln(1 + B_{M,0})}{\ln(1 + \varphi(1 - s^{3/2}))} - 1 \right)^{-1} \approx \frac{\varphi(1 - s^{3/2})}{\ln(1 + B_{M,0})}. \tag{E.33}$$

Using the approximation allows for an analytical solution of the integral,

$$\epsilon_\tau \approx \int_0^1 \frac{\varphi(1 - s^{3/2})}{\ln(1 + B_{M,0})} \mathrm{d}s = \frac{0.6\varphi}{\ln(1 + B_{M,0})} = 0.6\varphi^*. \tag{E.34}$$

This shows that the error depends linearly on the modified mass ratio parameter φ^*, and is valid for $\varphi^* \lesssim 0.1$, as shown in Fig. E.5. For larger φ^* the error deviates from the linear relation, and has a different dependence on the initial mass transfer number.

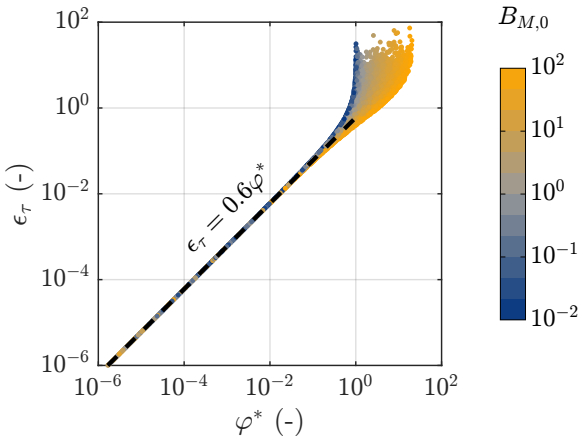

Figure E.5: Relative error of the evaporation time for a single droplet in a finite environment (closed system, pure mass transfer). The error is plotted versus the modified mass ratio φ^* and colored by the initial mass transfer number $B_{M,0} \in [0.01, 100]$ (logarithmic scale).

Heat and Mass Transfer

To include the effect of heat transfer, the full evaporation model is used, as described in Sec. 3.2. The gas-phase equations are given by Eqs. (3.1), (3.2) and (3.4) with only time derivatives and source terms remaining due to the assumption of a homogeneous system with no net flux across the boundaries. The time derivative of the pressure, which appears in the balance equation for the absolute enthalpy, Eq. (3.4), is also neglected, which is consistent with the assumption of low Mach numbers. The equations are solved numerically for a set of different initial gas and droplet properties and different gas volumes, and the resulting evaporation times are compared to the reference evaporation time in an infinite environment constituted by the initial gas state. Figure E.6 shows that the error mainly depends linearly on the modified mass ratio φ^*, as was demonstrated for the case with pure mass transfer. However, the effect of heat transfer introduces an additional scatter. From the results shown in Fig. E.6 it can be seen that the relation found on the basis of pure mass transfer, $\epsilon_\tau = 0.6\varphi^*$, serves here as a lower limit for the error, while the upper limit is given by $\epsilon_\tau \approx 2\varphi^*$. Furthermore, the mass transfer number now takes a much smaller range of values. Nevertheless, its inclusion in the error relation (i.e., the use of φ^* instead of φ) leads to a more accurate estimate of the error.

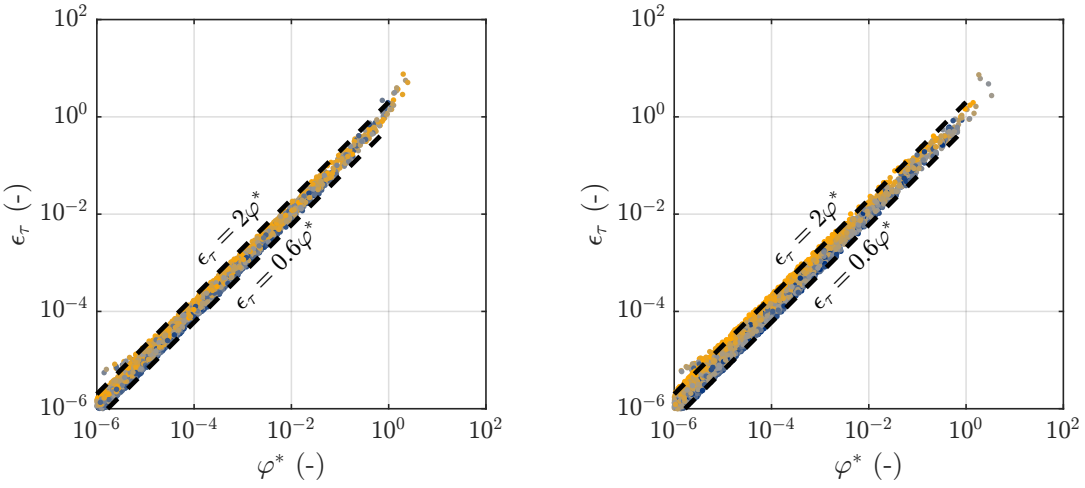

(a) Ethanol droplet, $B_{M,\mathrm{ref}} \in [0, 3]$. **(b)** n-Heptane droplet, $B_{M,\mathrm{ref}} \in [1, 5]$.

Figure E.6: Relative error of the evaporation time for a single droplet in a finite environment (closed system, heat and mass transfer). The error obtained from fuel species ethanol and n-heptane is plotted versus the modified mass ratio φ^* and colored by the reference mass transfer number.

E.4.4 Relation for Convective Environments (Transient Case)

The derivation of the error relation given by Eq. (5.24) from the corresponding relation for the steady-state evaporation rate, Eq. (5.16), follows the same procedure as presented in Appendix E.4.2. By setting

$$\alpha = \frac{1}{\pi} \frac{\mathrm{Pe}_{\Delta x}}{\mathrm{Sh}^*}, \tag{E.35}$$

the error relations given by Eqs. (5.12) and (5.16) have exactly the same form. Following the derivations from Appendix E.4.2, the relation for the relative error of the evaporation time is given by

$$\epsilon_\tau = \frac{2}{3\alpha} \left(\frac{\Delta x}{d_0} \right)^{-1}. \tag{E.36}$$

Inserting the expression for α given by Eq. (E.35) directly leads to Eq. (5.24).

E.5 Application of the Error Relations to CFD Simulations

E.5.1 Computational Setup

Having derived the error relations based on a single droplet in an infinite environment, their usage and effectiveness in practical CFD of turbulent reacting flows will now be demonstrated by comparing *a priori* estimates with *a posteriori* errors from Euler-Lagrange simulations. To this end, simulations of evaporating droplets in statistically homogeneous turbulence are performed at different grid resolutions, considering both non-reactive and reactive conditions. The computational setup is similar to the setup used to examine the two-phase coupling between the stochastic particles and the fuel droplets (cf. Sec. 6.1), and is only briefly summarized here. The computational domain is a cubic box with length $L = 15\,\mathrm{mm}$ and periodic boundary conditions. The initial gas is pure nitrogen in the non-reactive case and a mixture of nitrogen and oxygen with mass fractions similar to those of air in the reactive case, with an initial temperature and pressure of $T_0 = 1500\,\mathrm{K}$ and $p_0 = 1\,\mathrm{atm}$, respectively. The velocity field is initialized with statistically homogeneous turbulence with a Taylor Reynolds number of $\mathrm{Re}_\lambda = 16$, which ensures sufficient resolution of the turbulence even at the lower grid resolutions (see Tab. E.1). The fuel droplets are composed of pure ethanol with initial properties $d_0 = 20\,\mu\mathrm{m}$ and $T_{d,0} = 300\,\mathrm{K}$, and are distributed randomly within the domain. Different droplet loadings are

Table E.1: Grid resolution characteristics of the simulations for demonstrating the use of the error relations in practical CFD. The table relates the cell size to the Kolmogorov length scale η, the initial droplet diameter d_0, and the nominal droplet distance Δ_L.

N_x	$\Delta x/\eta$	$\Delta x/d_0$	$\Delta_L(=50d_0)/\Delta x$	$\Delta_L(=20d_0)/\Delta x$	$\Delta_L(=15d_0)/\Delta x$
64	1.0	11.7	4.3	1.7	1.3
96	0.7	7.8	6.4	2.6	1.9
128	0.5	5.9	8.5	3.4	2.6
192	0.3	3.9	12.8	5.1	3.8
256	0.2	2.9	17.1	6.8	5.1

considered, and the relevant mesh-droplet characteristics are reported in Tab. E.1. Note that values smaller than $\Delta_L/d_0 \approx 15$ cannot be used here, since this would lead to saturated conditions in the gas and thus prevent complete evaporation.

E.5.2 Non-Reacting Case

First, the non-reacting case is considered. Figure E.7(a) shows the average evaporation times obtained from the respective simulations and normalized by the evaporation time of an isolated droplet in an infinite environment given by the initial gas state. It can be seen that the evaporation time not only increases with decreasing $\Delta x/d_0$ (as expected), but also increases with decreasing Δ_L/d_0. This is because no mass can leave the computational domain, and the higher the droplet loading, the higher the average fuel concentration in the domain, so the ambient conditions can no longer be assumed to be constant. Accordingly, the evaporation in an infinite environment no longer provides a suitable reference solution, and the effect of the surrounding droplets must be taken into account. A more appropriate choice of the grid independent reference solution is given here by the evaporation of an isolated droplet in a finite environment with the characteristic volume of each droplet, $V = \Delta_L^3$, which is treated as a closed system that preserves mass and energy between the gas and the liquid phase. The gas state in this system is characterized by a single composition vector (representing the mean composition) that evolves in time, and serves as the ambient condition for the evaporation model. The solution of this zero-dimensional problem was discussed in detail in Appendix E.4.3, where analytical solutions were derived describing the asymptotic regime for sufficiently large Δ_L/d_0. Here, the reference solution is obtained through a numerical solution of the corresponding gas and droplet equations to eliminate the scatter around the asymptotic solution. It should be noted that the calculation of the reference solution does not require data from the simulations and can be done prior to the simulation without significant effort (e.g., by placing the droplet in a single computational cell of volume Δ_L^3 with periodic boundary conditions, and running the CFD solver until

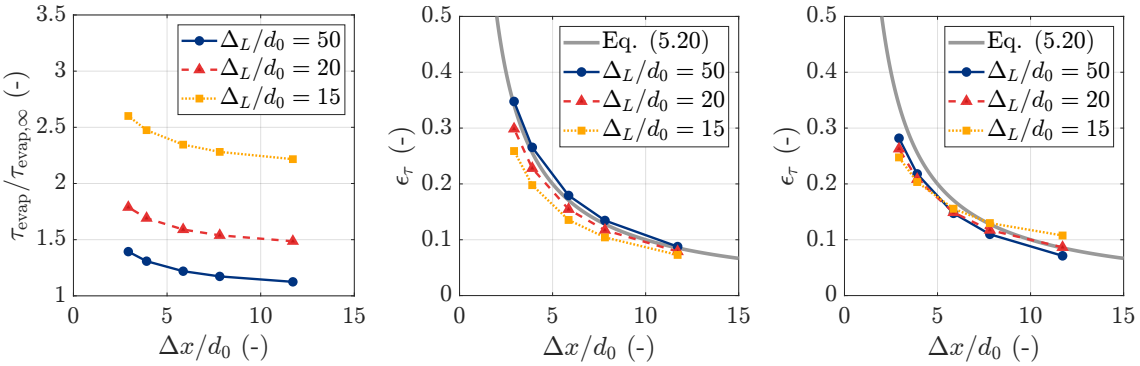

(a) Normalized evaporation time (quiescent environment).

(b) Relative error (quiescent environment).

(c) Relative error (with turbulence).

Figure E.7: Comparison of predicted and calculated errors from the non-reactive simulations. The grid-independent reference solution for the error definition is given by the evaporation of a single droplet in a finite and homogeneous environment with $V = \Delta_L^3$.

the droplet has disappeared).

Simulations are first performed without an initial velocity field to focus exclusively on the effect of multiple droplets, adding the effect of turbulence in a second step. Figure E.7(b) shows the calculated errors from the simulations with quiescent environment and compared to the error relation given by Eq. (5.25), which reduces to Eq. (5.20) for the present setup. The case with $\Delta_L/d_0 = 50$ features excellent agreement with the error relation, since droplets do not interact with each other and can be treated as isolated droplets with constant ambient conditions. For the higher droplet loadings there is a slight deviation from the error relation that becomes more significant as Δ_L/d_0 and $\Delta x/d_0$ decrease, but overall the agreement is still good, indicating that the error relation can be used for systems involving multiple droplets, provided an appropriate reference solution is used. A possible reason for the (slight) deviation could be the nonlinearity of the evaporation model, which implies that the average evaporation time (which is used for comparison with the error relation) is not equivalent to the evaporation time that results from the mean gas state (which is used as reference solution). Another reason could be the fact that the inter-droplet space is increasingly poorly resolved as Δ_L/d_0 and $\Delta x/d_0$ decrease, and therefore discretization effects around the cell containing the droplet might not be captured accurately. Finally, Fig. E.7(c) shows the results for the simulations involving homogeneous turbulence, demonstrating that the errors determined from the simulations still follow the error relation reasonably well. Note that the effect of turbulence is also taken into account in the reference solution by using the characteristic rms velocity as the free-stream velocity.

The case with $N_x = 64$ grid cells per dimension ($\Delta x/d_0 \approx 11.7$) and $\Delta_L/d_0 = 20$ is chosen to give further details on the usage of the error relation given by Eq. (5.25),

which is composed of the three individual relations represented by Eqs. (5.20), (5.22) and (5.24). The first relation, Eq. (5.20), is only a function of the cell size, and directly leads to an error estimate of $\epsilon_\tau = (\Delta x/d_0)^{-1} \approx 8.5\,\%$. The second relation, Eq. (5.22), requires the calculation of the modified mass ratio according to Eq. (5.21). The density ratio is evaluated using the initial conditions, $\rho_{l,0}/\rho_{g,0} \approx 3450$, and for the mass transfer number the value associated with the wet-bulb conditions of the reference solution is used, giving $B_{M,\mathrm{ref}} \approx 1.5$. This gives a modified mass ratio of $\varphi^* \approx 1.225$, and finally leads to an error estimate of $\epsilon_\tau = 0.6\varphi^* \approx 74\,\%$. The relation for convective environments, Eq. (5.24), is a function of the cell Péclet number, which is evaluated here using the rms velocity, leading to $\mathrm{Pe}_{\Delta x} \approx 2.3$. Assuming $\mathrm{Sh}^* \approx 2$, Eq. (5.24) predicts an error of $\epsilon_\tau \approx 15\,\%$. The actual error is then given by the minimum value of the three relations, here $\epsilon_\tau \approx 8.5\,\%$. From the simulation an error of $\epsilon_\tau \approx 8.6\,\%$ is obtained, which is in very good agreement with the error prediction. Note that the nominal droplet distance, Δ_L/d_0, does not appear explicitly in the error relations, but is accounted for by the definition of the reference solution.

E.5.3 Reacting Case

Simulations are now performed including chemical reactions. In that case, the previously used reference solution can no longer be used, as it does not take into account the effects of combustion in the gas phase. A simple approach to prove the validity of the error relations, which implicitly incorporates chemistry effects into the reference solution, would be to feed the evaporation model with the time-varying mean gas state from the simulation. However, this approach has been found to underestimate the evaporation rates, resulting in evaporation times being larger than those obtained from the simulations. This is attributable to the fact that local flame structures around the droplets enhance the evaporation process, which is not reflected by the use of global averages. A suitable reference solution should therefore incorporate the effects of envelope flames on the evaporation process while ensuring consistency with the numerical solution in the limit $\Delta x \to \infty$. Since the reference solution does not need to be explicitly known for the application of the error relations, and since the focus here is on verifying the functional description of the error, the reference solution is determined such that the errors from the simulations fit the given error relation. The results are plotted in Fig. E.8, showing excellent agreement between the calculated errors and the error relation given by Eq. (5.20), except for the largest cell size. This proves that the derived error relations remain valid also in the case of chemically reacting turbulent flows.

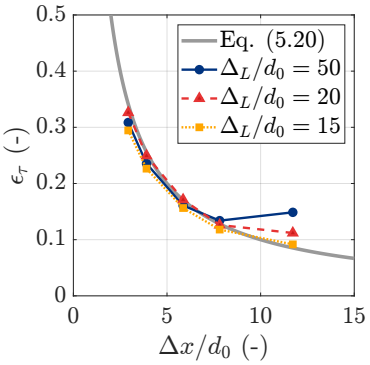

Figure E.8: Comparison of predicted and calculated errors from the reactive simulations. The reference solution that is required for the calculation of the error was determined such that the errors from the simulations fit the error relation.

E.5.4 Conclusions

The validity of the error relations in practical CFD of turbulent reacting flows was demonstrated by comparing *a priori* estimates with *a posteriori* errors from the simulations, where good to excellent agreement was found. This proves that the functional description of the error induced by the PSI-cell model is also valid for practical applications of spray combustion, despite the fact that it was derived based on an isolated droplet in a non-reacting infinite environment.

In practical simulations, the definition of a suitable reference solution is often complicated by the fact that the ambient conditions change in time (caused, for example, by droplet interactions and chemical reactions). However, for an estimation of the numerical error, the reference solution does not need to be explicitly known. The error is then to be interpreted as the error related to a grid-independent solution that is obtained if the cell size approaches infinity.

Appendix F

Grid Convergence Study of the Droplet-Laden Double Shear Layer

A grid convergence study of the temporally evolving droplet-laden double shear layer is performed. The computational setup is described in detail in Sec. 7.1. Three different grid resolutions are considered, and the characteristic grid parameters are reported in Tab. F.1. Compared to the reference case (18 M) that is used for the *a priori* analysis in Ch. 7, the grid resolution is refined and coarsened by 50 %, respectively. The numerical time step is set to $\Delta t = 1.2\,\mu s$ in all three simulations, resulting in a maximum Courant number of $\mathrm{CFL}_{\max} = 0.6$ for the finest mesh resolution. Note that a variable time step was used in Ch. 7, resulting in slight differences in the CP-DNS data. Table F.1 also lists the corresponding CPU hours. Cases 5 M and 18 M are run on a server with a dual Intel Xeon Gold 6226 CPU using 16 and 24 cores, respectively, while case 62 M is run on three servers, each with a dual AMD EPYC 7543 CPU, using 168 cores in total.

A comparison of the mean streamwise velocity and the turbulent kinetic energy at different times is shown in Fig. F.1. Both quantities are calculated by averaging the data in homogeneous directions, and are plotted versus the normalized cross-stream direction. While the mean streamwise velocity is accurately reproduced by all grids, the turbulent kinetic energy exhibits some sensitivity towards the mesh resolution. However, no clear trends can be observed, with both the 5 M and the

Table F.1: Parameters for the grid convergence study of the droplet-laden double shear layer configuration. Note that the simulations were run on different computers, so CPU hours are not directly comparable.

Case	N_x	N_y	N_z	N_{total}	Δx	$\Delta x/d_0$	# cores	CPU hours
5 M	192	224	128	5 505 024	180 µm	6.0	16	834
18 M	288	336	192	18 579 456	120 µm	4.0	24	1968
62 M	432	504	288	62 705 664	80 µm	2.7	168	17 235

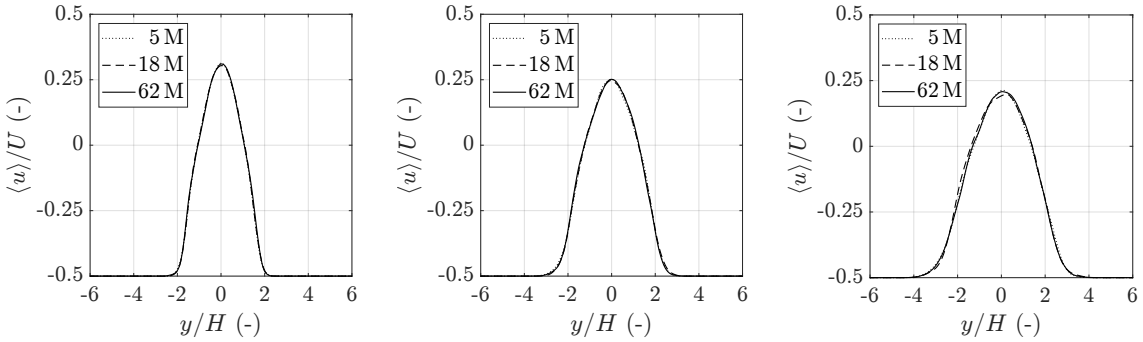

(a) Mean streamwise velocity at times $t/t_j = \{20, 30, 40\}$ (from left to right).

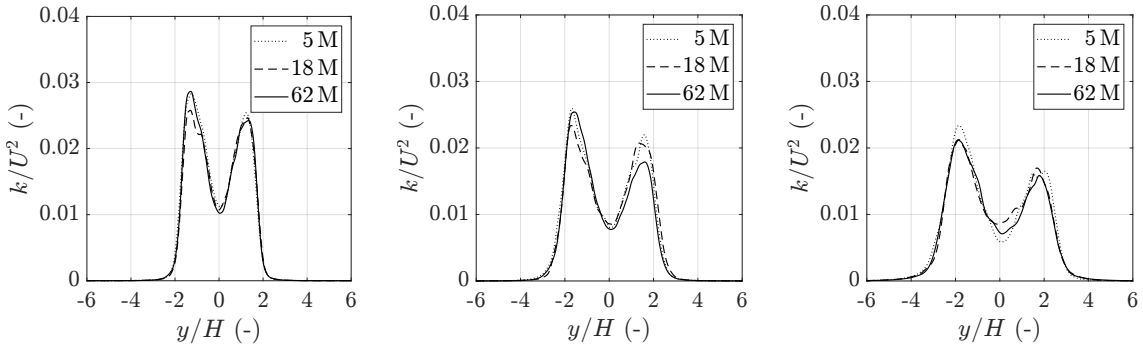

(b) Turbulent kinetic energy at times $t/t_j = \{20, 30, 40\}$ (from left to right).

Figure F.1: Mean streamwise velocity and turbulent kinetic energy obtained from the CP-DNS using different grid resolutions.

18 M meshes giving partially better agreement with the finest grid resolution, so a grid refinement does not generally lead to improvements here. Further, it can be seen that the turbulent kinetic energy profiles are not fully symmetric, which is a result of the initial turbulent perturbations (cf. Fig. 7.2(a)).

Mean and rms profiles of mixture fraction and temperature at different times are shown in Fig. F.2. Overall, the influence of the grid resolution is very small, and all three cell sizes considered here lead to very similar results. Only the temperature distribution shows a slightly higher sensitivity towards the grid resolution, where in regions of the maximum mean temperature differences of the order of about 100 K can be observed (Fig. F.2(c)). Again, the averaged profiles are not fully symmetric, as already observed for the turbulent kinetic energy.

Conditional averages are shown in Fig. F.3. At $t/t_j = 20$, there is a very good match of the conditionally averaged temperatures, whereas at later times the two lower grid resolutions slightly overpredict the conditional mean temperature by about 100 K. For the conditional fluctuations (Fig. F.3(b)) no clear trend can be seen, where both the 5 M and 18 M meshes partially lead to the best agreement with the highest grid resolution (62 M). However, the deviations remain on a relatively small level (about 50 K at maximum).

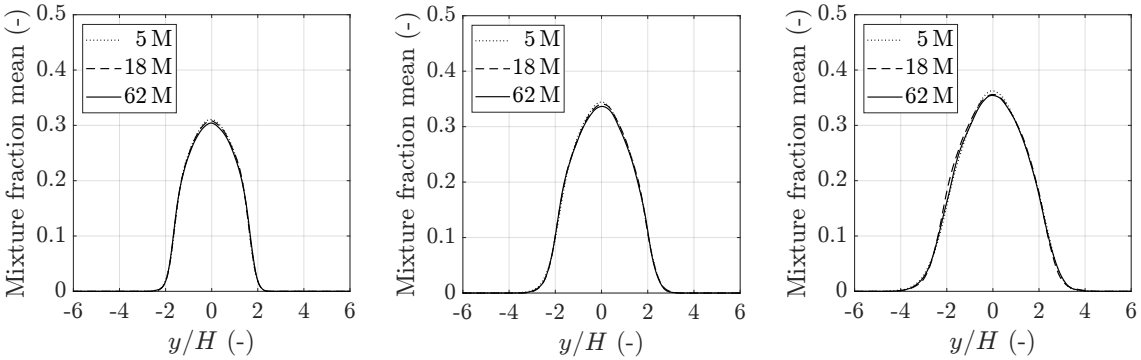

(a) Mixture fraction mean at times $t/t_j = \{20, 30, 40\}$ (from left to right).

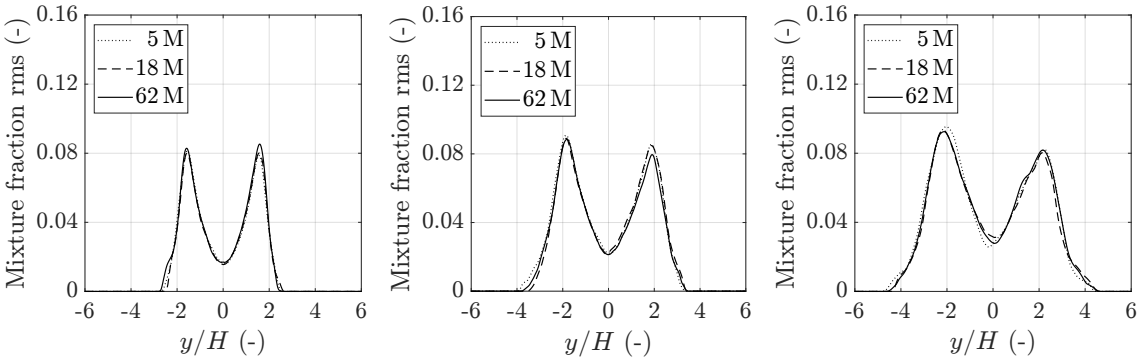

(b) Mixture fraction rms at times $t/t_j = \{20, 30, 40\}$ (from left to right).

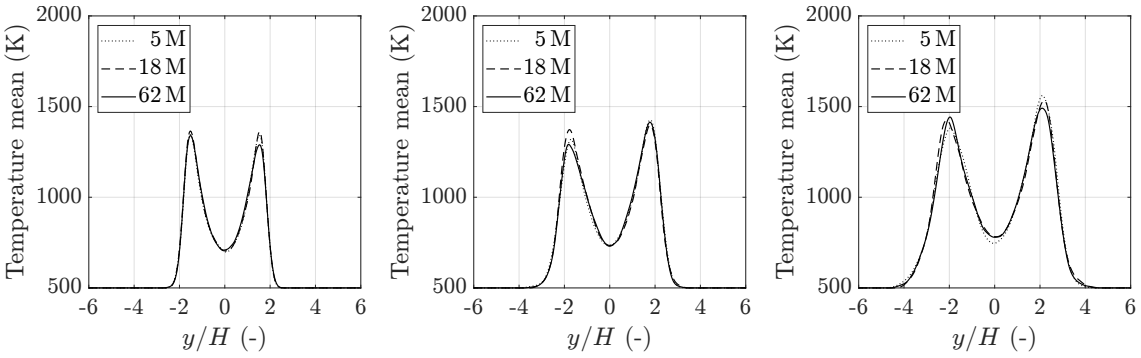

(c) Temperature mean at times $t/t_j = \{20, 30, 40\}$ (from left to right).

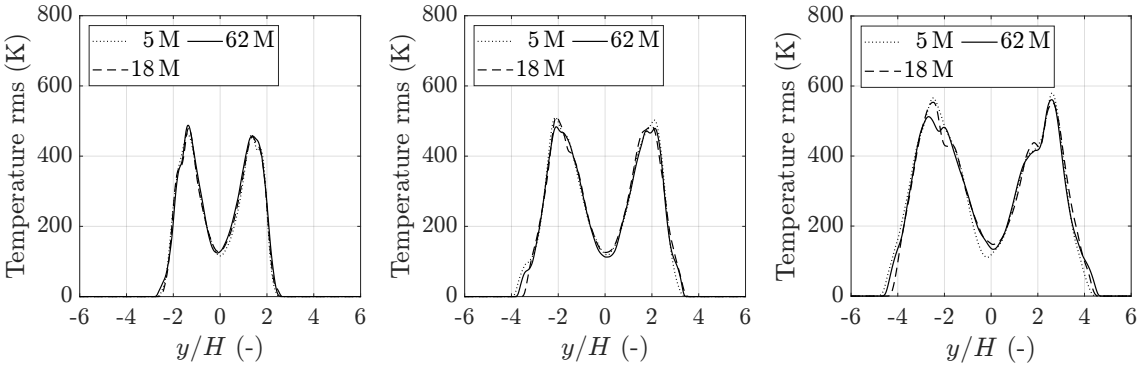

(d) Temperature rms at times $t/t_j = \{20, 30, 40\}$ (from left to right).

Figure F.2: Mean and rms of mixture fraction and temperature obtained from the CP-DNS using different grid resolutions.

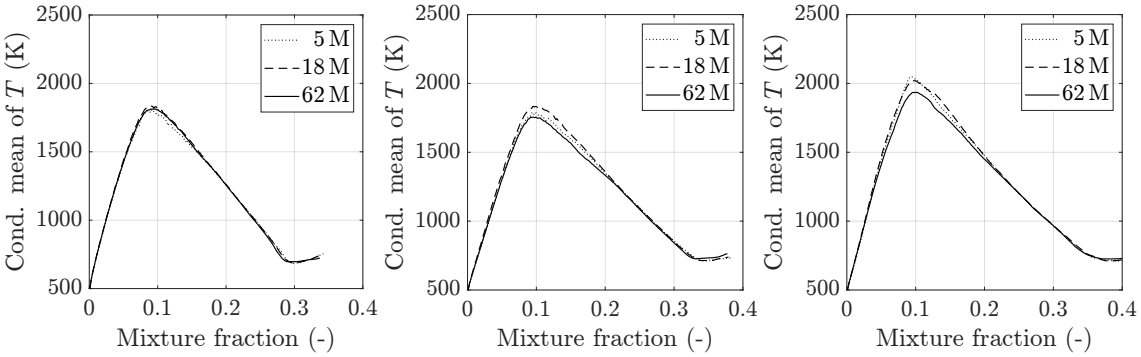

(a) Conditional mean of temperature at times $t/t_j = \{20, 30, 40\}$ (from left to right).

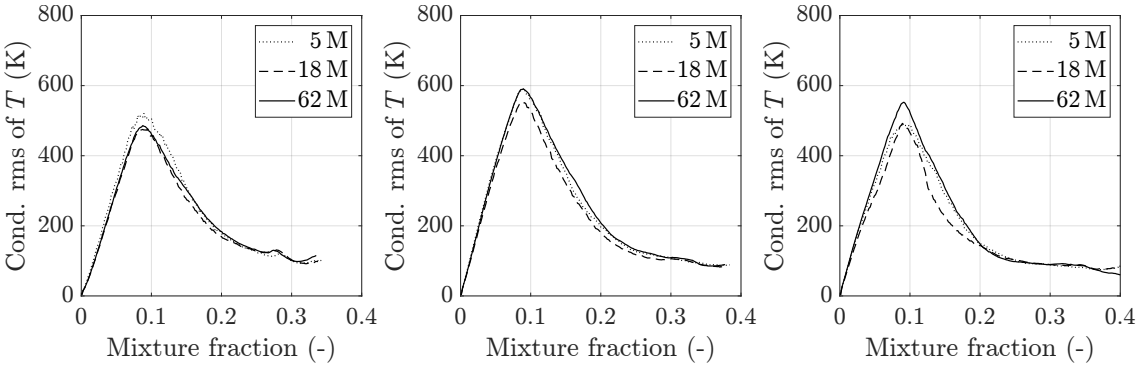

(b) Conditional rms of temperature at times $t/t_j = \{20, 30, 40\}$ (from left to right).

Figure F.3: Conditional mean and rms of temperature obtained from the CP-DNS using different grid resolutions.

Finally, Fig. F.4 provides a comparison of the characteristic droplet properties. Again, the differences between the three mesh resolutions are very small, and the droplet dispersion is accurately described by all three meshes (cf. Fig. F.4(a)). Looking at the distribution of the droplet diameter (Fig. F.4(b)), a clear trend can be observed, where a finer mesh leads to a slight delay of the evaporation process, resulting in larger droplet sizes. This is due to the dependence of the evaporation rate on the local cell size, as discussed in detail in Sec. 5.2. The distribution of the droplet temperature exhibits very good agreement of case 18 M with case 62 M, while the lowest grid resolution leads to slight deviations (cf. Fig. F.4(c)).

The analysis in Sec. 5.2 has elaborated relationships for estimating the error of the evaporation rate and time in Euler-Lagrange simulations, which will now be applied to the shear layer setup. The error of the evaporation time is described by Eq. (5.25), and consists of three individual relations. For the present setup, the relation that treats the computational cell as a closed system, Eq. (5.22), turns out to predict much larger errors than the other two relations and is therefore irrelevant here. Accordingly, the error is mainly determined by Eq. (5.20) as a function of $\Delta x/d_0$, while the effect of convection that is represented by Eq. (5.24) can

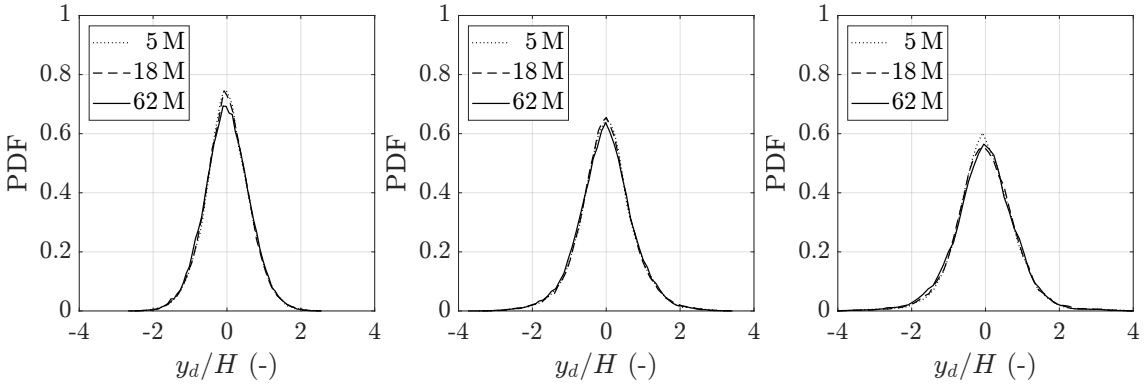

(a) PDF of the droplet positions (y-direction) at times $t/t_j = \{20, 30, 40\}$ (from left to right).

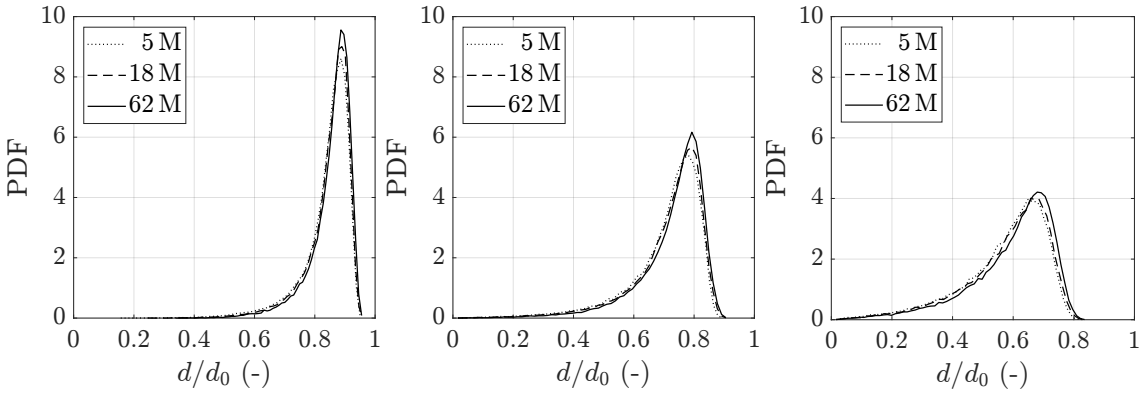

(b) PDF of the droplet diameters at times $t/t_j = \{20, 30, 40\}$ (from left to right).

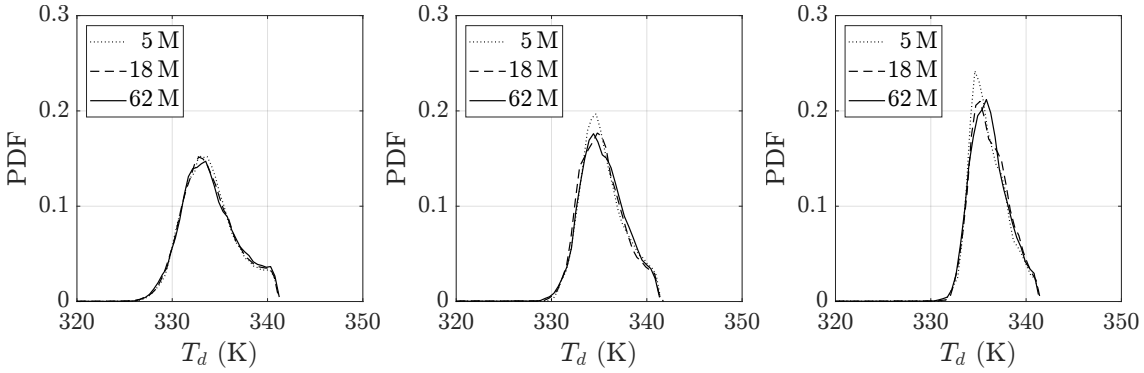

(c) PDF of the droplet temperatures at times $t/t_j = \{20, 30, 40\}$ (from left to right).

Figure F.4: Droplet properties obtained from the CP-DNS using different grid resolutions.

reduce the error depending on the cell Péclet number. The application of Eq. (5.24) requires the definition of suitable ambient conditions for the evaporation process, which is not straightforward due to the temporal development of turbulence and combustion in the shear layer. Here, averaged values for the relative velocity between the droplets and the gas as well as for the diffusivity are used, which are extracted from the CP-DNS and evaluated at the positions of the droplets, while the modified Sherwood number is approximated as two. This results in errors of the order of

$9\,\% \lesssim \epsilon_\tau \lesssim 16\,\%$ for case 5 M, $20\,\% \lesssim \epsilon_\tau \lesssim 25\,\%$ for case 18 M, and $\epsilon_\tau \approx 38\,\%$ for case 62 M. Due to the fact that the evaporation time is not completely covered by the simulation time (droplets still have about 60 % of their initial diameter at the end of the simulation, cf. Fig. F.4(b)), it is to be expected that the errors occurring in the simulations are smaller, as the error of the evaporation time represents an accumulated error of the instantaneous evaporation rate. This could explain why the effect of the cell size is rather small in the simulations as shown by the grid convergence study, in addition to the uncertainty in the definition of suitable ambient conditions for the evaluation of the error relations.

Bibliography

[1] A. Abdelsamie, G. Lartigue, C. E. Frouzakis, and D. Thévenin. The Taylor-Green vortex as a benchmark for high-fidelity combustion simulations using low-Mach solvers. *Computers & Fluids*, 223:104935, 2021.

[2] B. Abramzon and W. A. Sirignano. Droplet vaporization model for spray combustion calculations. *International Journal of Heat and Mass Transfer*, 32 (9):1605–1618, 1989.

[3] Y. Addad, I. Zaidi, and D. Laurence. Quasi-DNS of natural convection flow in a cylindrical annuli with an optimal polyhedral mesh refinement. *Computers & Fluids*, 118:44–52, 2015.

[4] V. Armenio and V. Fiorotto. The importance of the forces acting on particles in turbulent flows. *Physics of Fluids*, 13(8):2437–2440, 2001.

[5] V. Armenio, U. Piomelli, and V. Fiorotto. Effect of the subgrid scales on particle motion. *Physics of Fluids*, 11(10):3030–3042, 1999.

[6] N. Ashgriz. *Handbook of Atomization and Sprays: Theory and Applications*. Springer Science & Business Media, Berlin Heidelberg, 2011.

[7] Y. Baba and R. Kurose. Analysis and flamelet modelling for spray combustion. *Journal of Fluid Mechanics*, 612:45–79, 2008.

[8] S. Basu, A. K. Agarwal, A. Mukhopadhyay, and C. Patel. *Droplets and Sprays: Applications for Combustion and Propulsion*. Springer, 2017.

[9] R. W. Bilger. Conditional moment closure for turbulent reacting flow. *Physics of Fluids*, 5(2):436–444, 1993.

[10] R. W. Bilger. A mixture fraction framework for the theory and modeling of droplets and sprays. *Combustion and Flame*, 158(2):191–202, 2011.

[11] R. W. Bilger, S. B. Pope, K. N. C. Bray, and J. F. Driscoll. Paradigms in turbulent combustion research. *Proceedings of the Combustion Institute*, 30 (1):21–42, 2005.

[12] M. Bini and W. P. Jones. Particle acceleration in turbulent flows: A class of

nonlinear stochastic models for intermittency. *Physics of Fluids*, 19(3):035104, 2007.

[13] M. Bini and W. P. Jones. Large-eddy simulation of particle-laden turbulent flows. *Journal of Fluid Mechanics*, 614:207–252, 2008.

[14] M. Bini and W. P. Jones. Large Eddy Simulation of an evaporating acetone spray. *International Journal of Heat and Fluid Flow*, 30(3):471–480, 2009.

[15] R. B. Bird, W. E. Stewart, and E. N. Lightfoot. *Transport Phenomena*. John Wiley & Sons, New York, second edition, 2002.

[16] G. Borghesi, E. Mastorakos, C. B. Devaud, and R. W. Bilger. Modeling evaporation effects in conditional moment closure for spray autoignition. *Combustion Theory and Modelling*, 15(5):725–752, 2011.

[17] G. Borghesi, E. Mastorakos, and R. S. Cant. Complex chemistry DNS of n-heptane spray autoignition at high pressure and intermediate temperature conditions. *Combustion and Flame*, 160(7):1254–1275, 2013.

[18] J. Boussinesq. Essai sur la théorie des eaux courantes. In *Mémoires présentés par divers savants à l'Académie des Sciences*, volume 23, pages 1–680. Imprimerie Nationale, Paris, France, 1877.

[19] E. Buckingham. On physically similar systems; illustrations of the use of dimensional equations. *Physical Review*, 4(4):345–376, 1914.

[20] A. Burcat and B. Ruscic. Third Millenium Ideal Gas and Condensed Phase Thermochemical Database for Combustion (with Update from Active Thermochemical Tables). Technical report, Argonne National Laboratory, Chicago, Illinois, 2005.

[21] P. L. Carroll and G. Blanquart. A proposed modification to Lundgren's physical space velocity forcing method for isotropic turbulence. *Physics of Fluids*, 25(10):105114, 2013.

[22] C. Celis and L. F. Figueira da Silva. Lagrangian Mixing Models for Turbulent Combustion: Review and Prospects. *Flow, Turbulence and Combustion*, 94: 643–689, 2015.

[23] S. Chandrasekhar. Stochastic Problems in Physics and Astronomy. *Reviews of Modern Physics*, 15(1):1, 1943.

[24] C. Chauveau, F. Halter, A. Lalonde, and I. Gökalp. An experimental study on the droplet vaporization: Effects of heat conduction through the support fiber. In *22nd Annual Conference on Liquid Atomization and Spray Systems (ILASS Europe 2008)*, Lake Como, Italy, 2008.

[25] H. H. Chiu and T. M. Liu. Group Combustion of Liquid Droplets. *Combustion Science and Technology*, 17(3-4):127–142, 1977.

[26] H. H. Chiu, H. Y. Kim, and E. J. Croke. Internal group combustion of liquid droplets. In *Symposium (International) on Combustion*, volume 19, pages 971–980. Elsevier, 1982.

[27] X. Chu, E. Laurien, and D. M. McEligot. Direct numerical simulation of strongly heated air flow in a vertical pipe. *International Journal of Heat and Mass Transfer*, 101:1163–1176, 2016.

[28] M. J. Cleary and A. Y. Klimenko. A Generalised Multiple Mapping Conditioning Approach for Turbulent Combustion. *Flow, Turbulence and Combustion*, 82(4):477–491, 2009.

[29] M. J. Cleary and A. Y. Klimenko. Multiple Mapping Conditioning: A New Modelling Framework for Turbulent Combustion. In T. Echekki, editor, *Turbulent Combustion Modeling*, chapter Seven, pages 143–173. Springer Science & Business Media, 2010.

[30] M. J. Cleary and A. Y. Klimenko. A detailed quantitative analysis of sparse-Lagrangian filtered density function simulations in constant and variable density reacting jet flows. *Physics of Fluids*, 23(11):115102, 2011.

[31] M. J. Cleary, A. Y. Klimenko, J. Janicka, and M. Pfitzner. A sparse-Lagrangian multiple mapping conditioning model for turbulent diffusion flames. *Proceedings of the Combustion Institute*, 32(1):1499–1507, 2009.

[32] R. Clift, J. R. Grace, and M. E. Weber. *Bubbles, Drops, and Particles*. Academic Press, New York San Francisco London, 1978.

[33] P. J. Colucci, F. A. Jaberi, P. Givi, and S. B. Pope. Filtered density function for large eddy simulation of turbulent reacting flows. *Physics of Fluids*, 10(2): 499–515, 1998.

[34] F. Contino, H. Jeanmart, T. Lucchini, and G. D'Errico. Coupling of in situ adaptive tabulation and dynamic adaptive chemistry: An effective method for solving combustion in engine simulations. *Proceedings of the Combustion Institute*, 33(2):3057–3064, 2011.

[35] A. W. Cook, J. J. Riley, and G. Kosály. A Laminar Flamelet Approach to Subgrid-Scale Chemistry in Turbulent Flows. *Combustion and Flame*, 109(3): 332–341, 1997.

[36] C. T. Crowe, M. P. Sharma, and D. E. Stock. The Particle-Source-In Cell (PSI-CELL) Model for Gas-Droplet Flows. *Journal of Fluids Engineering*, 99

(2):325–332, 1977.

[37] C. T. Crowe, J. D. Schwarzkopf, M. Sommerfeld, and Y. Tsuji. *Multiphase Flows with Droplets and Particles*. CRC Press, second edition, 2011.

[38] R. L. Curl. Dispersed Phase Mixing: I. Theory and Effects in Simple Reactors. *American Institute of Chemical Engineers*, 9(2):175–181, 1963.

[39] N. Darabiha, F. Lacas, J. C. Rolon, and S. Candel. Laminar Counterflow Spray Diffusion Flames: A Comparison Between Experimental Results and Complex Chemistry Calculations. *Combustion and Flame*, 95(3):261–275, 1993.

[40] A. Dasgupta, E. Gonzalez-Juez, and D. C. Haworth. Flame simulations with an open-source code. *Computer Physics Communications*, 237:219–229, 2019.

[41] T. E. Daubert and R. P. Danner. *Data compilation tables of properties of pure compounds*. Design Institute for Physical Property Data, American Institute of Engineers, 1985.

[42] J. R. DeBonis. Solutions of the Taylor-Green Vortex Problem Using High-Resolution Explicit Finite Difference Methods. In *51st AIAA Aerospace Sciences Meeting*, page 382, 2013.

[43] F. X. Demoulin and R. Borghi. Modeling of Turbulent Spray Combustion with Application to Diesel Like Experiment. *Combustion and Flame*, 129(3): 281–293, 2002.

[44] C. Dopazo. Relaxation of initial probability density functions in the turbulent convection of scalar fields. *Physics of Fluids*, 22(1):20–30, 1979.

[45] C. Dopazo. Recent developments in pdf methods. In P. A. Libby and F. A. Williams, editors, *Turbulent Reacting Flows*, chapter Seven, pages 375–474. Academic Press, 1994.

[46] C. Dopazo and E. E. O'Brien. An approach to the autoignition of a turbulent mixture. *Acta Astronautica*, 1(9-10):1239–1266, 1974.

[47] P. Durand, M. Gorokhovski, and R. Borghi. An Application of the Probability Density Function Model to Diesel Engine Combustion. *Combustion Science and Technology*, 144(1-6):47–78, 1999.

[48] T. Echekki and E. Mastorakos. *Turbulent Combustion Modeling: Advances, New Trends and Perspectives*, volume 95. Springer Science & Business Media, 2010.

[49] S. Elghobashi. On Predicting Particle-Laden Turbulent Flows. *Applied Scientific Research*, 52(4):309–329, 1994.

[50] S. Elghobashi and G. C. Truesdell. Direct simulation of particle dispersion in a decaying isotropic turbulence. *Journal of Fluid Mechanics*, 242:655–700, 1992.

[51] G. Erlebacher, M. Y. Hussaini, C. G. Speziale, and T. A. Zang. Toward the Large-Eddy Simulation of Compressible Turbulent Flows. *Journal of Fluid Mechanics*, 238:155–185, 1992.

[52] I. S. Ertesvåg and B. F. Magnussen. The Eddy Dissipation Turbulence Energy Cascade Model. *Combustion Science and Technology*, 159(1):213–235, 2000.

[53] G. M. Faeth. Current status of droplet and liquid combustion. In *Energy and Combustion Science*, pages 149–182. Elsevier, 1979.

[54] G. M. Faeth. Evaporation and combustion of sprays. *Progress in Energy and Combustion Science*, 9(1-2):1–76, 1983.

[55] J. H. Ferziger, M. Perić, and R. L. Street. *Computational Methods for Fluid Dynamics*. Springer-Verlag, fourth edition, 2020.

[56] R. O. Fox. *Computational Models for Turbulent Reacting Flows*. Cambridge University Press, 2003.

[57] J. H. Friedman, J. L. Bentley, and R. A. Finkel. An algorithm for finding best matches in logarithmic time. *ACM Transactions on Mathematical Software*, 3:209–226, 1976.

[58] C. Fureby, G. Tabor, H. G. Weller, and A. D. Gosman. A comparative study of subgrid scale models in homogeneous isotropic turbulence. *Physics of Fluids*, 9(5):1416–1429, 1997.

[59] D. V. Gaitonde and M. R. Visbal. High-Order Schemes for Navier-Stokes Equations: Algorithm and Implementation into FDL3DI. Technical report, Air Force Research Lab Wright-Patterson AFB OH Air Vehicles Directorate, 1998.

[60] S. Galindo, F. Salehi, M. J. Cleary, and A. R. Masri. MMC-LES simulations of turbulent piloted flames with varying levels of inlet inhomogeneity. *Proceedings of the Combustion Institute*, 36(2):1759–1766, 2017.

[61] S. Galindo-Lopez, F. Salehi, M. J. Cleary, A. R. Masri, G. Neuber, O. T. Stein, A. Kronenburg, A. Varna, E. R. Hawkes, B. Sundaram, A. Y. Klimenko, and Y. Ge. A stochastic multiple mapping conditioning computational model in OpenFOAM for turbulent combustion. *Computers & Fluids*, 172:410–425, 2018.

[62] F. Gao and E. E. O'Brien. A large-eddy simulation scheme for turbulent

reacting flows. *Physics of Fluids*, 5(6):1282–1284, 1993.

[63] C. Gardiner. *Stochastic Methods: A Handbook for the Natural and Social Sciences*. Springer-Verlag, Berlin Heidelberg, 2009.

[64] E. Garnier, N. Adams, and P. Sagaut. *Large Eddy Simulation for Compressible Flows*. Springer Science & Business Media, Berlin Heidelberg, 2009.

[65] J. W. Gärtner, A. Kronenburg, and T. Martin. Efficient WENO library for OpenFOAM. *SoftwareX*, 12:100611, 2020.

[66] H.-W. Ge and E. Gutheil. Probability density function (PDF) simulation of turbulent spray flows. *Atomization and Sprays*, 16(5), 2006.

[67] H.-W. Ge and E. Gutheil. Simulation of a turbulent spray flame using coupled PDF gas phase and spray flamelet modeling. *Combustion and Flame*, 153(1-2):173–185, 2008.

[68] H.-W. Ge, I. Düwel, H. Kronemayer, R. W. Dibble, E. Gutheil, C. Schulz, and J. Wolfrum. Laser-Based Experimental and Monte Carlo PDF Numerical Investigation of an Ethanol/Air Spray Flame. *Combustion Science and Technology*, 180(8):1529–1547, 2008.

[69] Y. Ge, M. J. Cleary, and A. Y. Klimenko. Sparse-Lagrangian FDF simulations of Sandia Flame E with density coupling. *Proceedings of the Combustion Institute*, 33(1):1401–1409, 2011.

[70] Y. Ge, M. J. Cleary, and A. Y. Klimenko. A comparative study of Sandia flame series (D–F) using sparse-Lagrangian MMC modelling. *Proceedings of the Combustion Institute*, 34(1):1325–1332, 2013.

[71] J. Geiser. Iterative operator-splitting methods with higher-order time integration methods and applications for parabolic partial differential equations. *Journal of Computational and Applied Mathematics*, 217(1):227–242, 2008.

[72] P. Gerlinger. *Numerische Verbrennungssimulation: Effiziente numerische Simulation turbulenter Verbrennung*. Springer-Verlag, Berlin Heidelberg New York, 2005.

[73] D. G. Goodwin, H. K. Moffat, I. Schoegl, R. L. Speth, and B. W. Weber. Cantera: An Object-oriented Software Toolkit for Chemical Kinetics, Thermodynamics, and Transport Processes. `https://www.cantera.org`, 2021. Version 2.5.1.

[74] J. D. Gounder, A. Kourmatzis, and A. R. Masri. Turbulent piloted dilute spray flames: Flow fields and droplet dynamics. *Combustion and Flame*, 159 (11):3372–3397, 2012.

[75] C. Greenshields and H. Weller. *Notes on Computational Fluid Dynamics: General Principles*. CFD Direct Ltd, Reading, UK, 2022. Available online: `https://doc.cfd.direct/notes/cfd-general-principles/index` (accessed June 12, 2023).

[76] E. Hairer and G. Wanner. *Solving Ordinary Differential Equations II: Stiff and Differential-Algebraic Problems*. Springer-Verlag, Berlin Heidelberg, second edition, 1996.

[77] Y. Haruki, A. L. Pillai, T. Kitano, and R. Kurose. Numerical investigation of flame propagation in fuel droplet arrays. *Atomization and Sprays*, 28(4): 357–388, 2018.

[78] E. R. Hawkes, R. Sankaran, J. C. Sutherland, and J. H. Chen. Scalar mixing in direct numerical simulations of temporally evolving plane jet flames with skeletal CO/H2 kinetics. *Proceedings of the Combustion Institute*, 31(1): 1633–1640, 2007.

[79] D. C. Haworth. Progress in probability density function methods for turbulent reacting flows. *Progress in Energy and Combustion Science*, 36(2):168–259, 2010.

[80] F. Herning and L. Zipperer. Calculation of the viscosity of technical gas mixtures from the viscosity of the individual gases. *Gas und Wasserfach*, 79: 69–73, 1936.

[81] P. Hertz. Über den gegenseitigen durchschnittlichen Abstand von Punkten, die mit bekannter mittlerer Dichte im Raume angeordnet sind. *Mathematische Annalen*, 67(3):387–398, 1909.

[82] C. Heye, V. Raman, and A. R. Masri. LES/probability density function approach for the simulation of an ethanol spray flame. *Proceedings of the Combustion Institute*, 34(1):1633–1641, 2013.

[83] C. Heye, V. Raman, and A. R. Masri. Influence of spray/combustion interactions on auto-ignition of methanol spray flames. *Proceedings of the Combustion Institute*, 35(2):1639–1648, 2015.

[84] Hirschfelder, J. O. and Curtiss, C. F. and Bird, R. B. *Molecular Theory of Gases and Liquids*, volume 1. John Wiley & Sons, New York, first edition, 1964.

[85] C. Hollmann and E. Gutheil. Modeling of turbulent spray diffusion flames including detailed chemistry. In *Symposium (International) on Combustion*, volume 26, pages 1731–1738. Elsevier, 1996.

[86] C. Hollmann and E. Gutheil. Flamelet-Modeling of Turbulent Spray Diffusion Flames Based on a Laminar Spray Flame Library. *Combustion Science and Technology*, 135(1-6):175–192, 1998.

[87] A. T. Hsu and J.-Y. Chen. A continuous mixing model for PDF simulations and its applications to combusting shear flows. In *8th Symposium on Turbulent Shear Flows*, 1991.

[88] G. L. Hubbard, V. E. Denny, and A. F. Mills. Droplet evaporation: Effects of transients and variable properties. *International Journal of Heat and Mass Transfer*, 18(9):1003–1008, 1975.

[89] Z. Huo, F. Salehi, S. Galindo-Lopez, M. J. Cleary, and A. R. Masri. Sparse MMC-LES of a Sydney swirl flame. *Proceedings of the Combustion Institute*, 37(2):2191–2198, 2019.

[90] N. Iaroslavtceva, A. Kronenburg, and O. T. Stein. Multiple Mapping Conditioning Mixing Time Scales for Turbulent Premixed Flames. *Flow, Turbulence and Combustion*, pages 1–21, 2022.

[91] IEA. World Energy Outlook 2022. `https://www.iea.org/reports/world-energy-outlook-2022`, 2022. IEA, Paris.

[92] F. A. Jaberi, P. J. Colucci, S. James, P. Givi, and S. B. Pope. Filtered mass density function for large-eddy simulation of turbulent reacting flows. *Journal of Fluid Mechanics*, 401:85–121, 1999.

[93] S. James, M. S. Anand, and S. B. Pope. The Lagrangian PDF Transport Method for Simulations of Gas Turbine Combustor Flows. In *38th AIAA/ASME/SAE/ASEE Joint Propulsion Conference & Exhibit*, 2002.

[94] J. Janicka, W. Kolbe, and W. Kollmann. Closure of the transport equation for the probability density funcfion of turbulent scalar fields. *Journal of Non-Equilibrium Thermodynamics*, 4(1):47–66, 1979.

[95] H. Jasak. *Error Analysis and Estimation for the Finite Volume Method with Applications to Fluid Flows*. PhD thesis, Imperial College, University of London, 1996.

[96] P. Jenny, D. Roekaerts, and N. Beishuizen. Modeling of turbulent dilute spray combustion. *Progress in Energy and Combustion Science*, 38(6):846–887, 2012.

[97] X. Jiang, G. A. Siamas, K. Jagus, and T. G. Karayiannis. Physical modelling and advanced simulations of gas–liquid two-phase jet flows in atomization and sprays. *Progress in Energy and Combustion Science*, 36(2):131–167, 2010.

[98] C. Jiménez, F. Ducros, B. Cuenot, and B. Bédat. Subgrid scale variance and

dissipation of a scalar field in large eddy simulations. *Physics of Fluids*, 13(6): 1748–1754, 2001.

[99] R. J. Kee, F. M. Rupley, E. Meeks, and J. A. Miller. CHEMKIN-III: A FORTRAN Chemical Kinetics Package for the Analysis of Gas-phase Chemical and Plasma Kinetics. Technical Report SAND96-8216, Sandia National Laboratories, Livermore, CA, 1996.

[100] C. A. Kennedy, M. H. Carpenter, and R. M. Lewis. Low-storage, explicit Runge–Kutta schemes for the compressible Navier–Stokes equations. *Applied Numerical Mathematics*, 35(3):177–219, 2000.

[101] N. Khan. *Sparse Lagrangian MMC-LES Combustion Modelling of Liquid Sprays*. PhD thesis, School of Aerospace, Mechanical and Mechatronic Engineering, The University of Sydney, Sydney, NSW 2006, Australia, 2017.

[102] N. Khan, M. J. Cleary, O. T. Stein, and A. Kronenburg. A two-phase MMC–LES model for turbulent spray flames. *Combustion and Flame*, 193:424–439, 2018.

[103] J. Kirchmann, A. Kronenburg, O. T. Stein, and M. J. Cleary. Two-phase sparse-Lagrangian MMC-LES of dilute ethanol spray flames. *Proceedings of the Combustion Institute*, 38(2):3343–3350, 2021.

[104] T. Kitano, J. Nishio, R. Kurose, and S. Komori. Effects of ambient pressure, gas temperature and combustion reaction on droplet evaporation. *Combustion and Flame*, 161(2):551–564, 2014.

[105] A Y. Klimenko. Multicomponent diffusion of various admixtures in turbulent flow. *Fluid Dynamics*, 25(3):327–334, 1990.

[106] A. Y. Klimenko and R. W. Bilger. Conditional moment closure for turbulent combustion. *Progress in Energy and Combustion Science*, 25(6):595–687, 1999.

[107] A. Y. Klimenko and M. J. Cleary. Convergence to a Model in Sparse-Lagrangian FDF Simulations. *Flow, Turbulence and Combustion*, 85(3-4): 567–591, 2010.

[108] A. Y. Klimenko and S. B. Pope. The modeling of turbulent reactive flows based on multiple mapping conditioning. *Physics of Fluids*, 15(7):1907–1925, 2003.

[109] P. E. Kloeden and E. Platen. *Numerical Solution of Stochastic Differential Equations*. Springer, 1992.

[110] E. Komen, A. Shams, L. Camilo, and B. Koren. Quasi-DNS capabilities of OpenFOAM for different mesh types. *Computers & Fluids*, 96:87–104, 2014.

[111] E. M. J. Komen, L. H. Camilo, A. Shams, B. J. Geurts, and B. Koren. A quantification method for numerical dissipation in quasi-DNS and under-resolved DNS, and effects of numerical dissipation in quasi-DNS and under-resolved DNS of turbulent channel flows. *Journal of Computational Physics*, 345:565–595, 2017.

[112] A. Krisman, J. C. K. Tang, E. R. Hawkes, D. O. Lignell, and J. H. Chen. A DNS evaluation of mixing models for transported PDF modelling of turbulent nonpremixed flames. *Combustion and Flame*, 161(8):2085–2106, 2014.

[113] E. H. Kung and D. C. Haworth. Transported Probability Density Function (tPDF) Modeling for Direct-Injection Internal Combustion Engines. *SAE International Journal of Engines*, 1(1):591–606, 2009.

[114] K. K. Kuo. *Principles of Combustion*. John Wiley & Sons, 2005.

[115] C. K. Law. Recent advances in droplet vaporization and combustion. *Progress in Energy and Combustion Science*, 8(3):171–201, 1982.

[116] S. B. Lee. A study on temporal accuracy of OpenFOAM. *International Journal of Naval Architecture and Ocean Engineering*, 9:424–438, 2017.

[117] A. H. Lefebvre and V. G. McDonell. *Atomization and Sprays*. CRC Press, 2017.

[118] R. J. LeVeque. *Finite Volume Methods for Hyperbolic Problems*. Cambridge University Press, Cambridge, 2002.

[119] T. S. Lund. The Use of Explicit Filters in Large Eddy Simulation. *Computers & Mathematics with Applications*, 46(4):603–616, 2003.

[120] T. S. Lundgren. Distribution Functions in the Statistical Theory of Turbulence. *Physics of Fluids*, 10(5):969–975, 1967.

[121] K. Luo, O. Desjardins, and H. Pitsch. DNS of droplet evaporation and combustion in a swirling combustor. *Center for Turbulence Research, Annual Research Briefs*, pages 253–265, 2008.

[122] K. Luo, H. Pitsch, M. G. Pai, and O. Desjardins. Direct numerical simulations and analysis of three-dimensional n-heptane spray flames in a model swirl combustor. *Proceedings of the Combustion Institute*, 33(2):2143–2152, 2011.

[123] B. F. Magnussen. The Eddy Dissipation Concept: A Bridge Between Science and Technology. In *ECCOMAS Thematic Conference on Computational Combustion*, Lisbon, Portugal, 2005.

[124] B. F. Magnussen and B. H. Hjertager. On mathematical modeling of turbulent

combustion with special emphasis on soot formation and combustion. In *Symposium (International) on Combustion*, volume 16, pages 719–729. Elsevier, 1977.

[125] G. Maragkos, S. Verma, A. Trouvé, and B. Merci. Evaluation of OpenFOAM's discretization schemes used for the convective terms in the context of fire simulations. *Computers & Fluids*, 232:105208, 2022.

[126] T. Martin and I. Shevchuk. Implementation and Validation of Semi-Implicit WENO Schemes Using OpenFOAM®. *Computation*, 6(1):6, 2018.

[127] S. Mathur, P. K. Tondon, and S. C. Saxena. Thermal conductivity of binary, ternary and quaternary mixtures of rare gases. *Molecular Physics*, 12(6):569–579, 1967.

[128] M. R. Maxey and J. J. Riley. Equation of motion for a small rigid sphere in a nonuniform flow. *Physics of Fluids*, 26(4):883–889, 1983.

[129] M. R. Maxey, B. K. Patel, E. J. Chang, and L.-P. Wang. Simulations of dispersed turbulent multiphase flow. *Fluid Dynamics Research*, 20(1-6):143, 1997.

[130] A. D. McNaught. *Compendium of Chemical Terminology*. International Union of Pure and Applied Chemistry (IUPAC), 2014.

[131] D. W. Meyer and P. Jenny. Micromixing models for turbulent flows. *Journal of Computational Physics*, 228(4):1275–1293, 2009.

[132] R. S. Miller, K. Harstad, and J. Bellan. Evaluation of equilibrium and non-equilibrium evaporation models for many-droplet gas-liquid flow simulations. *International Journal of Multiphase Flow*, 24(6):1025–1055, 1998.

[133] S. Mitarai, J. J. Riley, and G. Kosály. A Lagrangian study of scalar diffusion in isotropic turbulence with chemical reaction. *Physics of Fluids*, 15(12):3856–3866, 2003.

[134] S. Mitarai, J. J. Riley, and G. Kosály. Testing of mixing models for Monte Carlo probability density function simulations. *Physics of Fluids*, 17(4): 047101, 2005.

[135] J. J. Monaghan. Smoothed particle hydrodynamics. *Reports on Progress in Physics*, 68(8):1703, 2005.

[136] M. Mortensen and R. W. Bilger. Derivation of the conditional moment closure equations for spray combustion. *Combustion and Flame*, 156(1):62–72, 2009.

[137] F. Moukalled, L. Mangani, and M. Darwish. *The Finite Volume Method in*

Computational Fluid Dynamics. Springer-Verlag, Cham Heidelberg New York Dordrecht London, 2016.

[138] C.-D. Munz and T. Westermann. *Numerische Behandlung gewöhnlicher und partieller Differenzialgleichungen*. Springer-Verlag, Berlin Heidelberg New York, third edition, 2012.

[139] M. Muradoglu, S. B. Pope, and D. A. Caughey. The Hybrid Method for the PDF Equations of Turbulent Reactive Flows: Consistency Conditions and Correction Algorithms. *Journal of Computational Physics*, 172(2):841–878, 2001.

[140] B. Naud. *PDF modeling of turbulent sprays and flames using a particle stochastic approach*. PhD thesis, TU Delft, 2003.

[141] S. Navarro-Martinez, A. Kronenburg, and F. Di Mare. Conditional Moment Closure for Large Eddy Simulations. *Flow, Turbulence and Combustion*, 75 (1-4):245–274, 2005.

[142] G. Neuber, A. Kronenburg, O. T. Stein, and M. J. Cleary. MMC-LES modelling of droplet nucleation and growth in turbulent jets. *Chemical Engineering Science*, 167:204–218, 2017.

[143] F. Nicoud, H. B. Toda, O. Cabrit, S. Bose, and J. Lee. Using singular values to build a subgrid-scale model for large eddy simulations. *Physics of Fluids*, 23(8):085106, 2011.

[144] H. Nomura, Y. Ujiie, H. J. Rath, J. Sato, and M. Kono. Experimental Study on High-Pressure Droplet Evaporation Using Microgravity Conditions. In *Symposium (International) on Combustion*, volume 26, pages 1267–1273. Elsevier, 1996.

[145] E. E. O'Brien. The Probability Density Function (pdf) Approach to Reacting Turbulent Flows. *Turbulent Reacting Flows*, pages 185–218, 1980.

[146] Y. Pei, E. R. Hawkes, S. Kook, G. M. Goldin, and T. Lu. Modelling n-dodecane spray and combustion with the transported probability density function method. *Combustion and Flame*, 162(5):2006–2019, 2015.

[147] C. Pera, J. Réveillon, L. Vervisch, and P. Domingo. Modeling subgrid scale mixture fraction variance in LES of evaporating spray. *Combustion and Flame*, 146(4):635–648, 2006.

[148] R. H. Perry, D. W. Green, and J. O. Maloney. *Perry's Chemical Engineers' Handbook*. McGraw-Hill Education, New York, seventh edition, 1997.

[149] N. Peters. Laminar diffusion flamelet models in non-premixed turbulent com-

bustion. *Progress in Energy and Combustion Science*, 10(3):319–339, 1984.

[150] N. Peters. *Turbulent Combustion*. Cambridge University Press, Cambridge, 2004.

[151] C. D. Pierce and P. Moin. A dynamic model for subgrid-scale variance and dissipation rate of a conserved scalar. *Physics of Fluids*, 10(12):3041–3044, 1998.

[152] H. Pitsch. Large-Eddy Simulation of Turbulent Combustion. *Annual Review of Fluid Mechanics*, 38:453–482, 2006.

[153] BP p.l.c. bp Statistical Review of World Energy. `https://www.bp.com/en/global/corporate/energy-economics/statistical-review-of-world-energy.html`, 2022.

[154] T. Poinsot and D. Veynante. *Theoretical and Numerical Combustion*. R.T. Edwards, Inc., Philadelphia, 2005.

[155] B. E. Poling, J. M. Prausnitz, and J. P. O'Connell. *The Properties of Gases and Liquids*. McGraw Hill Professional, Madison, fifth edition, 2000.

[156] S. B. Pope. A Monte Carlo Method for the PDF Equations of Turbulent Reactive Flow. *Combustion Science and Technology*, 25:159–174, 1981.

[157] S. B. Pope. An improved turbulent mixing model. *Combustion Science and Technology*, 28(3-4):131–145, 1982.

[158] S. B. Pope. PDF methods for turbulent reactive flows. *Progress in Energy and Combustion Science*, 11(2):119–192, 1985.

[159] S. B. Pope. Computations of Turbulent Combustion: Progress and Challenges. In *Symposium (International) on Combustion*, volume 23, pages 591–612. Elsevier, 1990.

[160] S. B. Pope. Mapping Closures for Turbulent Mixing and Reaction. *Theoretical and Computational Fluid Dynamics*, 2(5-6):255–270, 1991.

[161] S. B. Pope. Lagrangian PDF Methods for Turbulent Flows. *Annual Review of Fluid Mechanics*, 26:23–63, 1994.

[162] S. B. Pope. Computationally efficient implementation of combustion chemistry using in situ adaptive tabulation. *Combustion Theory and Modelling*, 1:41–63, 1997.

[163] S. B. Pope. *Turbulent Flows*. Cambridge University Press, Cambridge, 2000.

[164] S. B. Pope. Ten questions concerning the large-eddy simulation of turbulent flows. *New Journal of Physics*, 6(1):35, 2004.

[165] S. B. Pope. Small scales, many species and the manifold challenges of turbulent combustion. *Proceedings of the Combustion Institute*, 34(1):1–31, 2013.

[166] J. Pozorski and S. V. Apte. Filtered particle tracking in isotropic turbulence and stochastic modeling of subgrid-scale dispersion. *International Journal of Multiphase Flow*, 35(2):118–128, 2009.

[167] J. Pozorski and M. Wacławczyk. Mixing in Turbulent Flows: An Overview of Physics and Modelling. *Processes*, 8(11):1379, 2020.

[168] A. Prosperetti and G. Tryggvason. *Computational Methods for Multiphase Flow*. Cambridge University Press, Cambridge, 2009.

[169] A. Putnam. Integratable form of droplet drag coefficient. *ARS Journal*, 31 (10):1467–1468, 1961.

[170] V. Raman, H. Pitsch, and R. O. Fox. Hybrid large-eddy simulation/Lagrangian filtered-density-function approach for simulating turbulent combustion. *Combustion and Flame*, 143(1-2):56–78, 2005.

[171] R. H. Rangel and W. A. Sirignano. An Evaluation of the Point-Source Approximation in Spray Calculations. *Numerical Heat Transfer*, 16(1):37–57, 1989.

[172] B. Rembold and P. Jenny. A multiblock joint PDF finite-volume hybrid algorithm for the computation of turbulent flows in complex geometries. *Journal of Computational Physics*, 220(1):59–87, 2006.

[173] M. Rieth, F. Proch, O. T. Stein, M. W. A. Pettit, and A. M. Kempf. Comparison of the Sigma and Smagorinsky LES models for grid generated turbulence and a channel flow. *Computers & Fluids*, 99:172–181, 2014.

[174] H. Ritchie, M. Roser, and P. Rosado. Our World In Data: CO2 Emissions by Fuel. `https://ourworldindata.org/emissions-by-fuel`, 2020.

[175] H. Ritchie, M. Roser, and P. Rosado. Our World In Data: Energy Production and Consumption. `https://ourworldindata.org/energy-production-consumption`, 2022.

[176] P. Sagaut. *Large Eddy Simulation for Incompressible Flows*. Springer Science & Business Media, Berlin Heidelberg, third edition, 2005.

[177] F. Salehi, M. J. Cleary, A. R. Masri, Y. Ge, and A. Y. Klimenko. Sparse-Lagrangian MMC simulations of an n-dodecane jet at engine-relevant conditions. *Proceedings of the Combustion Institute*, 36(3):3577–3585, 2017.

[178] S. Sazhin. *Droplets and Sprays*. Springer, 2014.

[179] S. S. Sazhin. Advanced models of fuel droplet heating and evaporation. *Progress in Energy and Combustion Science*, 32(2):162–214, 2006.

[180] S. S. Sazhin. Modelling of fuel droplet heating and evaporation: Recent results and unsolved problems. *Fuel*, 196:69–101, 2017.

[181] S. S. Sazhin. *Droplets and Sprays: Simple Models of Complex Processes*. Springer, 2022.

[182] S. S. Sazhin, T. Kristyadi, W. A. Abdelghaffar, and M. R. Heikal. Models for fuel droplet heating and evaporation: Comparative analysis. *Fuel*, 85(12-13): 1613–1630, 2006.

[183] H. Schlichting and K. Gersten. *Grenzschicht-Theorie*. Springer-Verlag, Berlin Heidelberg New York, tenth edition, 2006.

[184] E. Sharma and S. De. MMC-LES of spray combustion: Analysis of mixing timescales and flame structure. *Combustion and Flame*, 251:112708, 2023.

[185] E. Sharma, S. De, and M. J. Cleary. LES of a lifted methanol spray flame series using the sparse Lagrangian MMC approach. *Proceedings of the Combustion Institute*, 38(2):3399–3407, 2021.

[186] E. Sharma, S. De, and M. J. Cleary. A fully dynamic mixing time-scale model for the sparse Lagrangian multiple mapping conditioning approach. *Combustion and Flame*, 238:111872, 2022.

[187] W. A. Sirignano. Fuel droplet vaporization and spray combustion theory. *Progress in Energy and Combustion Science*, 9(4):291–322, 1983.

[188] W. A. Sirignano. *Fluid Dynamics and Transport of Droplets and Sprays*. Cambridge University Press, 1999.

[189] W. A. Sirignano. Advances in droplet array combustion theory and modeling. *Progress in Energy and Combustion Science*, 42:54–86, 2014.

[190] J. Smagorinsky. General Circulation Experiments with the Primitive Equations: I. The Basic Experiment. *Monthly Weather Review*, 91(3):99–164, 1963.

[191] V. Smil. *Energy Transitions: Global and National Perspectives*. Praeger, second edition, 2016.

[192] M. Sontheimer, A. Kronenburg, and O. T. Stein. Analysis of Multiphase MMC Coupling Using DNS of a Reacting Double Shear Layer. In *Proceedings of the 9th European Combustion Meeting*, Lisbon, Portugal, 2019.

[193] M. Sontheimer, A. Kronenburg, and O. T. Stein. Analysis of the particle-

source-in-cell model for LES of spray combustion. In *29. Deutscher Flammentag*, Bochum, Germany, 2019.

[194] M. Sontheimer, O. T. Stein, and A. Kronenburg. Analysis of multiphase MMC coupling using DNS of an evolving droplet-laden double shear layer. In *17th Int. Conference on Numerical Combustion*, Aachen, Germany, 2019.

[195] M. Sontheimer, A. Kronenburg, and O. T. Stein. Effects of PSI-cell modeling on subgrid-scale mixture fraction variance for LES of spray combustion. In *30. Deutscher Flammentag*, Hannover-Garbsen, Germany, 2021.

[196] M. Sontheimer, A. Kronenburg, and O. T. Stein. Grid dependence of evaporation rates in Euler-Lagrange simulations of dilute sprays. *Combustion and Flame*, 232:111515, 2021.

[197] M. Sontheimer, A. Kronenburg, and O. T. Stein. Two-phase coupling for MMC-LES of spray combustion. *Proceedings of the Combustion Institute*, 38 (2):3361–3369, 2021.

[198] M. Sontheimer, A. Kronenburg, and O. T. Stein. A comparative study of two-phase coupling models for a sparse-Lagrangian particle method. *Proceedings of the Combustion Institute*, 39(2):2643–2652, 2023.

[199] D. B. Spalding. Mixing and chemical reaction in steady confined turbulent flames. In *Symposium (International) on Combustion*, volume 13, pages 649–657. Elsevier, 1971.

[200] C. Straub, A. Kronenburg, O. T. Stein, G. Kuenne, J. Janicka, R. S. Barlow, and D. Geyer. Multiple mapping conditioning coupled with an artificially thickened flame model for turbulent premixed combustion. *Combustion and Flame*, 196:325–336, 2018.

[201] C. Straub, A. Kronenburg, O. T. Stein, R. S. Barlow, and D. Geyer. Modeling stratified flames with and without shear using multiple mapping conditioning. *Proceedings of the Combustion Institute*, 37(2):2317–2324, 2019.

[202] C. Straub, A. Kronenburg, O. T. Stein, S. Galindo-Lopez, and M. J. Cleary. Mixing Time Scale Models for Multiple Mapping Conditioning with Two Reference Variables. *Flow, Turbulence and Combustion*, 106(4):1143–1166, 2021.

[203] S. Subramaniam and S. B. Pope. A Mixing Model for Turbulent Reactive Flows based on Euclidean Minimum Spanning Trees. *Combustion and Flame*, 115(4):487–514, 1998.

[204] R. Sun and H. Xiao. Diffusion-based coarse graining in hybrid continuum–discrete solvers: Theoretical formulation and a priori tests. *International Jour-*

nal of Multiphase Flow, 77:142–157, 2015.

[205] B. Sundaram, A. Y. Klimenko, M. J. Cleary, and Y. Ge. A direct approach to generalised multiple mapping conditioning for selected turbulent diffusion flame cases. *Combustion Theory and Modelling*, 20(4):735–764, 2016.

[206] W. Sutherland. The Viscosity of Gases and Molecular Force. *Philosophical Magazine*, 36(223):507–531, 1893.

[207] J. C.-K. Tang. *Modelling of Multiphase Flames Using Direct Numerical Simulation and Transported PDF Methods*. PhD thesis, School of Mechanical and Manufacturing Engineering, The University of New South Wales, 2018.

[208] J. C. K. Tang, H. Wang, M. Bolla, A. Wehrfritz, and E. R. Hawkes. A DNS evaluation of mixing and evaporation models for TPDF modelling of nonpremixed spray flames. *Proceedings of the Combustion Institute*, 37(3): 3363–3372, 2019.

[209] J. C. Tannehill, D. A. Anderson, and R. H. Pletcher. *Computational Fluid Mechanics and Heat Transfer*. Taylor & Francis, Washington, D.C., second edition, 1997.

[210] P. Trisjono and H. Pitsch. Systematic Analysis Strategies for the Development of Combustion Models from DNS: A Review. *Flow, Turbulence and Combustion*, 95:231–259, 2015.

[211] S. R. Turns. *An Introduction to Combustion: Concepts and Applications*. McGraw-Hill, New York, second edition, 2000.

[212] S. Ukai, A. Kronenburg, and O. T. Stein. LES-CMC of a dilute acetone spray flame. *Proceedings of the Combustion Institute*, 34(1):1643–1650, 2013.

[213] S. Ukai, A. Kronenburg, and O. T. Stein. Simulation of dilute acetone spray flames with LES-CMC using two conditional moments. *Flow, Turbulence and Combustion*, 93:405–423, 2014.

[214] H. K. Versteeg and W. Malalasekera. *An Introduction to Computational Fluid Dynamics: The Finite Volume Method*. Pearson Education, Amsterdam, second edition, 2007.

[215] D. Veynante and L. Vervisch. Turbulent combustion modeling. *Progress in Energy and Combustion Science*, 28(3):193–266, 2002.

[216] J. Villermaux and J. C. Devillon. Représentation de la coalescence et de la redispersion des domaines de ségrégation dans un fluide par un modèle d'interaction phénoménologique. In *Proceedings of the 2nd International Symposium on Chemical Reaction Engineering*, pages 1–13. Elsevier, 1972.

[217] S. Vo, A. Kronenburg, O. T. Stein, and E. R. Hawkes. Direct Numerical Simulation of Non-premixed Syngas Combustion Using OpenFOAM. In *High Performance Computing in Science and Engineering '16*, pages 245–257. Springer-Verlag, 2016.

[218] S. Vo, O. T. Stein, A. Kronenburg, and M. J. Cleary. Assessment of mixing time scales for a sparse particle method. *Combustion and Flame*, 179:280–299, 2017.

[219] S. Vo, A. Kronenburg, O. T. Stein, and M. J. Cleary. MMC-LES of a syngas mixing layer using an anisotropic mixing time scale model. *Combustion and Flame*, 189:311–314, 2018.

[220] A. W. Vreman. *Direct and large-eddy simulation of the compressible turbulent mixing layer*. PhD thesis, Univeristy of Twente, 1995.

[221] A. W. Vreman. An eddy-viscosity subgrid-scale model for turbulent shear flow: Algebraic theory and applications. *Physics of Fluids*, 16(10):3670–3681, 2004.

[222] B. Wang, A. Kronenburg, G. L. Tufano, and O. T. Stein. Fully resolved DNS of droplet array combustion in turbulent convective flows and modelling for mixing fields in inter-droplet space. *Combustion and Flame*, 189:347–366, 2018.

[223] B. Wang, A. Kronenburg, and O. T. Stein. Modelling Sub-Grid Passive Scalar Statistics in Moderately Dense Evaporating Sprays. *Flow, Turbulence and Combustion*, 103(2):519–535, 2019.

[224] B. Wang, A. Kronenburg, and O. T. Stein. A new perspective on modelling passive scalar conditional mixing statistics in turbulent spray flames. *Combustion and Flame*, 208:376–387, 2019.

[225] Z. J. Wang, K. Fidkowski, R. Abgrall, F. Bassi, D. Caraeni, A. Cary, H. Deconinck, R. Hartmann, K. Hillewaert, H. T. Huynh, N. Kroll, G. May, P.-O. Persson, B. van Leer, and M. Visbal. High-order CFD methods: current status and perspective. *International Journal for Numerical Methods in Fluids*, 72(8):811–845, 2013.

[226] J. Warnatz, U. Maas, and R. W. Dibble. *Combustion*. Springer Science & Business Media, Berlin Heidelberg, fourth edition, 2006.

[227] H. G. Weller, G. Tabor, H. Jasak, and C. Fureby. A tensorial approach to computational continuum mechanics using object-oriented techniques. *Computers in Physics*, 12(6):620–631, 1998.

[228] C. K. Westbrook and F. L. Dryer. Simplified Reaction Mechanisms for the Oxidation of Hydrocarbon Fuels in Flames. *Combustion Science and Technology*, 27(1-2):31–43, 1981.

[229] W. Xie, Q. Xie, H. Zhou, and Z. Ren. An exponential distribution scheme for the two-way coupling in transported PDF method for dilute spray combustion. *Combustion Theory and Modelling*, pages 1–24, 2019.

[230] J. Xu and S. B. Pope. PDF calculations of turbulent nonpremixed flames with local extinction. *Combustion and Flame*, 123(3):281–307, 2000.

[231] J. Yang and A. Kronenburg. Revisiting modelling mixing time scales of Lagrangian filtered density function methods. In *12th Mediterranean Combustion Symposium*, Luxor, Eqypt, 2023.

[232] J.-R. Yang and S.-C. Wong. On the discrepancies between theoretical and experimental results for microgravity droplet evaporation. *International Journal of Heat and Mass Transfer*, 44(23):4433–4443, 2001.

[233] J.-R. Yang and S.-C. Wong. An experimental and theoretical study of the effects of heat conduction through the support fiber on the evaporation of a droplet in a weakly convective flow. *International Journal of Heat and Mass Transfer*, 45(23):4589–4598, 2002.

[234] T. Yang, Y. Yin, H. Zhou, and Z. Ren. Review of Lagrangian stochastic models for turbulent combustion. *Acta Mechanica Sinica*, 37(10):1467–1488, 2021.

[235] Y. Yang, H. Wang, S. B. Pope, and J. H. Chen. Large-eddy simulation/probability density function modeling of a non-premixed CO/H2 temporally evolving jet flame. *Proceedings of the Combustion Institute*, 34(1): 1241–1249, 2013.

[236] A. Yoshizawa. Statistical theory for compressible turbulent shear flows, with the application to subgrid modeling. *Physics of Fluids*, 29(7):2152–2164, 1986.

[237] M. C. Yuen and L. W. Chen. On Drag of Evaporating Liquid Droplets. *Combustion Science and Technology*, 4:147–154, 1976.

[238] F. Zhang, H. Bonart, T. Zirwes, P. Habisreuther, H. Bockhorn, and N. Zarzalis. Direct Numerical Simulation of Chemically Reacting Flows with the Public Domain Code OpenFOAM. In *High Performance Computing in Science and Engineering '14*, pages 221–236. Springer-Verlag, 2015.

[239] J. Zhang, T. Li, H. Ström, and T. Løvås. Grid-independent Eulerian-Lagrangian approaches for simulations of solid fuel particle combustion. *Chem-*

ical Engineering Journal, 387:123964, 2020.

[240] L. Zhao, M. J. Cleary, O. T. Stein, and A. Kronenburg. A two-phase MMC-LES model for pyrolysing solid particles in a turbulent flame. *Combustion and Flame*, 209:322–336, 2019.

[241] X.-Y. Zhao and D. C. Haworth. Transported PDF modeling of pulverized coal jet flames. *Combustion and Flame*, 161(7):1866–1882, 2014.

[242] Y. Zhiyin. Large-eddy simulation: Past, present and the future. *Chinese Journal of Aeronautics*, 28(1):11–24, 2015.

[243] T. Zirwes, P. Habisreuther, M. Hansinger, H. Bockhorn, M. Pfitzner, and D. Trimis. Quasi-DNS Dataset of a Piloted Flame with Inhomogeneous Inlet Conditions. *Flow, Turbulence and Combustion*, 104:997–1027, 2020.

[244] T. Zirwes, M. Sontheimer, F. Zhang, A. Abdelsamie, F. E. Hernández Pérez, O. T. Stein, H. G. Im, A. Kronenburg, and H. Bockhorn. Assessment of Numerical Accuracy and Parallel Performance of OpenFOAM and its Reacting Flow Extension EBIdnsFoam. *Flow, Turbulence and Combustion*, 111(2):567–602, 2023.

[245] M. R. G. Zoby, S. Navarro-Martinez, A. Kronenburg, and A. J. Marquis. Evaporation rates of droplet arrays in turbulent reacting flows. *Proceedings of the Combustion Institute*, 33(2):2117–2125, 2011.

Data Storage

The following table provides details on data storage for the publications that are part of the present work as well as for the present thesis itself.

Table F.2: Details on data storage for the publications that are part of the present work as well as for the present thesis itself. #storage = /itv/storage/ITV-DATABASE/ITV/PUBLICATIONS/; #itvStorage = /itv/itvStorage/oldEmployees/itvmso/

Publication	GitHub (TEX files, scripts)	Simulation data (input files, selected output data, raw data)	Code
ECM 2019 [192]	2019_Sontheimer_ECM	Input files, log files, animations: #storage/CONFERENCE/2019_Sontheimer_ECM	mmcMPDNSFoam-4.x (SHA 7a5755fa)
NC 2019 [194]	2019_Sontheimer_NC	The setup is the same as used in ECM 2019. Animation: #storage/CONFERENCE/2019_Sontheimer_NC	mmcMPDNSFoam-4.x (SHA 25c74473)
DFT 2019 [193]	2019_Sontheimer_DFT	The data can be generated using the MATLAB scripts.	In GitHub repository
PCI 2021 [197]	2021_Sontheimer_PCI	Input files, selected output data, animations: #storage/JOURNAL/2021_Sontheimer_PCI Full simulation data: #itvStorage/SimulationData/2021_Sontheimer_PCI	mmcMPDNSFoam-4.x (SHA 505c4316)
CNF 2021 [196]	2021_Sontheimer_CNF	All data are stored in the GitHub repository	In GitHub repository
DFT 2021 [195]	2021_Sontheimer_DFT	Input files, log files: #storage/CONFERENCE/2021_Sontheimer_DFT Full simulation data: #itvStorage/SimulationData/2021_Sontheimer_DFT	mmcMPDNSFoam-4.x (SHA f26b4773)
PCI 2023 [198]	2023_Sontheimer_PCI	Input files, selected output data: #storage/JOURNAL/2023_Sontheimer_PCI Full simulation data: #itvStorage/SimulationData/2023_Sontheimer_PCI	mmcMPDNSFoam-4.x (SHA fbe026cd)
PHD	2023_Sontheimer_PHD	Full simulation data (time delay model, Sec. 6.4.4): #itvStorage/SimulationData/2023_Sontheimer_PCI Full simulation data (Chs. 7 and 8 and Appendix D.4.2): #itvStorage/SimulationData/2023_Sontheimer_PHD	Time delay model (Sec. 6.4.4): #itvStorage/OpenFOAM/itvmso-4.x/ mmcDropletFoam-4.x_TimeDelay Shear layer (Chs. 7 and 8): mmcDropletFoam-4.x (SHA 7223cce)